Synthesis and Characterization of Multifunctional Nanohydroxyapatite Modified with Bismuth and Iron for Defluoridation, Photocatalysis and Antibacterial Studies

Dagne Bayih Adamu

A Dissertation Submitted to

The Department of Applied Chemistry

School of Applied Natural Science

Presented in Partial Fulfillment of the Requirement for the Degree of Doctor of Philosophy in Material Chemistry

Office of Postgraduate Studies

Adama Science and Technology University

June, 2024

Adama, Ethiopia

Synthesis and Characterization of Multifunctional Nanohydroxyapatite Modified with Bismuth and Iron for Defluoridation, Photocatalysis and Antibacterial Studies

Dagne Bayih Adamu

Supervisors:

Dr. Enyew Amare Zereffa (Major Supervisor)

Dr. Teshome Abdo Segne (Co-Supervisor)

A Dissertation Submitted to

The Department of Applied Chemistry

School of Applied Natural Science

Presented in Partial Fulfillment of the Requirement for the Degree of Doctor of Philosophy in Material Chemistry

Office of Postgraduate Studies

Adama Science and Technology University

June, 2024

Adama, Ethiopia

Declaration

I hereby declare that this Dissertation entitled "**Synthesis and Characterization of Multifunctional Nanohydroxyapatite Modified with Bismuth and Iron for Defluoridation, Photocatalysis and Antibacterial Studies**" is my original work. That is, it has not been submitted for the award of any academic degree, diploma or certificate in any other university. All sources of materials used for this thesis have been duly acknowledged through appropriate citations.

Dagne Bayih Adamu	_____	_____
Name of student	Signature	Date

Recommendation

We, the supervisors of this dissertation, hereby certify that we have read and revised the dissertation entitled "**Synthesis and Characterization of Multifunctional Nanohydroxyapatite Modified with Bismuth and Iron for Defluoridation, Photocatalysis and Antibacterial Studies**" prepared under our guidance by Dagne Bayih Adamu submitted in partial fulfillment of the requirements for the degree of Doctor of Philosophy in Material Chemistry. Therefore, we recommend the submission of the dissertation to the department for further review and defense.

Dr. Enyew Amare Zereffa	_____	_____
Major Supervisor	Signature	Date
Dr. Teshome Abdo Segne	_____	_____
Co-supervisor	Signature	Date

Approval Page of Ph.D. Dissertation

We hereby certify that the recommendations and suggestions made by the board of examiners are appropriately incorporated into the final version of the dissertation entitled "**Synthesis and Characterization of Multifunctional Nanohydroxyapatite Modified with Bismuth and Iron for Defluoridation, Photocatalysis and Antibacterial Studies**" by Dagne Bayih Adamu

Major Supervisor	Signature	Date
Co-supervisor	Signature	Date

We, the undersigned, members of the Board of Examiners of the dissertation open defense by Dagne Bayih Adamu have read and evaluated the dissertation entitled "**Synthesis and Characterization of Multifunctional Nanohydroxyapatite Modified with Bismuth and Iron for Defluoridation, Photocatalysis and Antibacterial Studies**" and examined the candidate during open defense. This is, therefore, to certify that the dissertation is accepted for partial fulfillment of the requirement of the degree of Doctor of Philosophy in Material Chemistry.

Chairperson	Signature	Date
Internal Examiner	Signature	Date
External Examiner 1	Signature	Date
External Examiner 2	Signature	Date

Finally, approval and acceptance of the dissertation is contingent upon submission of its final copy to the Office of Postgraduate Studies (OPGS) through the candidate's Department Graduate Council (DGC) and School Graduate Committee (SGC).

Department Head	Signature	Date
School Dean	Signature	Date
Office of Postgraduate Studies, Dean	Signature	Date

ACKNOWLEDGEMENTS

First of all, my deepest gratitude goes to my advisors, Dr. Enyew Amare and Dr. Teshome Abdo for their all-rounded and unhindered guidance as well as mentorship from the beginning to the end of the work. I would like to acknowledge Ministry of Education, Adama Science and Technology University, and Haramaya University for financial support. I would like to thank the Department of Material Science and Engineering, for the X-ray Diffraction and Ultraviolet-Visible Spectroscopy measurements as well as access to the photo-reactor. I want to appreciate Adama Public Health Referral and Research Laboratory Center for the facilitations of antibacterial activity test.

Furthermore, I would like to give my greatest appreciation to Dr. Lemma Teshome Tufa along with his laboratory staff for characterizing my samples using Scanning Electron Microscopy, Transmission Electron Microscopy and, X-ray Photoelectron Spectroscopy at the Department of Chemistry, Chemistry Engineering and Applied Chemistry, Chungnam National University, Daejeon 34134, Republic of Korea. I am so thankful to Dr. Mohd Hasmizam Razali who helped me in the X-ray Diffraction characterization at the School of Fundamental Science, Faculty of Science and Marine Environmental, Universiti Malaysia Terengganu, 21030 Kuala Nerus, Terengganu, Malaysia.

I want to acknowledge Dr. Bedasa Abdisa and Dr. Dereje Tsegaye for their constructive comments, suggestions, and follow up on the progress of this work. In addition, I want to say thank you to Professor Neeraj K. Gupta who helped me with the write-up of the dissertation, manuscript preparation, and facilitation of sample characterization in India. I am so grateful to my friend Enyew Alemayehu (Ph.D. candidate at the National Taiwan University of Science and Technology) for his support in the preliminary characterizations of samples and collections of up-to-date articles on the subject matter. In addition, I want to thank Mr. Bundi Roba academic and research assistant of the Department of Chemical Engineering, School of Mechanical, Chemical and Materials Engineering, for his help on the use of Ion Selective Electrode during fluoride ions adsorption experiment. Besides, I appreciate all academic and research assistance from the Department of Applied Chemistry, School of Natural Science, for their continued and friendly assistance throughout my work.

Last but not least, I would like to express my gratitude to my family members who have helped me mentally all the time around. I thank my wife Asnakech Abebe for her unconditional love, determination and support.

TABLE OF CONTENTS

CONTENT **PAGE**

LIST OF TABLES

TABLES **PAGE**

LIST OF FIGURES AND ILLUSTRATIONS

FIGURE **PAGE**

LIST OF ABBREVIATIONS AND ACRONYMS

ATCC	American Type Culture Collection
BET	Brunauer-Emmett-Teller
CB	Conduction Band
DMSO	Dimethyl Sulfoxide
DRS	Diffusive Reflectance Spectroscopy
EDS	Energy Dispersive Spectroscopy
FE-SEM	Field Emission- Scanning Electron Microscopy
FTIR	Fourier Transform Infrared
HA	Hydroxyapatite
HR-TEM	High Resolution Transmission Electron Microscopy
MB	Methylene Blue
MBC	Minimum Bactericidal Concentration
MHA	Muller-Hinton Agar
MIC	Minimum Inhibitory Concentration
MO	Methyl Orange
PZC	Point of Zero Charge
SEM	Scanning Electron Microscopy
UV-Vis	Ultraviolet-Visible
VB	Valence Band
WHO	World Health Organization
XPS	X-ray Photoelectron Spectroscopy
XRD	X-ray Diffraction

ABSTRACT

Water pollution and bacterial infection are two serious problems in the globe. The substitution of metal ions in the hydroxyapatite (HA) structure enhances its application for water treatment and antibacterial activity. This work applied co-precipitation technique to synthesize pristine as well as Bi^{3+} and Fe^{3+}doped HA nanomaterials for the investigation of fluoride (F^-) ions removal, methyl orange (MO) dye degradation, and antibacterial activity against E. coli and S. aureus bacteria. X-ray Diffraction characterization results revealed that the synthesized HA nanomaterials have hexagonal structures with a space group of P63/m, and crystallite size in the range of 15.21 – 25.67 nm. The size variation associated with the difference in ionic radii of Ca^{2+}, Fe^{3+} and Bi^{3+} ions. Elemental composition analysis inferred that calcium to phosphorous ratio decreased as the amount of Bi^{3+} and Fe^{3+} increased in the dopant, which shows direct replacement of Ca^{2+} ions. Brunauer-Emmette-Teller analysis confirms the surface areas of pristine, Bi^{3+} doped, Fe^{3+} doped, and Fe^{3+} and Bi^{3+} co-doped samples are 49.77, 55.01, 117.62, and 130.24 m2/g, respectively. Optical property analysis showed that the energy bandgap of the nanomaterials decreased as the amount of Bi^{3+} and Fe^{3+} increased in the doped HA nanomaterials, due to the presence of the different electronic transition of the dopant ions. In the batch F^- ions adsorption experiment, maximum adsorption capacities of 66.12, 78.71, 80.93, and 97.36 mg/g were obtained for pristine, Bi^{3+}doped, Fe^{3+}doped, and Bi^{3+} and Fe^{3+} co-doped adsorbents, respectively. This indicates that the active sites of HA nanomaterial increased through Bi^{3+} and Fe^{3+}ions doping. Similarly, the co-doped HA nanomaterials showed better photocatalytic degradation of MO dye over the pristine and single-doped samples due to the synergistic roles of Fe^{3+} and Bi^{3+} ions. The in vitro antibacterial activity test using the disc diffusion technique indicated that maximum inhibition zones of 18.3 and 18.6 mm were obtained for the co-doped sample against E. coli and S. aureus bacteria, respectively. The values are under the category of strong response but still lower than the inhibition zone of the positive control. Thus, the better performance on F^- adsorption, photocatalytic degradation of MO, and antibacterial activity with the ease of synthesis make Bi^{3+} and Fe^{3+} doped HA nanomaterials attractive for water treatment, environmental remediation and biomedical applications.

***Keywords**: Hydroxyapatite, Doping, Nanomaterials, Adsorption, Degradation, Antibacterial activity*

CHAPTER ONE

INTRODUCTION

1.1 Background of the Study

Water makes up more than 70% of the Earth's surface and is the most vital substance for humans and all other living things (Chenoweth, 2008; Gambhir *et al.*, 2012; Hossain, 2015). However, pollution and other related issues cause a lack of clean, and safe water globally. Rapid industrialization, population growth, and uncontrolled urbanization are some of the reasons that hasten water pollution (Bello *et al.*, 2017). Developing countries, in particular, dump industrial effluents into rivers and streams without the required treatment (Awoke *et al.*, 2016; Tadesse *et al.*, 2018; Zinabu *et al.*, 2018). In Ethiopia, 90–96% of industries release their waste into aquatic environments and open areas without any sort of treatment (Tadesse *et al.*, 2018). On the other hand, research report indicates that the main supply of drinking water in developing nations is groundwater. However, in many places of the world, high amounts of fluoride and other potentially harmful substances have made many groundwater sources unfit for human use (Shaji *et al.*, 2024). Fluoride (F^-) is one of the major water pollutants mainly from the soil and to some extent from industrial activities. More than 260 million people globally, nearly 81 million in Africa, and 8 million in Ethiopia have been exposed to drinking water containing F^- levels greater than the WHO-recommended limit (1.5 mg/L) (Demelash *et al.*, 2019; Shaji *et al.*, 2024). It harms human health when consumed through drinking water in quantities above 1.5 mg/L over an extended period. The most prominent health risk is dental and skeletal fluorosis, observed in diverse world states, including Ethiopia (Fernando *et al.*, 2019; Tomar *et al.*, 2015).

Techniques like precipitation, ion exchange, adsorption, membrane separation and electrochemical approaches are reported in the literature for removing F^- ions (Alhassan *et al.*, 2021; He *et al.*, 2020; Huang L. *et al.*, 2022). However, it has been discovered that the adsorption process outperforms other methods regarding price, effectiveness, design simplicity, and convenience (Gai Deng, 2021; He *et al.*, 2020; Rathnayake *et al.*, 2022). Various adsorbents like aluminum-containing materials (Alhassan *et al.*, 2021), modified-biomaterials (Hegde *et al.*, 2020; Huang L. *et al.*, 2022), composites (Wei *et al.*, 2022), metal oxide and hydroxides (Gai Deng, 2021; Tolkou *et al.*, 2021), carbon-based materials (Gai Deng, 2021; Tolkou *et al.*, 2021; Wan *et al.*, 2021), natural minerals and industrial wastes (Gai

Deng, 2021; He *et al.*, 2020; Olejarczyk *et al.*, 2022), metal-organic frameworks (He *et al.*, 2020; Tolkou *et al.*, 2021), and layered double hydroxides (He *et al.*, 2020) have been used for F^- ions removal. Nevertheless, most adsorbents are not readily available, are expensive, applied at a limited pH scale, have sluggish removal rate, and inefficient in removing F^- ions (Alhassan *et al.*, 2021; Huang L. *et al.*, 2022; Rathnayake *et al.*, 2022).

The other pollutants affecting water quality are dyes released from different factories, like the textile industry (Liu *et al.*, 2022). Nearly 50% of the synthetic dyes used in the textile industry are thought to leak into the environment because they do not bond to the fabric (Krishnamoorthy *et al.*, 2021). From the synthetic dyes used in different industries, azo dyes accounts the largest percentage (Wu *et al.*, 2021). Azo dyes can have detrimental effects on the quality of surface and groundwater by obstructing light, interfering with plant and algae photosynthesis, and lowering the amount of dissolved oxygen in the water (Liu *et al.*, 2022). It has also been reported that azo dyes have a very poisonous and carcinogenic effect for human and aquatic life (Dutta *et al.*, 2022; Krishnamoorthy *et al.*, 2021; Liu *et al.*, 2022). One of the synthetic azo dye is methyl orange (MO), which is used in different industries. MO is toxic, carcinogenic, mutagenic, tumorigenic, teratogenic, and genotoxic (Dutta *et al.*, 2022; Khan A. U. *et al.*, 2022; Kishor *et al.*, 2021).

Various techniques are available for the removal of MO dye, such as chemical oxidation, biological treatment, membrane separation, adsorption, and photocatalysis (Dutta *et al.*, 2022; Khan A. U. *et al.*, 2022; Kishor *et al.*, 2021). Heterogeneous photocatalysis becomes crucial for transforming organic contaminants into non-toxic forms (Liu *et al.*, 2016; Shariffuddin *et al.*, 2013). Several different nanostructured materials have been utilized to photodegrade MO dye. TiO_2, ZnO, CuO, Fe_2O_3, SnO_2, NiO, MnO_2, graphene oxide, and metallic nanoparticles are a few of them (Emmanuel *et al.*, 2023; Kgatle *et al.*, 2021; Raliya *et al.*, 2017). However, most of these photocatalysts have their drawbacks, including the high electron-hole pair recombination rate, high cost, and limited availability, and the majority of them are used in the UV region only, which accounts for just 3-5% of solar radiation (Chahal *et al.*, 2020; Folawewo Bala, 2022; Lee *et al.*, 2020).

One of the growing dilemma in the healthcare sector is caused by the proliferation of bacterium types that are resistant to antibiotics (Chen *et al.*, 2019). Statistics show that antibiotic-resistant bacterial illnesses claimed the lives of almost 700,000 people in 2015; by 2050, the number of

deaths from these infections is predicted to rise to 10,000,000 (Yang *et al.*, 2023). *Enterococcus faecium*, *Staphylococcus aureus*, *Klebsiella pneumoniae*, *Acinetobacter baumannii*, *Pseudomonas aeruginosa*, *Enterobacter* spp., and *Escherichia coli* are antibiotic resistant bacteria having high morbidity and mortality rates (Edis *et al.*, 2022). Typically, traditional systematic drug administration, in which antibiotics are absorbed into the bloodstream, treats infections brought on by various bacteria. However, it has significant disadvantages, like the limited drug penetration into the target region. An alternate therapeutic strategy is to develop an antibacterial agent directly to the surgical site (Prodan *et al.*, 2019).

One of the nanomaterials that have been used in different areas of research is hydroxyapatite (HA). HA is a bio-ceramic having a composition similar to the minerals that make up bone and teeth (Yuan *et al.*, 2018). HA with chemical representation $Ca_{10}(PO_4)_6(OH)_2$, possesses hexagonal symmetry with space group of $P6_3/m$ (Tite *et al.*, 2018). It has been employed in biomedical fields due to its biocompatibility, bioactivity, osteoconductivity and similar composition to mammalian hard tissue (Lim *et al.*, 2023). HA is frequently utilized as an implant or coating for metallic implants due to its limited solubility in physiological conditions, strong osseointegration potential, osteoconductive, bioactive, and does not cause inflammatory reactions when it comes into contact with hard tissues (Ungureanu *et al.*, 2023). In general, HA has a variety of applications, including tissue engineering, drug delivery, cancer treatment, sensors, fertilizer, fluorescence and chromatography (Al-Ahmed *et al.*, 2020; Fihri *et al.*, 2017). Due to the high stability under reducing and oxidizing circumstances, advantageous surface features, amphoteric nature and porosity, HA emerges as a leading choice as an adsorbent and photocatalyst (Chen *et al.*, 2018; Guo *et al.*, 2019; Manoj *et al.*, 2019). However, HA needs modification due to its inefficient in removing some of the pollutants under some circumstances, its high bandgap energy, and less bactericidal activity (Chen *et al.*, 2019; Mohseni-Salehi *et al.*, 2018; Tomar *et al.*, 2015).

The tunable crystalline structure of HA makes it easy to modify its properties in several ways, including ion doping/substitution. Doping HA with dozens of different ions has been attempted to advance its applicability (Yilmaz *et al.*, 2019). HA's physicochemical properties are expected to differ significantly depending on the kind of substitution and the site under consideration (Ca^{2+}, PO_3^{4-}, and OH^-) (Cacciotti, 2019). Both cationic and anionic substitutions in the HA structure altered the degree of crystallinity, crystallite size, solubility, thermal stability, lattice characteristics, unit cell volume, surface charge distribution, morphology, and

others (Cacciotti, 2016; Reger *et al.*, 2019). However, in order to change the optical as well as magnetic properties, and to make the HA surface more positive, cationic substitution is preferable over the anionic substitution (Chen *et al.*, 2018; Kurinjinathan Arul, 2018), and the change in these properties broadens the application areas. Notably, more than one metal ion (co-doping/multiple substitutions) improves the various properties and applications due to a synergetic effect (Sprio *et al.*, 2020; Yilmaz *et al.*, 2019). According to previous studies, doping HA with various metal ions boosted its capacity for adsorption, antimicrobial activity, and photocatalytic performance (Chen *et al.*, 2018; Hossain *et al.*, 2022; Nam *et al.*, 2018).

HA has been synthesized and studied in a variety of forms and sizes. Compared to micro-size, nano-size HA demonstrates improved properties and applications. Smaller particle sizes, regulated morphology, and higher specific surface areas have sparked significant interest in fundamental scientific research and amassed various applications (Subramanian *et al.*, 2019). Pristine and ion-substituted HA can be synthesized using sol-gel, aqueous precipitation, hydrothermal, and micro-emulsion techniques. Each method has benefits and drawbacks of its own. Particle aggregation, difficulty in managing the process parameters, and the expense of raw materials or equipment are a few drawbacks (Fihri *et al.*, 2017). Regarding this, comparatively aqueous precipitation is an energy-saving, affordable, less time-consuming, eco-friendly, non-intermediate formation, high yield, and facile method (Sharma *et al.*, 2022).

In recent times, compounds of bismuth (Bi) have been the focus of exploration for the replacement of photocatalysts available on the market due to their high photocatalytic performance and exceptional properties, such as non-toxicity, ability to convert light to heat, strong light absorption in different regions, superior chemical stability, low recombination rate, facilitate the migration and separation of photo-generated charge carriers, and rich crystal chemistry (Ajiboye *et al.*, 2021), especially when they contain Bi in the +3 state are the most efficient and stable photocatalysts. Similarly, iron-containing compounds have the advantages of a narrow band gap, high conductivity, intense light trapping, inexpensive, and wide availability (Hrubiak *et al.*, 2018; Laurier *et al.*, 2013). Moreover, the presence of metal ions in the structure of photocatalytic material can trap both holes and electrons and facilitate the production of reactive species like hydroxyl and super-oxide radicals (Mancuso *et al.*, 2020). The availability of iron (Fe) can improve the separation characteristics of HA as an adsorbent and photocatalyst, since Fe^{3+} ions doped HA has strong paramagnetic properties (Iannotti *et al.*, 2017; Morsi Abd Elhamid, 2019), and such materials are easily separated by applying

external magnetic fields (Yu *et al.*, 2018). Moreover, Fe-containing materials strongly tend to remove F^- ions (Corral-Capulin *et al.*, 2019; Ogata *et al.*, 2020). Generally, Fe and Bi are relatively non-toxic (Tite *et al.*, 2018; Vazquez-Munoz *et al.*, 2020), and the presence of metal ions in the HA structure improves adsorption, photocatalysis and antibacterial activity.

Therefore, finding a suitable material with a strong capacity to remove the F^- ions, better photocatalytic performance for degrading dye molecules, and strong antibacterial activity is an open door for research.

To the best of current knowledge, no research on the synthesis and applications of Bi^{3+} and Fe^{3+} ions co-doped HA is disclosed in the open literature. In addition, no research reports are available on the defluoridation and photocatalytic applications of Bi^{3+} and Fe^{3+} single-doped HA nanomaterials. Thus, this dissertation work aimed to prepare pristine and doped HA using Bi^{3+} and Fe^{3+} ions by employing co-precipitation technique for the applications of F^- ions removal, photocatalytic degradation of MO and antibacterial activity against *Staphylococcus aureus* (*S. aureus*) and *Escherichia coli* (*E. coli*) bacteria.

1.2 Statement of the Problem

The discharge of significant amount of MO dye, and the presence of excess F^- ions in the water system deteriorate its quality for different purposes. On the other hand, multi-drug resistant bacterial infection is increasing at an alarming rate. Because of these, researchers have been exploring for materials to treat the targeted water pollutants, and bacterial infections by using various techniques. Unfortunately, the actual implementation of many of the techniques is constrained by high prices, the production of secondary sludge, inefficiency of the materials, toxicity of the materials, and other issues. Even if HA becomes the primary choice for defluoridation by different researchers, still it needs modification to further enhance the adsorption capacity. Previous reports indicate that trivalent metal ions doping in the HA structure increased the F^- ions removal capacity compared to the pristine and divalent metal ions doped HA (Chen *et al.*, 2018; Nie *et al.*, 2012).

Similarly, high cost, bandgap problem, and low adsorption capacity are some of the drawbacks of photocatalytic materials used for the degradation of organic dyes. However, metal ions doped HA nanomaterials show a promise in the photocatalysis process and this open up new

avenues for environmental remediation (Hossain *et al.*, 2022; Manoj *et al.*, 2019), since they have strong light absorption tendency and lower bandgap energy. Previous reports indicate that the bandgap of HA decreased through doping of Cu^{2+}, Fe^{3+}, Tb^{3+}, and Ti^{4+} metal ions (Hadagalli *et al.*, 2021; Jiménez-Flores *et al.*, 2017; Kalita *et al.*, 2022). However, further improvement on the properties and photocatalytic performance of HA-based nanomaterials still is necessary. In addition, the synergistic roles of multiple metal ions doping (co-doping) in the photocatalytic performance of HA nanomaterial have to be evaluated.

In the same way, the presence of several metal ions like Ag^{+}, Cu^{2+}, Mg^{2+}, Zn^{2+}, Ga^{3+}, and Sm^{3+} in the HA biomaterial structure enhance the antibacterial activity (Iconaru *et al.*, 2020; Mariappan *et al.*, 2017; Shokri *et al.*, 2022; Yuan *et al.*, 2018). However, prolonged exposure of some of the metal ions, like Ag^{+}, causes cytotoxicity to human cell (Li *et al.*, 2022; Qiao *et al.*, 2019). Thus, the use of relatively non-toxic metal such as Bi, and Fe (Vazquez-Munoz *et al.*, 2020; Zeng *et al.*, 2019), for antibacterial activity have an advantage.

Therefore, the intention of this research work is to enhance the capacity of HA nanomaterial for environmental remediation and biomedical application through metal ions doping.

Substitution of Ca^{2+} ions by trivalent metal ions like Bi^{3+} and Fe^{3+} ions is expected to bring a positive surface charge on the HA structure which is more favorable to interact with F^{-} ions and MO (anionic dye) through electrostatic interaction. Moreover, the bandgap energy, photocatalytic activity, defluoridation capacity, and antibacterial property of HA will be tuned through modification with these metal ions.

1.3 Objective

1.3.1 General Objective

The general objective of this dissertation work was to synthesize Bi^{3+} and Fe^{3+} modified HA nanomaterials for the applications of F^{-} ions removal, dye degradation, and antibacterial activity.

1.3.2 Specific Objectives

The specific objectives of the dissertation work were:

- To synthesize pristine HA, Bi^{3+} ions doped HA, Fe^{3+} ions doped HA, and (Bi^{3+}, Fe^{3+}) ions co-doped HA nanomaterials
- To characterize the synthesized nanomaterials using XRD, FTIR, SEM, FE-SEM, HR-TEM, EDS, XPS, BET, and UV-Vis/DRS
- To investigate the F^{-} ions removing efficiency of the synthesized nanomaterials
- To investigate the photocatalytic degradation of MO dye using the synthesized nanomaterials
- To investigate the antibacterial activities of the synthesized biomaterials against *E. coli* and *S. aureus* bacterial strains

1.4 Significance of the Study

Safe drinking water is necessary for human health, and this can be assured by removing pollutants from water by applying environmentally friendly techniques, using low-cost, recyclable, and environmentally friend materials. HA-based nanomaterials are synthesized using an economical and facile co-precipitation method from low-cost precursors, at low temperatures, and the materials also applied at low temperature. Hence, modified HA multifunctional materials developed for this work are degradable, recyclable, and less toxic, does not contribute to any secondary pollution and resulted with improved performances.

As a result, the outcome of this research work will be used as a baseline for researchers to develop further low-cost, recyclable and environmentally friendly adsorbent, photocatalyst and antibacterial agents based on HA and its modified forms. Moreover, the finding of the work may be useful for the community, regulatory body, and health sector.

1.5 Scope of the Study

This research work limited to the synthesis, characterization, and investigation of pristine HA, Bi^{3+}ions doped HA, Fe^{3+}ions doped HA, and $Bi^{3+}$and Fe^{3+}ions co-doped HA nanomaterials. The doped HA nanomaterials were synthesized with different amounts of Bi^{3+} and Fe^{3+} ions. The synthesized nanomaterials were characterized using FTIR, XRD, EDS, BET, SEM, FE-

SEM, HR-TEM, XPS and UV-Vis/DRS techniques. The synthesized and characterized materials were used to remove F^- ions, for the photocatalytic degradation of MO dye, and as an antibacterial activity against *E. coli and S. aureus* bacteria. Due to time, resource and financial constraints, the antibacterial study focus on only the two bacterial strains.

CHAPTER TWO

LITERATURE REVIEW

2.1 Hydroxyapatite

HA, a key inorganic substance in biology and chemistry, is a top-notch substance with a wide range of biological uses (Adeogun *et al.*, 2018). It is a member of calcium orthophosphates, simply abbreviated as $CaPO_4$, with a Ca/P ratio of 1.67. Different forms of $CaPO_4$ are available with a Ca/P ratio in the range of 0.5 – 2. The Ca/P ratio in the range of 1.5 – 1.67 are called apatite (Dorozhkin, 2016). Apatite have general formula $M_{10}(XO_4)_6Y_2$. "M" can be any of the following: $Ca^{2+,}$ Sr^{2+}, Ba^{2+}, Cd^{2+}, Pb^{2+} and sometimes Na^+, K^+, and Al^{3+}; "XO_4" is typically PO_4^{3-}, VO_4^{3-}, or AsO_4^{3-}; and "Y" is a monovalent anion, such as OH^-, F^- and Br^- (Gopi *et al.*, 2015). HA is the naturally occurring and the most stable (next to fluorapatite) form of calcium orthophosphates (Dorozhkin, 2016; Jeong *et al.*, 2019).

In its crystal lattice, HA displays ionic (Ca–O) and covalent (P–O and O–H) bonding. A contact angle of roughly 10 degree has been reported for pure HA, which is incredibly hydrophilic. Since HA is a ceramic calcium compound, it is brittle but has a very high compressive strength (up to 917 MPa) and a very weak tensile property (Panda *et al.*, 2021). In theory, HA is composed of 18.45 weight percent P and 39.68 weight percent Ca, with a weight ratio of 2.151 for Ca to P (Lim *et al.*, 2023). The HA naturally found in bone tissues takes the shape of needle-like or rod-like crystals that are nanometer-sized and measure 5 - 25 nm in width, 50 - 60 nm in length, and thicknesses of 2 - 5 nm. The apatite phase is poorly crystallized and non-stoichiometric, with ions such as F^-, Na^+, and CO_3^{2-} embedded in a collagen matrix (Balhuc *et al.*, 2021; Suresh Kumar *et al.*, 2020).

Pure HA powder usually has a white color, conversely, the colors of natural apatite might be dark, gray, greener, or yellower, resembling the stains caused by dental fluorosis (Agbeboh *et al.*, 2020). Basically, microcluster and nanocrystalline are two forms of HA currently used in the biomedical as well as environmental fields. Because of their larger surface area, nanocrystalline HA have a high affinity for binding to materials, which could enhance re-mineralization. It is also believed that nanocrystalline HA are more efficient in managing biofilms than micro- size HA. Particles that are nanoscale are sufficiently tiny to have direct interactions with bacterial membranes (Chen *et al.*, 2021). The length scale of a nanoscale is 1–100 nm. These dimensions give rise to a unique particle activity. Their small size and vast

response surface improve the material's hydration, giving it improved physical and chemical properties (Bordea *et al.*, 2020). Because of its unique characteristics, which include its small size, highly specialized surface area, and more active site, nanocrystalline HA demonstrates outstanding efficiency as an absorbent material when compared to the larger micro scale HA. Because of the high surface energy required by the highly specific surface area, co-precipitation and the ionic exchange process are encouraged. Atoms are exposed on the surface due to a more active location. When it comes into contact with the surrounding, it can connect with foreign materials (Balasooriya *et al.*, 2022).

Based on the different arrangement of the OH group in the crystal structure, HA exists in two different forms, monoclinic (space group $P2_1/b$) with lattice parameters a = 9.421 Å, b = 2a, c = 6.881 Å, $\gamma = 120^o$ and hexagonal (space group $P6_3/m$) having lattice parameters a = b = 9.432 Å, c = 6.881 Å, $\gamma = 120^o$ in which the hexagonal one is the stable one (Dorozhkin, 2016; Jeong *et al.*, 2019; Tite *et al.*, 2018). The disordered arrangement of OH groups, where the head-to-tail and tail-to-head arrangements alternate throughout the channel in the hexagonal symmetry, contrasts with the ordered, head-to-tail arrangement of OH groups located in the center of every other Ca-II triangle in the monoclinic symmetry (Dorozhkin, 2016). The hexagonal unit cell structure of HA is given in Figure 1.

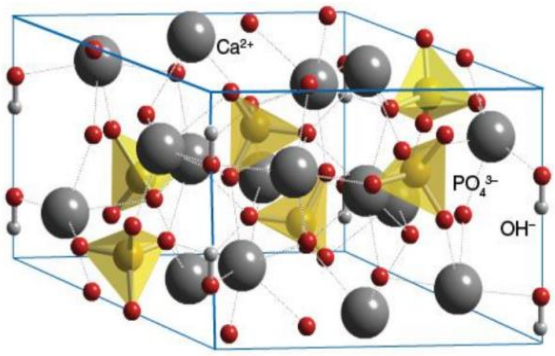

Figure 1. Crystal structure of hexagonal HA (Pazourková *et al.*, 2015).

The ten Ca^{2+} ions in the HA structure are located in two crystallographic distinct symmetries, simply represented as Ca-I and Ca-II, which is demonstrated in Figure 2. The four Ca^{2+} ions (Ca-I) are arranged in columns along the three-fold axes and coordinated to nine oxygen atoms through six shorter bonds that roughly outline a trigonal prism and three longer bonds that cap the prism faces. The Ca-O polyhedra share the trigonal faces to create chains parallel to the c-axis. Two triangular sets are formed by the remaining six Ca^{2+} ions (also known as triangular Ca or Ca-II). The Ca-II ions make seven-coordinate bonds, through six oxygen atoms and one

OH^- ion. The six PO_4^{3-} ions are arranged in extended triangular locations identical to the Ca-II ions. The oxygen atoms in the phosphate tetrahedra connect the nearby Ca-I and Ca-II polyhedra (Mathew Takagi, 2001; Moradi Alvani, 2019).

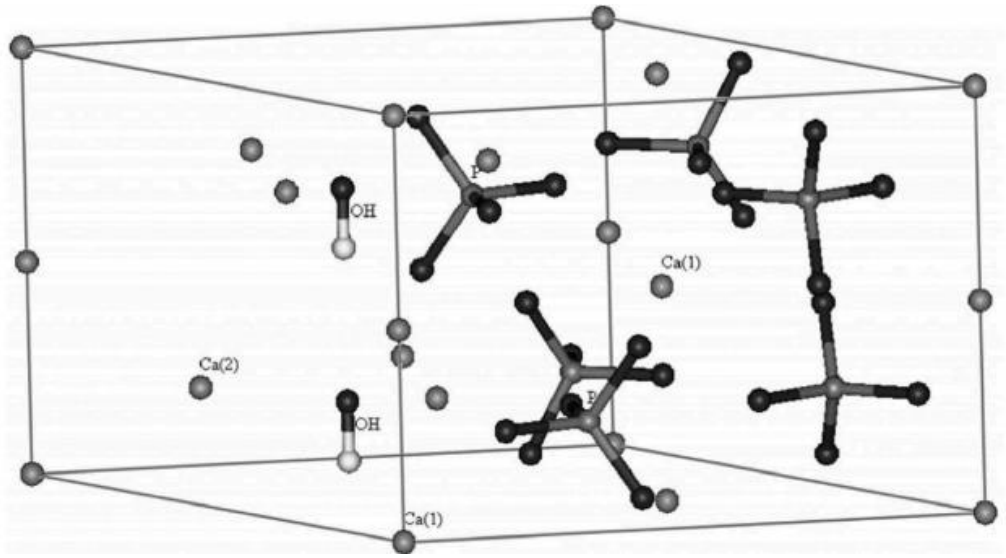

Figure 2. Ca-I and Ca-II sites of hexagonal HA structure (Basu Basu, 2019).

2.2 Doping Hydroxyapatite

2.2.1 Single-doping

In the HA crystal lattice, the PO_4^{3-} tetrahedrons are joined together by Ca^{2+} bridges. The space between PO_4^{3-} groups is relatively large allowing the accommodation of foreign atoms with quite different diameters from Ca^{2+} ion (Tite *et al.*, 2018). Numerous elements from the periodic table have been and continue to be employed as dopants for HA (Cacciotti, 2016; Kaygili *et al.*, 2021; Tite *et al.*, 2018). To alter the HA crystal structure's characteristics, various ionic substitutions have been made. It is widely recognized that adding smaller size of foreign atoms than the Ca^{2+} ions to the HA structure can increase lattice disorder, decrease particle size, decrease crystallinity degree, and encourage bio-resorption (Neacsu *et al.*, 2019).

The Ca^{2+}, PO_4^{3-}, or OH^- groups in HA can be partially replaced by both cationic and anionic substituents (Nagyne-Kovacs *et al.*, 2018). Cationic doping substitutes the calcium site while anion doping substitutes OH^- (type-A), PO_4^{3-} (type-B) or both OH^- and PO_4^{3-} simultaneously (AB-type) (Tite *et al.*, 2018). Research reports indicate that the major ionic substituents for HA

lattice are carbonate and magnesium ions from the anionic and cationic substituents respectively, due to their strong biological activities (Mahanty Shikha, 2023; Zeng *et al.*, 2019; Zhao *et al.*, 2016). Numerous physical characteristics, including crystallite size, crystallographic micro-strain, and mechanical strengthening, can be altered by substituting carbonate (Zeng *et al.*, 2019). Since carbonated HA is more soluble than pure HA, it exhibits stronger bioactivity and improves bone apposition rates. Furthermore, due to the smaller particle size of carbonated HA, tissue-implant interactions will undoubtedly be improved (Othman *et al.*, 2016).

The addition of Mg^{2+} ions prevents HA nucleation as well as the growth and stabilization of more acidic precursors. High Mg^{2+} concentrations in HA also led to higher HPO_4^{2-} incorporation, increased dissolution extent, crystal size, and decreased crystallinity. Similarly, doping HA using rare-earth elements such as erbium, europium, lanthanum, terbium, and dysprosium enhanced the photoluminescence properties. Because of their excellent thermal and chemical stabilities, crisp emission bands, high luminescence quantum yields, photo-stabilities, and less toxicity compared to other photo-luminescent materials now on the market, rare earth-based compounds provide significant and beneficial advantages (Neacsu *et al.*, 2019). On the other hand, study indicate that the mechanical characteristics of HA improved when the amount of Sr^{2+} ions increased as a dopant (Ungureanu *et al.*, 2023). In addition, the HA's thermal and electrical conductivity enhanced as the Gd^{3+} ions concentration rose because of the Ca^{2+} cation vacancies brought on by Gd^{3+} ions doping (Demirel *et al.*, 2021). Furthermore, Na^{+} ion which exists as a trace element in natural bone, can improve thermal stability and bone metabolism by forming vacancies for some of the Ca^{2+} sites in the HA lattice during its substitution (Zeng *et al.*, 2019).

The magnetic property of biomaterials is crucial in combating bone cancer because it can kill cancerous cells by a variety of techniques, such as cell labeling and hyperthermia. Thus, researchers used magnetic metal ions like Fe^{3+}, Ni^{2+}, and Co^{2+} ions in the HA structure as a dopant (Kurinjinathan Arul, 2018). The magnetic metal ion doped HA nanomaterials are very important for targeted drug delivery, magnetic resonance imaging, and cell separations that can be altered by applying an external magnetic field (Kurinjinathan *et al.*, 2020; Sheikh *et al.*, 2018). In addition, magnetic HA nanomaterials have strong adsorption capacity for uranium, and cadmium ions (Chen *et al.*, 2022; Guo *et al.*, 2019). The application of bone healing is significantly impacted by the dielectric characteristic of HA. Furthermore, because bone

formation increases with negative charge and decreases with positive charge, the presence of an electric field promotes fracture repair. It appears that this process involves the adsorption of Ca^{2+}, which serves as a nucleation point. Numerous metal ions, including Sr^{2+}, Ba^{2+}, Cd^{2+}, Ag^{+}, Mg^{2+}, Zn^{2+}, Ni^{2+}, Co^{2+}, and Pb^{2+}, are employed to regulate the structure and dielectric characteristics of HA bio-ceramic materials (Helen Kumar, 2019).

During cationic substitution, the change in properties of HA is dependent not only on the type of metal ions but also the size of the cations. Generally, the substitution of smaller size cations decreases the crystallinity and crystallite size whereas substitution with larger size cations increase the crystallinity and crystallite size of HA materials. For instance Zn^{2+}, Mg^{2+}, Fe^{3+} and Sr^{2+} ions reduce the crystallinity of HA (Garbo *et al.*, 2020; Sheikh *et al.*, 2018), however, substituents like Bi^{3+} ions increase the crystallinity (Al-Hazmi, 2016). When metal ions are introduced in the HA structure, maintaining charge neutrality is a crucial criterion. Charge imbalance in the crystal lattice does not result from the replacement of Ca^{2+} ions with divalent cations, but it occurs in the case of monovalent, trivalent and tetravalent ions replacement. Either by creating additional vacancies or by simultaneously substituting cations and anions would correct the imbalance due to the substitution (Cacciotti, 2016).

The other important point for cation doping is the position of the dopant in preference to Ca-I and Ca-II sites. In general, larger-size with smaller charge cations prefer the Ca-II site, whereas smaller-size with greater charge cations prefer the Ca-I site (Phatai *et al.*, 2018; Wei *et al.*, 2019), but sometimes this may not be true. Practically, the type of the anions in the ion channel, the charge of the cations, and the strength of the bonds connecting the ions to the nearby atoms all affect substitution preferences. Because of its larger ion-oxygen bond distance, the Ca-I site could also hold big ions. The c-axis lengthens as more substituted ions are added to Ca-I due to the reciprocal repulsion, which is partially regulated by the ion accommodation at the Ca-II site (Basu Basu, 2019). Some metal ions could also substitute both the Ca-I and Ca-II sites. For example, Sr^{2+} ions can occupied Ca-I and Ca-II sites. The Ca-I site substitution is preferred for low doping concentrations (1-3%), while the Ca-II site substitution is preferred for high doping concentrations (>10%). Thus, the amount of Sr^{2+} ions utilized to dope the HA has been found to influence the substitution mode (Ungureanu *et al.*, 2023).

2.2.2 Multiple/Co-doping

More than one element substituted (co-doped) HA nanomaterials has drawn more and more interest recently since the normal characteristics of HA can be altered in these materials to target particular reactions (Garbo *et al.*, 2020). Multiple/co-doping improves the physical, structural, chemical, and biological properties of HA while also more closely resembling the chemical composition of biological apatite. Multiple dopants are predicted to be able to enhance the positive impacts of each ion in light of the enhanced features reported in the case of mono-substituted systems (Cacciotti, 2019), even if only few works are available compared to single-doped HA reported in the literature (Yilmaz *et al.*, 2019), and shown in Figure 3. In general, co-doping improves mechanical, biological, magnetic, optical, and electrical characteristics as well as the stability and antibacterial activities of HA (Yedekçi *et al.*, 2021).

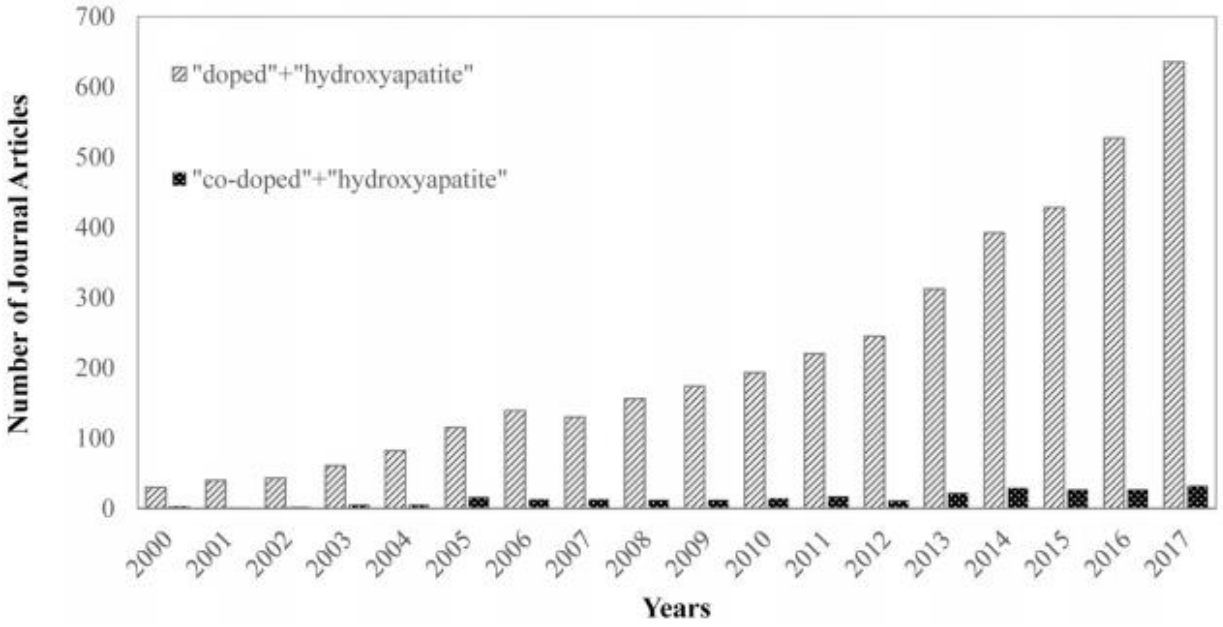

Figure 3. Comparison of articles published annually on single and co-doped HA reported on Science Direct from 2000 – 2017 (Yilmaz *et al.*, 2019).

For instance, Fe^{3+} and Zn^{2+} ions co-doped HA nanomaterial (Ramya *et al.*, 2014), the photoluminescence, dielectric, and magnetic characteristics were improved, leading to increased magnetization and resistivity. This was caused by the ionic polarization, which produced superparamagnetic particles, whereas the pristine HA was diamagnetic. Fe^{3+} and Cu^{2+} ions co-doped HA nanomaterial (Kalita *et al.*, 2022) indicates light absorption in the range of 210 – 550 nm, and even beyond 600 nm wavelength due to the d-d transition as well as

charge transfer transition, while the pristine HA has absorption only in the UV region (200-300 nm).

Similarly, optical property of Nd^{3+} and Yb^{3+} ions co-doped HA nanoparticles (Nardi *et al.*, 2021), emits light at different wavelength. According to the $^4F_{3/2} \rightarrow {}^4I_{11/2}$ transition, Nd^{3+} ions significantly emits at 1060 and 1071 nm when HA is doped with both Yb^{3+} and Nd^{3+} ions. In addition, there is a noticeable Yb^{3+} ions emission at 980 nm, which is associated with the $^2F_{5/2} \rightarrow {}^2F_{7/2}$ transition. It is clear that the Yb^{3+} ions emission at 980 nm is approximately 30 times more intense than it would be in the absence of Nd^{3+} ions co-doping. This is because Yb^{3+} ions are efficiently pumped by the resonant energy transfer from Nd^{3+} ions centers in addition to diffuse laser excitation. On the other hand, the presence of rare-earth metal ions such as Gd^{3+},Yb^{3+}, Tm^{3+}, and Eu^{3+} as multiple dopant in the HA structure (Ignjatović *et al.*, 2019) changes the magnetic behavior of HA from diamagnetic to paramagnetic.

Like that of the single-doping, multiple ion doping alters crystallinity, crystallite size, and unit cell volumes. For example, (Chen *et al.*, 2014) synthesized Eu^{3+} and Fe^{3+} ions co-doped HA, and obtained crystalline HA with reduced cell parameters when the percentage of Fe^{3+} ion is high. An experimental investigation by (Targonska *et al.*, 2020) indicates that when the Ca^{2+} ions were replaced by Eu^{3+} and Bi^{3+}cations (co-doping), the unit cell characteristics changed, which resulted in the shifts of the crystallographic planes towards lower 2θ angles. It can also be seen that there is a correlation between the tendency for the average grain size to grow and the rise in the concentration of Bi^{3+} ions in the matrix. Similarly, (Mahmood *et al.*, 2020) synthesized Sr^{2+} and Er^{3+} ions co-doped HA, and the result indicates that when the percentage of Er^{3+} ions rises, the degree of crystallinity steadily decline, demonstrating that Er^{3+} ions enter the HA structure and cause deformation. However, a progressive increase or decrease was not seen for either the lattice parameter as well as the volume of the unit cell. This may be due to the Er^{3+} ions substitution ranges changed from sample to sample, or the impact of CO_3^{2-} ions substitution could have had an impact by being substituted in PO_4^{3-} or OH^- ions into the HA lattice.

2.3 Applications of Hydroxyapatite

Because of its unique properties, ability to create a strong link with osseous tissues, and natural occurrence in the human body, HA nanomaterials have been commonly utilized in biomedical

applications such as orthopedic, orthodontic, tissue engineering, drug delivery, cancer therapy, molecular and cell imaging, and many others (Munir *et al.*, 2022). However, HA is not appropriate for load-carrying applications due to its low fracture toughness, brittleness, and inadequate mechanical strength. Another significant disadvantage associated with HA uses in biomedical sector is the potential for infections caused by pathogenic bacteria. Thus, the solution for the above limitations of HA is metal ion doping (Radulescu *et al.*, 2023). Research reports also show that, HA has been used in different areas beyond the biomedical sector. Specially, metal ion-doped HA can be used for catalysis (Martínez-Hernández *et al.*, 2020), environmental remediation, and many other sectors (Ibrahim *et al.*, 2020).

2.3.1 Hydroxyapatite for Fluoride Removal Application

The proportion of HA in an animal bone is roughly 70%. Bone char is made of animal bone that has been burnt and crushed. It was one of the earliest media suggested for F^- ions removal from water. However, bone char is not acceptable as a typical material for F^- ions removal. Using bone char directly to remove F^- ions will result in low defluoridation capacities. Additionally, water that has been treated with bone char may smell bad and appear yellowish, making it unfit for drinking. This issue is being addressed by using synthetic HA as an adsorbent and anion exchanger, because it has a better defluoridation capability than bone char. HA has numerous benefits, including high stability, biocompatibility, affordability, recyclability, promising surface properties and non-toxicity (Rathnayake *et al.*, 2022).

2.3.1.1 Defluoridation Capacity Enhancement of Hydroxyapatite

Up to now, different attempts have been made to enhance the defluoridation of HA materials. Some of these are by compositing it with organic and inorganic materials, incorporation of metal ions into the structure, or modifications of the size and morphology of pristine HA materials. Recent research reports indicate that the defluoridation capacity of HA has been significantly improved by the preparation of a composite of HA with different substances. For instance, (Sekar *et al.*, 2022) evaluated the defluoridation performance of pristine HA and HA/Na-alginate nanocomposite using an initial concentration in the range of 50 – 500 mg/L F^- ions at a pH of 7, and they obtained defluoridation capacity of the pristine and nanocomposite as 10 mg/g, and 50 ± 5 mg/g, respectively. Similarly, (Huang *et al.*, 2020) also found a defluoridation capacity of 215.52 mg/g using $Al(OH)_3$-modified HA nanosheet by employing

an initial concentration in the range of 5 – 200 mg/L, at the temperature of 318 K. However, in this case the defluoridation capacity of non-modified HA nanomaterials was not reported, they stated that from the "series of synthesized samples the nanohydroxyapatite with highest defluoridation capacity and best morphology was chosen for modifying". Furthermore, (Wimalasiri AKD Veromee Kalpana *et al.*, 2021) studied the defluoridation performance of HA-CeO_2, and HA-CeO_2/$La(OH)_3$ composites with different ratios of HA-CeO_2/$La(OH)_3$, and found adsorption capacities of 322.6, 200.0, and 625.0 mg/g for HA-CeO_2, HA-CeO_2/$La(OH)_3$ (2:1 ratio), and HA-CeO_2/$La(OH)_3$ (3:2 ratio), respectively, at a pH of 5.8 and initial concentration of F^- ions in the range of 70 – 2800 mg/L.

The other alternative to increase the defluoridation capacity of HA is using ionic doping/substitution (Chen *et al.*, 2018; Mondal *et al.*, 2016; Nie *et al.*, 2012). For example, (Nie *et al.*, 2012) compared the F^- ions removal tendency of pristine and Al^{3+} ions doped HA adsorbents, and they found that Al^{3+} ions doped HA has 32.57 mg/g adsorption capacity, while the pristine HA has adsorption capacity of only 16.38 mg/g. Similarly, (Chen *et al.*, 2018) studied the defluoridation performances of pristine HA as well as HA substituted by Mg^{2+}, Al^{3+}, and La^{3+} ions and found that the defluoridation capacities of pristine HA 4.12 mg/g, and for metal ions-doped HA adsorbents were in the order of Al^{3+} ions doped HA (46.729 mg/g) > La^{3+} ions doped HA (23.598 mg/g) > Mg^{2+} ion doped HA (18.018 mg/g) using similar experimental conditions. On the other hand, (Nagaraj *et al.*, 2018) performed the F^- ions removal efficiencies of pristine HA and nanocomposite of multi-mineral (Al^{3+}, La^{3+} and Ce^{3+}) substituted HA. They obtained adsorption capacities of 8.36 mg/g and 6.8 mg/g, for the nanocomposite and pristine HA adsorbents, respectively.

The adsorption capacity of HA has also been enhanced by changing its morphology, crystallinity, and size. When the crystallinity of HA becomes lower; its particle size decreases, but the surface area increases. The increasing surface area leads to increase in the number of active sites on the HA surface, which will cause a remarkable enhancement of the adsorption capacity (Wei *et al.*, 2015). For example, (Gao *et al.*, 2019), performed defluoridation activity of the synthesized hierarchical hollow HA microspheres, and the adsorption capacity of the adsorbent obtained was 29.82 mg/g, which is higher than the adsorption capacities of HA-based adsorbents, except some of the HA nanocomposites listed in their comparison. On the other hand, (He *et al.*, 2016), tested the F^- ions removal capacity of ultra-long HA nanowires, and they found 40.7 mg/g of F^- ions adsorption capacity, the value

is higher than all the HA-based adsorbents given in their comparison analysis. In general, according to the review work reported by (Rathnayake *et al.*, 2022), HA nanowires show substantially better adsorption capabilities than other HA pristine materials of various morphologies, even if there are variations of different experimental conditions. The defluoridation capacities of some selected HA-based materials modified in different ways are given in Table 1.

Table 1. Defluoridation capacities of HA-based adsorbents

Adsorbent	Conc. (mg/L)	Dose (g/L)	pH	Time (min)	Temp (^oC)	qe (mg/g)	Reference
HA nanowire-$Al(OH)_3$	200	0.5	7	180	45	107.41	(He *et al.*, 2017)
Al^{3+} doped HA	5 – 10	0.1	5.7	25	55	46.729	(Chen *et al.*, 2018)
Nanocrystalline-HA	5 – 40	3	6	60	25	22.3	(Nayak *et al.*, 2017)
HA-nanowire	1 – 200	0.5	7	180	45	40.7	(He *et al.*, 2016)
Porous nano-HA	1 – 200	2	6.8	< 2	–	54.0	(Wimalasiri AKD Veromee K *et al.*, 2021)
HA-hollow-microspheres	10 – 100	0.4	7	9	25	29.82	(Gao *et al.*, 2019)
HA/Na-alginate nanocomposite	500	1	7	90	30	55	(Sekar *et al.*, 2022)
HA-CeO_2-$La(OH)_3$ composite	70 – 2800	4	5.8	4	27	625.0	(Wimalasiri AKD Veromee Kalpana *et al.*, 2021)

2.3.1.2 Experimental Conditions that Affect Fluoride Ions Removal

The literature has examined a variety of factors in connection to HA's capacity to remove F^- ions, including temperature, contact time, amount of adsorbent, solution pH, F^- ions concentration, and the presence of concurrent ions. Measuring the contact time, in particular, can reveal if the adsorption equilibrium is there or not. Contact time strongly affects the F^- ions

adsorption in aqueous solution (Balasooriya *et al.*, 2022). Literature reports (He *et al.*, 2017; Nayak *et al.*, 2017; Sekar *et al.*, 2022) indicated that pristine and modified HA adsorbents have the potential to remove F^- ions in an equilibrium time range of 60 to 180 minutes. However, other research indicates that the F^- ions adsorption equilibrium durations on the HA structure are either too long (Singh *et al.*, 2020) or too short (Gao *et al.*, 2019). These equilibrium time variation may be due to the effect of initial F^- ions concentration, the mechanism of adsorption (chemical or physical), the number of active sites on the HA surface, and the use of activation energy during adsorption.

A research work by (Aw *et al.*, 2022) assessed the impact of contact time, which ranged from 25 to 250 minutes, on the effectiveness of F^- ions elimination using hydroxyapatite modified *Corbula trigona* shell powder. They found that the F^- ions adsorption efficiency on the adsorbent was demonstrated to rise quickly before roughly approaching a constant value (89.4%), which denotes the equilibrium level. According to their conclusion, three different phases can be identified in the F^- ions sorption process. First, there is an early phase that lasts less than 150 minutes and is characterized by a quick removal efficiency of F^- ions. This demonstrates that the affinity for the adsorbent surface and diffusion forces via the porous media are responsible for the sorption reaction's rapidity. The F^- ions move from the surface of the HA-based adsorbent to its interior pores during the second phase. Eventually, the F^- ions removal efficiency stays constant in the last phase (after 175 minutes) demonstrating the saturation of the adsorption sites and the equilibrium level. Similarly, (Samant *et al.*, 2017), examined the impact of contact time on the percentage elimination of F^- ions at pH 6.3 by altering the time from 15 to 140 minutes, using nanocrystalline HA derived from *limacine artica* shells adsorbent. Up to 60 minutes, the adsorption percentage increased to 94% before reaching a maximum value at which point the removal percentage plateaued. This was explained by the fact that F^- ions equilibrium was reached in bulk solution with the adsorbed layer after 60 minutes.

The effective removal of F^- ions is reliant on the starting concentration because with greater F^- ions concentrations, the binding sites for adsorption become limited for a given adsorbent dosage (Rathnayake *et al.*, 2022). Most of the time 5 – 10 mg/L of F^- ions concentration is considered as the optimum initial concentration for effective removal (Huang *et al.*, 2020; Nagaraj *et al.*, 2018; Samant *et al.*, 2017). However, the F^- ions adsorption capacity of pristine and modified HA materials given in Table 1 indicates that the adsorption capacity of a given

adsorbent increases with increasing initial concentration of F^- ions, without considering the variation of other parameters. For instance, (Nagaraj *et al.*, 2018) used F^- ions initial concentration values ranging from 2 – 10 mg/L for the investigation of the impact of changing the starting concentration of the F^- ions on the adsorption efficiencies of pristine and metal ions doped HA nanocomposite. They found an adsorption efficiency of 48.6% and 56.4% for the pristine HA and the nanocomposite, respectively at an initial F^- ions concentration of 2 mg/L. However, at the initial F^- ions concentration of 4 mg/L, the efficiency increased to 61.7% for the pristine HA, and 66.8% for the nanocomposite. Likewise, there was a direct correlation between the adsorption capacity and the F^- ions concentrations. Adsorption capacities of 1.72 mg/g for the nanocomposite and 1.54 mg/g, for pristine HA at the initial F^- ions concentration of 2 mg/L were obtained. On the other hand, the adsorption capacity increased to 2.58 mg/g (pristine) and 2.86 mg/g (nanocomposite) when the concentration of F^- ions was raised to 3 mg/L. At a starting concentration of 10 mg/L, the defluoridation efficiency for pristine HA was 84%, whereas for the nanocomposite it was 97%.

The adsorbent dose is the other crucial factor that significantly affects the amount of F^- ions that is adsorbed per unit weight of the adsorbent. As adsorbent dosage is increased, adsorbents become more effective at adsorbing F^- ions. This might be explained by the existence of several F^- ions binding sites, since more surfaces are available for the adsorption of a restricted amount of F^- ions concentration. However, after a certain point further increasing of dosage may not increase the adsorption efficiency due to the interactions of the active sites of the adsorbent with each other (Rathnayake *et al.*, 2022). For example, (Huang *et al.*, 2020) conducted an experiment to examine the impact of adsorbent dose on F^- ions adsorption using $Al(OH)_3$-HA nanosheet at pH 7 with an initial F^- ions concentration of 5 mg/L. Evidently, as the adsorbent dose increased from 0.01 to 0.1 g, the F^- ions adsorption capacity fell from 19.89 to 2.44 mg/g.

The other important factor that affects F^- ions adsorption on the HA structure is the pH of the solution. This is because the HA surface is highly affected by the H^+ ions or OH^- ions in the solution. At the lower pH, the surface will be protonated which will increase the F^- ions adsorption, but at higher pH, the excess OH^- ions will repel the F^- ions and depress the adsorption tendency. The optimum pH values reported for the removal of F^- ions in different works were from slightly acidic to neutral (Rathnayake *et al.*, 2022). Similarly, (Samant *et al.*, 2017), analyzed the effect of varying solution pH for the defluoridation performance of nanocrystalline HA derived from *Limacine artica* shells. Their finding showed that as the pH

rose from 2.1 to 6.3, the percentage of elimination increased progressively from 56.81% to a high of 92.51%. There was a noticeable drop in F^- ions removal with additional pH increases. If the F^- ions removal would have been occurred by only electrostatic forces of interaction, the adsorption removal have to be increased until pH of 8.28 (point of zero charge of the material). However, the fact that the highest removal occurred at pH 6.3 indicated that the F^- ions adsorption mechanism at the HA surface contact was not solely dependent on HA's surface charge. They conclude that some other factors such as dissolution of apatite in the acidic solution may contribute for the adsorption performance. In another study by (Sekar *et al.*, 2022) using HA/Na-alginate nanocomposite, the impact of starting pH was investigated over a range of pH values from 3 to11. They obtained the maximum adsorption capacity in the acidic media (pH 3). According to their conclusion this is because of the presence of more electrostatic contact between the F^- ions and the positive surface charge at lower pH values. Additionally, the ion exchange mechanism between the F^- ions and surface functional groups is accelerated by the decreased colloidal stability. However, because of the electrostatic repulsion between the negatively charged adsorbents and F^- ions, the adsorption capacity steadily declined in alkaline condition.

Depending on whether the adsorption is exothermic or endothermic, temperature has also an impact on the adsorption processes. This is because the mobility of the adsorbed molecule will increase with rising temperature. A growing number of molecules might also develop the necessary energy to engage in interaction with the active sites on the adsorbent's surface. Additionally, rising temperatures may cause the internal structure of the adsorbent to inflate, allowing a high number of adsorbed molecules or ions to penetrate further (Nayak *et al.*, 2017). The effect of temperature on F^- ions adsorption through the surface of HA was examined by (Roy Das, 2016). It is shown that the percentage of F^- ions removed first rises as temperature rises from 35 ^oC to 50 ^oC. Defluoridation efficiency falls after 50 ^oC. The number of F^- ions that accumulate on the adsorbent surface during the chemisorption process increases the attraction force between the F^- ions and HA. However, as the temperature rise over 50 ^oC and the charge density of F^- ions rises, the adsorbate and adsorbent surface experience an increase in repulsive force. This causes the defluoridation efficiency to initially rise and subsequently fall.

2.3.1.3 Defluoridation Mechanism by Hydroxyapatite

The processes by which HA removes F^- ions are the subject of in-depth investigation by different researchers (Chen *et al.*, 2018; Huang *et al.*, 2020; Nayak *et al.*, 2017). Adsorption mechanisms can be caused via chemisorption between the adsorbent and adsorbate, or by the physically adsorbing molecules on the surface of the adsorbent, which facilitates the relatively weaker van der Waals forces. Physical adsorption (either on the surface or internally diffused), electrostatic interactions (H-bonding, ion-pair formation or complexation), ion exchange, and dissolution-precipitation processes are the typical four mechanisms involved in the removal of F^- ions by HA and HA-based materials. The different mechanisms of defluoridation by HA are given in Figure 4. Each mechanism in the F^- ions adsorption depends on various factors, including pH and temperature (Chen *et al.*, 2018; Nayak *et al.*, 2017; Rathnayake *et al.*, 2022).

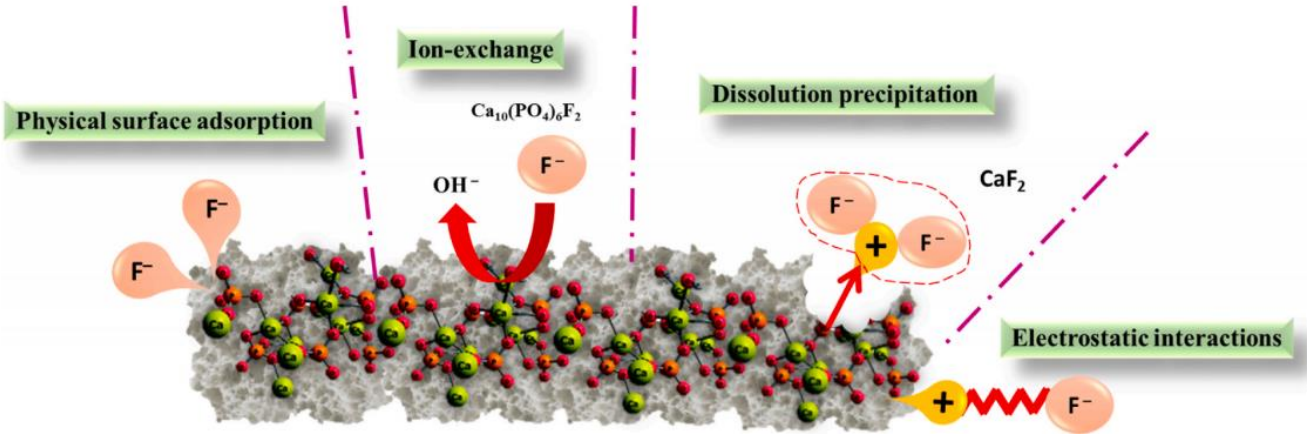

Figure 4. Different mechanisms for F^- ions removal by HA nanomaterial (Rathnayake *et al.*, 2022)

Physical adsorption is the outcome of a particular interaction being established between the adsorbate and the adsorbent's active site. It is the physical bonding of adsorbate to the adsorbent by van der Waals forces, then the adsorbate forms multilayer adsorption (Rathnayake *et al.*, 2022). The physical adsorption of F^- ions on the metal ion doped HA surface (Chen *et al.*, 2018), can be explained according to Equation 1:

$$Ca_{(10-bx/2)}M_x(PO_4)_6(OH)_2 + nF^- \leftrightarrow Ca_{(10-bx/2)}M_x(PO_4)_6(OH)_2 \ldots nF^- \quad (1)$$

Where, M represents the metal ion incorporated, b represents the charge of the corresponding metal ion, and n represents the number of F^- ions adsorbed.

On the other hand, there are electrostatic interactions between the oppositely charged species that allow the positively charged active sites on the HA surface to form different bonds with

the negatively charged F^- ions. The forces that have been created between F^- ions and HA are not very strong. Therefore, by washing the adsorbent with a suitable solvent, the adsorbed F^- ions can be removed from the HA surface. This kind of physical adsorption makes it easier to recycle HA as an adsorbent repeatedly. It is vital to note that the process of physical adsorption can be significantly impacted by the pH of the medium. The material will have a positively charged surface at pH values lower than the point of zero charge, which can promote electrostatic interactions with negatively charged F^- ions (Balasooriya *et al.*, 2022; Rathnayake *et al.*, 2022). The mechanism of H-bonding between HA nanomaterial and F^- ions (Balasooriya *et al.*, 2022), is given by Equation 2:

$$Ca_{10}(PO_4)_6(OH)_2 + F^- \rightarrow Ca_{10}(PO_4)_6(OH)_2 \ldots F^- \quad (2)$$

Similarly, the electrostatic interaction by complex formation (Chen *et al.*, 2018), is also given by Equation 3:

$$Ca_{(10-ax/2)}M_x(PO_4)_6(OH)_2 + zF^- \rightarrow [Ca_{(10-ax/2)}M_x(PO_4)_6(OH)_2F_z]^{z-} \quad (3)$$

The other mechanism that supports HA's defluoridation ability is ion exchange. Negatively charged F^- ions are substituted for the negatively charged hydroxyl ions on the HA surface during this ion exchange process (Rathnayake *et al.*, 2022). As reported by (Balasooriya *et al.*, 2022), the ion exchange mechanism of HA nanomaterial for the removal of F^- ions may be a partial or complete replacement of OH^- ions by the F^- ions based on Equations 4 and 5, respectively.

$$Ca_{10}(PO_4)_6(OH)_2 + F^- \rightarrow Ca_{10}(PO_4)_6(FOH) + OH^- \quad (4)$$

$$Ca_{10}(PO_4)_6(OH)_2 + 2F^- \rightarrow Ca_{10}(PO_4)_6(F)_2 + 2OH^- \quad (5)$$

The literature reveals that surface adsorption and ion exchange mechanisms are the dominant, while dissolution and precipitation are also reported for defluoridation by HA (Singh *et al.*, 2020; Sternitzke *et al.*, 2012). Calcium ions (Ca^{2+}) concentration in the solution might rise because of HA dissolution, which is particularly enhanced under acidic conditions. In this case the F^- ions in the solution react with Ca^{2+} ions and form calcium fluoride (CaF_2) (Rathnayake *et al.*, 2022), as indicated in Equation 6.

$$Ca_{10}(PO_4)_6(OH)_2 + 20F^- \rightarrow 10CaF_2 + 6PO_4^{3-} + 2OH^- \quad (6)$$

2.3.2 Photocatalytic Application of Hydroxyapatite

The strong adsorption tendency, low cost, eco-friendliness, reusability, and direct generation of $\bullet O_2^-$ and •OH radicals during irradiation by UV light encourages the usage of HA for

photocatalysis (Jiménez-Flores *et al.*, 2017; Liu *et al.*, 2016; Valizadeh *et al.*, 2014). However, it is important to note that pure HA material's photocatalytic removal effectiveness is still unsatisfactory (Zou *et al.*, 2020a; Zou *et al.*, 2020b), due its high bandgap energy (4 – 6 eV) (Hadagalli *et al.*, 2021; Jiménez-Flores *et al.*, 2017). The optical bandgap helps to explain the material's capacity to create electron-hole pairs, which are necessary for the oxidizing or reducing species that initiate photocatalytic reactions. These optical characteristics are greatly influenced by the existence of vacancies, self-interstitial atoms, substitutional and interstitial impurity atoms, and crystalline defects, and all are fully dependent on the crystalline structure (Rojas-Trigos *et al.*, 2019).

To overcome the low photocatalytic activities of HA material, researchers used different techniques. For example, some of the research groups prepared composites of HA with different semiconductors such as TiO_2 (Bouyarmane *et al.*, 2021; Mohseni-Salehi *et al.*, 2018), ZnO (Labrag *et al.*, 2021), CdS (Lei *et al.*, 2020), Fe_2O_3 (Labrag *et al.*, 2020), and decorating with reduced graphene oxides (Zou *et al.*, 2020b). Another strategy to enhance the photocatalytic degradation efficiency of HA towards numerous pollutants is doping with different metal ions (Hossain *et al.*, 2022; Khan A. *et al.*, 2022; Manoj *et al.*, 2019; Pereira Rocha *et al.*, 2021). The presence of metal ions as dopants alter the charge carrier recombination rates, which affects photo-reactivity. By delaying recombination and lengthening the lifespan of the photo-generated charge carriers, these dopant ions function as shallow traps for both electrons and holes, enhancing photocatalytic activity (Irfan *et al.*, 2017). For instance, (Hossain *et al.*, 2022) investigated the photocatalytic performances of pristine and Cu-doped HA towards Congo red dye, and obtained degradation efficiency of 45% and 93% for the pristine and doped HA respectively. Similarly, (Jiménez-Flores *et al.*, 2017) synthesized Tb^{3+} ions doped HA for the photocatalytic degradation of 2,4-D and the result indicates that the photocatalytic degradation efficiency of the photocatalyst increases with the percentage of Tb^{3+} ions introduced into the HA structure. The pristine HA has percentage degradation of less than 20%, but the 10% Tb^{3+} ions doped HA has degradation efficiency of near to 100 %. On the other hand, (Salhi *et al.*, 2015) studied the photocatalytic degradation efficiency of Ti^{4+} ions doped HA for methylene blue (MB) dye. The percentage degradation of MB increased from 77% to 93% as the percentage of Ti^{4+} ions increased from 3% to 11% in the HA structure. They concluded that the pristine HA has a degradation efficiency of not more than 5% up to 4 hours of irradiation time. Furthermore, (Al-Ahmed *et al.*, 2020) performed the photocatalytic activity of Pd^{2+} ions doped HA (with various ratios of Pd^{2+} ions) for MB dye. They concluded

that the efficiency of photodegradation increases with increasing the number of Pd^{2+} ions doped. The non-doped HA has only 26.35% degradation efficiency, while the highest amount of Pd^{2+} ions doped HA has a degradation efficiency of 86.4% after 120 minutes irradiation time.

The high photocatalytic degradation efficiency of metal ion-doped HA is associated with the high light harvesting potential and lowering of bandgap energy. The bandgap energy of metal ion-doped HA is reportedly significantly lower than that of pure HA. For instance, the bandgap energy of Ti^{4+} ions doped HA decreases as the concentration of Ti^{4+} ions incorporated in the HA structure increases, as reported by (Adamiano *et al.*, 2017). At the highest concentration of Ti^{4+} ions inserted, a value of 3.54 eV bandgap energy was obtained. Similarly, (Hadagalli *et al.*, 2021) obtained bandgap energy of Fe^{3+} substituted HA in the range between 1.84 – 2.18 eV, as the concentration of Fe^{3+} ions increased from 0.01 to 0.05 M. But the bandgap energy of the non-doped HA was 5.95 eV.

2.3.2.1 Photocatalytic Degradation Mechanisms of Hydroxyapatite Based Materials

In general, the use of HA as a photocatalyst makes sense when we consider that the catalytic phenomenon is caused by photoinduced electronic excitation, which is linked to oxygen vacancies. This excitation helps to form radicals that can oxidize pollutant molecules and react with water and other ions to form hydroxyl radical, which then degrades the pollutant through a series of reactions (Pereira Rocha *et al.*, 2021). Different researchers reported the possible photocatalytic degradation of using different dye molecules. For instance, (Sathiyavimal *et al.*, 2020) suggested the mechanism of photocatalytic degradation of crystal violet (CV) and Congo red (CR) dyes as shown in Figure 5, using HA synthesized from fish bone. In a nutshell, sunlight irradiation caused an excitation of electron from valence band (VB) to the conduction band (CB), which produced electron-hole pairs and caused the degradations of CV and CR. Superoxide anion radical and hydroxyl radicals were produced by the interaction between the positive charge of the mesoporous holes and the negative charge of the electrons. The positive holes (h^+) that break down the adsorbed CV and CR molecules into smaller molecules of CO_2 and H_2O are tightly attached to these active species of HA. Moreover, the rapid breakdown of CV and CR was made possible by the mesoporous HA's higher adsorption ability.

Similarly, (Hossain *et al.*, 2022) proposed the possible photocatalytic degradation mechanism of Congo red dye using Cu^{2+} ions doped HA. According to their explanation, the dye molecules can be broken down by the free radicals, electrons, and holes acting as photocatalytic agents. Strong oxidizing agents can be produced by the holes created when electrons are excited from the VB to the CB. More reactive species are produced as a result of the e^- and h^+ recombination being delayed while the photon is still being absorbed by the photocatalyst. The energy of the VB and CB affects this recombination of e^- and h+. according to their finding, for the purpose of photocatalyzing Congo red dye using pristine and Cu^{2+} ions doped HA (with various ratios of Cu^{2+} ions), both radicals can be produced because all the samples showed greater negative potentials of CB than the redox potential of O_2 /$\bullet O_2^-$ (−0.33 eV) and more positive potentials of VB than that of OH/•OH (1.99 eV).

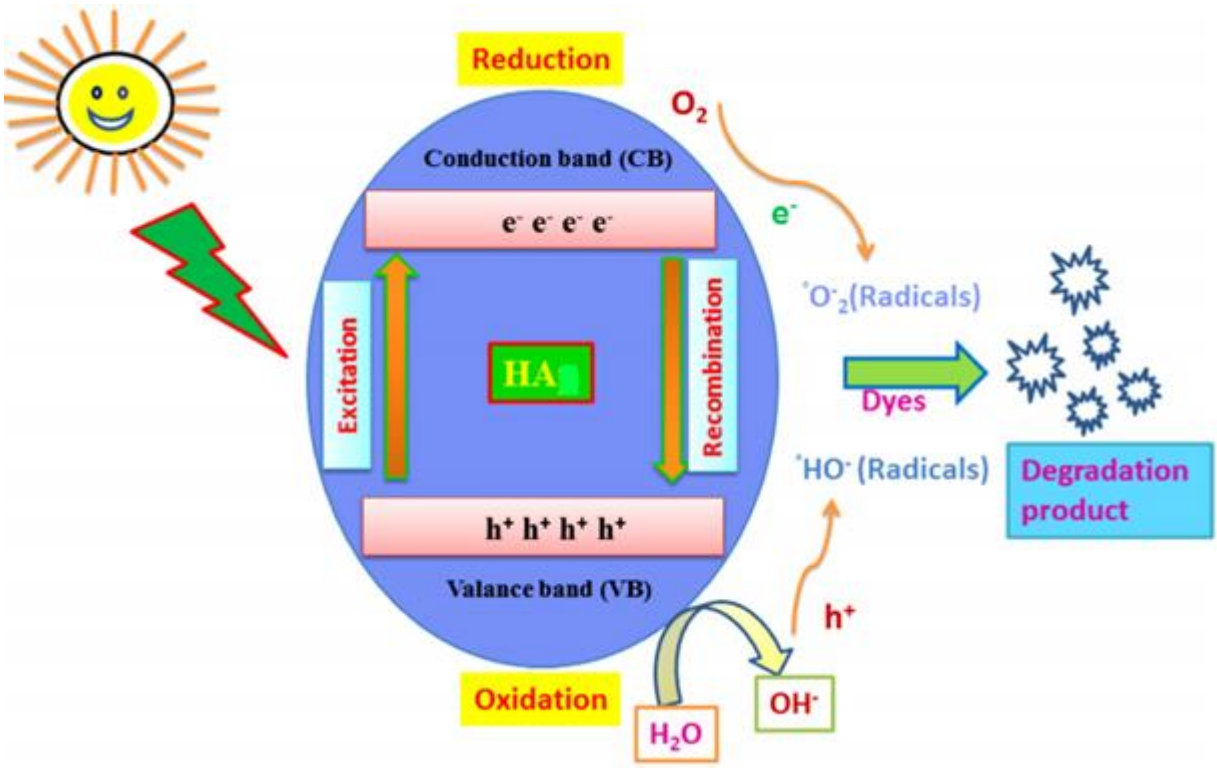

Figure 5. Photocatalytic mechanism of azo dyes degradation using HA as photocatalyst (Sathiyavimal *et al.*, 2020).

2.3.3 Antibacterial Activity of Hydroxyapatite

It is reported that, ceramic biomaterials are used in about 2.9 million joint replacement procedures performed annually worldwide, including 1.4 million hip, 1.1 million knee, and

over 100,000 shoulder. Similarly, more than 2.2 million bone transplant procedures are carried out annually in the globe (Yedekçi *et al.*, 2021). However, the most common and serious side effects of using biomaterials as surgical device or as an implant is device-induced microbial infection (Alwine *et al.*, 2023). Even if HA has been the most studied bio-ceramic material (Yedekçi *et al.*, 2021), it has no intrinsic antibacterial activity (Chen *et al.*, 2019; Li *et al.*, 2022; Prodan *et al.*, 2019), rather it may adhere to proteins, amino acids and other organic materials that are suitable for the growth of bacteria (Huang *et al.*, 2015; Jadalannagari *et al.*, 2014). Implants used in orthopedic surgery are more prone to infection. In the vicinity of an implant, bacteria can attach to the surface and create biofilms, which can result in implant-associated infections. Compared to planktonic bacteria, bacteria in biofilms are far more resistant to antimicrobial agents, and they are also protected from the host's immune system and external toxins. Additionally, the development of biofilm may result in implant failures, and in more extreme circumstances, patient fatality. Similar to hip and knee arthroplasty, revision implant surgeries can put a strain on patients' physical well-being (Chen *et al.*, 2019).

According to the findings, *S. aureus* and *E. coli* are not only multidrug-resistant pathogens but also broadly drug-resistant and pan drug-resistant germs. For instance, *S. aureus* isolates are reportedly becoming more resistant to a wider range of antibiotic substances. An earlier report showed that, 40% of nosocomial S. aureus strains were resistant to methicillin, vancomycin, and carbapenem, further undermining the efficacy of conventional antibiotic therapy (Lv *et al.*, 2020). Similarly, the report given by (Prodan *et al.*, 2019), the majority of implant-related infections from 1033 total hip and total knee prosthetic arthroplasty cases were brought on by *aerobic cocci*, most frequently *S. aureus*, (23%) and *coagulase negative staphylococci* (25%). However, more recent reports (Rosman *et al.*, 2022; Shuaishuai *et al.*, 2023) stated that S. aureus is considered as the major pathogen that brought implant associated infection. In general, *E. coli* and *S. aureus* are the two most common bacteria that cause invasive infections on people’s healthcare providers and are acquired in hospitals (Poolman Anderson, 2018). They also cause superficial and systemic infections as well as bacteremia and sepsis (Frickmann *et al.*, 2019).

Since nanomaterials have a higher surface area to volume ratio than corresponding bulk materials, and a higher ratio of atoms on the surface to atoms inside the material, they have emerged as novel antimicrobial agents for the treatment and prevention of infectious diseases with proven efficacy against resistant bacteria (Hochvaldová *et al.*, 2022; Sharmin *et al.*, 2021).

The presence of metal ions like Ag^{+}, Cu^{2+}, and Ga^{3+} in the HA nanostructure improves its antibacterial activity (Mariappan *et al.*, 2017; Shokri *et al.*, 2022; Wilcock *et al.*, 2017). On the other hand, compounds of Bi and Fe show antibacterial activities. For instance, Bi compounds in the Bi^{3+} form have strong antibacterial activities, and are relatively non-toxic to humans and to the environment (Ciobanu Harja, 2019; Stephens *et al.*, 2020; Vazquez-Munoz *et al.*, 2020). Similarly, Fe and its oxides have a strong biocompatibility nature (Irshad *et al.*, 2017), non-toxic, and have strong antibacterial activities against different bacterial strains (Armijo *et al.*, 2020). The presence of Fe ions facilitates the generation of reactive oxygen species through the Fenton reaction, and this puts oxidative stress on the bacterial cell (Vitta *et al.*, 2020).

Research reports also indicate that, co-doping (multiple ion substitution) in the HA structure enhanced the antibacterial activity towards different bacterial strains (Huang *et al.*, 2015; Shokri *et al.*, 2022), due to the synergetic effects of the different metal ions (Yilmaz *et al.*, 2019). For example, (Shokri *et al.*, 2022) investigated the antibacterial activities of pristine HA, Zn^{2+} ions doped,, Ga^{3+} ions doped, and Zn^{2+} and Ga^{3+} co-doped HA nanopowders with different concentrations (125, 250, 500, and 1000 mg/L) against *S. aureus* and *E. coli* bacterial strains. The findings showed that all doped HA nanopowders had significantly stronger antibacterial activity than pure HA nanopowder against both *E. coli* and *S. aureus* bacteria. In comparison to Zn^{2+} ions doped HA nanopowder, the bacterial mortality of both strains is significantly higher in Zn^{2+} and Ga^{3+} ions co-doped HA nanopowder. The study also showed that the higher the Ga^{3+} ions percentage in the sample, the better antibacterial activity. Their result indicates bacterial survival rates dropped from 40% to roughly 20% as the ratio of gallium content increased from 0.2 to 0.6 in the Zn^{2+} and Ga^{3+} ions co-doped HA nanopowder, however, the pristine HA has bacterial viability of near to 100%. They concluded that the increased synergistic role of Ga^{3+} and Zn^{2+} ions release may be responsible for the enhanced antibacterial activity of Ga^{3+} ions doped HA and Zn^{2+} and Ga^{3+} ions co-doped HA nanopowders with increasing Ga^{3+} ions content.

Even if the inhibitory mechanism of metal containing nanoparticle' is not adequately described, certain types of mechanisms have been proposed in the literature. From these oxidative stress caused by reactive oxygen species generated, the metal ions or the nanoparticle itself interacting with protein, DNA, and cell membrane which leads to bacterial cell destruction, are the most likely mechanisms of actions reported previously (Li D. *et al.*, 2021; Sharmin *et al.*, 2021). Before other mechanisms are used, cell penetration is frequently the first stage in a

microbial cell inhibition process. The primary penetrating mechanism of nanoparticles is their adsorption or diffusion at the cell surface. Adsorption can occur when nanoparticles adhere to the negatively charged functional groups of proteins, destroying the proteins and killing the cells (Sharmin *et al.*, 2021). General mechanisms of antimicrobial action of nanoparticles are summarized according to the schematic given in Figure 6.

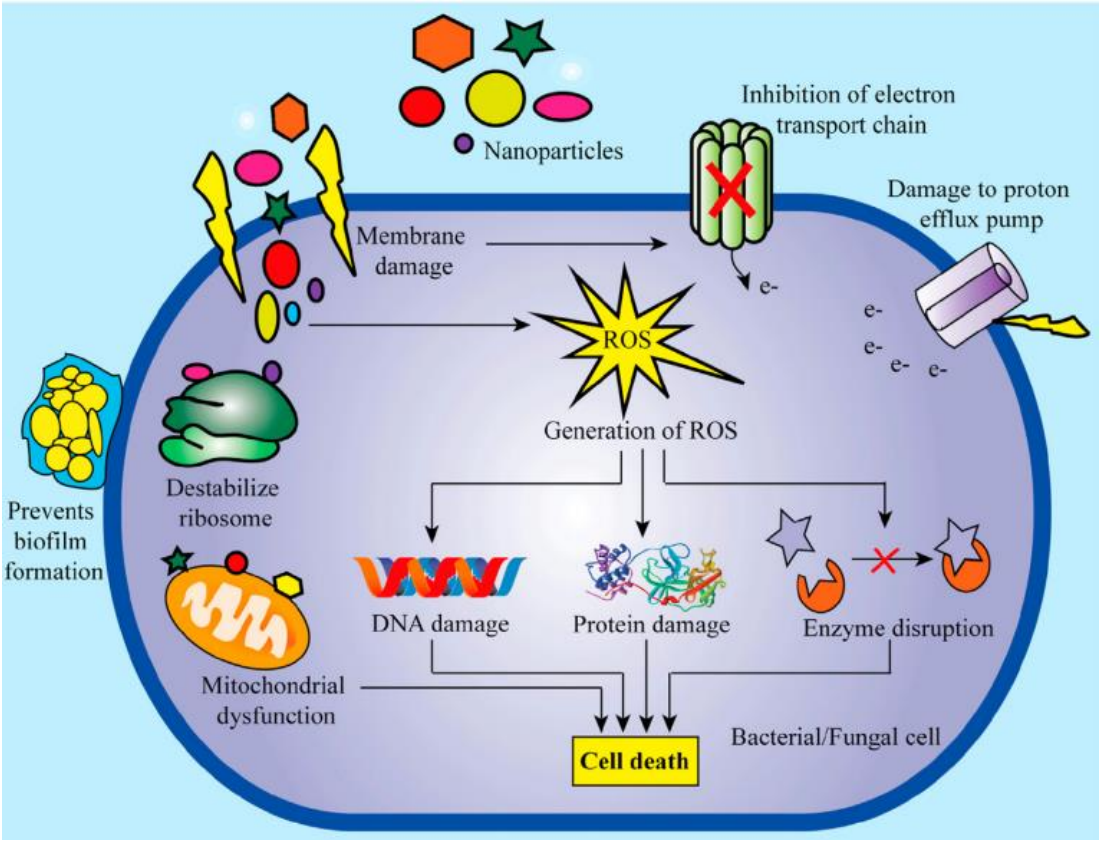

Figure 6. Schematic representation of antimicrobial mechanisms of nanoparticles (Sharmin *et al.*, 2021)

2.4 Synthesis Methods of Hydroxyapatite

Different techniques are available for the synthesis of HA (Cox *et al.*, 2015; Gopi *et al.*, 2015), the most commonly used methods are aqueous precipitation, sol-gel, emulsion, and hydrothermal method (Panda *et al.*, 2021). The process parameters for the different methods are widely varied, so particle morphologies, sizes, crystallinity, phase purity, and stability vary widely between and within each synthesis method (Cox *et al.*, 2015). For the preparations of adjustable shape, uniform composition, narrow particle size distribution, large specific surface area, fine grain, non-agglomerate, superior performance and others properties of

nanocrystalline HA, researchers are constantly trying to update and develop each method. Agglomeration and the formation of particles with non-uniform size distributions are some limitations of the methods (Cai *et al.*, 2019).

2.4.1 Precipitation

HA synthesis using precipitation is simply mixing aqueous solution of salts of calcium and phosphate with controlled pH and temperature by stirring the mixture constantly followed by drying the precipitate at a given temperature. This method is the most popular and widely researched technique for the synthesis of HA due to its versatile and economic advantages. The morphology of the product obtained from the precipitation method can be affected by temperature, time, Ca^{2+} ion concentration, surfactant, calcination and the use of different reagents. It is commonly observed that HA nanoparticles synthesized through chemical precipitation are often highly agglomerated (Nayak, 2010; Pang Bao, 2003). This method is simple and easy to prepare and the powder has high purity, fine particles, low reaction temperature and low cost (Dou *et al.*, 2018; Mateus *et al.*, 2013). The other advantage of this technique is that a relatively large amount of HA can be produced in the absence of organic solvents at a reasonable cost. Besides the ease of producing HA nanoparticles through the precipitation route, another advantage of this technique is that particle sizes can be effectively controlled, and it increase with increasing temperature (Loo *et al.*, 2008). The linear increase in particle size is therefore a good indication that the sizes of the nanomaterial can be tailored (Loo *et al.*, 2010).

However, this method has some limitations such as the difficulty in controlling the pH value above nine to avoid the formation of calcium-deficient HA, which during sintering forms tri-calcium phosphates. The other disadvantage is that the precipitation method has poor uniformity, and may be agglomerated, which makes it possible to generate calcium-deficient apatite with lattice defects and a Ca/P ratio less than 1.67. Therefore, the reaction conditions must be strictly controlled to make the precursors fully react at a reasonable temperature, pH and reaction time. Adding appropriate dispersants, controlling the precipitation rate, and washing the product multiple times improve the purity of nanohydroxyapatite (Mateus *et al.*, 2013).

2.4.2 Sol-gel

Sol-gel method normally involves the use of metal alkoxides or organometallic compounds as precursors. In this process, the precursors undergo a series of hydrolysis and polycondensation reactions to form a colloidal suspension or a sol and it is transformed into a solid gel. Finally drying of the gel followed by calcination at different temperatures to obtain the nanopowder (Dou *et al.*, 2018). It is an effective method for the synthesis of nanophase HA, due to the possibility of a strict control of process parameters (Balamurugan *et al.*, 2006). This method offers a molecular-level mixing of Ca and P, which is capable of improving the different properties of HA to a significant extent (Arole Munde, 2014). This technique has attracted much attention recently (Weng *et al.*, 2003), due to its well-known inherent advantages such as homogeneous molecular mixing, low processing temperature, the ability to generate nano-sized particles, the tremendous flexibility to generate nanocrystalline powders, bulk amorphous monolithic solids and thin films (Brinker Scherer, 2013). This method does not require pH control, high temperature, vigorous agitation, or long reaction time (Gopi *et al.*, 2015), it gives products of high purity and narrow particle size distribution. However, the application of this method is restricted by the high raw material price, the toxicity of organic solvents, and the easy and rapid aggregation of particles during heat treatment (Dou *et al.*, 2018).

2.4.3 Micro-emulsion

Micro-emulsion is a technique based on the use of two immiscible liquids such as water that has a high dielectric constant being dispersed under agitation in an oil phase, having a low dielectric constant, both phases stabilized by an amphiphilic surface-active agent or surfactant to control interfacial tension. Micro-droplets of water, formed when the aqueous phase is dispersed surrounded by a monolayer of surfactant molecules in the hydrocarbon phase, are stabilized in a non-aqueous phase by a surfactant acting as a micro-reactor or nano-reactor in which reactions are conducted. These self-assembling media of reverse micelles can be used in the synthesis of nano-phase materials without excessive agglomeration, and with high surface area. It is one of the few techniques, able to produce a particle size in the range of nanometers with minimum agglomeration (Mateus *et al.*, 2013; Pileni, 2003). Experimental conditions such as aqueous/organic phase volume ratio, pH, aging time, aging temperature and concentration in the aqueous phase can affect the crystalline phase, surface area, particle size and morphology of HA nanomaterials (Loo *et al.*, 2010).

2.4.4 Hydrothermal

Hydrothermal refers to the chemical reaction of substances in a sealed heated solution above ambient temperature and pressure (Dou *et al.*, 2018) using an autoclave and it allows for the synthesis of fine-grained and highly pure single crystals, with controlled morphology and narrow size distribution. In this method, the Ca/P ratio for the product can be improved with an increase in hydrothermal pressure or temperature (Janaćkovića *et al.*, 2007). The main advantage of this method is that the product has high crystallinity and no need for secondary crystallization treatment, thus reducing the chance of HA particle agglomeration during re-crystallization. However, the method also has a complex process (Xu *et al.*, 2020) , and it is difficult to obtain the HA powder of quantitative Ca/P, and the quality is unstable. Studies have found that the shape and size of HA can be regulated by changing the hydrothermal temperature, hydrothermal time and reaction concentration. This method enables the production of HA nanomaterials having different shapes, such as spherical, rod-like, needle-like, flake, hexagonal prism, plate and spine-like structures (Dou *et al.*, 2018).

2.5 Characterization Techniques of Hydroxyapatite

2.5.1 Structural Analysis Techniques

X-ray powder diffraction (XRD) is a non-destructive, quick analytical method that is used primarily to identify the crystallographic structure of a substance and can give details on the dimensions of unit cells. The physical and chemical characteristics of crystalline powders, thin films, and other solid materials can all be measured with this technology. The fundamental principle of X-ray diffraction is the constructive interference of monochromatic X-rays with a crystalline material. When the conditions are in line with Bragg's Law ($n\lambda = 2d \sin \theta$), the incident rays interact with the sample in a way that produces constructive interference and a diffracted beam. To understand X-ray diffraction from a crystal, W.L. Bragg thought that it might be an issue of X-ray reflection from the atomic planes of the crystal in line with the rules of reflection. It is a powerful technique to determine the crystal structure and to check the phase purity of HA materials (Cengiz *et al.*, 2008).

Fourier-transform-infra red spectroscopy (FTIR) gives information regarding the presence or absence of surface functional groups of the materials. The spectrum is mostly recorded in the range of 400 to 4000 cm^{-1} with a given resolution at room temperature. The most relevant peaks for HA are associated with the vibrations corresponding to P-O, and O-H bonds (Ye *et al.*, 2009). FTIR analysis gives information regarding the mechanism of reaction when HA is modified with organic as well as inorganic substances (Manatunga *et al.*, 2018; Valizadeh *et al.*, 2014). Metal ion substitution in the HA structure changes the position and intensity of some peaks. For example (Trinkunaite-Felsen *et al.*, 2015) investigated that the O–H band at 633 cm^{-1} and the PO_4^{3-} band at 564 cm^{-1} decreases in intensity due to substitution of Ca^{2+} ions by Fe^{3+} ions, and they concluded that when the amount of Fe^{3+} ions further increased, the O–H vibrational bands diminished.

Diffuse reflectance spectroscopy (DRS) with a UV-visible spectrophotometer is one of the widely used methods to investigate the optical characteristics of solids, which is associated with changes in structure or functional group. The classical Kubelka-Munk (K-M) model has been commonly used in this context to comprehend light scattering from semiconductor powder materials' surfaces (Landi Jr *et al.*, 2022). First, the signal from the well-known reference material that is non-absorbing is gathered. Then, instead of the reference, the holder containing the grain sample is placed. Due to its non-reactivity and transparency at energy less than 3.5 eV, barium sulfate ($BaSO_4$) is the preferred reference material for measurements in the visible range (Murzin *et al.*, 2023). Cation doping in the HA structure changes the light absorption property of the host material. For example, (Hadagalli *et al.*, 2021) investigated the optical properties of pristine and Fe^{3+} ions doped HA materials, it is clear that the doped HA particles display absorption in the UV-visible range (200 nm–400 nm) and in the visible portion (300 nm–700 nm), but pristine HA powder exhibits no absorption in the visible range. Furthermore, the intensity of the absorption bands increased with increasing the amount of Fe^{3+} ions in the doped samples.

2.5.2 Composition Analysis Techniques

The elemental composition of HA can be determined using X-ray photoelectron spectroscopy (XPS) and energy dispersive X-ray spectroscopy (EDX). XPS is a technique for surface characterization utilized for various materials using photoionization and energy-dispersive analysis of the photoelectrons released. Each element has a unique binding energy linked to a

particular atomic orbital, resulting in a distinctive collection of peaks in the photoelectron spectrum at specific kinetic energies governed by the photon energy and the electrons' binding energy. As a result, the existence of distinctive peaks at specific energies denotes the presence of a particular element in the sample. The peak's intensity is proportional to the element's concentration in the sampled region. Additionally, the chemical state of the emitting surface component atoms can slightly modify the shape of each peak and the binding energy, providing additional information on chemical bonds. Hydrogen and helium are not detectable by XPS, even though it can be utilized for all other elements (Stevie Donley, 2020). The two most crucial factors for determining an element's chemical state in a sample are peak position and peak energy separation (Sheikh *et al.*, 2018). For instance, (Hadagalli *et al.*, 2021) studied the chemical composition of Fe^{3+} ions doped HA using XPS, and confirmed the presence of Ca, P, O and Fe in their respective oxidation state in the synthesized samples. Their result also indicates that O exists in different chemical environments due to the presence of OH^- and PO_4^{3-} functional groups.

Similarly, with the aid of the potent tool known as energy-dispersive X-ray spectroscopy (EDS), one can examine the elemental makeup of a target sample. The ability of high-energy electromagnetic radiation (X-rays) to release "core" electrons from an atom is the main underlying mechanism that makes EDS work. A higher energy electron can fill the hole left by the removal of these electrons, and when it relaxes, it will release energy. By exposing a sample to X-rays, one may determine which elements are present and in what proportion by measuring the energy released during this relaxation process, which is specific to each element on the periodic table (Piburn Barron, 2013). For example, (Jiménez-Flores *et al.*, 2017) determined the chemical composition of Tb^{3+} ions doped HA using EDS, and the analysis result indicated that all the expected elements were detected in the respective samples. Moreover, the ratio of Ca/P was decreased as the amount of Tb^{3+} ions further increased in the doped samples.

2.5.3 Particle Size and Surface Property Analysis Techniques

Scanning electron microscopy (SEM), transmission electron microscopy (TEM) and Brunauer-Emmett-Teller (BET) analysis are the commonly used techniques for the analysis of morphology, particle size, and surface area as well as the porosity of a given material, respectively. SEM is used to observe the surface structure and to check the presence of agglomerated particles in a given synthesized material. The specimen is exposed to a narrow

electron beam from an electron gun, which rapidly moves over or scans the surface of the specimen. This causes the release of a shower of secondary electrons and other types of radiation from the specimen surface. The intensity of these secondary electrons depends upon the shape and the chemical composition of the irradiated object. These electrons are collected by a detector, which generates electronic signals. These signals are scanned in the manner of a digital camera to produce an image (Akhtar *et al.*, 2018).

Cation doping on HA structure brings a change in morphology, for example, (Wei *et al.*, 2019) used SEM to examine the morphology of synthesized pristine HA as well as Se^{4+} and Sr^{2+} ions co-doped HA powders. The findings show that the pure HA particles are lengthy rods with a consistent size distribution between 100 and 150 nm. The morphology of the Se^{4+} ions doped HA sample is like that of the pristine HA, but some minimum particles of various sizes have been deposited on the surface. Through doping of Sr^{2+} ions, the samples' morphology significantly altered from being long rod-like to short rod. With an increase in strontium level, the samples' crystallinity deteriorated, agglomeration was more likely to happen, the size of the particles shrank, and eventually, the form changed to an irregular ellipsoid.

In transmission electron microscopy (TEM), an electron beam from an electron gun is transmitted through an ultra-thin section of the sample and the image is magnified by the electromagnetic fields. It is used to observe finer details of the internal structures of the materials. The specimen to be examined is prepared as an extremely thin dry film or as an ultra-thin section on a small screen and is introduced into the microscope at a point between the magnetic condenser and the magnetic objective. The magnified image may be viewed on a fluorescent screen through an airtight window or recorded on a photographic plate by an in-built camera. It is used for detailed analysis of particle size, shape and surface characteristics. High-resolution transmission electron microscope (HR-TEM) can also give the crystalline phase of HA materials. For instance, (Guo *et al.*, 2019) determined the crystalline phase and lattice fringes of pristine HA and Fe^{2+} ions doped HA by HR-TEM. The observation indicated that the crystalline phase of pristine HA with well-resolved lattice fringes is confirmed, and the distance (0.344 nm) between the consecutive lattice fringes agrees well with the (002) plane of HA. However, the lattice fringes have shrunk in the case of Fe^{2+} ions doped HA. This is most likely caused by Fe^{2+} ions being incorporated into the HA crystal lattices.

Based on measurements of the gas (usually N_2) adsorption, the specific surface area, pore size and pore volume of several solid materials have been determined. The BET theory was

developed to determine the specific surface area based on the physical adsorption of gases on porous material's interior and external surfaces. The amount of adsorbed gas is proportional to the combined exterior and internal surface areas of the respective materials and is dependent on the relative vapor pressure. Adsorption isotherm refers to the relationship between the amount of gas adsorbed and the relative vapor pressure at constant temperature (Manoj *et al.*, 2019). The porosity characteristics of the material often affect how nitrogen adsorbs and desorbs. Type IV isotherm (H3 type) normally reflects the presence of mesoporous materials through the established hysteresis loop seen (Karunakaran *et al.*, 2019). For instance, (Al-Ahmed *et al.*, 2020) analyzed the textural properties of pristine and Pd^{2+} ions doped HA using the BET technique and the result showed that surface area, pore volume and average pore size were enhanced by Pd^{2+} ions doping in the HA structure. All these parameters further increased with the increase of the doped Pd^{2+} ions amount.

2.6 Impact of Fluoride and Organic Dyes on Environment and Human Health

Fluorine is the most reactive electronegative element. The processes of weathering and water circulation beneath soil layers and rocks cause fluorine to leach and dissolve into groundwater. Fluorine has a strong affinity for picking up electron and producing F^- ion. In groundwater the concentration of F^- ions reaches up to 35 mg/L. The geographic location affects the concentration of F^- ions in groundwater resources, which is mostly related to the existence of adjacent volcanic activity. Some of the areas with high F^- ions concentrations are found in the East African Rift, in Turkey, China, the United States, South America, Japan, Australia, etc. F^- is regarded as an important chemical since it helps to build and maintain dental health. However, drinking water containing high F^- ions concentration has been linked to some health risks. Numerous well-known negative consequences are caused by F^- ions absorption, tissue distribution, and bioaccumulation in bones and teeth (Alkurdi *et al.*, 2019). Excessive exposure to F^- ions can give rise to several adverse health effects (Fernando *et al.*, 2019; Tang *et al.*, 2018), such as loss of calcium from the tooth matrix, causing cavity formation, and ultimately leading to dental fluorosis followed by skeletal fluorosis. In addition, it may cause knock knee syndrome and neurological damage (Nayak *et al.*, 2017; Suriyaraj Selvakumar, 2016; Tang *et al.*, 2018).

Similarly, dyes utilized in several industries are regarded as the main water pollutants. There are around 100,000 different types of dyes available in the world, with azo (-N = N-) dyes

being the most multipurpose and dominant class (nearly 70%). In the course of the dye manufacture and dying process, 15% of the approximately $1x10^6$ tons of dyes generated each year are discarded into water-receiving bodies. These dye effluents seriously threaten the environment and living things. Particularly, azo dyes may have mutagenic and carcinogenic effects on people or aquatic life when present in trace concentrations. Dyes are also associated with problems with the liver, kidneys, and nervous system (Dutta *et al.*, 2022). Methyl orange (MO), its chemical structure is given in Figure 7, is a common and typical example of an azo-anionic dye. It is non-biodegradable in nature and is not removed efficiently by the traditional treatment methods (Neethu Choudhury, 2018; Wu *et al.*, 2021).

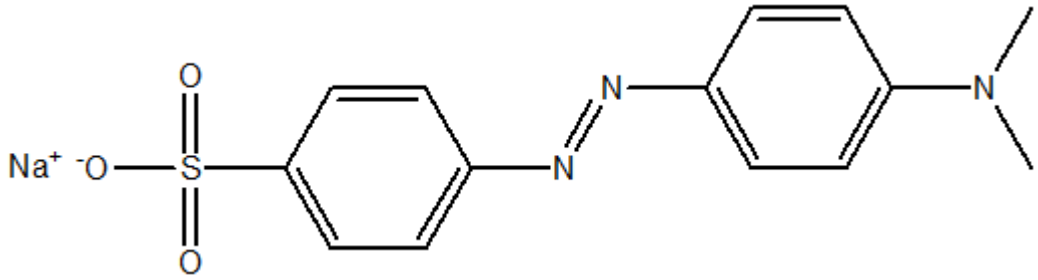

Figure 7. Chemical structure of MO dye

It is a synthetic organic dye, which is highly soluble in water. Textile, dyeing, leather, and paper sectors are just a few that frequently use MO dye. MO is frequently employed in research labs as a pH indicator. The direct discharge of MO into soils and water sources without suitable treatment, puts humans, other animals, and aquatic and terrestrial creatures at risk. MO hinders light penetration into deep water even at low concentrations, which negatively impacts photosynthesis. Additionally, it affects the gaseous solubility of water, which is essential for aquatic creatures. MO causes lung and intestinal cancer as well as hypersensitivity, allergies, and dermatitis. Its severe toxicity, teratogenicity, carcinogenicity, and mutagenicity have already been established (Khan A. U. *et al.*, 2022).

2.7 Analytical Techniques for the Removal of Fluoride Ions and Dyes

Until now, numerous technologies have been developed for the removal of pollutants from aqueous solution such as chemical precipitation, ion exchange, adsorption, membrane filtration, biological methods, photocatalysis and electrochemical treatment (Azzaza *et al.*, 2016; Ossman, 2017; Sulyman *et al.*, 2017). Unfortunately due to high costs, the formation of secondary sludge, incomplete removal and other factors restrict the practical applications of

many of these methods. The adsorption process is superior to other techniques for F^- ions removal in terms of cost, efficiency, simplicity of design and ease of operation (Gai Deng, 2021; He *et al.*, 2020). On the other hand, heterogeneous photocatalysis has become the first choice by researchers recently for the destruction of organic pollutants (dyes) into non-toxic forms, which may not be removed using other treatment techniques (Liu *et al.*, 2016; Shariffuddin *et al.*, 2013).

2.7.1 Adsorption

Adsorption is the process in which the adsorbate is accumulated on the adsorbent surface. It is the mass transfer process by which a substance is transferred from the liquid phase to the surface of a solid, and becomes bound by physical and/or chemical interactions (Sadegh *et al.*, 2017). This interaction brings about the adhesion of the particles of the adsorbate on the surface of the adsorbent (Omo-Okoro *et al.*, 2018). The adsorption process is generally classified as physical adsorption) in which, an adsorbate is bound to the surface by weak van der Waals forces, and chemical adsorption, an adsorbate is attached through covalent bonding or due to electrostatic attraction (Sadegh *et al.*, 2017). Adsorption is the most attractive option owing to its low cost, ease of use, low energy requirement, the possibility of separating the sorbent materials after treatment, efficiency even at low concentration, reversibility and others (Kuang *et al.*, 2020). The adsorption process is dependent on several factors such as the initial level of adsorbate, pH of solution, adsorbent dosage, rate of mixing and temperature (Omo-Okoro *et al.*, 2018).

2.7.1.1 Adsorption Models

Adsorption models can be classified into two categories, isotherm and kinetics models. The model that defines the type of interaction between the adsorbate and adsorbent, and the surface properties of the adsorbent are termed as isotherm models. The other category that defines the rate of adsorption is identified as kinetics model. Adsorption usually results in the removal of pollutants from the solution and concentrating them at a surface, until the amount of pollutant remaining in the solution is in equilibrium with that at the surface. This equilibrium is described by expressing the amount of pollutant adsorbed per unit mass of adsorbent as a function of the concentration of pollutant remaining in the solution. An expression of this type is termed an adsorption isotherm (El-Naas Alhaija, 2013). Adsorption isotherms give qualitative information about the nature of the adsorbate to adsorbent surface interaction as

well as the specific relation between the concentration of adsorbate and its degree of accumulation onto the surface at a specified temperature (Özsin *et al.*, 2019). Adsorption isotherm helps to describe the surface processes of adsorbent, the type of adsorbent monolayer or multilayer, and the capacity of the adsorbent (Karimi *et al.*, 2019).

Different research reports indicate that Freundlich and Langmuir isotherm models are the most commonly used isotherms for modeling adsorption processes in the liquid phase. Langmuir adsorption which was primarily designed to describe gas-solid phase adsorption is also used to quantify and contrast the adsorptive capacity of various adsorbents. Langmuir isotherm accounts for the surface coverage by balancing the relative rates of adsorption and desorption, dynamic equilibrium (El-Naas Alhaija, 2013). In general the Langmuir model is based on the following assumptions: molecules are adsorbed at a fixed number of well-defined localized sites, adsorption is limited to a single layer of adsorbate molecules, the enthalpy of adsorption is the same for all molecules and there are no interactions between molecules adsorbed on neighboring sites (Chen, 2015; El-Naas Alhaija, 2013). On the other hand, the Freundlich isotherm model is the earliest known relationship describing non-ideal and reversible adsorption, which can be applied to multilayer adsorption, based on an assumption concerning the energetic surface heterogeneity. The model applies to adsorption processes that occur on heterogonous surfaces and defines the exponential distribution of active sites and their energies (Chen, 2015).

Adsorption kinetic studies provide information about optimum conditions, the mechanism of sorption, and possible rate-controlling steps. It describes reaction pathways, as well as the time to reach the equilibrium. Kinetics also shows a large dependence on the physical and chemical characteristics of the adsorbent material, which also influence the adsorption mechanism that can be either film or pore diffusion or the combination of both depending on the system hydrodynamics. Kinetic models that are used to describe the rate and mechanisms of adsorption are pseudo-first order, pseudo-second order, Elovich, and intra-particle diffusion (Wang Guo, 2020). The Lagergren pseudo-first order model is most commonly used to describe the adsorption of adsorbate from a liquid solution. In the case of the pseudo-second order model, the rate-limiting step is the surface adsorption that involves chemisorption, where the adsorbate removal from a solution is due to physicochemical interactions between the two phases (El-Naas Alhaija, 2013).

2.7.1.2 Thermodynamics of Adsorption

To understand the effect of temperature and to conclude whether the adsorption process is spontaneous or not, thermodynamic parameters such as Gibbs free energy change (ΔG°), enthalpy change (ΔH°), and the entropy change (ΔS°) can be used extensively. The value of ΔG indicates the spontaneity and feasibility of the adsorption process whereas ΔH value tells us the endothermic or exothermic nature of the sorption process. Similarly, the ΔS value shows whether the disorderliness increased or decreased during the adsorption process (El-Kafrawy *et al.*, 2017; Özsin *et al.*, 2019).

2.7.2 Photocatalysis

One type of advanced oxidation process that relies on the use of catalysts in the presence of light energy is photocatalysis. Compared to traditional treatment technologies, photocatalysis offers several advantages, such as softer reaction conditions, fast reaction rates with little energy consumption, and use of solar light (Wang *et al.*, 2022). Organic pollutants can be broken down by photocatalysis into relatively less-toxic inorganic substances like water and carbon dioxide. Electrons are promoted from the VB to the CB and positive holes are simultaneously generated in the VB when the photocatalyst is exposed to an energy-dense light source. These charge carriers that are produced by light interaction may either recombine or interact with pollutant molecules on the surface of the photocatalyst (Rocha *et al.*, 2022).

2.7.2.1 Mechanism of Photocatalysis

To produce different oxidant radicals like the hydroxyl radical (•OH) superoxide radical ($•O_2$), and hydrogen peroxide (H_2O_2), photogenerated electron-hole pairs (e^-/h^+) react with adsorbed molecules such as water, oxygen, or hydroxyl groups on the surface of the photocatalyst. These free radicals (mainly •OH) attack the majority of organic pollutants to convert into smaller fragments like CO_2, H_2O, and inorganic ions (Mohseni-Salehi *et al.*, 2018; Rocha *et al.*, 2022) according to Figure 8, and the reactions can be summarized using Equations 7 - 13 (Goodarzi *et al.*, 2023; Wang *et al.*, 2022).

$$\text{Photocatalyst} + h\boldsymbol{\nu} \rightarrow h^+ + e^- \quad (7)$$

$$h^+ + H_2O \rightarrow •OH + H^+ \quad (8)$$

$$e^- + O_2 \rightarrow •O_2^- \quad (9)$$

$$\bullet O_2^- + 2H^+ + e^- \rightarrow H_2O_2 \quad (10)$$

$$H_2O_2 + e^- \rightarrow \bullet OH + OH^- \quad (11)$$

$$\bullet O_2^- + H^+ \rightarrow \bullet OOH \quad (12)$$

$$\text{Pollutants + active radicals} \rightarrow CO_2 + H_2O + \text{harmless products} \quad (13)$$

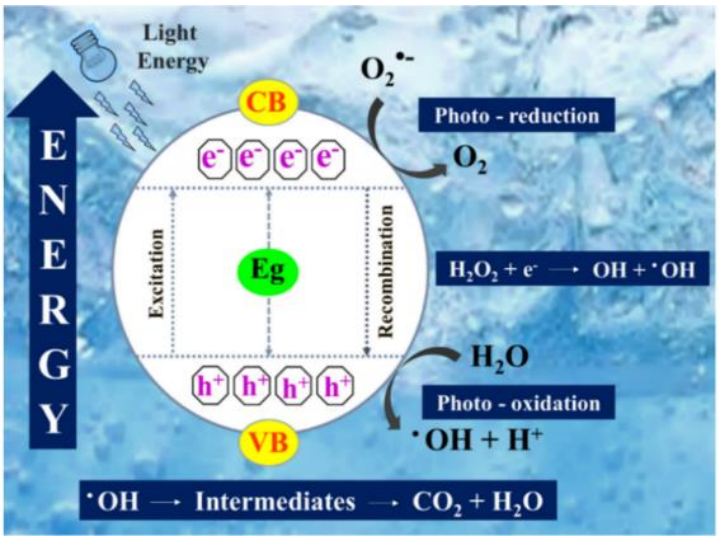

Figure 8. Representation of the semiconductor-based photocatalytic mechanisms (Rocha *et al.*, 2022)

Generally, (Wang *et al.*, 2022) summarized the photocatalysis processes into five steps: adsorption of the target substrate from the surrounding environment onto the photocatalyst surface initiates photocatalytic reactions (i), absorption of light with photon energies greater than the photocatalyst's bandgap energy results in the generation of photogenerated electron (e^-) – hole (h^+) pairs in the bulk phase (ii), migration of e and h^+ to the photocatalyst's surface to take part in the redox reaction and concurrently recombination of some photogenerated carriers from the catalyst's surface and interior (iii), the oxidation and reduction of H_2O molecules and O_2 adsorbed on the surface of the photocatalyst to hydroxyl radicals (•OH) and superoxide radicals ($\bullet O_2$), respectively, by h^+ in the VB, and e^- in the CB as well as the migration of e^- and h^+ to the surface of the photocatalyst to participate in the redox reaction and concurrently pollutants can break down into small molecules like H_2O and CO_2 (iv), the degraded small molecules are desorbed from the interface to the bulk solution (v), and the photoreaction proceeds.

2.7.2.2 Factors Affecting Photocatalytic Performance

The chemistry of the material, and the reaction conditions are two fundamental factors (Goodarzi *et al.*, 2023). Bandgap, crystallinity, composition, electron-hole recombination rate, light absorption capacity, surface area, and adsorption capability can affect photocatalytic activity (Natarajan *et al.*, 2018). The efficiency of the photocatalytic reaction depends on the relationship between the recombination and separation kinetics, and charge transfer. To increase the photo-oxidation of the target contaminant, the first step is to slow the recombination process (the main constraint). In general, pollutant concentration, photocatalyst dose, solution pH, kind of reactive oxygen species, light source, photocatalyst structure, bandgap energy, etc. are vital aspects during the photocatalysis process (Rocha *et al.*, 2022; Wang *et al.*, 2022).

2.7.2.3 Bandgap of Photocatalyst

The determination of the bandgap energy (Eg) is one of the most important factors in determining the photocatalytic performance of a semiconductor. The Kubelka-Munk theory in combination with the Tauc plot method can be used to determine a semiconductor's bandgap energy. The Kubelka-Munk (K-M) theory can be used for opaque materials having less photo-absorption properties, like that of powder materials and rough surfaces. This function depends on the reflecting (R) of light from the surface of an opaque sample (Goodarzi *et al.*, 2023). Tauc introduced a method for determining a semiconductor's bandgap energy by using UV-visible spectroscopy in 1966. This approach allows to express the relationship between bandgap energy, (Eg), and optical absorption coefficient, α using Equation 14 as follows (Goodarzi *et al.*, 2023):

$$(\alpha h\nu) = A\,(h\nu - E_g)^n \tag{14}$$

Where α is the optical absorption coefficient, $h\nu$ is incident photon energy, A is constant, E_g is bandgap energy, and n is a parameter that shows the type of electron transition and has values of 1/2, 2, 3/2, and 3, which indicates indirect allowed, direct allowed, indirect forbidden, and direct forbidden transitions, respectively.

CHAPTER THREE

MATERIALS AND METHODS

3.1 Chemicals and Instruments

This dissertation work used the following analytical grade chemicals without further purification. Calcium nitrate tetrahydrate ($Ca(NO_3)_2.4H_2O$, 99%, CARELABMED, India), Di-ammonium hydrogen phosphate ($(NH_4)_2HPO_4$, 99%, BLULUX, India), Ferric nitrate nonahydrate ($Fe(NO_3)_3.9H_2O$, 98%, Techno Pharm Chem, India), Bismuth nitrate pentahydrate ($Bi(NO_3)_3.5H_2O$, 99.5%, UNI-Chem, India), Sodium hydroxide (NaOH, 98%, LOBA Chemie, India), Sodium fluoride (NaF, 99.5%, BLULUX, India), Methyl orange ($C_{14}H_{14}N_3NaO_3S$, 99%, LOBA Chemie, India) and De-ionized water. The instruments XRD (XRD-7000, SHIMADZU Corporation, Japan), FT-IR (JASCO, FT/IR-6600, Japan), SEM-EDS (Hitachi S4800 SEM, Japan), TEM (HR-TEM Thermo Fischer Scientific, USA), XPS (Thermo Scientific K-Alpha$^+$, USA), BET (Quantachrome Instruments, AsiQwin, version 5.21, USA), FE-SEM (JSM-7800F, Japan) and UV-Vis (UV-3600Plus Series, SHIMADZU, Japan) were also used.

3.2 Experimental Procedure

3.2.1 Synthesis of Pristine Nanohydroxyapatite

Pristine HA nanomaterial was synthesized by adjusting Ca/P molar ratio of to 1.67, using co-precipitation technique following previous procedures (Anwar *et al.*, 2017; Fernando *et al.*, 2015), with the. First, using de-ionized water, $118.08x10^3$ mg/L $Ca(NO_3)_2.4H_2O$ and $39.62x10^3$ mg/L $(NH_4)_2HPO_4$ solutions were prepared separately. Next, $CaNO_3.4H_2O$ solution was added dropwise into the $(NH_4)_2HPO_4$ solution. Similarly, a 4 $x10^3$ mg/L of NaOH solution was added in the mixture continuously as a source of OH^-, and to keep the pH of the solution at 10 throughout the synthesis. The mixture was continuously heated for 3 hours at 80 $^{\circ}$C and stirred at 800 rpm. Then, the product was allowed to settle for 15 hours at room temperature, and impurities were removed by washing with de-ionized water. The washed product was oven-dried at 110 $^{\circ}$C for 24 hours, ground using mortar and pestle, and made ready for characterization and application. The synthesized nanomaterial was coded as HA. The synthesis is based on the reaction given in Equation 15.

$$10Ca(NO_3)_2.4H_2O + 6(NH_4)_2HPO_4 + 8NaOH \rightarrow Ca_{10}(PO_4)_6(OH)_2 + 12NH_4NO_3 + 8NaNO_3 + 46H_2O \quad (15)$$

3.2.2 Synthesis of Bismuth Doped and Iron Doped Hydroxyapatites

Bi^{3+} and Fe^{3+} ions doped HA nanomaterials, $Ca_{10-x}M_x(PO_4)_6(OH)_2$, with x = 0.1, 0.3, 0.5 and 0.7, (M = Bi^{3+} and Fe^{3+}) were synthesized based on the molar ratio of (Ca + M)/P equals to 1.67, and following similar procedure with the synthesis of pristine HA except the use of $Bi(NO_3)_3.5H_2O$, and $Fe(NO_3)_3.9H_2O$ as sources of Bi^{3+} and Fe^{3+} ions, respectively. The synthesis was performed using previous procedures (Srilakshmi Saraf, 2016; Xuan *et al.*, 2015). For the synthesizing of Bi^{3+} doped HA nanomaterials: 0.606, 1.82, 3.03, and 4.24 g of $Bi(NO_3)_3.5H_2O$ were taken in different beakers and dissolved using 20% HNO_3, to prevent the precipitation of $Bi(OH)_3$. Similarly, 27.45, 28.04, 28.63, and 29.22 g $Ca(NO_3)_2.4H_2O$ were taken in different beakers and dissolved using de-ionized water. Next, the $Bi(NO_3)_3.5H_2O$ solutions were mixed with the respective $CaNO_3.4H_2O$ solutions in 250 mL volumetric flasks and filled with de-ionized water up to the mark and homogenized. During mixing, the solution that contains the lowest mass of $Bi(NO_3)_3.5H_2O$ was added to the solution that contains the highest mass of $Ca(NO_3)_2.4H_2O$ orderly. Then the bimetallic (Ca^{2+}, Bi^{3+}) solution from the burette was added dropwise into the phosphate $(NH_4)_2HPO_4$ source in the beaker with continuous addition of 4 $x10^3$ mg/L of NaOH solution in the mixture. The mixture was continuously heated for 3 hours at 80 ºC and stirring at 800 rpm. The precipitate was allowed to settle for 15 hours and washed several times using de-ionized water. Then it was oven-dried at 110 ºC for 24 hours, ground using mortar and pestle, and set for characterization and application studies. The synthesized materials were labeled 1% Bi-HA, 3% Bi-HA, 5% Bi-HA and 7% Bi-HA for x = 0.1, 0.3, 0.5 and 0.7, respectively. The reaction for the synthesis was based on Equation 16.

$$(10-x)Ca(NO_3)_2.4H_2O + xBi(NO_3)_3.5H_2O + 6(NH_4)_2HPO_4 + 8NaOH \rightarrow Ca_{10-x}Bi_x(PO_4)_6(OH)_2 + 12NH_4NO_3 + 8NaNO_3 + (46+x)H_2O \quad (16)$$

For the synthesis of Fe^{3+} ions doped HA nanomaterials: 3.53, 2.52, 1.51, and 0.505 g of $Fe(NO_3)_3.9H_2O$ were mixed with 27.45, 28.04, 28.63 and 29.22 g of $Ca(NO_3)_2.4H_2O$ in different beakers, respectively. The mixtures were dissolved using de-ionized water, and poured into 250 mL separate volumetric flasks with complete mass transfer. De-ionized water was filled up to the mark and homogenized very well. Mixing was done by taking the lowest

mass of $Fe(NO_3)_3.9H_2O$ with the highest mass of $Ca(NO_3)_2.4H_2O$ solutions orderly. Then, the bimetallic mixed solution from the burette was added dropwise to the phosphate source in the beaker. Similarly a $4x10^3$ mg/L NaOH solution was continuously added to the mixture, and the mixed solution was heated with continuous stirring for 3 hours at 80 ºC and 800 rpm. The precipitate was allowed to settle for 15 hours and washed using de-ionized water. Then, it was oven-dried at 110 ºC for 24 hours, ground using mortar and pestle and stored for characterization and application studies. The synthesized nanomaterials were labelled 1% Fe-HA, 3% Fe-HA, 5% Fe-HA and 7% Fe-HA for y = 0.1, 0.3, 0.5 and 0.7, respectively. The chemical reaction for the synthesis is based on Equation 17.

$$(10\text{-}y)Ca(NO_3)_2.4H_2O + yFe(NO_3)_3.9H_2O + 6(NH_4)_2HPO_4 + 8NaOH \rightarrow Ca_{10\text{-}y}Fe_y(PO_4)_6(OH)_2 + 12NH_4NO_3 + 8NaNO_3 + (46 + 5y)H_2O \quad (17)$$

3.2.3 Synthesis of Bismuth and Iron Co-doped Nanohydroxyapatite

Bi^{3+} and Fe^{3+} ions co-doped HAs, $Ca_{10-(x+y)}Bi_xFe_y(PO_4)_6(OH)_2$, with x or y = 0.3, 0.4, 0.5, and 0.6 were prepared by making x + y = 0.9, and considering the atomic ratio of (Ca + Bi + Fe)/P near to 1.67, and following a similar procedure to the synthesis of pristine and single-doped HA nanomaterials using previous procedures (Bhattacharjee *et al.*, 2020; Chen *et al.*, 2014). To each 1.51, 2.02, 2.52, and 3.03 g of $Fe(NO_3)_3.9H_2O$, 26.86 g of $Ca(NO_3)_2.4H_2O$ was added and the mixtures were dissolved using de-ionized water. In the same way, 1.82, 2.42, 3.03, and 3.64 g of $Bi(NO_3)_3.5H_2O$ were dissolved in separate beakers using 20% HNO_3, to prevent the precipitation of $Bi(OH)_3$. Then, solutions containing Ca^{2+} and Fe^{3+} were mixed with those containing Bi^{3+} in 250 mL volumetric flasks with complete mass transfers. Each flask was filled to the mark using de-ionized water, and homogenized very well. Mixing these solutions was by taking the highest mass of $Bi(NO_3)_3.5H_2O$ with the lowest mass of $Fe(NO_3)_3.9H_2O$ solutions and vice versa orderly. Next, the tri-metallic mixed solution was added dropwise into the solution of the phosphate source. In addition, $4x10^3$ mg/L solution of NaOH was added continuously in the mixture. Then the mixed solution was continuously heated for 3 hours at 80 ºC and stirred at 800 rpm. The product was allowed to settle for 15 hours, and impurities were removed by washing with de-ionized water. The washed products were oven-dried at 110 ^{o}C for 24 hours, characterized and used for different applications. The synthesized nanomaterials were coded as 3% Fe – 6% Bi-HA, 4% Fe – 5% Bi-HA, 5% Fe – 4% Bi-HA and 6% Fe – 3% Bi-HA for x = 0.3 and y = 0.6, x = 0.4 and y = 0.5, x = 0.5 and y = 0.4, and x = 0.6 and y = 0.3, respectively. The chemical reaction for the synthesis is given in Equation 18.

$$10\text{-}(x+y)Ca(NO_3)_2{\cdot}4H_2O + xBi(NO_3)_3{\cdot}5H_2O + yFe(NO_3)_3{\cdot}9H_2O + 6(NH_4)_2HPO_4 + 8NaOH \rightarrow Ca_{10\text{-}(x+y)}Bi_xFe_y(PO_4)_6(OH)_2 + 12NH_4NO_3 + 8NaNO_3 + (46 + x + 5y)H_2O \quad (18)$$

3.3 Characterization of Pristine and Doped Hydroxyapatite Nanomaterials

Using an X-ray diffractometer (XRD-7000, SHIMADZU Corporation, Japan) having a radiation source of CuKα1 (λ = 1.5406 nm), the phase purity, crystal size, crystal structure, and crystallinity of pristine and doped HA synthesized samples were determined at Adama Science and Technology University, Department of Material Science and Engineering. The instrument was operated at a voltage of 40 kV, and a current of 30 mA with a scan speed of 3^o min^{-1}, step size of 0.02^o and a scan range of 2θ from 20-80^o in continuous mode. The final diffraction data were matched with the standard JCPDS HA databases with the appropriate card numbers.

The presence and, or absence of the characteristic functional groups of pristine and doped HA were characterized by FTIR (JASCO, FT/IR-6600, Japan) in the range of 400-4000 cm^{-1} with a resolution of 4 cm^{-1} using KBr windows, and the spectrum was recorded at Bahir Dar University, School of Chemical and Food Engineering. Similarly, a UV-Vis/DRS spectrophotometer (UV-3600Plus Series) with a 5 nm slit width in the wavelength range of 300 – 800 nm was used to determine the optical properties of the nanomaterials in the presence of $BaSO_4$ as a reference. During the analysis, 0.15 g of each sample was mixed with 4.85 g $BaSO_4$, properly homogenized, and the reflectance was recorded. Finally, the bandgap energy of the materials was calculated using the Kubelka–Munk function and the Tauc plots. The analysis was done at Adama Science and Technology University, Department of Material Science and Engineering.

The surface morphology, size and level of aggregation/agglomeration of the pristine and doped HA materials were estimated from SEM (Hitachi S4800 SEM, Japan) and HR-TEM (HR-TEM, Thermo Fischer, USA) images. In addition to morphology and particle size analysis, an HR-TEM image was used to determine the sample's plane orientation (Miller indices, h k l). The analyses were done at the Chungnam National University, Department of Chemistry, Department of Chemical Engineering and Applied Chemistry, Republic of Korea. Using image j software, particle size and grain size were calculated. Furthermore, FE-SEM analysis was

performed to visualize highly minute topography characteristics on the surfaces of the materials. The analysis was done at the Foundation for Innovative and Technology Transfer, New Delhi, India.

The samples' atomic/weight% of the respective elements were analyzed using EDS. Similarly, XPS (Thermo Scientific K-Alpha, USA) was used to confirm the presence of the elements with their characteristics elemental state and environment in the doped HA sample. It was used to check the incorporation of the dopant metal ions with the required percentage and elemental state. The analysis was done at Chungnam National University, Department of Chemistry, Department of Chemical Engineering and Applied Chemistry, Republic of Korea.

The materials' surface area and pore volume were measured using a BET Surface Area Analyzer (Quantachrome Instruments, AsiQwin, version 5.21, USA), by nitrogen adsorption at -195.65 $^{\circ}$C and sample degassing at 200 $^{\circ}$C for 2.3 hours under vacuum. The analysis was done by taking 0.0541 g of the sample at the National Institute of Technology Karnataka, Surathka, India.

The pH drift (salt addition) approach was used to estimate the materials' point of zero charge (PZC) (Mahmood *et al.*, 2011). During the analysis, 40 mL of $8.5x10^3$ mg/L $NaNO_3$ was used in the experiment, and its pH was adjusted to 2 – 11 using $3.65x10^3$ mg/L of HCl and $4x10^3$ mg/L of NaOH solutions. The mixture was then stirred in an orbital shaker for 24 hours at room temperature while 0.1 g of the HA based-nanomaterials were added to each individual vessel. After the suspension had settled the pH was then determined. The analysis was done at Adama Science and Technology University, Applied Chemistry Department.

3.4 Fluoride Ion Adsorption Experiment

3.4.1 Solution Preparation and Adsorption Performance Analysis

A stock solution (1000 mg/L) of F^- ions was prepared by dissolving 0.2210 g of analytical grade NaF in de-ionized water and diluting it to 100 mL in a volumetric flask. From the stock solution, calibration solutions (0.19 mg/L and 190 mg/L), and working solutions (5, 10, 15, 20, 25, and 30 mg/L) of F^- ions were prepared by serial dilution. The as-synthesized HA-based materials were ground using mortar and pestle and sieved to get the uniform size of the adsorbents. Then, the materials' F^- ions removal capacities were examined using batch

adsorption by mixing 0.05 g of each of the adsorbents and 100 mL of 10 mg/L F^- ions in a sealed reaction vessel at room temperature. The mixture was shaken using an orbital shaker at 150 rpm for 10 hours (Tang *et al.*, 2018). After that, the adsorbent was separated from the solution, and the remaining F^- ions were analyzed by an ion-selective electrode, ISE (S-613 Series Ion Concentration Meter, Peak Instrument) after calibration of the instrument with 0.19 mg/L and 190 mg/L F^- solutions. The adsorption experiment was performed in triplicates and the mean value was reported. The percentage adsorption removal of the materials was calculated to identify the best adsorbents from each category to optimize adsorption parameters further. The quantity of F^- ions removed at equilibrium (qe) and the adsorption efficiency (%) were determined by Equations 19 and 20, respectively (Nayak *et al.*, 2017).

$$q_e = \frac{(C_o - C_e)V}{w} \tag{19}$$

$$Adsorption\ (\%) = \frac{(C_o - C_e)}{C_o}\ x\ 100 \tag{20}$$

Where Co and Ce are the initial and equilibrium concentration of F^- ions respectively, v is the volume of the solution in liter, and w is the mass of adsorbent taken in gram.

3.4.2 Adsorption Parameters Analysis and Reusability Studies

The adsorption parameters were investigated according to an earlier work (Tang *et al.*, 2018). During selections of adsorbents, 100 mL of an initial concentration of 10 mg/L of F^- ions, 0.5 g/L of the adsorbents, pH of 6.5, temperature of 25 $\pm$ 2 $^{\circ}$C, and agitation speed of 150 rpm were used. HA nanomaterials' F^- ions elimination effectiveness was investigated using pH of 3, 4, 5, 6, 7, 8, 9, 10, and 11. The solution pH was adjusted with $3.65x10^3$ mg/L HCl and $4x10^3$ mg/L NaOH solutions. To conduct the influence of contact time, samples were taken at predetermined intervals while the contact period was allowed to extend up to 4 hours, using 10 mg/L of F^- ions concentration at pH of 6.5. Initial F^- ions concentrations of 5, 10, 15, 20, 25, and 30 mg/L were used for the influence of initial concentration for contact time of 3 hours, and pH of 6.5. For the F^- ions adsorption, the adsorbent quantity of 0.05, 0.1, 0.2, 0.3, 0.4, and 0.5 g were used for 3 hours contact period, 10 mg/L of F^- ions concentration, and pH of 6.5. Five different temperatures (25, 30, 40, 50, and 60 $^{\circ}$C) were used to study the effect of temperature on F^- ions adsorption, with an adsorbent dose of 2 g/L and a contact time of 3 hours, 10 mg/L of F^- ions concentration, and pH of 6.5. By combining 20 mg/L of F^- ions and 2 g/L of the adsorbent with 0, 30, and 300 mg/L of chloride, nitrate, sulfate, and carbonate ions,

and fixing the time of contact for 3 hours, and pH of 6.5, the impact of common ions was investigated. The general adsorption-desorption experimental procedure is summarized in Figure 9.

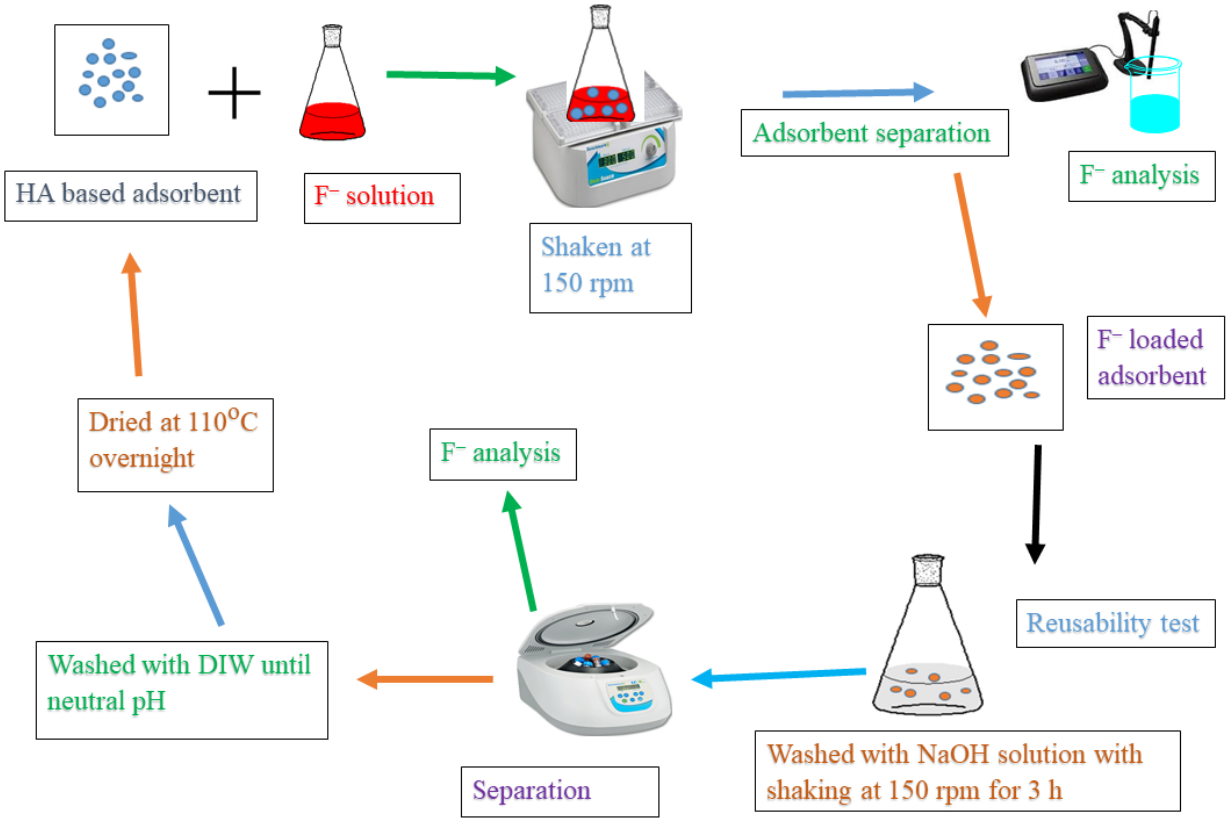

Figure 9. Adsorption-desorption experimental procedures

In the regeneration and reusability investigations, the F^- ions loaded adsorbent was washed using 100 mL of $40x10^3$ mg/L NaOH solution with stirring the mixture at 150 rpm for 3 hours. The adsorbent was extracted from the mixture by centrifugation, and the amount of F^- ions desorbed was measured. The extracted adsorbent was washed with de-ionized water until the pH reached 7. After 24 hours oven drying at 110 ^oC, it was reloaded by submerging it in a freshly prepared F^- ions solution (Indah *et al.*, 2018). The studies were conducted in triplicate for five consecutive rounds to investigate the recyclability and regeneration of HA-based materials. A 10 mg/L F^- ions, 2 g/L of adsorbents, 180 minutes of shaking at 150 rpm, and room temperature were used in this analysis.

3.5 Photocatalytic Activity Experiment

First, a stock solution (1000 mg/L) of MO was prepared, and from this solution working solutions of MO (5, 10, 15, and 20 mg/L) were prepared by serial dilution. A halogen lamp having a power of 150 W, and wavelength in the range of 320 -1100 nm, connected to a cooling water circulating system was used as a visible light source. Initially, the adsorption-desorption capability was evaluated using a 100 mL mixture of 40 mg of the photocatalyst and 5 mg/L of MO solution by stirring it at 600 rpm for 30 min without light. After that, the photocatalytic performance of the materials was analyzed by irradiating the mixture for 45 minutes with continuous stirring at room temperature. Then, the photocatalyst was separated from the solution by centrifugation, and absorbance of the supernatant solution was measured in the wavelength range of 200 – 800 nm using a UV-Vis spectrophotometer. The percent adsorption and degradation efficiency ɳ, (at the wavelength of 464 nm by applying Beer-Lambert's law) of the materials were calculated (Mohseni-Salehi *et al.*, 2018) using Equations 21 and 22, respectively.

$$Adsorption\ (\%) = \frac{(C_o - C_a)}{C_o}\ x\ 100 \quad (21)$$

$$ɳ\ (\%) = \frac{(C_a - C_t)}{C_a}\ x\ 100 \quad (22)$$

Where, C_o is the initial concentration of MO, C_a the concentration after 30 min stirring in the dark and C_t is the concentration at time t.

After identification of the best-performing material for the photocatalytic degradation of MO, the effect of different parameters such as pH, irradiation time, initial concentration of MO, and amount of the photocatalyst were evaluated as per previous report with slight modification (Azad Gajanan, 2017). Unless otherwise stated, 100 mL of 5 mg/L MO, 0.4 g/L of the photocatalyst, and 45 minutes of irradiation time were applied during the parameter effect analysis. The effect of pH on the photocatalytic degradation of MO was analyzed by taking pH 3, 5, 7, and 9. The effect of contact time was studied for up to 3 hours by taking samples at 20-minute interval. The effect of the catalyst amount was evaluated by taking 30, 40, 50 and 60 mg of the synthesized sample. Similarly, the effect of MO concentration on photocatalytic degradation efficiency was performed by taking MO concentrations of 5, 10, 15 and 20 mg/L solutions. The general experimental procedure is summarized in Figure 10.

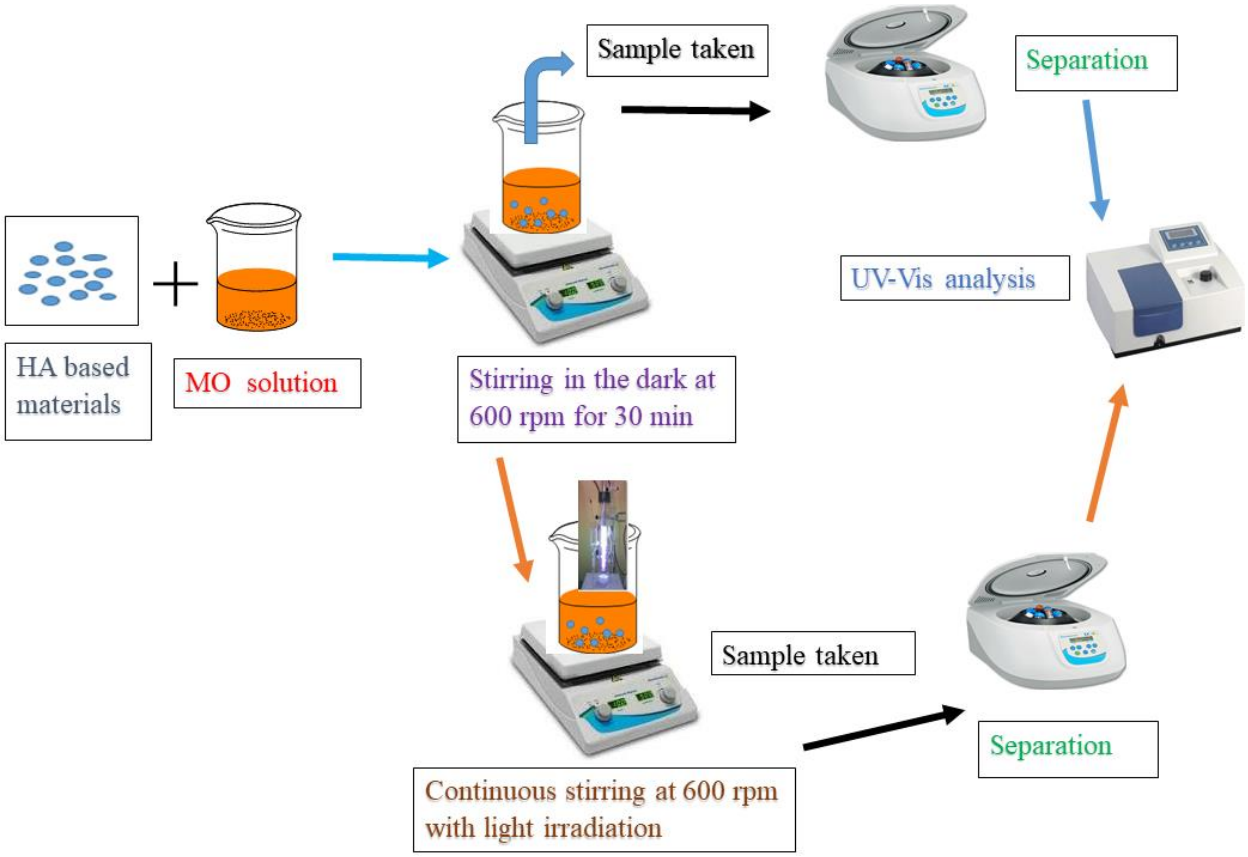

Figure 10. Photocatalytic experimental procedure

3.6 Antibacterial Activity

Gram-negative *Escherichia coli* (*E coli*, ATCC 25922) and gram-positive *Staphylococcus aureus* (*S. aureus*, ATCC 25923) bacteria were used in the agar diffusion method (Ciobanu C. *et al.*, 2015) to test the antibacterial properties of all the produced HA-based products. The Petri plate, cotton swabs, Muller-Hinton agar (MHA), and other materials and equipment were first decontaminated in an autoclave by heating them to 121 ºC for 20 minutes. The freshly made and sterilized MHA solution was poured into the sterilized Petri dishes at a consistent depth of about 4 millimeters and allowed to cool for 18 hours. The bacterial strains were subsequently activated by incubating overnight using chocolate agar at 37 ºC. The requisite nanomaterial suspensions were prepared using 5% dimethyl sulfoxide (DMSO) as the solvent. Using sterile tryptic soy broth, the bacterial strains were diluted to approximately 0.5 McFarland turbidity standard ($1x10^8$ CFU/mL) and incubated for 20 minutes at 37 ºC. Cotton swabs were used to inoculate the Petri dishes evenly with the diluted bacterial strains. Subsequently, 20 µL of the well-dispersed nanomaterials (5, 10, and 20 mg/L) and DMSO (negative control) were applied onto 6 mm standard discs in the Petri dishes. Standard co-

trimoxazole antibiotic discs were employed as the positive control. Finally, after all the Petri dishes were incubated at 37 ºC for 24 hours, the inhibition zone of each disc for the corresponding bacterial strains was assessed in triplicate and averages reported.

3.6.1 Determination of Minimum Inhibitory Concentration and Minimum Bactericidal Concentration

The dilution method (Owuama, 2017) was used for determining the minimum inhibitory concentration (MIC) and minimum bactericidal concentration (MBC) for both bacterial strains, with a minor modification of a prior publication (Jafari *et al.*, 2011). Initially, twenty test tubes were filled with 1 mL of Muller Hinton Broth solution. A 1 mL solution containing 20 mg/L of the nanomaterial was added to test tube one and thoroughly mixed with the culture medium. In this instance, the nanomaterial's concentration was reduced in half. Then, 1 mL was removed from test tube one, added to test tube two, and thoroughly mixed. Up to test tube twenty, the serial dilution procedure was repeated. Next, from test tube twenty, 1 mL was discarded to create equal quantities of each. Each test tube was then filled with 0.1 mL of a standard microbiological suspension containing 1.5×10^8 CFU/mL *E. coli*. Afterward, the test tubes were incubated for 24 hours at 37 °C for observation of the turbidity or growth made. Similar observations for negative control (which contained only agar media and the bacteria) and positive control (which contained only the HA-based nanomaterial and the agar media) were also done. Samples from the MIC test tubes containing no bacterial growth were cultured to estimate MBC. A loopful from the test tubes was inoculated on Muller Hinton Agar and incubated at 37 ºC for 24 hours, then observed for the signs of growth of bacteria.

3.7 Data Analysis

Different software packages were applied to analyze data obtained from the characterization and application experiments. Origin pro 2021 software was used to draw and analyze data from characterization techniques such as FTIR, XRD, BET, XPS, and UV-Vis. Similarly, it was used to analyze data obtained from the application experiments like adsorption, photocatalysis, and antibacterial activity. QualX software determined the card number and shape of the pristine and doped HA samples. Image j software was used to determine the grain size, particle size, and plane orientation of the synthesized HA nanomaterials obtained from SEM, FE-SEM, and

HR-TEM techniques. Similarly, CAVS software version 2.1 was used to analyze adsorption isotherm, kinetics, and thermodynamics. One way ANOVA test was applied for the evaluation of whether or not significance difference is available in the variations of the data produced. The reason behind the selection of one way ANOVA is that, only the effect of variation in dopant amount or the type of dopant on F^- ions removal was considered, but not the effect of dopant amount on the dopant type or vice versa, during the analysis.

CHAPTER FOUR

RESULTS AND DISCUSSION

4.1 Structural Analysis

4.1.1 XRD Analysis

The X-ray powder diffraction data for Fe^{3+} ions doped, Bi^{3+} ions doped, and Bi^{3+} and Fe^{3+} ions co-doped HA nanomaterials are given in Figures 11, 12, and 13, respectively and the diffraction data of pristine HA is presented in all the diffraction Figures for comparison purpose. The prominent diffraction peaks for pristine HA (Figures 11, 12 and 13) appeared at 2θ of 25.88, 31.84, 31.98, 32.84, 34.14, 39.84, 46.74, 49.46 and 53.1°. These peaks are corresponding to the planes of (002), (211), (112), (300), (202), (310), (222), (213) and (004), respectively. The diffraction data agree with that of HA (PDF No: 09-0432, JCPDS database), having a hexagonal-arrangement (a = b = 9.418 Å, c = 6.884 Å, and c/a = 0.731) and space group of $P6_3/m$ (Chen *et al.*, 2018; Suresh Kumar *et al.*, 2020). No diffraction peak/s observed to claim the presence of secondary phases in the pristine HA-synthesized material.

The crystallite size (D), lattice parameters (α and c), degree of crystallinity, C_X and unit cell volume V were estimated using Equations 23, 24, 25, and 26, respectively (Kaygili *et al.*, 2021)

.

$$D = \frac{k\lambda}{\beta Cos\theta} \tag{23}$$

$$\frac{1}{d^2} = \frac{4}{3}\left(\frac{h^2 + hk + k^2}{a^2}\right) + \frac{l^2}{c^2} \tag{24}$$

$$C_X \approx 1 - \frac{V_{112/300}}{I_{300}} \tag{25}$$

$$V = 0.866a^2\mathrm{c} \tag{26}$$

Where D is the mean crystalline size, k is the shape constant (0.9), λ is the wavelength of the radiation (0.15406 nm), β is the full width at half maxima (FWHM) of the peak intensity, θ is the diffraction angle, d is the distance between adjacent planes in the set of Miller indices (h k l), $V_{112/300}$ is the intensity of the hollow between (112) and (300) peaks and I_{300} is the intensity of (300) peak.

The result (Table 2) also indicates that the average crystallite size of synthesized HA was 20.96 nm, which is in the nano-range. Moreover, the result indicates the c/a ratio is lower than the

expected (0.731) value. This may be due to the substitution of the phosphate ions by the carbonate ions (B-type substitution) (Safarzadeh *et al.*, 2020; Zhao *et al.*, 2016), the carbonate that comes from atmospheric carbon dioxide. The other evidence that showed the presence of B-type carbonate substitution in the HA structure is the overlapping of the (211) and (112) planes (Safarzadeh *et al.*, 2020).

.

Fe^{3+} doped HA nanomaterials (Figure 11) have similar diffraction patterns with the pristine HA nanomaterial, and are also in agreement with that of HA (PDF No: 09-0432, JCPDS database) having hexagonal-arrangement and space group of $P6_3/m$. Here also, there is no an evidence that shows the presence of any impurity/secondary phase. Fe^{3+} ions doped HA nanomaterials show decrease in peak intensity, except the (210) plane in the case of 7% Fe-HA, compared to pristine HA. The decrease in intensities of the diffraction peaks are associated with the decrease in crystallinity of the formed products. The diffraction peak at the (112) plane slightly shifted to higher 2θ values as the Fe^{3+} ions level increases. This shift in peak position to the higher angle indicates the replacement of Ca^{2+} ions having larger ionic radius (0.099 nm) with Fe^{3+} ions having smaller ionic radius (0.064 nm) (Trinkunaite-Felsen *et al.*, 2015). In addition, the diffraction peaks at the (211) plane decreased in intensity, while the (112) plane increased in intensity as the amount of Fe^{3+} ions increased during doping. These indicated the presence of distortion during the substitution of Ca^{2+} ions by Fe^{3+} ions in the HA structure (Faeghinia Ebadzadeh, 2020; Meng *et al.*, 2022; Xu *et al.*, 2022). Furthermore, the result (Table 2) indicates that the degree of crystallinity and crystallite size decreased as Fe^{3+} ions were introduced into the HA structure. The lower ionic radius of Fe^{3+} ions compared to Ca^{2+} ions prevents the crystal growth of the HA structure (Sheikh *et al.*, 2018; Trinkunaite-Felsen *et al.*, 2015). The decrease in peak intensities and crystallinity may also be due to the presence of B-type carbonate. The results also indicate that all Fe^{3+} ions doped HA have crystallite sizes in the nano-level.

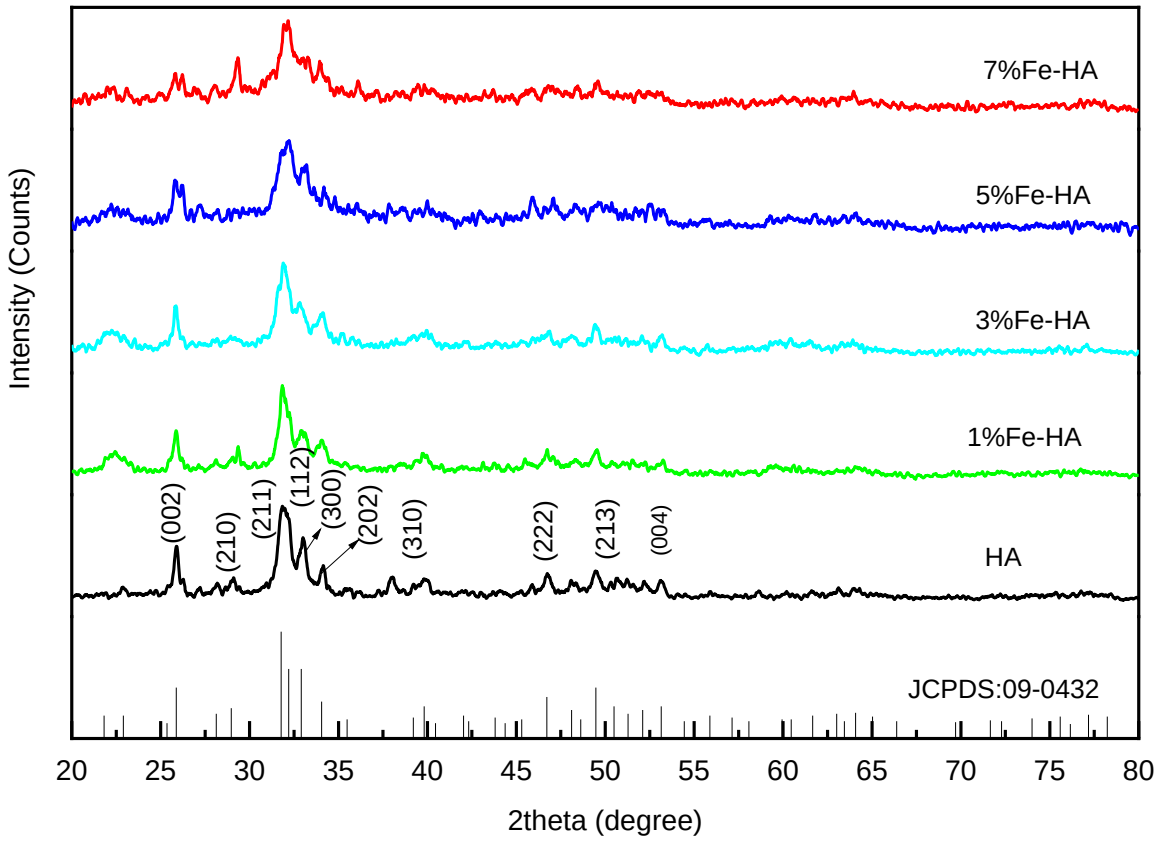

Figure 11. XRD patterns of pristine and Fe^{3+} ions doped HA nanomaterials

Incorporating Fe^{3+} ions into the lattice of calcium apatite changes the lattice parameters and unit cell volume (Table 2). Due to the lower ionic size of Fe^{3+} compared to Ca^{2+} ions, both the a-axis and c-axis have to be decreased, however the results indicate that the c-axis increased as Fe^{3+} ions introduced in the HA lattice. This is associated with the insertion of Fe^{3+} ions at the interstitial sites in addition to the substitution of Ca^{2+} ions (Avakyan *et al.*, 2021; Renaudin *et al.*, 2017), and the effect increases with increasing Fe^{3+} ions amount incorporated (Renaudin *et al.*, 2017). The change in lattice parameters also observed by the deviation of c/a ratios from the expected value. In the case of Fe^{3+} ions doped HA nanomaterials, the values of c/a ratio increased with the increasing of Fe^{3+} ions incorporated in the HA structure, which is due to the increasing of c value due to the interstitial doping as well as the decreasing of the a value due to the smaller size of Fe^{3+} ions.

Table 2. Crystallite size and lattice parameter values of pristine and doped HA nanomaterials

Samples	D (nm)	Lattice parameters (Å)		c/ a	C_X (%)	$V(Å^3)$
		a	c			
HA	20.96	9.429	6.880	0.7297	66.03	529.709
1% Fe-HA	15.21	9.422	6.884	0.7306	52.52	529.230
3% Fe-HA	17.64	9.419	6.884	0.7309	36.40	528.893
5% Fe-HA	19.82	9.419	6.890	0.7321	19.99	529.355
7% Fe-HA	21.17	9.417	6.896	0.7323	21.63	529.591
1% Bi-HA	23.06	9.439	6.884	0.7293	45.29	531.142
3%Bi-HA	24.69	9.440	6.886	0.7294	72.38	531.409
5% Bi-HA	24.90	9.441	6.882	0.7289	76.45	531.213
7% Bi-HA	25.67	9.450	6.890	0.7291	77.42	532.845
3% Fe-6% Bi-HA	22.45	9.439	6.889	0.7298	66.67	531.528
4% Fe-5% Bi-HA	21.42	9.437	6.886	0.7297	71.05	531.071
5% Fe-4% Bi-HA	17.81	9.436	6.882	0.7293	56.86	530.650
6% Fe-3% Bi-HA	19.24	9.430	6.880	0.7296	53.88	529.822

X-ray diffraction patterns of Bi^{3+} ions doped HA nanomaterials (Figure 12) are also in agreement with that of HA (PDF No: 09-0432, JCPDS database) having hexagonal-arrangement and space group of $P6_3/m$. In this case, an increment in the intensities of the diffraction peaks was observed as the amount of Bi^{3+} ions increased. In addition, a secondary phase was observed as the amount of Bi^{3+} ions incorporated into the HA structure increased. For instance, the presence of additional peaks at 2θ of 23.8 and 30.4, for 5% and 7% Bi-HA samples indicates availability of bismuth oxide carbonate ($Bi_2O_2CO_3$) tetragonal phase, which agrees with JCPDS file No. 041-1488 (Iyyapushpam *et al.*, 2015). Like that of Fe^{3+} ions doped HA, the diffraction patterns of Bi^{3+} ions doped HA nanomaterials also show variation in intensities of the prominent peaks when the amount of Bi^{3+} ions vary. For instance, when low amount of Bi^{3+} ions introduced (1% and 3%), the (112) diffraction peak becomes the most intense peak, whereas when the amount of Bi^{3+} ions increased (5% and 7%), intense peaks were observed in the (002) and (300) planes.

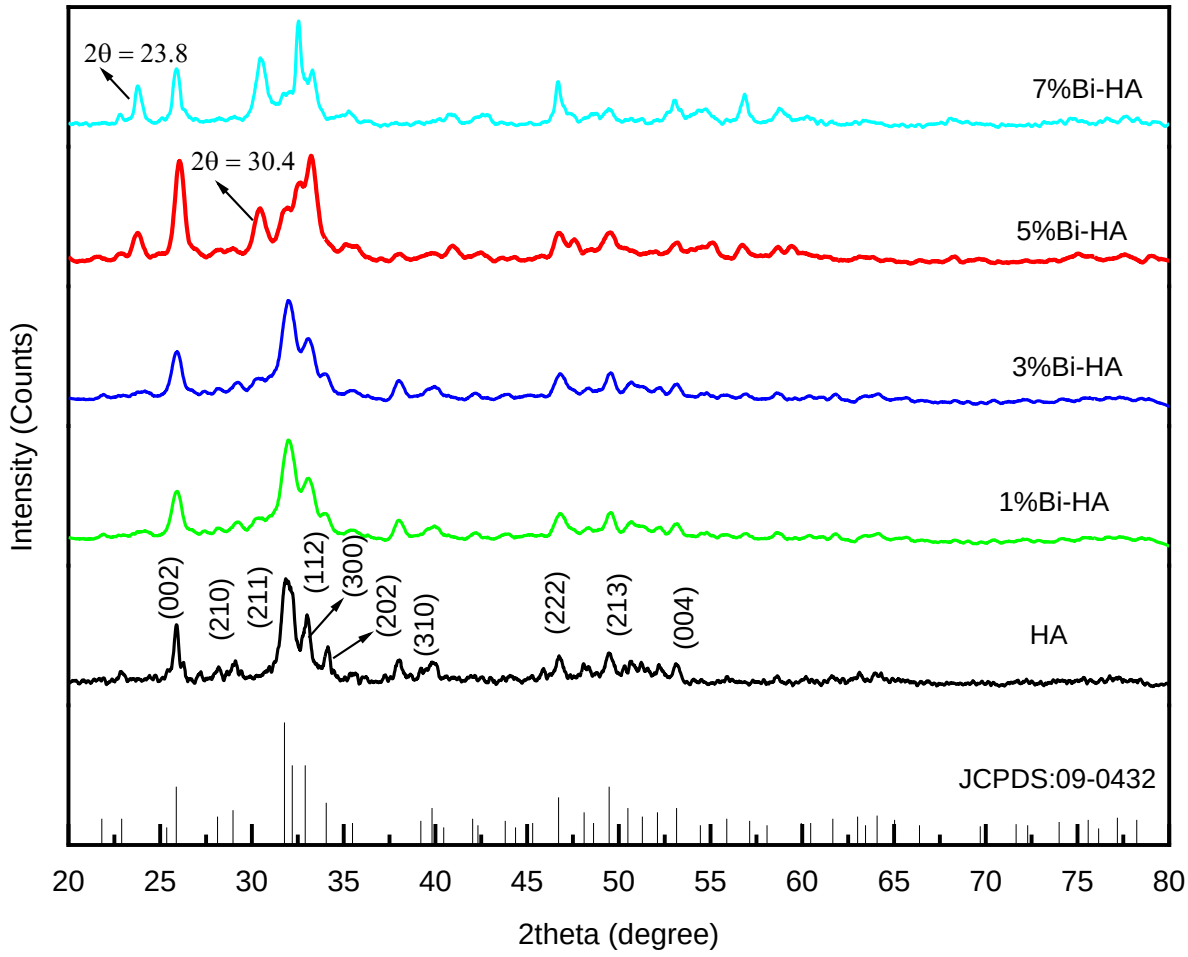

Figure 12. XRD patterns of pristine and Bi^{3+} ions doped HA nanomaterials

This indicates the presence of structural distortion on the lattice of HA due to the substitution of Ca^{2+} ions (0.099 nm) by Bi^{3+} ions (0.103 nm) which is associated to the ionic radii difference between the two metal ions (Ciobanu G. *et al.*, 2015). Incorporating cations having larger sizes than Ca^{2+} ions increased the crystallinity and crystallite size (Nagyne-Kovacs *et al.*, 2018; Ramakrishnan *et al.*, 2016). The incorporation of Bi^{3+} ions in HA's structure also changed the lattice parameters and unit cell volume of HA. Both the a-axis and c-axis increased as the dopant amount increased, indicating Bi^{3+} ions substitution in the apatite structure. In this case also, c/a ratio increased with the increasing c value due the larger ionic size of Bi^{3+} ions. Moreover, the results indicated that all Bi^{3+} ions doped HA materials also have crystallite sizes in the nano-level.

X-ray diffraction patterns of Bi^{3+} and Fe^{3+} ions co-doped HA nanomaterials (Figure 13) are also in agreement with that of HA (PDF No: 09-0432, JCPDS database) having hexagonal-

arrangement and space group of $P6_3/m$. No secondary phases and significant shifts in peak positions were observed in the co-doped HA nanomaterials due to the substitutions of Ca^{2+} ions with Bi^{3+} and Fe^{3+} ions. However, like that of single-doped HA nanomaterials, in the co-doped HA nanomaterials, there is a change in peak intensity as the percentages of Bi^{3+} and Fe^{3+} ions changed. For instance, the intense peak for 3% Fe – 6% Bi-HA is observed in the (202) plane with slight shift to the lower 2θ values due to the larger ionic size of Bi^{3+} ions; for 4% Fe – 5% Bi-HA, the intense peak becomes the (300) plane, and for 5% Fe – 4% Bi-HA and 6% Fe – 3% Bi-HA the intense peak observed in the (211) plane. This is the indication of the presence of change in the degree of crystallinity (crystal growth in different planes) or distortion during the substitution of Ca^{2+} ions by Bi^{3+} and Fe^{3+} ions, which is observed on the results given in Table 2. In general, in the co-doped HA nanomaterials, the intensity of the significant peaks increased with the percentage of Bi^{3+} ions, whereas the intensity decreased with increasing Fe^{3+} ions percentage. This is due to the size difference between the metal ions. In this case also all the synthesized co-doped samples have crystallite size in the nanometer range.

Fe^{3+} and Bi^{3+} ions in the co-doped HA structure also change lattice parameters and unit cell volume (Table 2). Substituting larger Ca^{2+} ions with smaller size Fe^{3+} ions, the a-axis and c-axis lattice parameters decreased as expected, the values further decreased as the amount of Fe^{3+} ions increased in the co-doped HA nanomaterials. However, the parameters increase as the amount of Bi^{3+} ions dopant increases (Table 2). Substituting Ca^{2+} ions with larger cations increases the crystallinity and crystallite size, whereas substituting by smaller cations decreases crystallite size and crystallinity. Similar results have been reported for Fe^{3+} ions doped (Ahmed *et al.*, 2017; Trinkunaite-Felsen *et al.*, 2015), Bi^{3+} ions doped (Ciobanu G. *et al.*, 2015), and Na^{+}, Mg^{2+}, Al^{3+}, Ce^{3+}, and Ti^{4+} ions doped HA materials (Nagyne-Kovacs *et al.*, 2018; Ramakrishnan *et al.*, 2016).

In general, the XRD results analysis for pristine, single and co-doped HA synthesized products confirmed the formations of pure (except for 5% Bi-HA, and 7%Bi-HA nanomaterials), and nano-size HA materials based on the protocols used in this work.

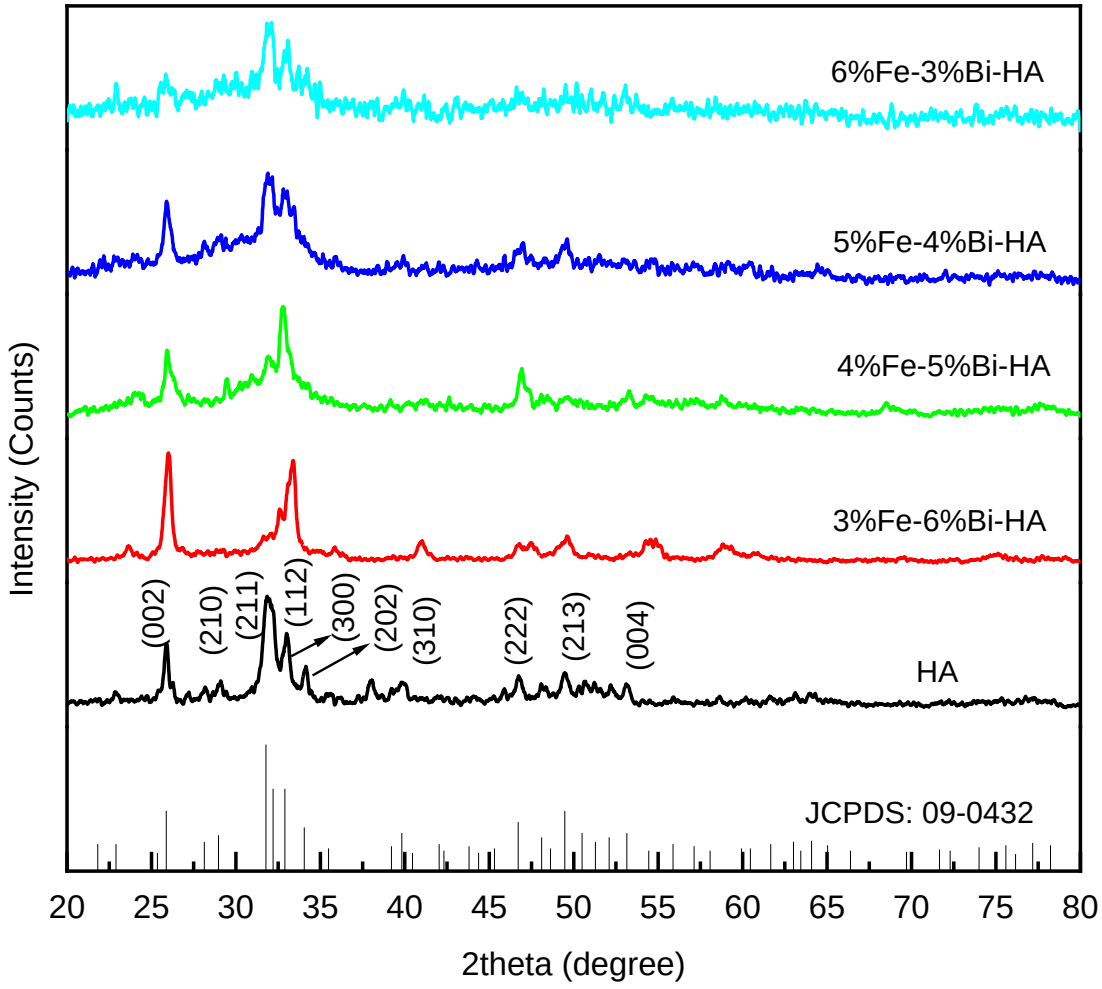

Figure 13. XRD patterns of pristine and Bi^{3+} and Fe^{3+} ions co-doped HA nanomaterials

4.1.2 FTIR Analysis

The FTIR spectra of pristine, Fe^{3+} ions, and Bi^{3+} ions doped (single and co-doped) HA nanomaterials are given in Figure 14. The spectra confirm the presence of characteristic HA bands like OH^{-}, PO_4^{3-} and adsorbed H_2O in all the nanomaterials synthesized samples. The FTIR spectrum of pristine HA shows a peak at 3693 cm^{-1} due to the asymmetric stretching of structural O-H; the peaks at 3427 cm^{-1} and 1631 cm^{-1} correspond to stretching and bending vibrations of adsorbed H_2O correspondingly (Krukowski *et al.*, 2018; Zeng *et al.*, 2019). Similarly, PO_4^{3-} shows asymmetric stretching at 1031 cm^{-1} and bending vibration at 602 cm^{-1} and 563 cm^{-1} (He *et al.*, 2017; Krukowski *et al.*, 2018). The 1411 cm^{-1} and 869 cm^{-1} peaks show B-type CO_3^{2-} substituted HA (Krukowski *et al.*, 2018; Zeng *et al.*, 2019), the CO_3^{2-} which comes from the absorption of atmospheric CO_2.

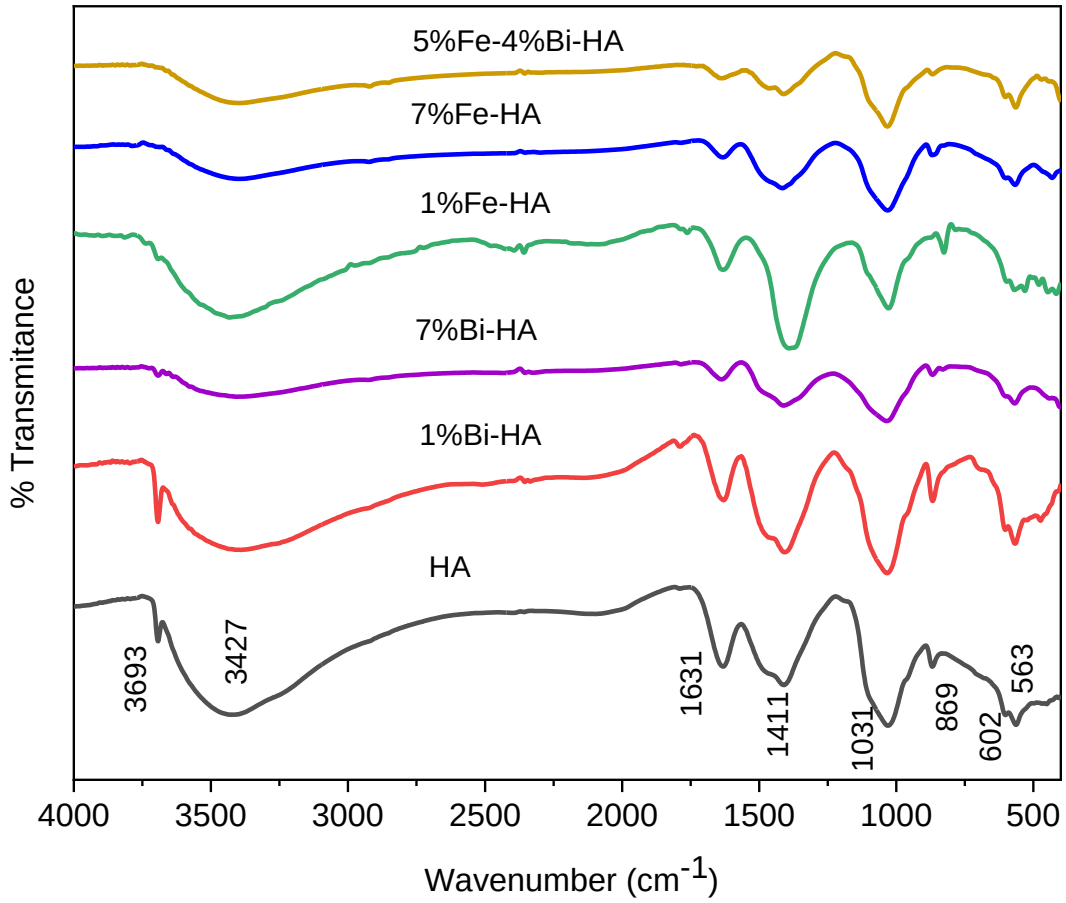

Figure 14. FTIR spectra of pristine and doped HA nanomaterials

In the case of Fe^{3+} ions doped HA, all the characteristic peaks that appeared in the pristine HA are observed except for some changes in intensity, position, and presence of some additional peaks. For example, the intensity of OH^- stretching at 3693 cm^{-1} was found to decrease; this may be due to the conversion of some of the OH^- ions into O^{2-} ion to balance the charge (Priyadarshini *et al.*, 2017; Ramakrishnan *et al.*, 2016). The absorption bands of adsorbed H_2O were observed at 3433 cm^{-1} and 1632 cm^{-1}, and that of phosphate appeared at 1028 cm^{-1}, 569 cm^{-1}, 531 cm^{-1}, and 480 cm^{-1}. Similarly, carbonate shows peaks at 1391 cm^{-1} and 826 cm^{-1}. Additional peaks were observed at 447 cm^{-1} and 416 cm^{-1}, possibly due to the linkage of Fe^{3+} ions with oxygen in the lattice since the Fe–O bond has vibration peaks in this range (Jayarathna *et al.*, 2015; Mercado *et al.*, 2014; Sujana Anand, 2010). The carbonate peak at 1391 cm^{-1} becomes broader and more intense; this may indicate the presence of more carbonate ions in Fe^{3+} ions doped HA nanomaterial. These changes in peak positions, shape, and additional absorption bands on the HA structure indicate structural distortions (Manatunga *et al.*, 2018).

The FTIR spectra of Bi^{3+} ions doped HA also showed the presence of OH^{-}, adsorbed H_2O, and phosphate functional groups with slight changes in intensity and positions. Like that of pristine and Fe^{3+} ions doped HA, Bi^{3+} ions doped HA nanomaterials have a peak at 3693 cm^{-1} due to the stretching of structural O-H, a broad peak at 3389 cm^{-1}, and a sharp peak at 1630 cm^{-1}, the stretching and bending vibrations of H_2O, respectively. Similarly, the phosphate group shows asymmetric stretching at 1034 cm^{-1} and bending vibration at 603 cm^{-1}, 567 cm^{-1}, and 474 cm^{-1}. The peaks at 1408 cm^{-1} and 868 cm^{-1} indicate B-type carbonate substituted HA nanomaterial. The stretching vibration of adsorbed H_2O (peak at 3389 cm^{-1}) shifted to the lower wavenumber during the substitution of Bi^{3+} ions into Ca^{2+} ions. The shift in the O-H stretching is an observation due to structural change when the trivalent metal ions incorporated in the Ca-II position of HA structure (Demirel *et al.*, 2021). In this case, especially for 1%, Bi-HA, there is no clear evidence that shows the presence of Bi–O linkage, this may be due to the variation of the interatomic distance between Bi^{3+} ions and O (Robles-Águila *et al.*, 2017), or it may be the overlap of the Bi-O bands to the phosphate bands since Bi-O bands are usually observed in the range of 400 – 700 cm^{-1} (He *et al.*, 2014; Labib, 2017). However, for 7% Bi-HA nanomaterial a less intense peak at 443 cm^{-1} was observed, which may be due to the Bi-O bond linkage.

The FTIR spectrum of Bi^{3+} and Fe^{3+} ions co-doped HA also indicates the presence of phosphate, adsorbed H_2O, and carbonate functional groups. A broad peak at around 3396 cm^{-1} is due to the vibrations of adsorbed H_2O; the sharp peak at 1636 cm^{-1} also confirmed the presence of adsorbed H_2O. The phosphate group shows asymmetric stretching at 1033 cm^{-1} and bending vibration at 602 cm^{-1} and 564 cm^{-1}. The 1412 cm^{-1} and 869 cm^{-1} peaks indicate B-type carbonate substituted HA nanomaterial. Due to the modification of HA by Bi^{3+} and Fe^{3+} ions, the FTIR spectrum of the co-doped HA resulted with the disappearance of the O-H stretching which was observed at 3693 cm^{-1} in the pristine and single-doped HA nanomaterials. The absence of the O-H stretching at 3693 cm^{-1} in the co-doped samples may indicate the charge discrepancy because of the substitution of Ca^{2+} ions by Bi^{3+} and Fe^{3+} ions (Priyadarshini *et al.*, 2017; Ramakrishnan *et al.*, 2016). In addition, the stretching vibration of O-H was shifted from 3427 cm^{-1} to 3396 cm^{-1} during substitution.

In general, the vibrational peak of structural O-H decreased as the percentage of the dopant (both Bi^{3+} and Fe^{3+} ions) increased in the single-doped HA nanomaterials; a similar result was reported in the literature (Trinkunaite-Felsen *et al.*, 2015). For Fe^{3+} ions doped HA nanomaterials, the peak intensity increased relatively for adsorbed water compared to the Bi^{3+}

ions doped and co-doped HA nanomaterials. This may be due to the higher hygroscopic nature of Fe^{3+} compounds than Bi^{3+} compounds (Ferri *et al.*, 2008).

4.1.3 UV-Vis/DRS Analysis

Apart from the impact on crystallinity, crystallite size, and lattice characteristics, the presence of a dopant in the host lattice also alters the material's bandgap energy and light absorption properties (Mohseni-Salehi *et al.*, 2018). During the UV-Vis/DRS analysis first the reflectance data was converted into apparent absorbance using the relationship of apparent absorbance (A) with reflectance (R) as A = log(1/R). The apparent absorbance spectra of pristine, Fe^{3+} ions doped, Bi^{3+} ions doped, and Bi^{3+} and Fe^{3+} ions co-doped HA nanomaterials are given in Figure 15, 16, 17, and 18, respectively. The spectrum of pristine HA (Figure 15a) shows an intense peak at 270 nm, which agree with previously reported works that claim pristine HA material absorbs mainly in the wavelength range of 200 – 270 nm (Lei *et al.*, 2020; Zou *et al.*, 2020a; Zou *et al.*, 2020b). However, the doped HA nanomaterials have absorption in the visible or near visible regions, which indicates the presence of red shift during the substitution of Ca^{2+} ions by Bi^{3+} and/ or Fe^{3+} ions. This is the indirect evidence of the incorporations of the dopant ions in the HA structure. The red shift in absorption indicates the decreasing bandgap energy of the nanomaterials due to the formation of new energy levels by the metal ions in between the VB and CB (Koohestani Sadrnezhaad, 2016).

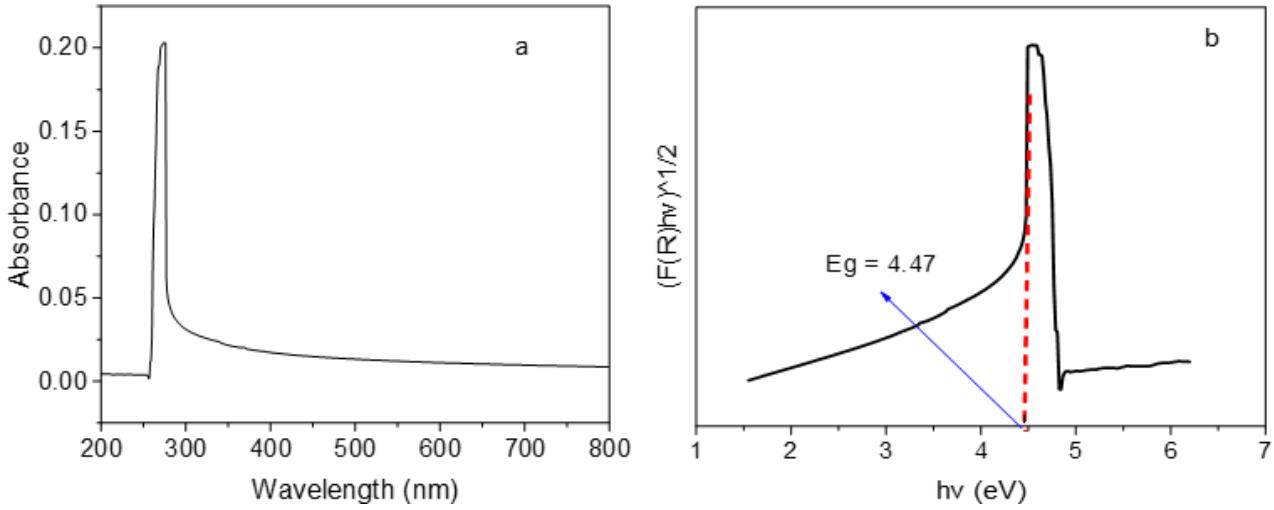

Figure 15. a) Apparent absorbance spectrum, and b) Tauc plot of pristine HA nanomaterial

The spectra of Fe^{3+} ions doped HA nanomaterials (Figure 16), indicate that the absorption wavelength extends to nearly 600 nm, which is in consistent with previous reports on Fe^{3+} ions doped HA (Chuaicham *et al.*, 2023; Shu *et al.*, 2023). This increment in edge wavelength (red-shift) as the amount of Fe^{3+} increased may be associated with; the excitation of 3d electrons of Fe^{3+} to the CB of the nanomaterial (Khan Swati, 2016; Mohseni-Salehi *et al.*, 2018), the d-d transition of Fe^{3+}, which is given by $^2T_{2g} \rightarrow {}^2A_{2g}, {}^2T_{1g}$ (Khan Swati, 2016), or the charge transfer of $O^{2-} \rightarrow Fe^{3+}$ (Bazin *et al.*, 2022). Similarly, the light absorption intensity of Fe^{3+} ions doped HA nanomaterials increased with the increase of Fe^{3+} ions doped in the HA structure. This phenomenon was also observed for Ba^{2+}, Zn^{2+}, La^{3+}, and Fe^{3+} ions doped HA materials reported in the literature (Helen Kumar, 2019). The higher the concentration of Fe^{3+} integrated, the more photons absorbed over a wider wavelength range. As a result, the material's utility range of light increase, potentially significantly increasing its photocatalytic activity when exposed to visible light (Khan Swati, 2016).

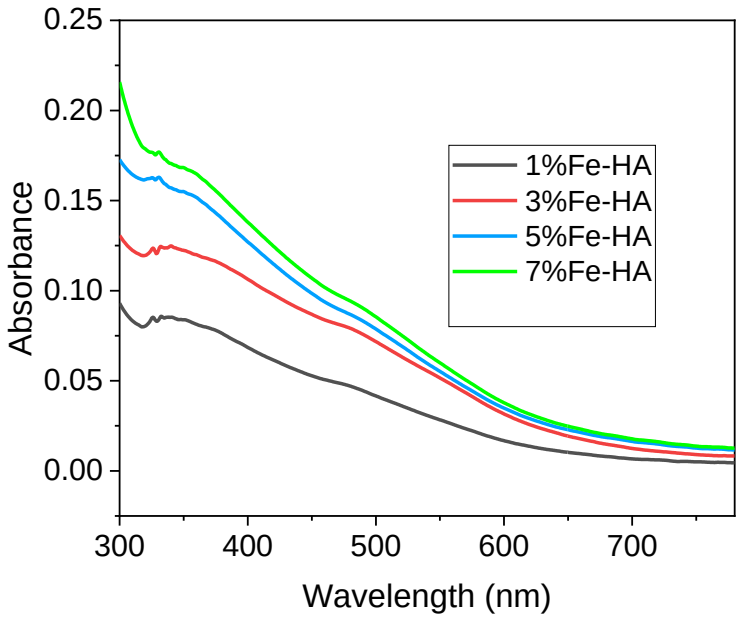

Figure 16. Apparent absorbance spectra of Fe^{3+} ions doped HA nanomaterials

For Bi^{3+} ions doped HA nanomaterials (Figure 17), they have strong absorption in the wavelength range of 300 – 420 nm. This change in light absorption property compared to the pristine HA is an evidence for the incorporation of Bi^{3+} ions in the HA structure. The increase in edge wavelength of Bi^{3+} ions doped HA nanomaterials compared to the pristine HA nanomaterial may correspond to the excitation of electron from the ground state of 6s energy level to 6s6p excited state ($^1S_0 \rightarrow {}^3P_1$) of Bi^{3+} ions (Chawla *et al.*, 2010; Dorenbos, 2021; Kowalczyk *et al.*, 2020). Compared to the d-d transition of electrons in the Fe^{3+} ions doped HA

nanomaterials, the s-p excitation of electrons in the Bi^{3+} ions doped HA nanomaterials needs high energy, which indicated that Bi^{3+} ions doped HA nanomaterials have light absorption in the lower wavelength than Fe^{3+} ions doped HA nanomaterials. However, like that of Fe^{3+} ions doped HA nanomaterials, Bi^{3+} ions doped HA nanomaterials also indicate that light absorption intensity increased with the increasing of Bi^{3+} ions amount incorporated into the HA structure. This confirms the possible usage of Bi^{3+} ions doped HA also as potential photocatalytic material in the UV-Vis range.

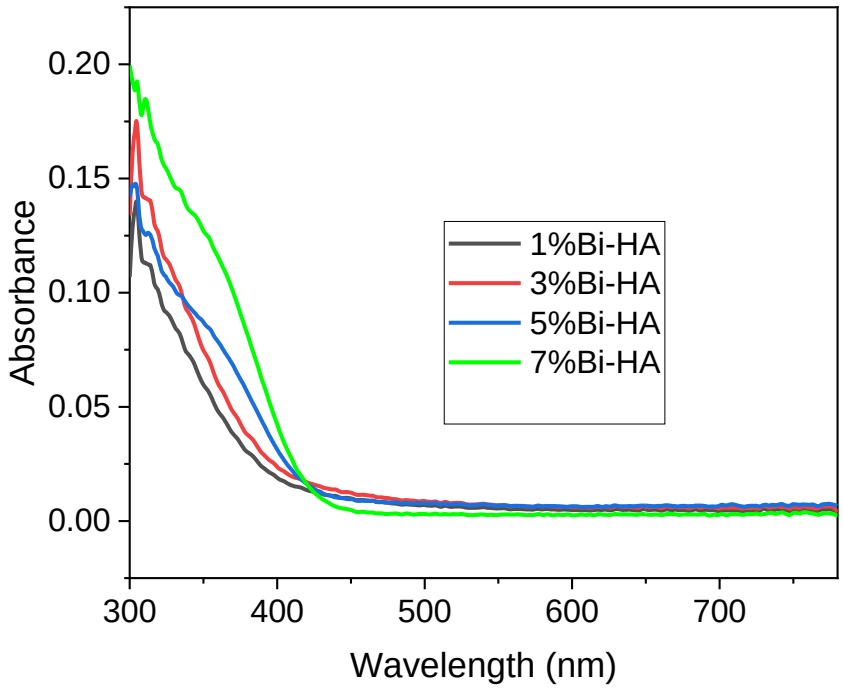

Figure 17. Apparent absorbance spectra of pristine and Bi^{3+} ions doped HA nanomaterials

In the case of Bi^{3+} and Fe^{3+} ions co-doped HA nanomaterials (Figure 18), the light absorption intensity increased with the increase of Fe^{3+} ions in the dopant percentage. Similarly, the edge wavelength increased with the increase of the amount of Fe^{3+} ions in the co-doped samples. This also correspond to the excitation of 3d electrons of Fe^{3+} to the CB of the HA crystal (Khan Swati, 2016; Mohseni-Salehi *et al.*, 2018), the d-d transition of Fe^{3+}, represented as $^2T_{2g} \rightarrow {}^2A_{2g}$, $^2T_{1g}$ (Khan Swati, 2016), or the charge transfer of $O^{2-} \rightarrow Fe^{3+}$ (Bazin *et al.*, 2022), in addition to the $^1S_0 \rightarrow {}^3P_1$ excitations of electrons of Bi^{3+} ions . More photons over a larger wavelength range are absorbed in the co-doped HA nanomaterials with greater Fe^{3+} concentrations. This implies that when the co-doped HA nanomaterials are exposed to visible light, the material's utility range of light increases, perhaps leading to a large rise in their photocatalytic activity (Khan Swati, 2016)

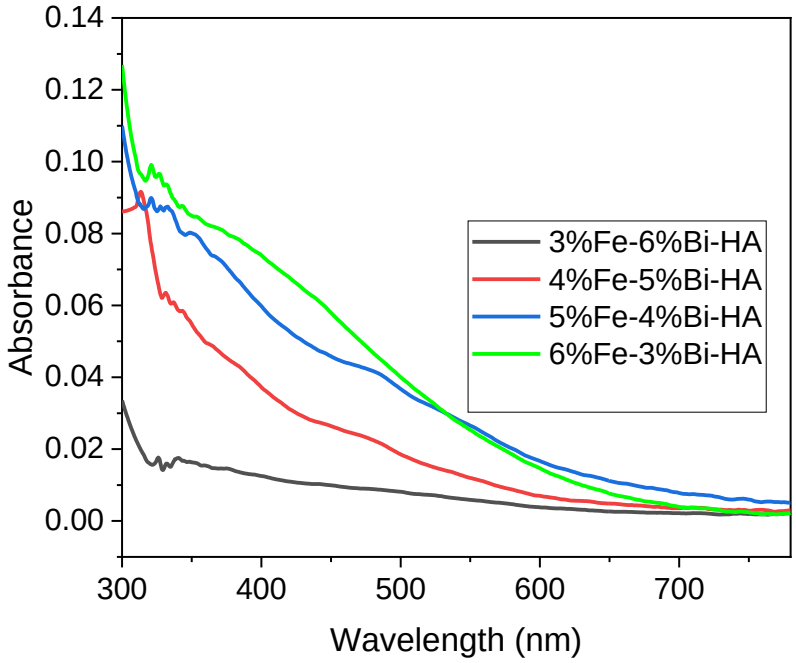

Figure 18. Apparent absorbance spectra of Bi^{3+} and Fe^{3+} ions co-doped HA nanomaterials

The optical bandgap of pristine and doped HA synthesized nanomaterials was determined from UV-Vis/DRS apparent absorbance spectra by converting the reflectance data to absorption coefficient using the Kubelka-Munk model according to Equation 27. Then the energy bandgap was estimated from the Tauc plot (Equation 28) by extrapolating in the linear portion of the curve, and considering that HA is an indirect bandgap material (Jiménez-Flores *et al.*, 2017; Rojas-Trigos *et al.*, 2019), since there is no straight line in the curve when the value of the electronic transition other than 1/2.

$$F(R) = \frac{K}{S} = \frac{(1-R)^2}{2R} \quad (27)$$

Where K is the absorption coefficient, S is the scattering coefficient, respectively, and R is the reflectance.

$$(F(R)h\nu)^{1/2} = A(h\nu - E_g) \quad (28)$$

Where E_g is energy bandgap (eV), ν is the frequency of light (s^{-1}), h is Planck's constant (J s), and A is the absorption constant. The Tauc plots for the synthesized Fe^{3+} ions doped, Bi^{3+} ions doped, and Be^{3+} and Fe^{3+} ions co-doped HA nanomaterials are given in Figures 19, 20, and 21, respectively.

As already discussed above and shown in the absorption spectrum (Figure 15a), the absorption edge for pristine HA is at around 270 nm wavelength, and the inflection point in the

$(F(R)h\nu)^{1/2}$ vs $h\nu$ curve shows the energy bandgap value of 4.47 eV (Figure 15b), which is lower than the values reported previously (Adamiano *et al.*, 2017; Hadagalli *et al.*, 2021; Jiménez-Flores *et al.*, 2017), but still greater than the values reported by other research groups (Bystrov *et al.*, 2016; Lv *et al.*, 2024; Shu *et al.*, 2023). The decrease in the bandgap energy of HA nanomaterial may be due to the presence of defects/vacancy such as Ca, O or OH in the crystal lattice (Bystrov *et al.*, 2016; Lv *et al.*, 2024; Rojas-Trigos *et al.*, 2019).

Fe^{3+} ions doped HA nanomaterials (Figure 19) showed bandgap energy values in the range of 1.84 – 2.64 eV, lower than the energy bandgap of pristine HA nanomaterial. But the values are in close agreement with a previous reports on Fe^{3+} ions doped HA materials (Hadagalli *et al.*, 2021; Shu *et al.*, 2023). The results indicate that as the amount of Fe^{3+} ions increased, the energy bandgap decreased, which agrees with the reports of Tb^{3+}, Fe^{3+}, and Ti^{4+} ions doped HA materials (Adamiano *et al.*, 2017; Hadagalli *et al.*, 2021; Jiménez-Flores *et al.*, 2017).

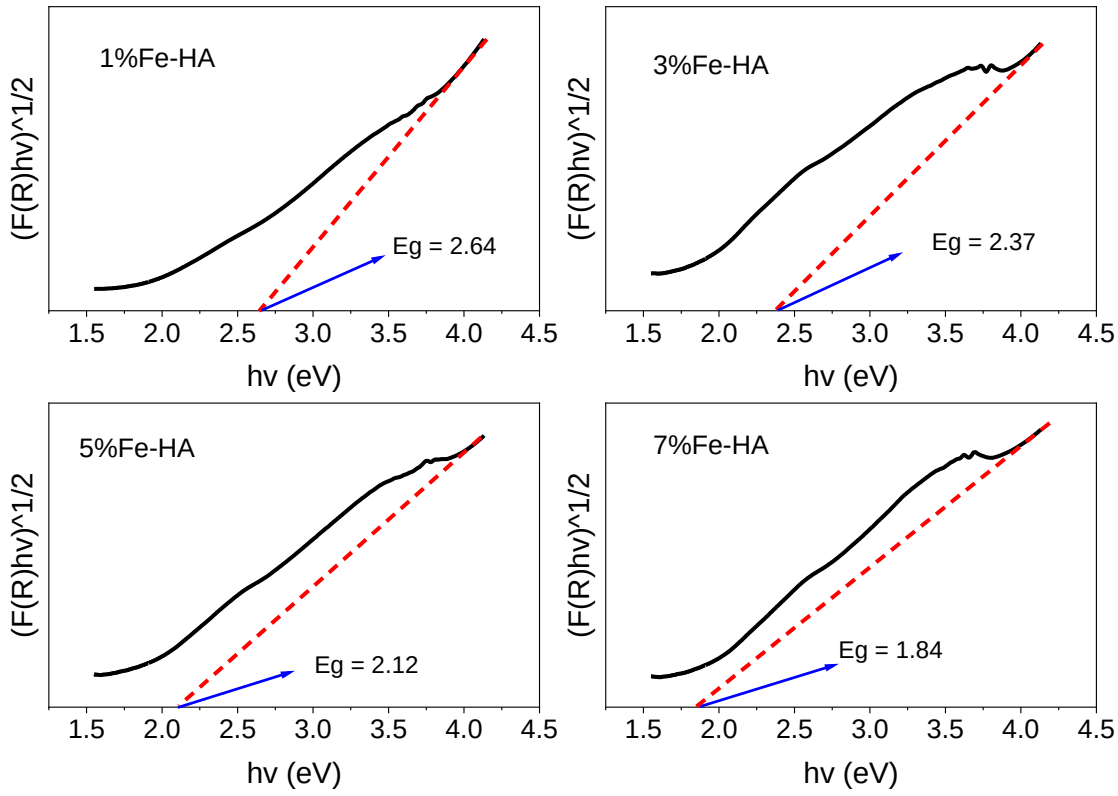

Figure 19. Tauc plots of Fe^{3+} ions doped HA nanomaterials

The decrease in bandgap energy indicates the formation of a new energy level (impurity) between the VB and CB of HA nanomaterials due to the imbalance of the electronic structures

of Ca^{2+} ions with that of Fe^{3+} dopant ions (Hadagalli *et al.*, 2021), which means that Fe^{3+} is an n-type dopant so that it makes the fermi-level appears near to the CB. Or lowering of the CB of HA-band structure by Fe^{3+} ions doping. This may help the easy excitation of the 3d electrons of Fe^{3+} ions to the CB of the HA structure (Mohseni-Salehi *et al.*, 2018). On the other hand, the interaction of the band electrons and the d electrons of the transition metal ions that replace the Ca^{2+} ions through p-d spin exchange accounts for the decrease in the bandgap energy. The HA structure has a high p-d mixing of the O and the transition metal ions (Kurinjinathan *et al.*, 2020; Mariappan *et al.*, 2017). This lower values of energy bandgap indicates that Fe^{3+} ions doped HA nanomaterial can possibly be used for photocalatytic activity in the visible range of electromagnetic radiation.

The calculated energy bandgap of Bi^{3+} ions doped HA nanomaterials (Figure 20), is in the range of 3.10 – 3.64 eV, lower than the bandgap value of pristine HA nanomaterial due to the modification of the CB, because of the n-type dopant of Bi^{3+} ions . In this case also, as the amount of dopant (Bi^{3+} ions) increased, the energy bandgap decreased, this may be associated with the polarizability of the $6s^2$ lone pair electrons of Bi^{3+} ions, and the excellent dispersion of the 6s orbital of Bi^{3+} ions aid in the migration and separation of photo-generated charge carriers, reducing the bandgap (Han, 2021). In addition, the bandgap energy obtained in the case of Bi^{3+} ions doped HA nanomaterials are lower than the pristine HA nanomaterial, this indicates that the photocatalytic activity usage of Bi^{3+} ions doped HA possibly better than the pristine HA nanomaterial.

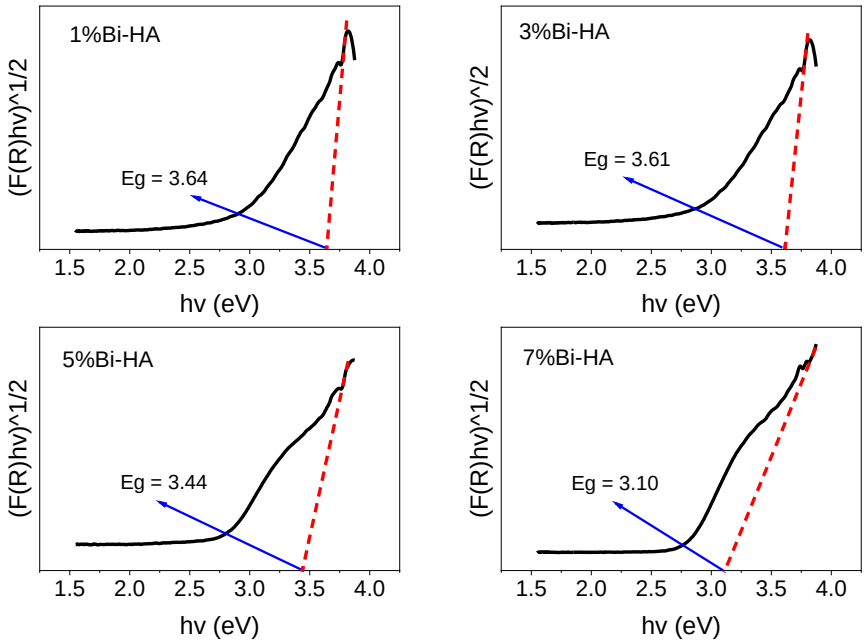

Figure 20. Tauc plots of Bi^{3+} ions doped HA nanomaterials

In the case of Bi^{3+} and Fe^{3+} ions co-doped HA nanomaterials (Figure 21), the energy bandgap values decreased with the increase of Fe^{3+} ions percentage in the dopant amount. The obtained energy bandgap of the co-doped HA nanomaterials account from 2.54 – 3.33 eV. The decreasing bandgap relative to the percentage of Fe^{3+} ions dopant may be associated with the excitation of the 3d electrons of Fe^{3+} ions to the CB of the HA structure (Mohseni-Salehi *et al.*, 2018). On the other hand, the interaction of the band electrons and the d electrons of the transition metal ions that replace the Ca^{2+} ions through p-d spin exchange accounts for the decrease in the band gap energy. The HA structure has a high p-d mixing of the O and the transition metal ions (Kurinjinathan *et al.*, 2020; Mariappan *et al.*, 2017). In general, doping of Bi^{3+} and Fe^{3+} ions (single and co-doping) in the HA nanostructure significantly reduced the bandgap energy. This shows that the modified nanomaterial possibly used for the degradation of pollutants using the ultraviolet-visible light range.

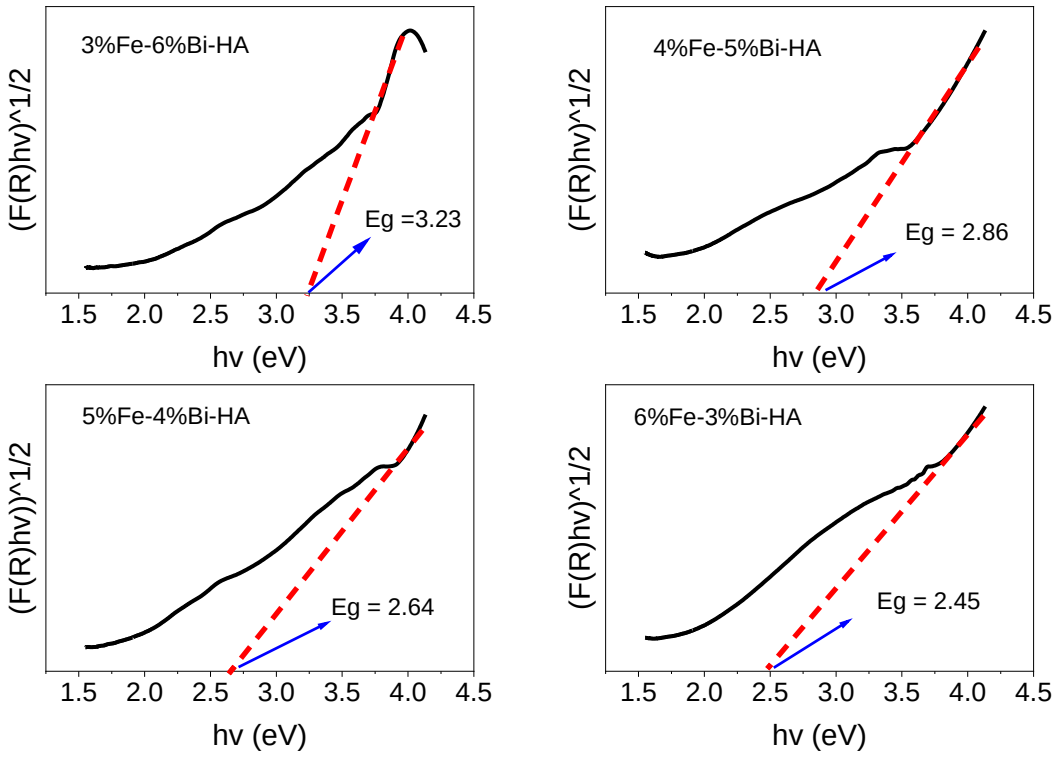

Figure 21. Tauc plots of Bi^{3+} and Fe^{3+} ions co-doped HA nanomaterials

4.2 Morphology Analysis

4.2.1 SEM Analysis

The SEM analyses of pristine, Fe^{3+} ions doped, Bi^{3+} ions doped, and Bi^{3+} and Fe^{3+} ions co-doped HA nanomaterials are given in Figure 22a, b, c, and d, respectively. The calculated particle sizes of the nanomaterials are summarized in Table 3. The results indicated that Fe^{3+} and Bi^{3+} ions doping (single and co-doping) into the HA structure changes the shape, degree of aggregation/agglomeration, and particle size of the HA nanomaterial. Previous reports also indicated that metal ions doping on the HA structure brings change in the shape and size of the apatite materials (Bhattacharjee *et al.*, 2020; Ignjatović *et al.*, 2019; Padmanabhan *et al.*, 2019; Wei *et al.*, 2019). These alterations in morphology are the result of the imbalance of the charge between the lattice cations and the dopants, which causes a redistribution of surface charges within the nuclei of developing crystals. Doping with trivalent metal ions may cause a brief electric dipole that could slow or speed up growth in specific crystallographic orientations by influencing the diffusion of anions from the solution to the developing surface. Notably, particle development happens by a phenomenon known as coalescence, which is the directed attachment of particles along their longer axis and the ensuing merger of the particles (Ignjatović *et al.*, 2019; Wei *et al.*, 2019). The dominant shape of the pristine HA nanomaterial (Figure 22a) is rod-like, which agrees with different reports on HA based materials synthesized by the chemical precipitation technique (Goldberg *et al.*, 2020; Wei *et al.*, 2019; Yuan *et al.*, 2018). The SEM image shows the presence of some aggregates and agglomerates having a particle size in the range of 16.20 – 48.24 nm, with a mean value of 28.20 nm.

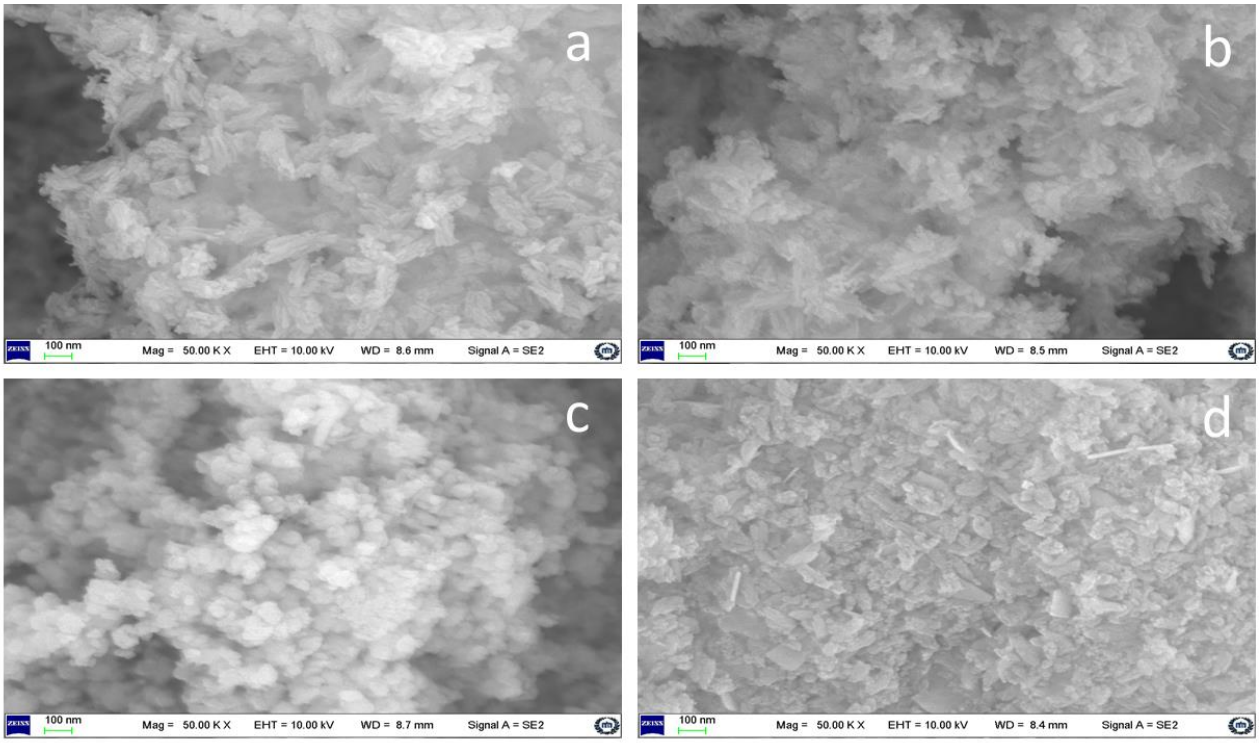

Figure 22. SEM images of a) HA, b) 1% Fe-HA, c) 1% Bi-HA, and d) 5% Fe - 4% Bi-HA nanomaterials

The SEM image of Fe^{3+} ions doped HA (Figure 22b) revealed the presence of an aggregate/agglomerate of a needle-like structure, which agree with previous report on Li^{+} ion doped HA nanoparticle (Padmanabhan *et al.*, 2019), this change in shape of the nanomaterial may be due to the lower ionic radius of Fe^{3+} ions. The high aggregation/agglomeration of Fe^{3+} ions doped hydroxyapatite may come from the extra positive charge compared to pristine or it may be due to the magnetic nature of Fe^{3+} ions, since magnetic material tend to aggregate/agglomerate (Serantes Baldomir, 2021). The size of needle-like particles decreased as Fe^{3+} ions introduced in the HA, which is consistent with previous reports on Mg^{2+} and Sr^{2+} ions doped HA materials (Alioui *et al.*, 2019; Wei *et al.*, 2019), and as observed in the XRD analysis. The decrease in particle size of the metal ions doped HA is related to the size of the metal ions that substitute the Ca^{2+} ions (Alioui *et al.*, 2019). The particle size range of Fe^{3+} ions doped HA nanomaterial was 16.39 – 40.21 nm, with a mean value of 25.70 nm.

The SEM image of Bi^{3+} ions doped HA nanomaterial (Figure 22c) shows the presence of elongated spherical particles, this agree with the result reported in the literature for Mg^{2+}, Zn^{2+}, and Ga^{3+} ions doped HA nanomaterials (Mahanty Shikha, 2023; Shokri *et al.*, 2022). The

particle size distribution of Bi^{3+} ions doped HA nanomaterial is in the range of 16.99 – 49.57 nm, and an average value of 30.29 nm. This value is greater than the pristine as well as Fe^{3+} ions doped HA nanomaterials, as observed also in the XRD analysis. Bi^{3+} ions doped HA nanomaterial also shows an agglomeration, which may be due to the presence of extra positive surface charge from Bi^{3+} ions in the structure.

Table 3. Particle size of pristine and doped HA nanomaterials

Sample	SEM size (nm)	FE-SEM size (nm)	TEM size (nm)
HA (pristine)	28.20	22.67	–
1% Bi-HA	30.29	20.87	–
7% Bi-HA	–	22.12	–
1% Fe-HA	25.70	16.58	–
7% Fe-HA	–	16.91	–
5% Fe-4% Bi-HA	27.94	17.47	17.70

Relatively, the morphology of Bi^{3+} and Fe^{3+} ions co-doped HA nanomaterial (Figure 22d) differs from pristine and single-doped HA nanomaterials. The SEM image comprises a rough surface of platelets, granular-structures, rice-like structures, and rod-like structures of less aggregated/agglomerated particle. This morphology agrees with previous reports on metal ions doped HA materials (Huang *et al.*, 2018; Mahanty Shikha, 2023; Yahia *et al.*, 2017). In this case, the particles are relatively uniformly distributed compared to pristine and single doped HA nanomaterials. The particle size distribution of Bi^{3+} and Fe^{3+} ions co-doped HA nanomaterial is in the range of 18.32 – 40.99 nm, with a mean value of 27.94 nm.

4.2.2 FE-SEM Analysis

The morphology of pristine, single and co-doped HA nanomaterials was further characterized by the FE-SEM analysis. The FE-SEM images (Figure 23) show the presence of granular/rod-like structures in all the characterized samples. The results agree with previous report on pristine, Mg^{2+}, Ag^{+} , and Hg^{2+} ions doped HA materials using FE-SEM analysis (Mahanty

Shikha, 2023; Pradhan *et al.*, 2020). The images also show the presence of more aggregation/agglomeration compared to the SEM images of the same materials. This may be due to the difference in the working conditions and sample preparation of the two characterization techniques. The FE-SEM image of pristine HA nanomaterial (Figure 23a) shows an aggregate/agglomerate of granular/rod-like structure with variable particle size distribution in the 13.42 – 47.08 nm range and an average value of 22.67 nm. The FE-SEM images of Fe^{3+} ions doped HA nanomaterials (Figure 23b and c) also showed rod/needle-like morphologies. The particle size distribution of 1% Fe-HA was 9.48 – 25.23 nm, with an average value of 16.58 nm. For that of 7% Fe-HA, the particle size distribution was in the range of 10.25 – 26.28 nm, with a mean value of 16.91 nm. The particle size distribution of Fe^{3+} ions doped HA nanomaterials are lower than the pristine HA, which agree with the XRD analysis. The lower particle sizes of Fe^{3+} ions doped HA nanomaterials compared to the pristine HA correspond to the smaller ionic size of Fe^{3+} ions than the Ca^{2+} ions.

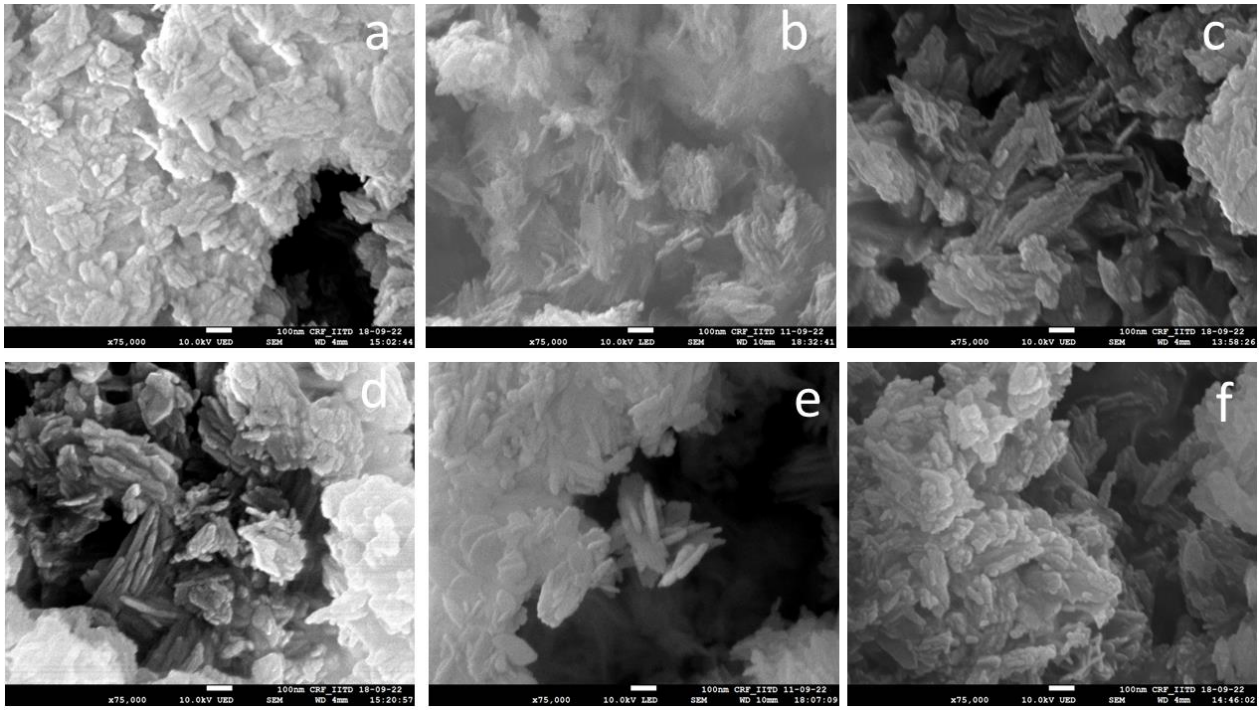

Figure 23. FE-SEM images of a) HA, b) 1% Fe-HA, c) 7% Fe-HA, d) 1% Bi-HA, e) 7% Bi-HA, and f) 5% Fe- 4% Bi-HA nanomaterials

The FE-SEM images of Bi^{3+} ions doped HA nanomaterials (Figure 23d and e) showed that Bi^{3+} ions doped HA nanomaterials have agglomerates of granular/rod-like morphologies, rough surfaces, and variable sizes. The FE-SEM images also indicate that the particle sizes of the

nanomaterials increased with the amount of Bi^{3+} ions added to the apatite structure, which agrees with the XRD analysis. The particle size of 1% Bi-HA was 10.87 – 33.71 nm, with an average value of 20.87 nm. However, that of 7% Bi-HA was in the range of 15.00 – 37.50 nm, with a mean value of 22.12 nm. Like that of the SEM image, the FE-SEM image of Bi^{3+} and Fe^{3+} ions co-doped HA nanomaterial (Figure 23f) shows granular/platelets, and rod like structures with different size distribution in the range of 10.57 – 34.40 nm, having an average value of 17.47 nm.

4.2.3 TEM Analysis

To reveal further the structure of Bi^{3+} and Fe^{3+} ions co-doped HA nanomaterial, TEM analysis was performed using 5% Fe – 4% Bi-HA synthesized nanomaterial, and the TEM image is given in Figure 24a. The image shows a rough surface with porous structure having long rod-like shape, which may be due to self-assembly of the nanoparticles. The particle size distribution of the co-doped sample using TEM analysis was in the range of 10.63 – 25.68 nm, and an average value of 17.70 nm. To determine the particle orientation, HR-TEM image was also obtained, and the result is given in Figure 24b.

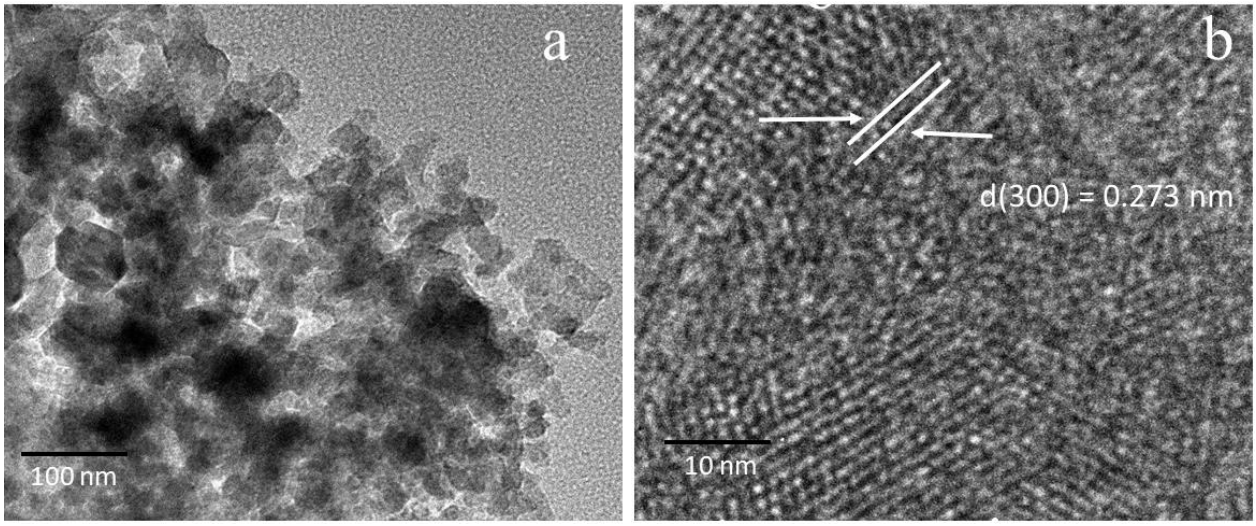

Figure 24. TEM image a) and HR-TEM image b) for 5% Fe - 4% Bi-HA nanomaterial

The inter-planar spacing of the co-doped HA nanomaterial shows well-resolved patterns of the nanomaterial with a d-spacing value of approximately 0.273 nm, which confirms the (300) plane of the hexagonal HA structure, and it agree with the XRD analysis. In general, the morphology analysis using SEM, FE-SEM, and TEM indicate the formation of nano-sized HA

materials, implies that the objective of synthesizing HA nanomaterials was accomplished. Moreover, the presence of rod-like structure and spherical shape in the HA nanomaterials encourages the usage of these materials for environmental remediation as well as biomedical applications (Lei *et al.*, 2019; Lv *et al.*, 2020; Nagaraj *et al.*, 2018).

4.3 BET Analysis

The nitrogen adsorption-desorption isotherm for pristine, Fe^{3+} ions, and Bi^{3+} ions doped (single and co-doped) HA nanomaterials are given in Figure 25. The results (the shape of nitrogen adsorption-desorption isotherm) indicate that the nanomaterials are classified under type IV isotherm, based on the International Union of Pure and Applied Chemistry classification, having the distinct hysteresis loops of type H3, which indicates the presence of non-rigid aggregates of plate-like particles or slit-shaped pores (Gao *et al.*, 2019; Karunakaran *et al.*, 2019; Manoj *et al.*, 2019). The hysteresis loop with P/Po > 0.4 also indicates the presence of mesoporous materials (Chen *et al.*, 2016).

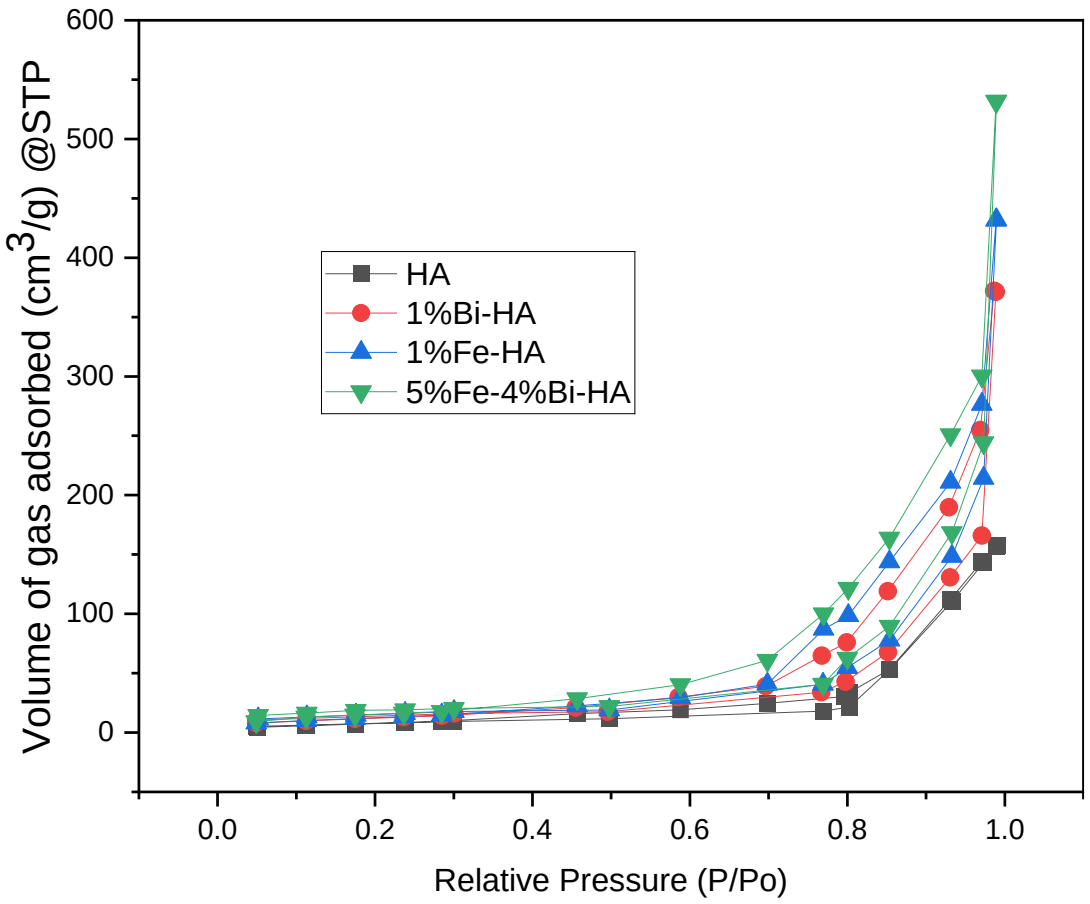

Figure 25. Nitrogen adsorption-desorption isotherm of pristine and doped HA nanomaterials

The BET analysis (Table 4) further indicates that modification using Bi^{3+} ions, and Fe^{3+} ions doping enhanced the specific surface area, pore size, and pore volume of HA. This implies that the modified HA nanomaterials adsorbed more nitrogen gas. The specific surface area, pore volume, and average pore radius of pristine HA were 49.77 m^2/g, 0.896 cm^3/g, and 1.207 nm, and that of Fe^{3+} ions doped, and Bi^{3+} ions doped HA nanomaterials were 117.62 m^2/g, 2.458 cm^3/g, 1.795 nm, and 55.01 m^2/g, 0.923 cm^3/g, 1.165 nm, respectively. The Bi^{3+} and Fe^{3+} ions co-doped HA nanomaterial's specific surface area, pore volume, and average pore radius were 130.24 m^2/g, 2.112 cm^3/g, and 1.705 nm, respectively. It indicated that, surface area of Bi^{3+} and Fe^{3+} ions co-doped HA nanomaterial is more significant than some of the modified HA materials reported so far (Gao *et al.*, 2019; Guo *et al.*, 2019; Karunakaran *et al.*, 2019; Manoj *et al.*, 2019). The enhanced surface area makes the materials to be chosen for adsorption, catalysis, and other similar applications.

Table 4. BET results of pristine and doped HA nanomaterials

Sample	Total pore volume (cm^3/g)	Specific surface area (m^2/g)	Average pore radius (nm)
HA	0.896	49.77	1.705
1% Bi-HA	0.923	55.01	1.165
1% Fe-HA	2.458	117.62	1.795
5% Fe-4% Bi-HA	2.112	130.24	1.207

4.4 Elemental Composition Analysis

4.4.1 EDS Analysis

The elemental composition of pristine, Fe^{3+} ions doped, Bi^{3+} ions doped, and Bi^{3+} and Fe^{3+} ions co-doped HA synthesized nanomaterials were analysed by EDS; the results are given in Figures 26, 27, 28, and 29, respectively. The Ca/P, and (Ca + M)/P ratios are summarised using Table 5. The analysis confirmed the presence of calcium (Ca), phosphorous (P), and oxygen (O) in the products. The compositional mass of the elements (O, Ca, and P) is near to the theoretical (expected) values. Moreover, the Ca-to-P ratio of pristine HA (Table 5) obtained from the EDS

spectra was 1.64, which is slightly lower than the expected value (1.67), and this is commonly observed during the synthesis of HA using the chemical precipitation technique.

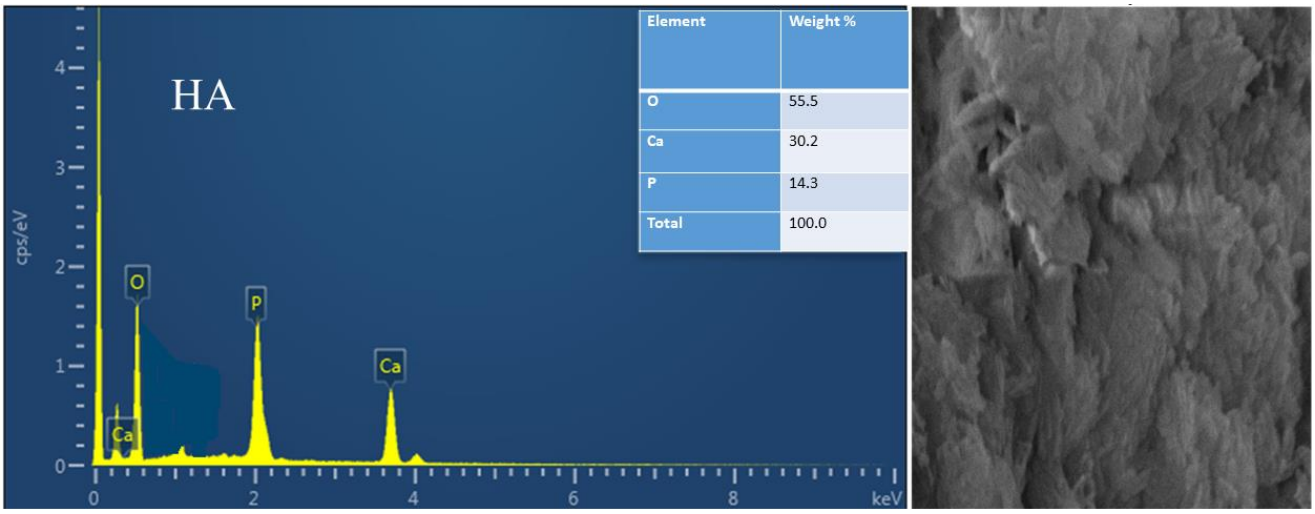

Figure 26. EDS spectrum of pristine HA nanomaterial

For Fe^{3+} ions doped HA nanomaterials, 1% Fe-HA and 7% Fe-HA, (Figure 27), Ca, P, O, and Fe were detected in both samples. The molar ratio of Ca/P for both samples were lower than 1.67, and the ratios decreased with increasing the amount of dopant, which indicates that Fe^{3+} ions were successfully substituted Ca^{2+} ions in the HA structure. The results agree with previous reports (Hadagalli *et al.*, 2021; Nam *et al.*, 2018; Priyadarshini *et al.*, 2017), of Cu^{2+}, Ce^{4+}, and Fe^{3+} ions doped HA materials using various ratios of the metal ions. The decreasing value of the Ca/P ratio as the amount of Fe^{3+} ions doped increased indicates the direct replacement of Ca^{2+} ions by Fe^{3+} ions in the HA structure. The results also indicate that the molar ratios of Ca^{2+} and Fe^{3+} to that of P were greater than that of the Ca/P ratio, as expected, which showed that Fe^{3+} ions replace certain amounts of Ca^{2+} ions.

Table 5. Calcium to phosphorous ratios of the synthesized nanomaterials using EDS analysis

Atomic ratios		HA	1% Bi-HA	7% Bi-HA	1% Fe-HA	7% Fe-HA	5% Fe – 4% Bi-HA
Ca/P	EDS	1.64	1.60	1.53	1.59	1.54	1.47
	Expected	1.67	1.65	1.55	1.65	1.55	1.52
(Ca + M)/P			1.60	1.61	1.65	1.69	1.67
	Expected		1.67	1.67	1.67	1.67	1.67

Note: M = Bi and/Fe

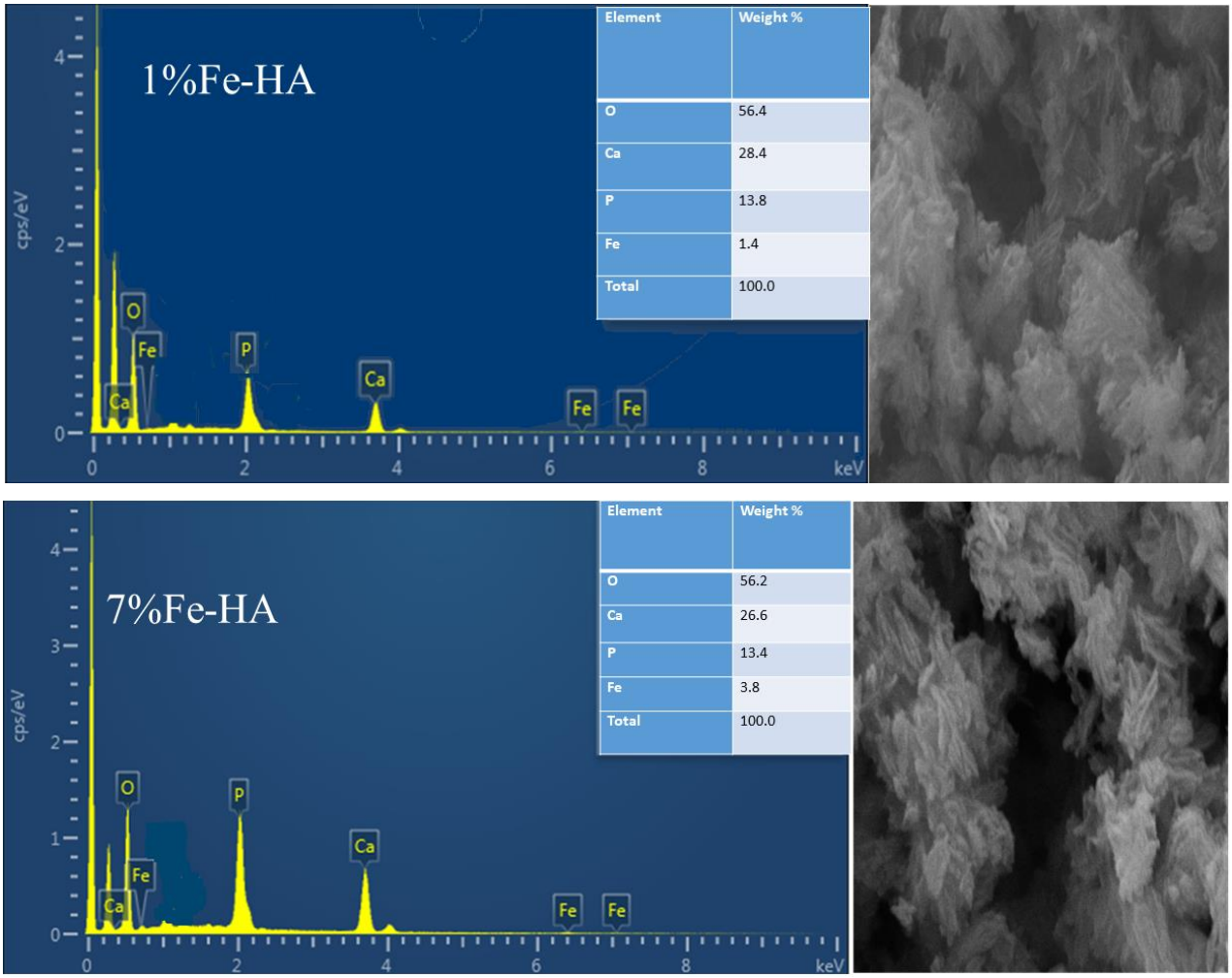

Figure 27. EDS spectra of Fe^{3+} ions doped HA nanomaterials

For Bi^{3+} ions doped HA nanomaterials (1% Bi-HA and 7% Bi-HA), in addition to Ca, P, and O, Bi was also detected by EDS analysis (Figure 28). The Ca/P ratios for 1% Bi-HA and 7% Bi-HA are 1.60 and 1.53, respectively (Table 5), which indicates that the synthesized HA nanomaterials are Ca-deficient. In this case also the ratio of (Ca + Bi)/P is greater than the Ca/P ratio, which indicates Be^{3+} ions replace Ca^{2+} ions during the synthesis.

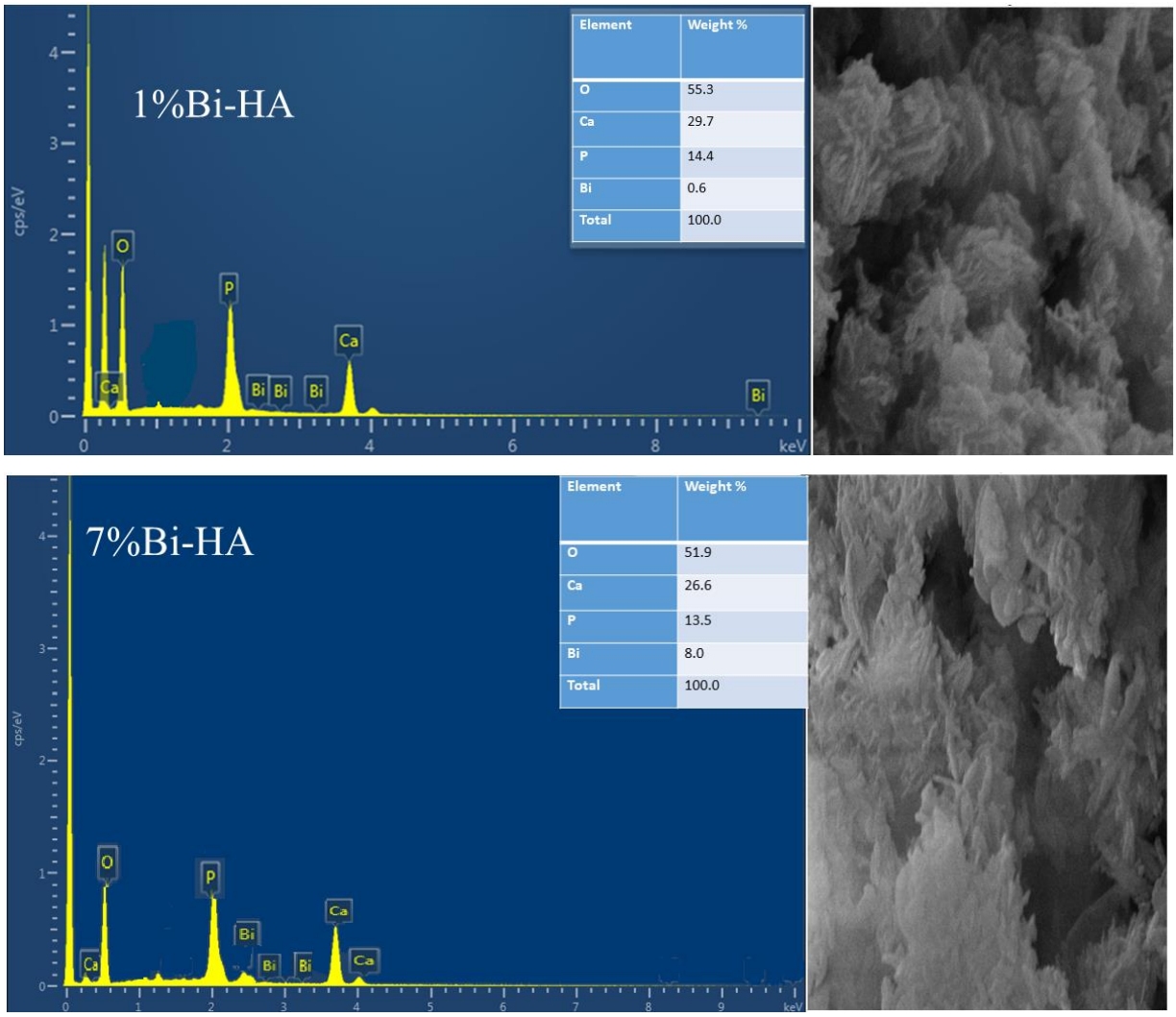

Figure 28. EDS spectra of Bi^{3+} ions doped HA nanomaterials

The EDS analysis for Bi^{3+} and Fe^{3+} ions co-doped HA (Figure 29) showed that Bi and Fe were detected in the co-doped sample in addition to that of O, P, and Ca elements. The ratio of Ca/P was lower than 1.67. However, the ratio of (Ca + Bi + Fe)/P was equal to the theoretical value (1.67), which indicates that Bi^{3+} and Fe^{3+} ions were successfully substituted Ca^{2+} ions in the HA structure of the co-doped sample.

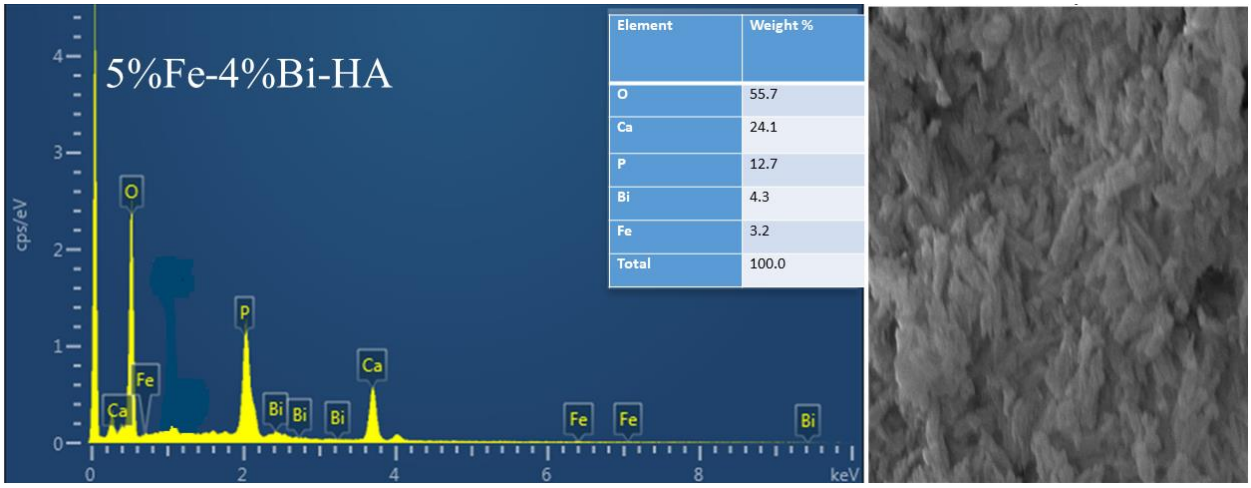

Figure 29. EDS spectra of Bi^{3+} and Fe^{3+} ions co-doped HA nanomaterial

4.4.2 XPS Analysis

The elemental composition and elemental state of Bi^{3+} and Fe^{3+} ions co-doped HA nanomaterial was also examined by XPS analysis, and the results are shown in Figure 30. Ca (2p), P (2p), O (1s), Bi (4f), Fe (2p), and C (1s) are present in the XPS survey spectrum of the Bi^{3+} and Fe^{3+} ions co-doped HA nanomaterial (Figure 30a), together with their corresponding binding energy values of 347.08, 133.08, 531.08, 158.08, 710.08, and 284.08 eV, respectively (Ciobanu Harja, 2019; Hadagalli *et al.*, 2021; Machado *et al.*, 2019). The CO_3^{2-} ions (Machado *et al.*, 2019), or hydrocarbon contamination during synthesis is typically the source of C (Lu *et al.*, 2000). According to XRD, and FTIR analysis, the source of C in this instance is CO_3^{2-} ions from atmospheric carbon dioxide. Furthermore, with a binding energy of 977.08 eV, O (KLL) was identified. The spectrum of Ca (Figure 30b) shows two peaks with binding energies of 347.28 eV (Ca 2p 3/2) and 350.88 eV (Ca 2p ½), with a spin-orbit splitting of 3.5 eV, which are associated with divalent Ca^{2+} ion in the HA structure (Li *et al.*, 2022; Sheikh *et al.*, 2018). The primary spectrum of P (Figure 30c) shows a single peak at a binding energy of 133.28 eV (P 2p), which corresponds to the P–O bond of the phosphate functional group in HA (Chusuei *et al.*, 1999). Deconvolution of this peak revealed two peaks with binding energies of 133.1 and 133.9 eV, associated with 2p ½ and 2p 3/2, respectively (Hadagalli *et al.*, 2021).

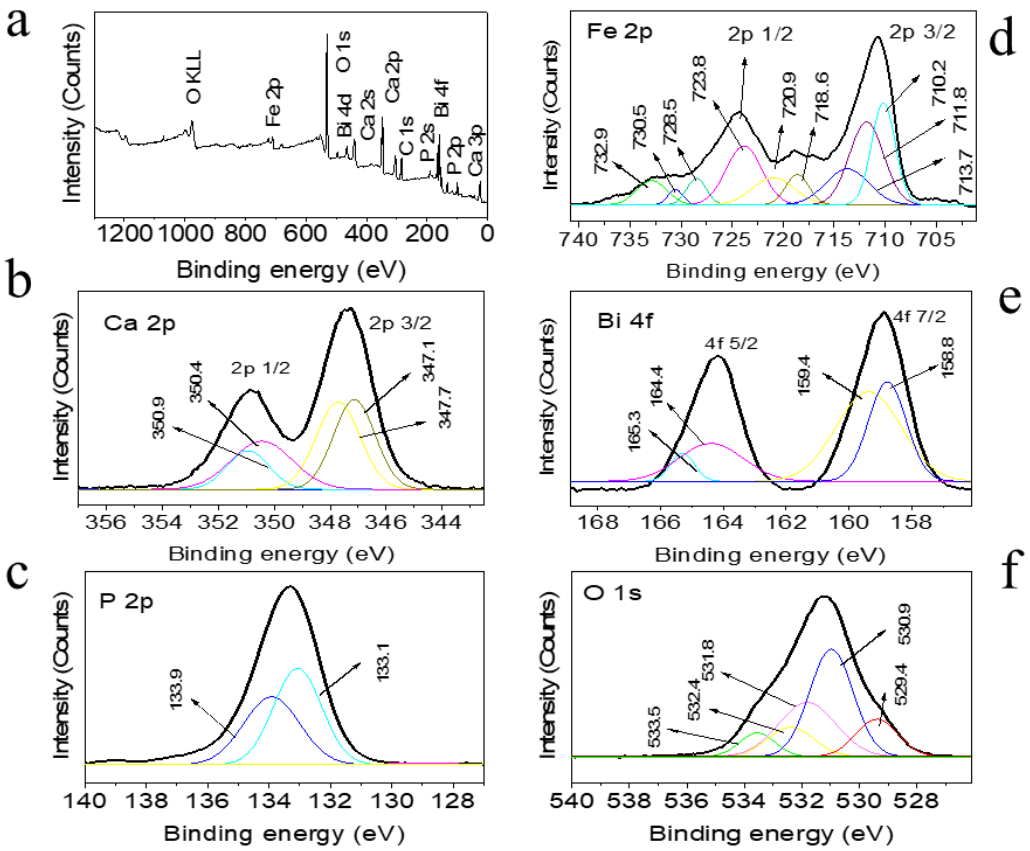

Figure 30. XPS spectra for 5% Fe - 4% Bi-HA (a) survey, and (b - f) for Ca, P, Fe, Bi, and O, respectively with the deconvoluted peaks.

Similarly, the deconvoluted spectrum of Fe (Figure 30d) shows two peaks with binding energies of 710.98 eV (Fe 2p 3/2) and 724.58 eV (Fe 2p ½), with spin-orbit splitting of 13.5 eV, characteristic of Fe ions in the +3 oxidation state (Hadagalli *et al.*, 2021; Sheikh *et al.*, 2018). Satellite peaks of Fe appeared at 718.9 eV for 2p 3/2 and 731.3 eV for 2p ½, respectively. In addition to these shake-up peaks, the peak with the binding energy of 723.8 eV inferred the linkage of Fe^{3+} to the PO_4^{3-} group in the HA structure (Hadagalli *et al.*, 2021). The spectrum of Bi (Figure 30e) showed two peaks with binding energies of 158.88 eV (Bi 4f 7/2) and 164.18 eV (Bi 4f 5/2), characteristic of Bi in the +3 oxidation state, which inferred that Bi^{3+} was successfully substituted in the HA structure. The deconvoluted spectrum of O 1s (Figure 30f) showed that O existed in different environments; the peaks at binding energies of 533.5, 532.4, 531.8, 530.9, and 529.4 eV correspond to CO_3^{2-} ions, adsorbed H_2O, OH^-, O^{2-}, and M–OH bond, respectively (Haber *et al.*, 1976; Qiao *et al.*, 2019; Wang *et al.*, 2017).

4.5 Defluoridation Analysis

4.5.1 Selections of Adsorbents

The most important criteria for the feasibility of an adsorbent are the adsorption efficiency and cost. It is therefore desirable to have a larger adsorption capacity per gram of raw material. A material's adsorption capability is mostly determined by its chemical makeup and some other considerations (Scheverin *et al.*, 2022). Because of this, initially the adsorbents that showed better F^- ions removal capacity were identified based on the method reported previously (He *et al.*, 2016), using triplicates by taking 10 mg/L of F^- ions concentration, 0.5 g/L of the adsorbents at pH of 6.5. The results (Figure 31) indicated that 1% Fe-HA, 1% Bi-HA and 5% Fe – 4% Bi-HA showed high F^- ions adsorption percentage from each category, and the co-doped HA nanomaterials have high F^- ions removal than the pristine as well as the single-doped HA nanomaterials. These observations could be explained by the fact that the major adsorption mechanisms at low concentrations and at acidic or neutral pH would be the ionic substitution of the F^- ions with the OH^- groups and electrostatic interaction between the F^- ions with the positive charge metal ions of HA surface (Chen *et al.*, 2018; Huang *et al.*, 2020; Scheverin *et al.*, 2022). However, according to this work the electrostatic interaction has more contribution for defluoridation than the ion-exchange mechanism. According to previous report (Chen *et al.*, 2018), the high defluoridation capacities of trivalent metal ions doped HA over divalent metal ion doped HA adsorbents may possibly possess high positive surface charge on the trivalent metal ions doped HA materials. The other factor that affects the defluoridation performance is the particle size of the adsorbent. The size of the particle has a significant impact on the HA's adsorption ability (Scheverin *et al.*, 2022).

The better adsorption capacity of 1% Bi-HA and 1% Fe-HA from their respective group may be due to the availability of more exchangeable OH^- ions and the smaller crystallite as well as particle sizes of the nanomaterials. As already discussed in the FTIR analysis (Section 4.1.2), when the amount of dopant (Fe^{3+} and Bi^{3+}) increased, the intensity of O-H stretching decreased which is associated with the conversion of some of the OH^- ions in to O^{2-} ions to balance the charge. Because of this, when the amount of Bi^{3+} and Fe^{3+} increased, the F^- ions removal by ion exchange decreased. However, when the amount of the dopant metal ions further incased (7% Bi-HA and 7% Fe-HA), the F^- ions removal increased, this may be associated with the increasing tendency of the active sites of the respective metal ions that interact with the F^- ions

electrostatically. In the case of the co-doped sample, the high F^- ion adsorption capacity of 5% Fe – 4% Bi-HA may be due to the particle size and the dopants introduced in the system. Because of this, the F^- ions adsorption studies were investigated using 1% Bi-HA, 1% Fe-HA, 5% Fe – 4% Bi-HA, and pristine HA for comparison.

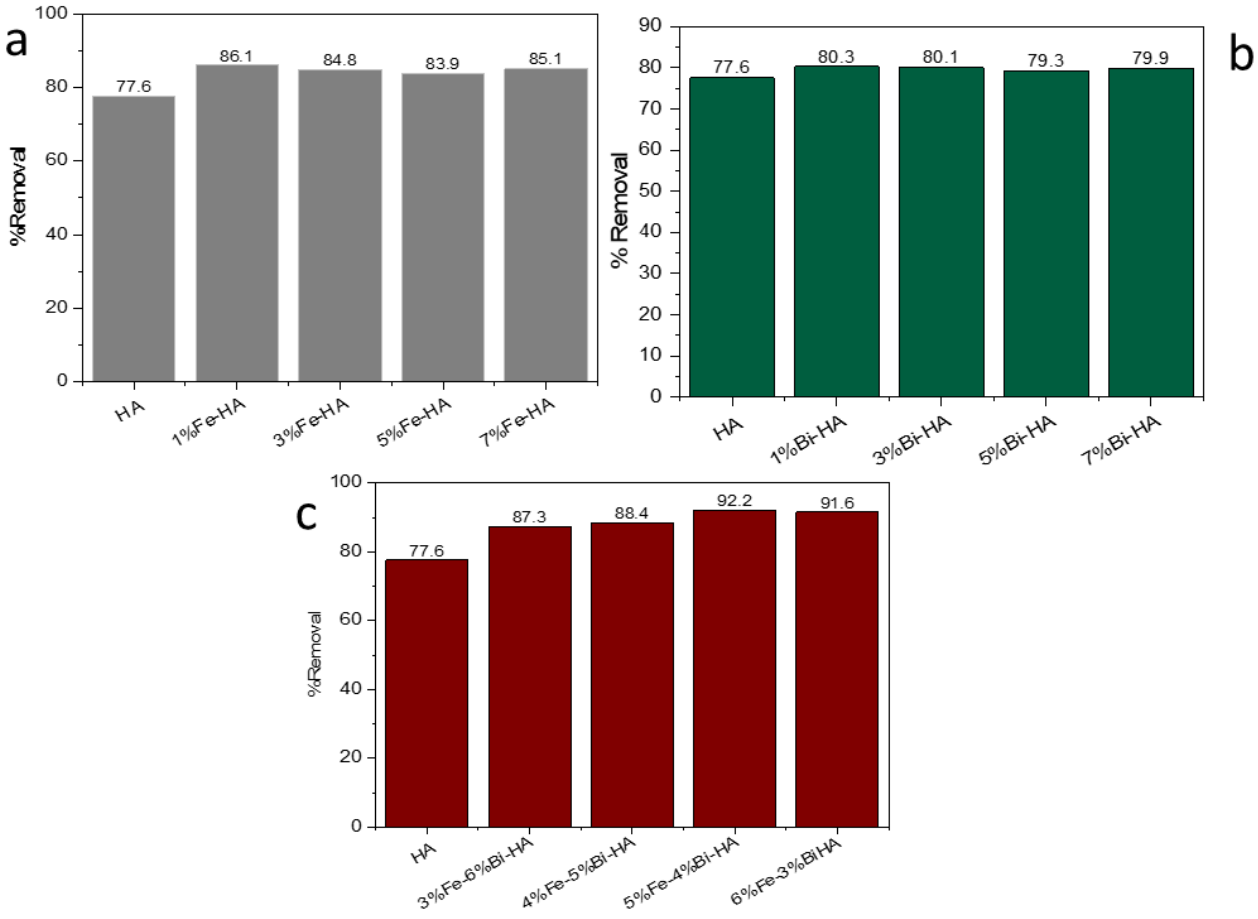

Figure 31. F^- ions adsorption performance of a) Fe^{3+} ions doped HA, b) Bi^{3+} ions doped HA, and c) Bi^{3+} and Fe^{3+} ions co-doped HA nanomaterials

Statistical analysis using one way ANOVA (Appendix 1, 2, and 3) on the effect of dopant amount for the F^- ions removal percentages of the nanomaterials indicated that there is no significant difference ($P > 0.05$) among the values except the Fe^{3+} ions doped HA nanomaterials, which have P value < 0.05. This indicates that for further defluoridation analysis, it is possible to use one of the four nanomaterials (with in the same category of dopant type) for Bi^{3+} ions doped, and Bi^{3+} and Fe^{3+} ions co-doped nanomaterials. However, for Fe^{3+} ions doped HA nanomaterials, only the one that has high adsorption efficiency (1% Fe-HA),

has to be selected for parameter optimization. Furthermore, the one way ANOVA test (Appendix 4, 5, and 6) on the effect of dopant type for F^- ions removal indicated that there is significant difference between the removal efficiencies ($P < 0.05$), which means that the defluoridation performances of Bi^{3+} ions doped HA nanomaterials are lower than that of Fe^{3+} ions doped HA nanomaterials, and these are also lower than the defluoridation performances of Bi^{3+} and Fe^{3+} ions co-doped HA nanomaterials.

4.5.2 Effect of pH on Adsorption and Point of Zero Charge

Point of zero charge (PZC) is the pH at which the net surface charge of the material is zero. The functional groups of a given material are protonated below pH at the PZC, which results in a positive surface charge for the material; these surface groups are deprotonated above the pH of PZC, resulting in a negative surface charge for the material. Therefore, the determination of the PZC can be used to infer potential adsorption mechanisms (Scheverin *et al.*, 2022). PZC of the synthesized nanomaterials was determined by plotting the change in pH against the initial pH of the solution. PZC of the synthesized pristine, Fe^{3+} ions doped, Bi^{3+} ions doped, and Bi^{3+} and Fe^{3+} ions doped HA nanomaterials were found to be 7.4, 7.8, 8.0, and 8.4, respectively (Figure 32a). This indicates that the surface charge of the pristine and doped HA nanomaterials is positive below the corresponding values of PZC due to the complexation with H^+ ions, and negatively charged above the values because of the complexation with the OH^- ions (Panchu *et al.*, 2022). PZC of HA nanomaterial increased when Bi^{3+} and Fe^{3+} ions introduce in the structure as dopants, and it agrees with previous reports on pristine and metal ion doped HA-based materials (Mondal *et al.*, 2016; Panchu *et al.*, 2022). The high PZC values of metal ions-doped HA nanomaterials indicate that the surface of each nanomaterial has extra positive charge due to the trivalent metal ions incorporated in the structure. The increased in PZC of the materials implies that it needs more OH^- ions (negative charge) to neutralize its surface.

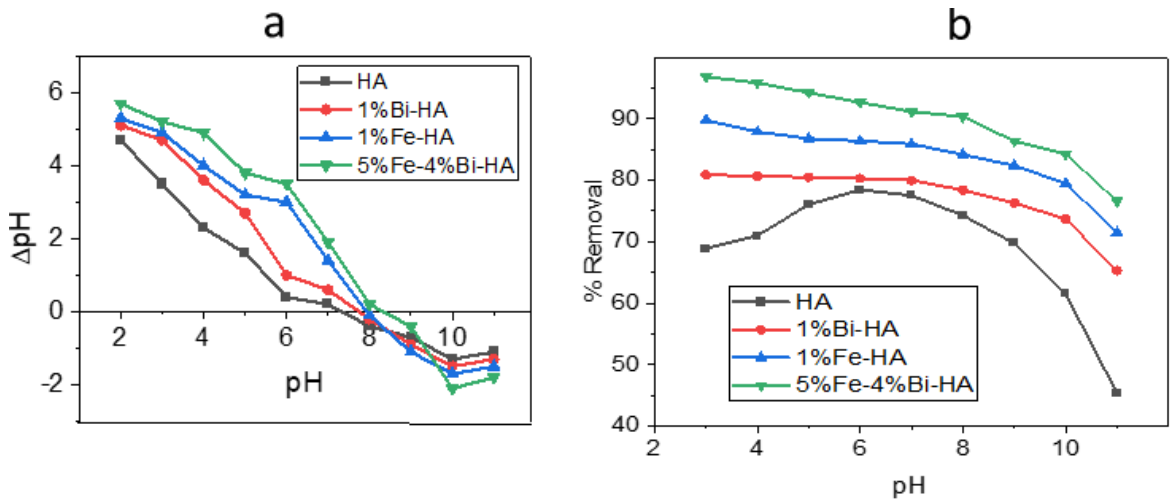

Figure 32. a) Point of zero charge, and b) influence of pH on F^- ions removal of synthesized nanomaterials using 10 mg/L F^- ions, 0.5 g/L dose, and 10 hours contact time.

The solution pH is one factor affecting the removal of F^- ions because a change in the pH of the solution could also change the surface properties and dissolution behavior of materials (Fernando *et al.*, 2019). At pH less than 3, pristine and doped HA nanomaterials were unstable (partially dissolved), which agrees with previous reports on HA-based materials (Fernando *et al.*, 2021; Yan *et al.*, 2022). Thus, the influence of pH on F^- ions removal efficiency was analyzed by taking pH 3, 4, 5, 6, 7, 8, 9, 10, and 11, which was also used in previous reports of HA-based materials for F^- ions adsorption (Moirana *et al.*, 2023; Mondal *et al.*, 2016; Nagaraj *et al.*, 2018), and 10 mg/L of F^- ions concentration. Initially, the pH of F^- ions solution was adjusted by using $3.65x10^3$ mg/L HCl and $4x10^3$ mg/L NaOH solutions. At pH lower than the PZC of the nanomaterials, the surface becomes suitable for F^- ions adsorption due to electrostatic interaction (Nagaraj *et al.*, 2018).

The results of F^- ions removal of pristine, Fe^{3+} ions doped, Bi^{3+} ions doped, and Bi^{3+} and Fe^{3+} ions co-doped HA nanomaterials are given in Figure 32b. The F^- ions removal tendency of pristine HA nanomaterial increased with the increase in pH and attained a maximum value of 78.46% at pH of 6; after that, (in the alkaline media) sharply decreased to 45.31% at pH = 11, the results agree with previous report on HA-based adsorbent (Samant *et al.*, 2017). The decrease in F^- ions removal of pristine HA in the acidic solution (pH below the PZC, 7.4) may be due to apatite dissolution (Wimalasiri AKD Veromee K *et al.*, 2021), according to the reaction given in Equation 29. Which indicates that the Ca^{2+} ions available in the solution are not sufficient to remove the F^- ions. However, in the case of alkaline pH, the electrostatic

repulsion between F^- ions, and OH^- ions decreases the removal percentage (Fernando *et al.*, 2021; Tang *et al.*, 2018).

$$Ca_{10}(PO_4)_6(OH)_2 + 8H^+ \leftrightarrow 10Ca^{2+} + 6HPO_4^{2-} + H_2O \quad (29)$$

In the case of doped samples (single and co-doped), the F^- ions removal efficiency was high in acidic media, and then decreased as pH increased. The high F^- ions removals of the doped HA nanomaterials in the acidic condition against to the pristine HA nanomaterial does not mean there is no dissolution of the doped nanomaterials. Rather, in addition to the Ca^{2+} ions, the dopant ions (Fe^{3+} and Bi^{3+}) could form complex with the F^- ions, and it makes the removal percentage increased. In addition, the surface of the modified HA nanomaterials is more positive in acidic condition, and becomes negative in the alkaline condition; which was observed in the PZC determination. The extra positive surface comes from the protonation, and from the additional charges of Fe^{3+} and Bi^{3+} ions. This result agrees with the literature on trivalent (Al^{3+}, Ce^{3+} and La^{3+}) metal ion-doped HA materials (Nagaraj *et al.*, 2018; Nie *et al.*, 2012), and HA-based composites (Huang *et al.*, 2020; Sekar *et al.*, 2022).

For Fe^{3+} ions doped HA nanomaterial, the measurements conducted at pH 3 and 11 the F^- ions removal efficiency changed from 89.80 to 71.50%. Similarly, the F^- ions removal efficiency of Bi^{3+} ions doped HA nanomaterial with the pH change from 3 to 11, the percentage removal was also changed from 80.9 to 65.3%. The material's adsorption efficiency was slightly changed up to alkaline conditions (from 80.9 to 80% for the pH change from 3 to 11). However, the removal percentage declined from 78.4 to 65.3% as pH was changed from 8 to 11. The adsorption efficiency results for Bi^{3+} and Fe^{3+} ions co-doped HA nanomaterial changed from 96.87% to 76.60% for the measurements conducted at the pH of 3 and 11. However, the efficiency changed from 96.87% to 91.17% as the pH changed from 3 to 7, and further declined as pH became alkaline (pH from 8 to 11). The results inferred that the surface of the co-doped sample is also positively charged at lower pH due to protonation and the extra charges of the dopant ions, and the surface became negatively charged in basic conditions due to an excess amount of OH^- ions, which repels the F^- ions in the removal process (Balasooriya *et al.*, 2022; Yan *et al.*, 2022).

The study generally, indicates that pristine as well as doped HA nanomaterials show change in F^- ions adsorption as pH changed. However specially the doped HA nanomaterials are less susceptible to pH change compared to Al^{3+}, La^{3+} and Ce^{3+} modified HA adsorbents reported in the literature (Nagaraj *et al.*, 2018; Nie *et al.*, 2012). Thus, Fe^{3+} and Bi^{3+} ions doped (single

and co-doped) HA nanomaterial can be recommended for F^- ions adsorption in a wide range of pH (from acidic to near alkaline conditions) Note: a pH of 6.5 (pH range of drinking water) was chosen to analyze the other adsorption parameters for pristine, Bi^{3+} ions doped, Fe^{3+} ions doped, and Bi^{3+} and Fe^{3+} ions co-doped HA nanomaterials.

4.5.3 The Effect of Contact Time for Fluoride Ions Adsorption

The variation of F^- ions removal capacities of pristine, Bi^{3+} ions doped, Fe^{3+} ions doped, and Bi^{3+} and Fe^{3+} ions co-doped HA nanomaterials were evaluated by varying the time of interaction up to 4 hours using 10 mg/L of F^- ions, pH 6.5, and 0.5 g/L of each nanomaterial. The rate of adsorption processes (Figure 33) for pristine and doped HA nanomaterials increased rapidly in the first 60 minutes and then slowly increased up to 180 minutes; after that the change in adsorption was near to constant. Because of this, 3 hours contact time was considered the optimum time for F^- ions adsorption by pristine and doped HA nanomaterials, and used for the calculation of experimental adsorption capacity and for other adsorption parameter studies.

Initially, the difference in adsorption percentage of pristine, Fe^{3+} ions doped, Bi^{3+} ions doped, and Bi^{3+} and Fe^{3+} ions co-doped HA nanomaterials were 8.3%, 9.21%, 7.28%, and 9.51%, respectively when the contact time changed from 20 – 80 minutes. After that the change in adsorption percentage was minimum. This indicates that the rate of F^- ions adsorption was fast in the co-doped HA nanomaterial compared to the pristine as well as single doped nanomaterials. This confirms the presence of extra active site (synergistic effect of Fe^{3+} and Bi^{3+} ions) of the co-doped nanomaterial for the F^- ions adsorption. The results inferred that in the first hour, all the energetic sites of pristine, Fe^{3+} ions doped, Bi^{3+} ions doped, and Bi^{3+} and Fe^{3+} ions co-doped HA nanomaterials are highly interacted with F^- ions; thus, the rate became fast. As the contact time increases, numerous energetic sites become occupied. The F^- ions, therefore, require more time to contact with remaining vacant active sites, and only some of them are adsorbed, so the rate becomes sluggish. The results also indicate that the Fe^{3+} ions, and Bi^{3+} ions doped (single and co-doped) HA nanomaterials have high adsorption percentage compared to the pristine HA nanomaterial at a specified contact time. Moreover, the optimum contact time obtained in this work (3 hours) is lower than the optimum contact time reported in the literature for some of the HA-based adsorbents (Nie *et al.*, 2012; Tomar *et al.*, 2015; Yu *et al.*, 2013). This shows that Fe^{3+} and Bi^{3+} ions doped HA nanomaterials can be considered as an efficient adsorbent for F^- ions removal from aqueous solution.

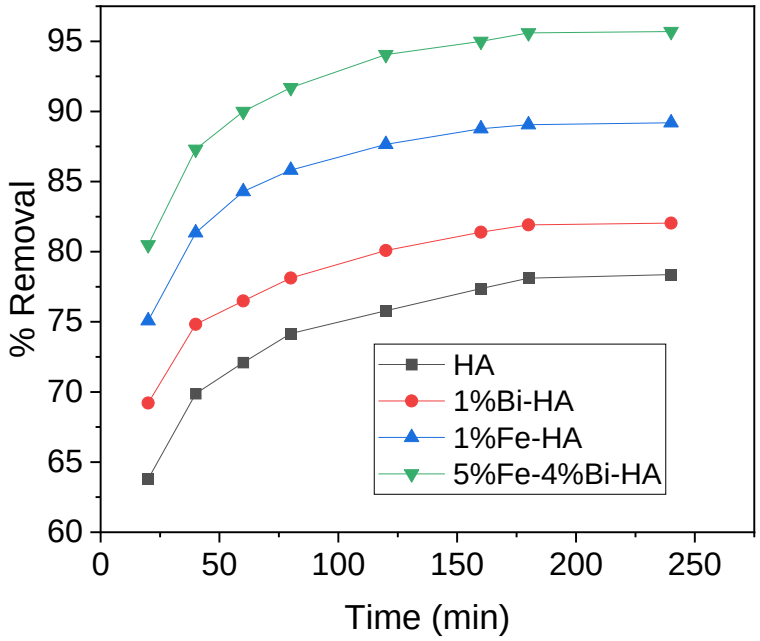

Figure 33. Effect of contact time on F^- ions adsorption by pristine and doped HA nanomaterials using 10 mg/L F^- ions, pH 6.5, and dose of 0.5 g/L.

4.5.4 The Effect of Initial Concentration of Fluoride Ions

The influence of F^- ions concentration was studied at pH 6.5, contact time of 3 hours, and dose of the nanomaterials 0.5 g/L. The initial concentration of F^- ions used were 5, 10, 15, 20, 25, and 30 mg/L. The starting concentration (5 mg/L) was selected by referring the different reports on F^- ions adsorption using HA-based materials (Chen *et al.*, 2018; Huang *et al.*, 2020; Nayak *et al.*, 2017), and also considering that at the lower concentrations of F^- ions, with the presence of sufficient amounts of the adsorbent, there will be enough active sites for adsorption (Nayak *et al.*, 2017). The results (Figure 34) indicated that the removal percentages of the pristine and doped HA nanomaterials decreased as the initial concentration increased. The high F^- ions uptake of the nanomaterials at the lower concentration indicates the presence of an adequate quantity of energetic sites of the nanomaterials (Nayak *et al.*, 2017). But at high concentration the available active sites of the adsorbents are not sufficient for further adsorption of the excess F^- ions available in the solution, or it could be because of the repulsion between the F^- ions in solution with those adsorbed on the surface of the nanomaterials (Roy Das, 2016).

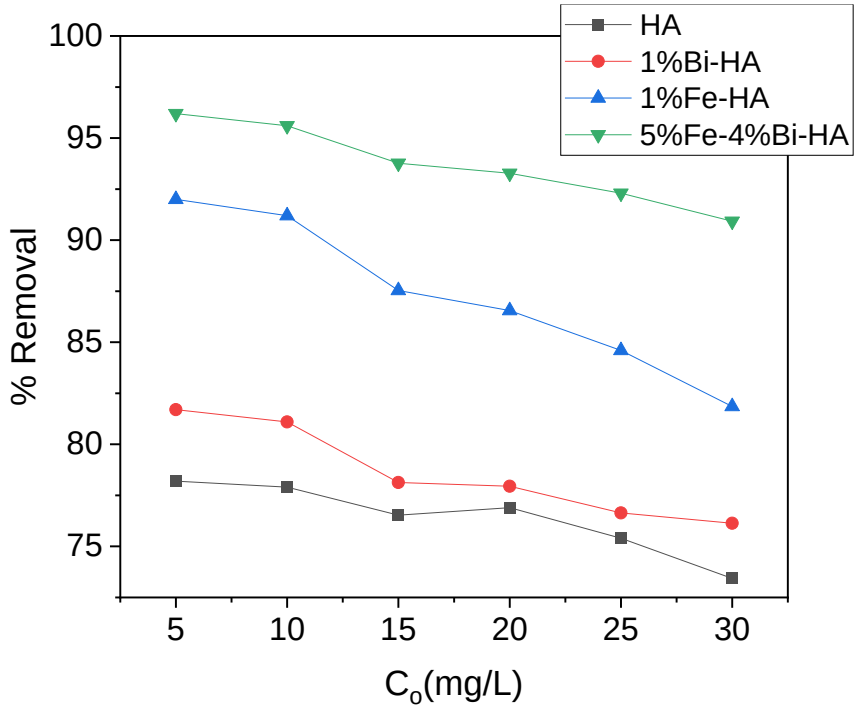

Figure 34. Effect of initial concentration on F^- ions adsorption for pristine and doped HA nanomaterials using contact time of 3 hours, pH 6.5, and dose of 0.5 g/L.

4.5.5 Effect of Adsorbent Amount on Fluoride Ion Adsorption

The influence of pristine and doped HA doses on F^- ions adsorption was evaluated at pH 6.5 using 10 mg/L F^- ions, interaction time 3 hours, and dose of the nanomaterials: 0.5, 1, 2, 3, 4, and 5 g/L, by shaking the mixture at 150 rpm. The results (Table 6) indicate that the concentration of F^- ions remaining in the solution after completion of the adsorption process was below the WHO maximum recommended limit (1.5 mg/L) in all the dose ranges studied for Fe^{3+} ions doped, and co-doped HA nanomaterials. For the Bi^{3+} ions doped HA nanomaterials, residual concentration of F^- ions below 1.5 mg/L was achieved at adsorbent dose greater than 2.0 g/L. However, for pristine HA nanomaterial, concentration of residue F^- ions was greater than the recommended limit (1.5 mg/L) in all the dosages used in this study.

Table 6. Residual F^- ions concentration at different nanomaterials dose

Dose (g/L)	Co (mg/L)	Ce (mg/L)			
		HA	1%Bi-HA	1%Fe-HA	5%Fe-4%Bi-HA
0.5	10	2.71	1.89	0.88	0.392
1	10	2.59	1.73	0.62	0.301
2	10	2.53	1.48	0.41	0.131
3	10	2.25	1.29	0.34	0.120
4	10	2.12	1.07	0.31	0.113
5	10	2.09	1.02	0.29	0.012

The sorption capacity of the nanomaterials (Figure 35) declined abruptly with an increase of the dose until 2.0 g/L, above which the change became relatively smaller. This is because when the dose of the nanomaterials is decreased, the number of energetic sites is inadequate for efficiently removing F^- ions. Conversely, as the dose of the nanomaterials increases, the number of energetic sites increases, enhancing defluoridation until the available sites become saturated. The decrease in sorption efficiency of the nanomaterials, even with increased dosage, may be due to adsorbent-adsorbent interaction (Nayak *et al.*, 2017).

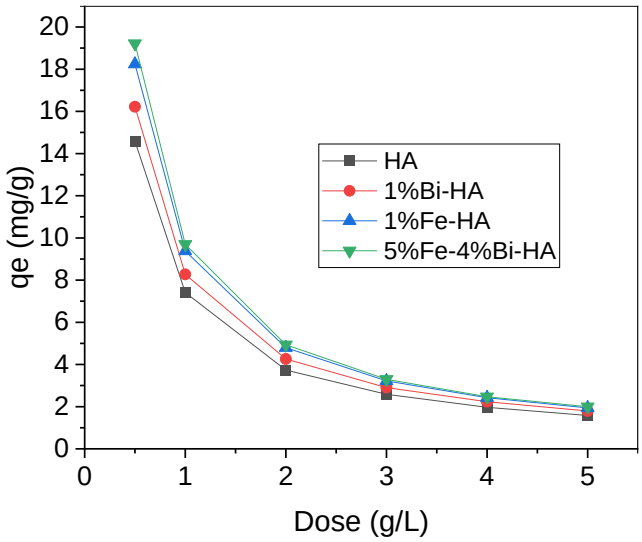

Figure 35. Influence of adsorbent dose on F^- ions adsorption by pristine and doped HA nanomaterials using 10 mg/L F^- ions, 3 hours contact time, and pH of 6.5.

4.5.6 Common Ion Effect on Fluoride Ion Adsorption

Natural water sources are complex matrices from the standpoint of adsorption processes because they have a variety of coexisting species that can fight with F^- ions for active adsorption sites (Mondal *et al.*, 2016). The anions mostly found in groundwater include nitrate, chloride, sulfate, bicarbonate, phosphate, and hydroxide (Sekar *et al.*, 2022). Thus, the effect of common ions was assessed by taking 0, 30 and 300 mg/L of chloride (Cl^-), nitrate (NO_3^-), sulfate (SO_4^{2-}) and carbonate (CO_3^{2-}) ions along with 20 mg/L of F^- ions, using 2 g/L of each of the nanomaterials. The results (Figure 36) indicated that the presence of Cl^-, NO_3^- and SO_4^{2-} ions has little effect on the adsorption of F^- ions, even at high concentrations of these common ions. However, the elimination of F^- ions was impacted by the presence of CO_3^{2-} ions, and the effect increased with the concentration of the CO_3^{2-} ions. Moreover, the results showed that the effect of CO_3^{2-} ions on F^- ions adsorption was more noticeable in pristine HA nanomaterial than for the doped HA nanomaterilas, which implies that the trivalent metal ions modified HA nanomaterials have more active sites for F^- ions adsorption compared to the pristine HA nanomaterial.

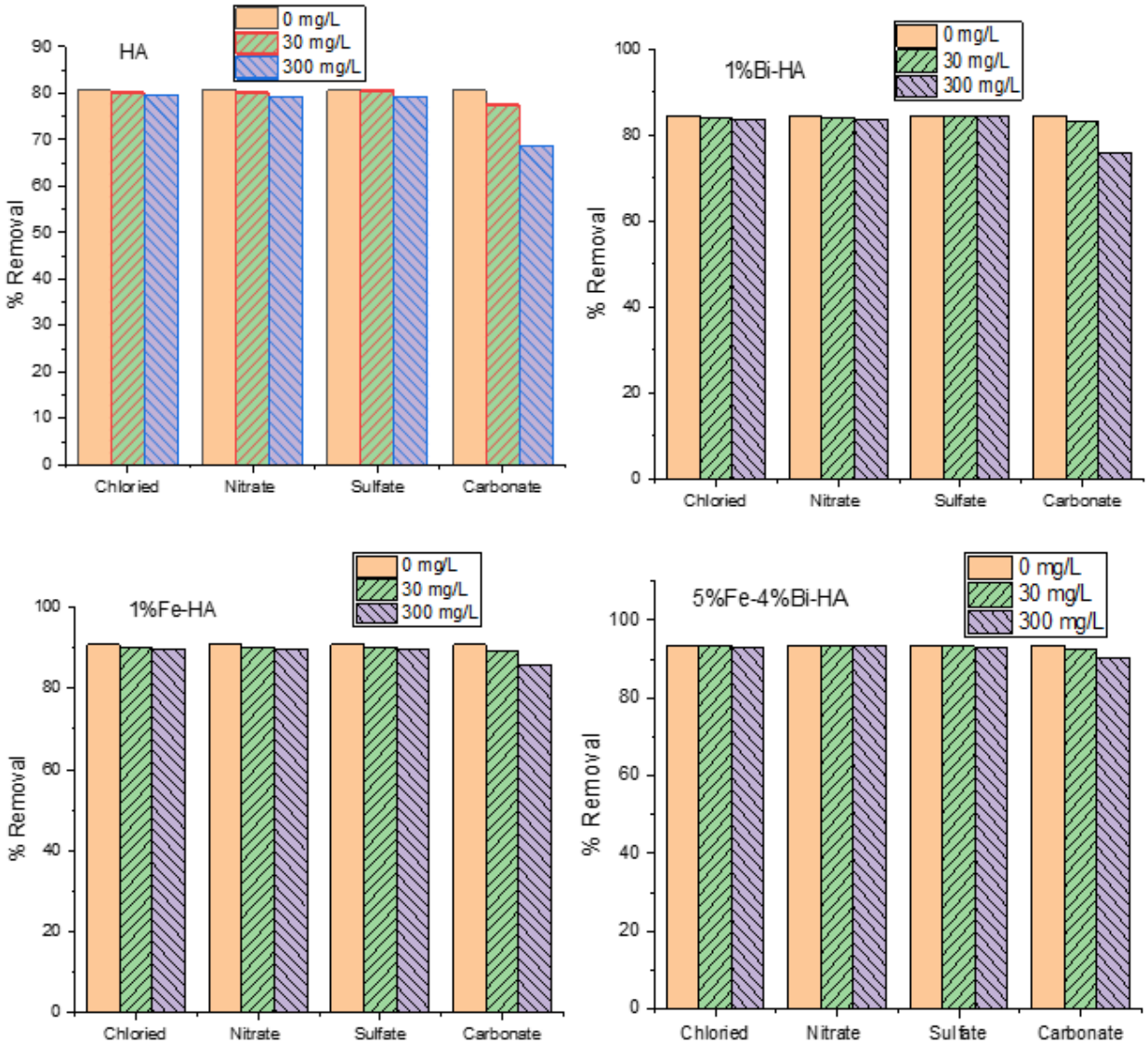

Figure 36. Effect of common ions on F^- ions adsorption by pristine and doped HA nanomaterials using 20 mg/L F^- ions, pH 6.5, contact time 3 hours, and dose of 2 g/L.

Previous research report (Gao *et al.*, 2019) also indicates that CO_3^{2-} ions have a more substantial effect on F^- ions adsorption than other anions like Cl^-, NO_3^- and SO_4^{2-} on the surface of HA based-materials. The reduced ability of the HA materials to remove F^- ions in the presence of CO_3^{2-} ions suggested that the competitiveness is mainly affected by charge, ionic size and concentration (Mondal *et al.*, 2016; Tang *et al.*, 2018). The high competitiveness of CO_3^{2-} ion on F^- ions adsorption compared to other ions (Cl^-, NO_3^- and SO_4^{2-}) may be due to the high charge-to-ionic size value. The order of charge to ionic radius for the studied anions is $CO_3^{2-} > SO_4^{2-} > NO_3^- > Cl^-$ (Nabizadeh *et al.*, 2015; Tang *et al.*, 2018). Anions having high charge-to-ionic size ratio have high columbic repulsion toward the F^- ions and reduce the adsorption tendency of F^- ions on the adsorbent surface (Nabizadeh *et al.*, 2015; Nagaraj *et al.*,

2018). The effect of CO_3^{2-} ions on the F^- ions adsorption towards pristine and doped HA may also be associated with the increasing solution pH due to the CO_3^{2-} ions. When CO_3^{2-} ions are introduced in an aqueous solution, the pH of the solution increases due to hydrolysis, and the formed OH^- ions repulse the F^- ions and reduce the adsorption (Sekar *et al.*, 2022).

4.5.7 Adsorption Kinetics Analysis

The general adsorption mechanism and possible rate-controlling phases, such as the mass transport and chemical reaction routes, are described by kinetics. One of the most important factors in selecting the best adsorbent material to use as a potential adsorbent is the rate of adsorption. The material should have a higher rate of adsorption and greater adsorption ability (Gao *et al.*, 2019; Scheverin *et al.*, 2022). To understand the adsorption kinetics and mechanism of adsorption, the experimental adsorption data obtained were linearly and non-linearly fitted with pseudo-first order (SFO), pseudo-second order (SSO), and Elovich models. Even if, it has been noted by other authors that the linearization biases the estimation of the model's parameter set, and encourage the use of non-linear expressions (Largitte Pasquier, 2016).

The SFO model predicts that saturation will happen during a brief contact time or that a single adsorbate will be adsorbed onto a single sorption site (Nayak *et al.*, 2017). SFO can be expressed based on Equation 30.

$$ln(q_e - q_t) = lnq_e - k_1 t \quad (30)$$

Where, q_t and q_e are the amounts (mg/g) of F^- ions adsorbed at time t, and equilibrium respectively, and k_1 (1/min) is the rate constant. In the linear fitting analysis, k_1 and q_e were calculated from the slope and intercept, respectively, using the graph $ln(q_e - q_t)$ vs t plot (Figure 37). The results (Table 7) indicates that the experimental values of adsorption capacity (qe) for HA, 1% Bi-HA, 1% Fe-HA, and 5% Fe-4% Bi-HA were 15.62, 16.38, 17.81, and 19.80 mg/g, respectively. The values of adsorption capacity obtained from linear fitting were 4.03, 3.40, 4.87, and 5.36 mg/g, and from the non-linear fitting the values were 15.15, 15.94, 17.42, and 18.79 mg/g, respectively.

Table 7. Parameters of the kinetic models for pristine and doped HA nanomaterials

Models	Parameters		HA	1% Bi-HA	1% Fe-HA	5% Fe-4% Bi-HA
	q_e, exp.		15.62	16.38	17.81	19.80
SFO	q_e	Linear	4.03	3.40	4.87	5.36
		Non-linear	15.15	15.94	17.42	18.79
	k_1	Linear	0.020	0.022	0.026	0.024
		Non-linear	0.086	0.096	0.094	0.081
	R^2	Linear	0.981	0.978	0.977	0.978
		Non-linear	0.988	0.991	0.993	0.965
SSO	q_e	Linear	16.08	16.77	18.21	20.44
		Non-linear	15.91	16.26	18.16	19.08
	k_2	Linear	0.010	0.011	0.012	0.008
		Non-linear	0.011	0.012	0.013	0.110
	R^2	Linear	0.999	0.999	0.999	0.999
		Non-linear	0.999	0.999	0.999	0.999
Elovich	α	Linear	0.289	0.384	0.351	0.403
		Non-linear	0.396	0.412	0.445	0.564
	β	Linear	0.854	0.965	0.884	0.589
		Non-linear	0.854	0.865	0.883	0.620
	R^2	Linear	0.965	0.963	0.932	0.916
		Non-linear	0.998	0.998	0.998	0.973

This shows the non-linear fitting result has close agreement with the experimental values. Similarly, the rate constant, k_1 values obtained from the non-linear fittings are four times the values obtained from linear fittings for all the nanomaterials used. Moreover, the regression coefficient (R^2) value is high in the non-linear fitting than the linear fitting results for the corresponding HA-based nanomaterials. Thus, it indicates that the non-linear fitting gives less biased results than the linear fitting for SFO model. The outcome of a linear regression process will be affected by variations in the axial settings of the linear equations (of separate models), which will thus have an impact on the model parameters. On the other hand, these linearization errors are avoided in non-linear analysis when all models are compared on the same abscissa and ordinate (Ferreira *et al.*, 2019; González-López *et al.*, 2022).

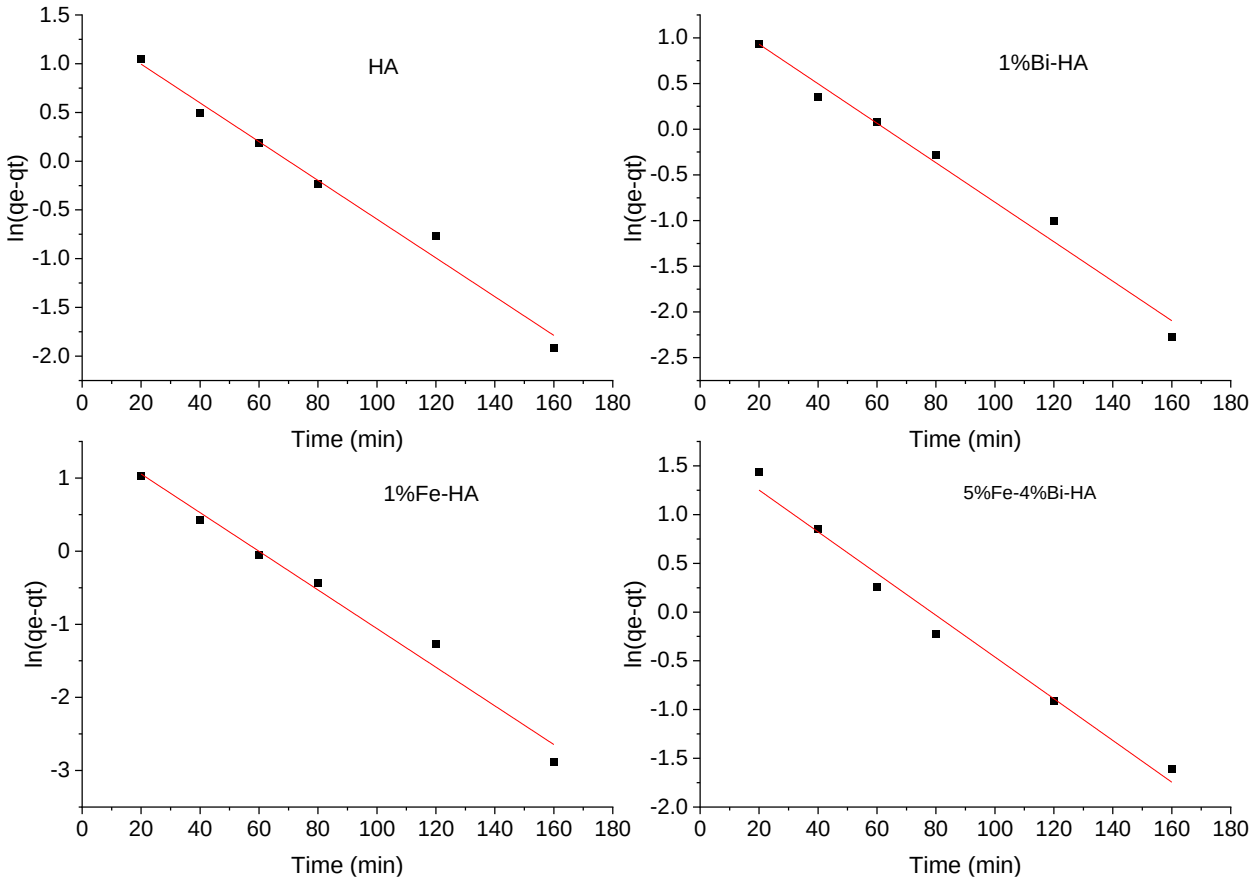

Figure 37. Linear plots of SFO kinetics for F^- ions adsorption by pristine and doped HA nanomaterials

The SSO based on the supposition that adsorption is a one-step process, and suggests that the process is chemical adsorption which involves valence forces by sharing or exchanging electrons between the adsorbent and adsorbate that might be the rate-limiting phase (Nayak *et al.*, 2017). The model is best described by using Equation 31.

$$\frac{t}{q_t} = \frac{1}{k_2 {q_e}^2} + \frac{t}{q_e} \quad (31)$$

Where k_2 (g/mg.min) is the rate constant. In this case also the values of k_2 and q_e were calculated from the slope and intercept of the graph given in Figure 38, for the linear fitting. Both linear and non-linear fitting gives high values of adsorption capacity (q_e), compared to SFO model (Table 7). The calculated values of adsorption capacity were 16.08, 16.77, 18.21, and 20.44 mg/g, using linear fitting, and 15.91, 16.26, 18.16, and 19.08 mg/g, by the non-linear fitting for HA, 1% Bi-HA, 1% Fe-HA, and 5% Fe-4% Bi-HA, respectively.

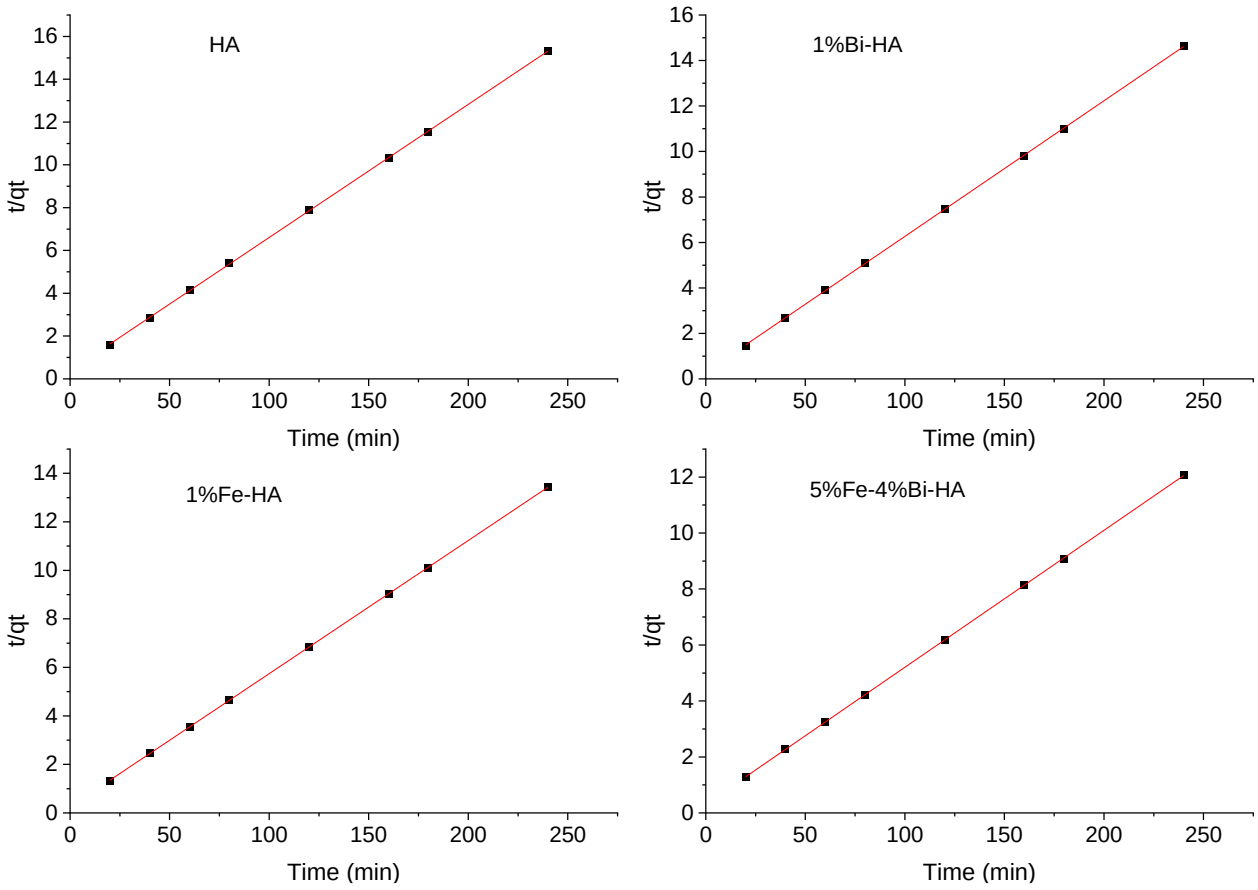

Figure 38. Linear SSO kinetics plots for F^- ions adsorption by pristine and doped HA nanomaterials

Still the non-linear fitting has close agreement with the experimental values of adsorption capacity compared to the linear fitting results. The non-linear fitting also gives high values of rate constant, k_2 compared to the linear fitting for the same nanomaterials type. However, the regression coefficient (R^2) values obtained from the linear and non-linear fittings are equal for all the nanomaterials. The kinetics parameters results obtained from SSO using linear and non-linear fittings are in close agreement to each other. In general, the data showed that SSO kinetics has relatively higher correlation coefficient values for all four analysed materials than SFO kinetics. Similarly, the equilibrium adsorption capacity (qe) values obtained from the model (SSO) for all the nanomaterials are closer to the experimental values than SFO. The non-linear fittings of the HA-based nanomaterials given in Figure 39 showed that SSO has better fits with the experimental values compared to other kinetics models used in this study. Thus, the results infer that the F^- ions' adsorption rate fits more closely to SSO, suggesting that ions'

sorption occurs by chemical processes (Chen *et al.*, 2018; Nayak *et al.*, 2017; Wang *et al.*, 2017).

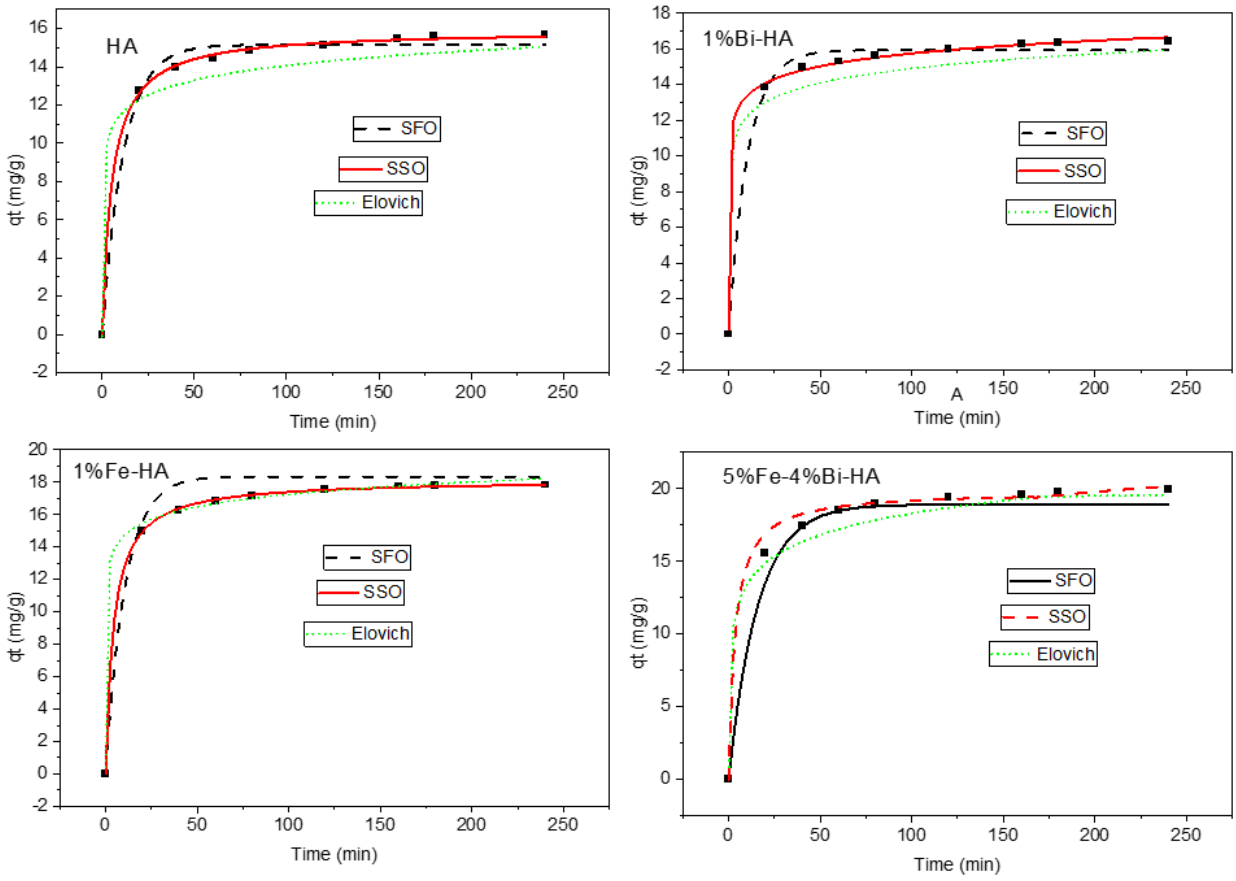

Figure 39. Non-linear kinetics fitting for F^- ions adsorption by pristine and doped HA nanomaterials

The Elovich model also describes an adsorption process that follows chemisorption. This model is used when the adsorbate ions and the surface sites interact chemically through a second-order mechanism. The linear form of Elovich equation can be represented by using Equation 32 (Nayak *et al.*, 2017).

$$q_t = \frac{1}{\beta} \ln(\alpha\beta) + \frac{1}{\beta} lnt \qquad (32)$$

Where α (mg/g.min) is the initial sorption rate constant, and β (mg/g) is the extent of surface coverage during chemisorption. The values of α and β were calculated from the intercept and slope, respectively, using the graph of $q_t$vs lnt as shown in Figure 40, for the linear fitting.

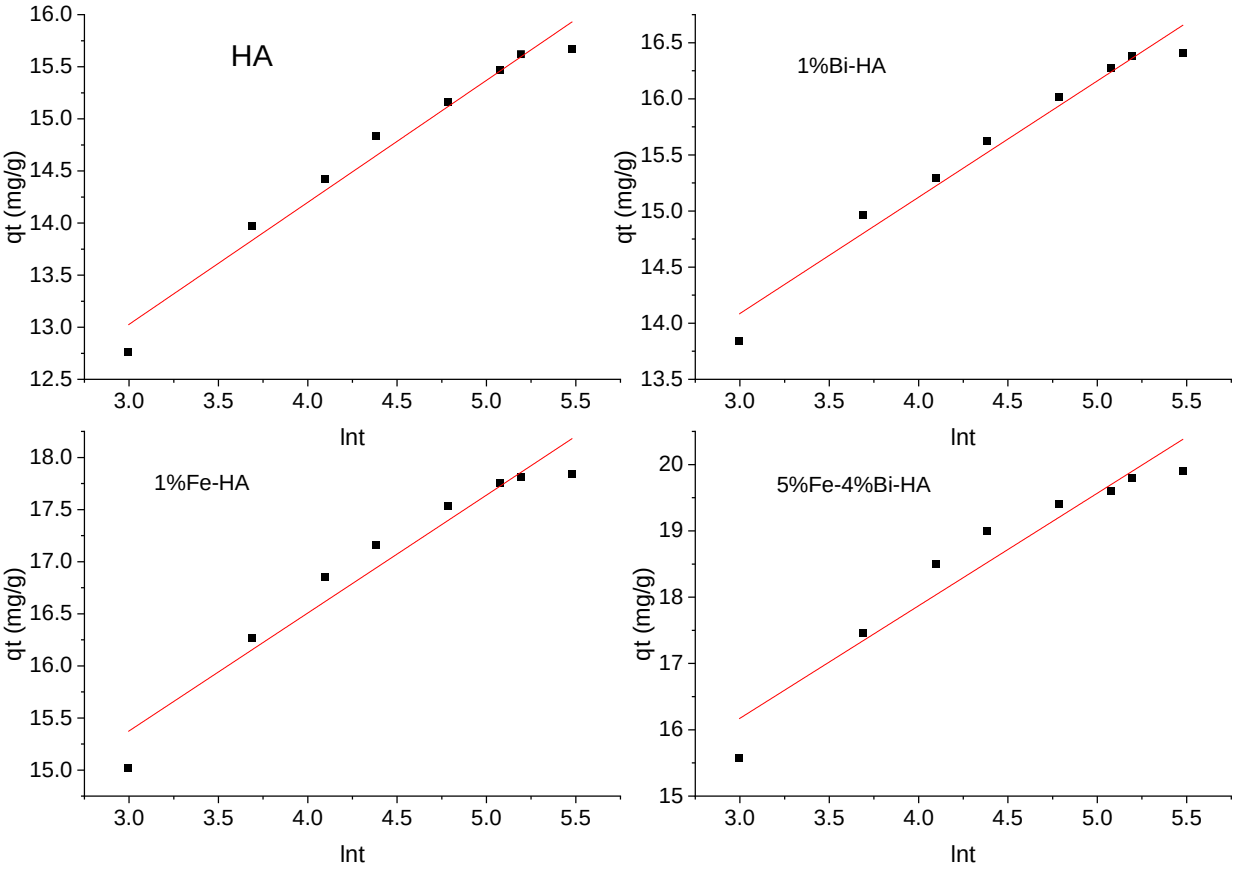

Figure 40. Linear Elovich kinetics plots for F^- ions adsorption by pristine and doped HA nanomaterials

The values of rate constant, α and regression coefficient (R^2) for the Elovich model were high in the non-linear fitting compared to the linear plot for the same nanomaterials type used in the adsorption experiment. However, the surface coverage β values obtained from linear and non-linear fittings are comparable to each other. The high values of regression coefficient (R^2) for this model provides more proof that the rate-determining step in the F^- ions adsorption process on HA-based nanomaterials is more of chemisorption (Aw *et al.*, 2022).

The comparison of linear and non-linear fitting results for the F^- ions adsorption using pristine and doped HA nanomaterials indicate that non-linear fitting gives results close to the experimental values obtained. Thus, considering the less biased results obtained and its simplicity to use, the non-linear fitting is recommended for F^- ions adsorption on HA-based nanomaterials. Since the simpler linearized forms that result from applying mathematical transformations to kinetic models have drawn criticism in recent years. Thus, linearization is not reliable to differentiate the goodness of the fit between SFO and SSO kinetic models (González-López *et al.*, 2022).

4.5.8 Adsorption Isotherm Analysis

An adsorption isotherm study shows how much adsorbate is adsorbed per unit mass of adsorbent as a function of its equilibrium concentration in the bulk medium at a constant temperature. Furthermore, this gives details on the maximum amount of adsorbate species that may be adsorbed as well as the material's effectiveness in removing the adsorbate from aqueous solution (Jeyaseelan Viswanathan, 2022). For the determination of adsorption isotherm, and F^- ions sorption mechanism, the experimental results for the pristine, Fe^{3+} ions doped, Bi^{3+} ions doped, and Bi^{3+} and Fe^{3+} ions co-doped HA nanomaterials were linearly and non-linearly fitted to the Langmuir, Freundlich, and Temkin isotherm models. The Langmuir isotherm model defines that adsorbent-adsorbate interaction forms a monolayer, and the adsorbent has uniform active sites with similar sorption energy (Girish, 2017), and is expressed by using Equation 33.

$$\frac{C_e}{q_e} = \frac{1}{bq_o} + \frac{C_e}{q_o} \tag{33}$$

Where q_e the amount of F^- ions adsorbed at equilibrium (mg/g), and C_e is its equilibrium concentration (mg/L), b (L/mg) is a constant related to adsorption equilibrium, and q_o is the maximum adsorption capacity (mg/g). The values of q_o and b were determined from the slope and intercept, respectively, of the graph of $\frac{C_e}{q_e}$ vs C_e plot given in Figure 41. The maximum experimental adsorption capacity (Table 8) for pristine, Fe^{3+} ions doped, Bi^{3+} ions doped, and Bi^{3+} and Fe^{3+} ions co-doped HA nanomaterials was 44.06, 45.68, 49.11, and 54.56 mg/g, respectively. However, the respective values from the Langmuir model became 71.56, 76.86, 86.80, and 100.00 mg/g using linear fitting analysis, and 66.12, 78.71, 80.91, and 97.36 mg/g using non-linear fitting. This indicates that the adsorption capacities obtained by using the non-linear regression analysis are relatively close to the experimental adsorption capacities compared to the linear fitting analysis, except the 1% Bi-HA. But the regression coefficient values obtained from linear fitting were higher than the values obtained from the non-linear fitting analysis except the 5% Fe-4% Bi-HA (gives equal values).

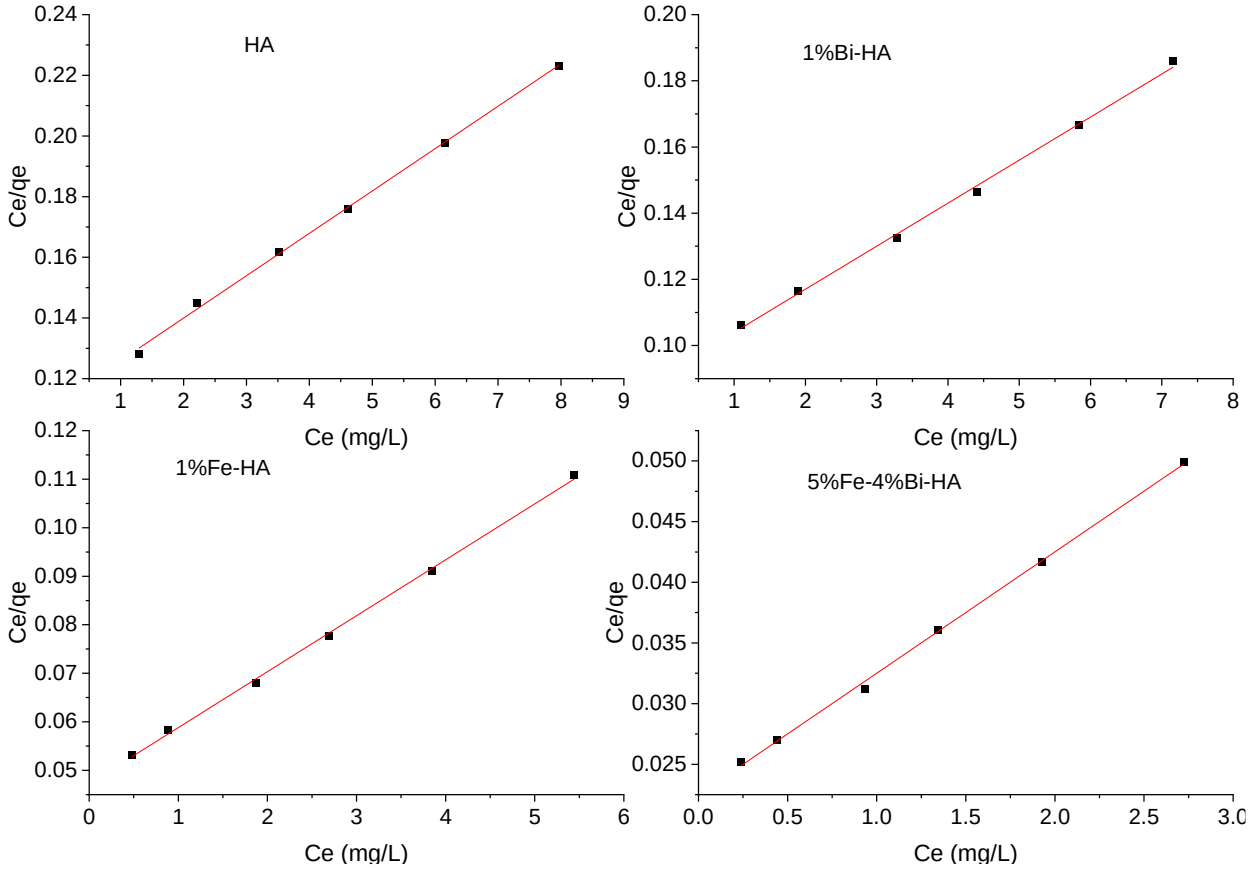

Figure 41. Linear Langmuir isotherm plots for F^- ions adsorption by pristine and doped HA nanomaterials

The HA-based nanomaterials used in this study (specially the co-doped nanomaterial) have high adsorption capacities (Table 8), compared to other HA-based adsorbents listed in Table 1, and those available in the literature, except HA-CeO_2-$La(OH)_3$ composite (Wimalasiri AKD Veromee Kalpana *et al.*, 2021). The high adsorption capacity of HA-CeO_2-$La(OH)_3$ composite may be associated to the use of high concentration of F^- ions during the isotherm study or may be the presence of additional exchangeable OH^- groups from $La(OH)_3$ group. On the other hand, the high adsorption capacity of the 5% Fe-4% Bi-HA may be associated with the strong interaction of trivalent metal ion-doped HA with F^- ions (Chen *et al.*, 2018), high fluoride ion removal efficiency of Fe-containing materials (Corral-Capulin *et al.*, 2019; Ogata *et al.*, 2020), the small size, and high surface area of the nanomaterials as observed in BET, FE-SEM and XRD. And may also be the strong interaction of rod-like morphology with F^- ions as reported in the literature (Nagaraj *et al.*, 2018).

Table 8. Isotherm constants of the different models for pristine and doped HA nanomaterials

Models	Parameters		HA	1% Bi-HA	1% Fe-HA	5% Fe-4% Bi-HA
	q_e, exp.		44.06	45.68	49.11	54.56
Langmuir	q_o	Linear	71.58	76.86	86.80	100.00
		Non-linear	66.12	78.71	80.93	97.36
	b	Linear	0.125	0.143	0.243	0.444
		Non-linear	0.047	0.048	0.280	0.363
	R^2	Linear	0.998	0.997	0.998	0.998
		Non-linear	0.987	0.993	0.988	0.998
Freundlich	n	Linear	0.97	0.90	0.67	0.69
		Non-linear	1.18	1.19	1.67	1.59
	K_f	Linear	6.49	7.98	16.99	29.19
		Non-linear	7.93	8.74	18.32	29.85
	R^2	Linear	0.977	0.982	0.967	0.973
		Non-linear	0.977	0.992	0.978	0.983
Temkin	B_T	Linear	20.25	19.40	16.22	18.16
		Non-linear	122.42	127.77	152.77	136.04
	K_T	Linear	1.02	1.23	3.36	6.35
		Non-linear	1.02	1.23	3.36	6.35
	R^2	Linear	0.979	0.959	0.977	0.971
		Non-linear	0.972	0.946	0.970	0.962

The Freundlich isotherm model that defines adsorbent-adsorbate interaction forms multilayer and the adsorbent surface is heterogeneous having different energies of the energetic sites (Girish, 2017). According to this model, stronger reactive sites are filled first, and as reactive site efficacy increases, the binding potency decreases (Jeyaseelan Viswanathan, 2022). The model is mathematically expressed by using Equation 34 as follows:

$$logq_e = logK_f + \frac{1}{n}\, logC_e \tag{34}$$

Where K_f ((mg/g)(L/mg)^1/n) is a constant related with the adsorption capacity and n is an empirical parameter indicating the extent of adsorption. The value of 1/n describes whether the adsorption process is favorable, 1/n in the range of 0.1 – 0.5) or unfavorable, 1/n greater than 2 (Moirana *et al.*, 2023). In general, the value of 1/n less than 1 implies the adsorbent has high

affinity to the F^- ions. The values of n and K_f were calculated from slope and intercept, respectively, of the graph $logq_e$ vs $logC_e$ as given in Figure 42. The calculated values of n and K_f for pristine, Fe^{3+} ions doped, Bi^{3+} ions doped, and Bi^{3+} and Fe^{3+} ions co-doped HA nanomaterials are given in Table 8. The values of 1/n for all the nanomaterials are in the range of 1.0 – 1.5 for the linear fitting, and less than 1.0 for the non-linear fitting analysis. Which indicates that the Freundlich isotherm model is favorable for F^- ions adsorption on HA-based nanomaterials according to the non-linear approach. Similarly, the regression coefficient (R^2) and K_f values of pristine and doped HA nanomaterials are higher in the case of non-linear fitting compared to the linear fitting. Thus, in this case also the non-linear fitting is recommended for the F^- ions adsorption using HA-based nanomaterials.

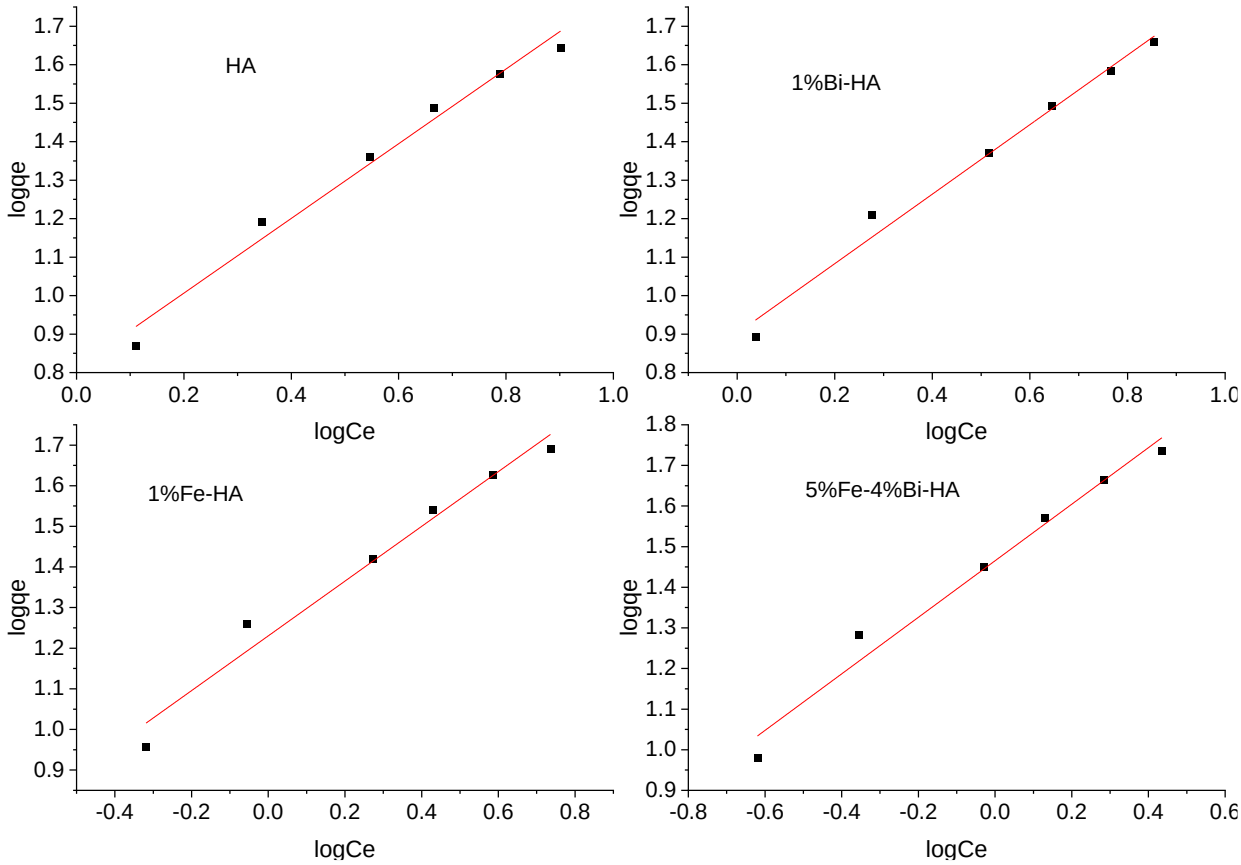

Figure 42. Linear Freundlich isotherm plots for F^- ions adsorption by pristine and doped HA nanomaterials

In the Temkin model, binding energies are uniformly distributed up to a maximum value, and the heat of adsorption of all molecules in the layer is assumed to drop linearly with coverage

at average concentrations (Edet Ifelebuegu, 2020). The model that reflects the persuaded heterogeneity due to the indirect adsorbate/adsorbent interaction is expressed using Equation 35:

$$q_e = B_T ln K_T + B_T ln C_e \quad (35)$$

Where, K_T (L/g) is the Temkin isotherm binding constant, and B_T (J/mg or J/mol.) is the constant related to the heat of sorption. The values of B_T and K_T were calculated from the slope and intercept, respectively, of the graph q_e vs lnC_e given in Figure 43. The intended values of the constants for the pristine and doped HA nanomaterials are given in Table 8.

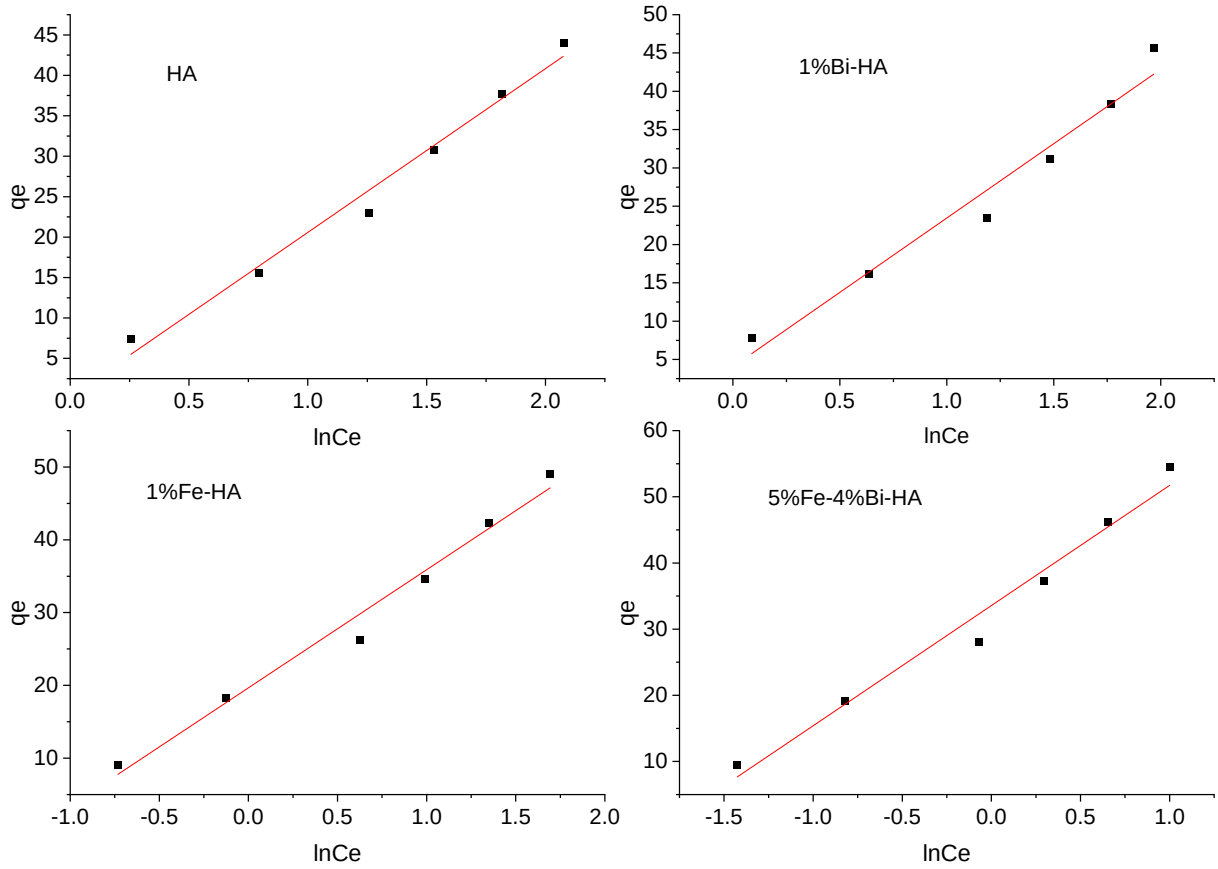

Figure 43. Linear Temkin isotherm plots for F^- ions adsorption by pristine and doped HA nanomaterials

Relatively large values of B_T for all the nanomaterials, and smaller values of R^2 compared to Langmuir and Freundlich models, indicate the non-favorability of the Temkin model to pronounce the investigational results of F^- ions sorption. In the Temkin isotherm model the values of K_T obtained from linear and non-linear fittings for all the nanomaterials are the same. However, the values of regression coefficient (R^2) were high in the linear fitting compared to

the non-linear fitting analysis, which was also observed in the Langmuir isotherm model. From the non-linear fitting graphs (Figure 44) of the three models for all the nanomaterials, and the data of R^2 from linear and non-linear fitting for Langmuir, Freundilch and Temkin, given in Table 8, it can be conclude that the Langmuir model better fits with the investigational results for all the nanomaterials.

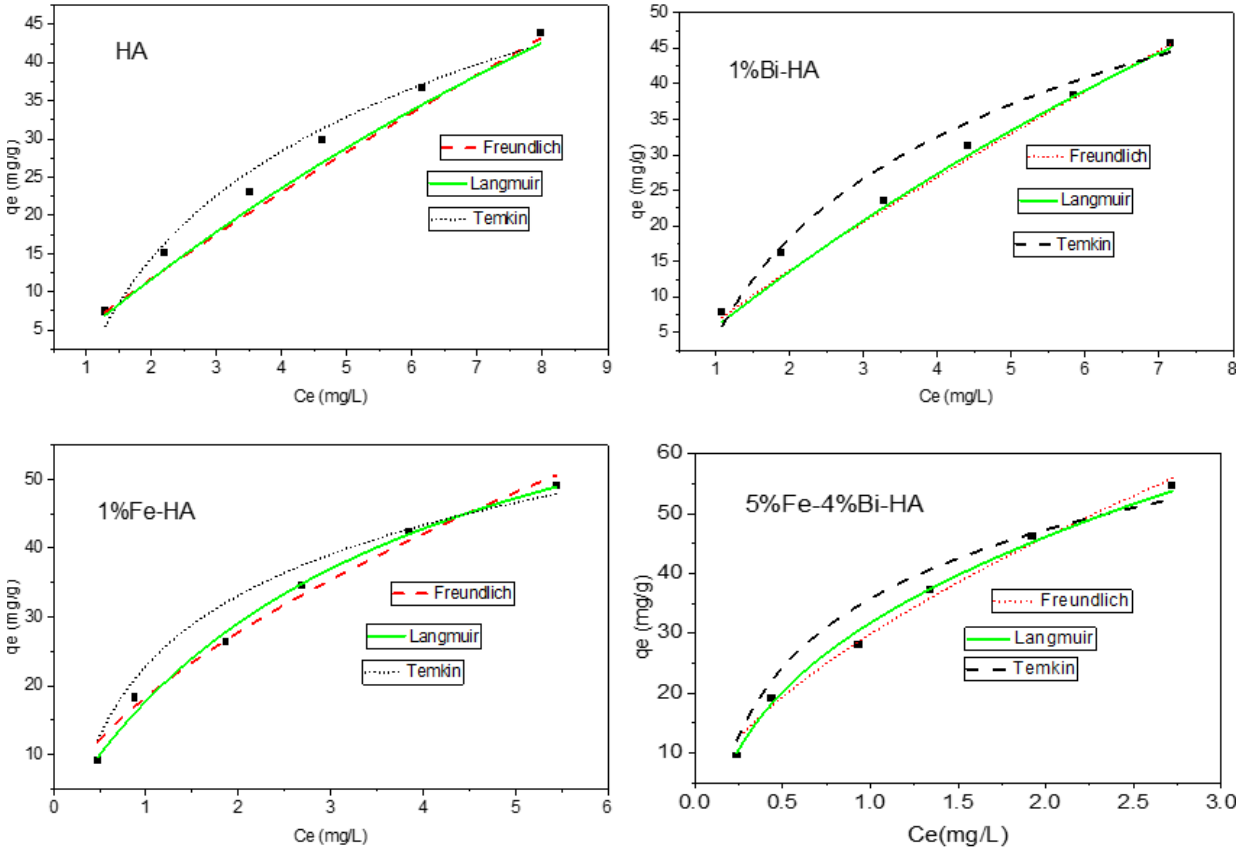

Figure 44. Non-linear fittings of isotherm models for F^- ions adsorption by pristine and doped HA nanomaterials

However, to determine the best isotherm adsorption model, comparing the R^2 values alone is insufficient and some other error functions, like chi-square (χ^2), mean square error (MSE), and root mean square error ($RMSE$) are also required (Benmessaoud *et al.*, 2020; Paranjape Sadgir, 2023; Yilmaz *et al.*, 2019), and expressed using, Equation 36, 37, and 38, respectively.

$$\chi 2 = \frac{\sum(q_{e\,exp} - q_{e\,cal})2}{q_{e\,cal}} \quad (36)$$

$$MSE = \frac{100}{n-2}\sum_{i=1}^{n}(q_{e\,exp} - q_{e\,cal})2 \quad (37)$$

$$RMSE = \sqrt{\frac{100}{n-2}\sum_{i=1}^{n}(q_{e\ exp} - q_{e\ cal})2} \quad (38)$$

Where,$q_{e\ exp}$ is the adsorption capacity obtained from the experiment, $q_{e\ cal}$ is the adsorption capacity obtained from the models, and n is the number of data points. Generally as the values of these error functions increases, the deviation from experimental and calculated value increased. The calculated values of $\chi 2$, MSE, and $RMSE$ for pristine and doped HA nanomaterials are given in Table 9. The results indicate that the Langmuir model has the lowest $\chi 2$, MSE, and $RMSE$ values for all the nanomaterials compared to the Freundlich and Temkin isotherm models. Thus, the Langmuir model has high contribution for F^- ions adsorption on the surface of HA-based synthesized nanomaterials. This implies that the sorption process is more of a monolayer on homogeneous surface for the pristine as well as doped HA nanomaterials (Chen *et al.*, 2018). Generally, the adsorption kinetics and isotherm studies showed that the adsorption capacity of the co-doped HA nanomaterial is higher than that of pristine and single-doped HA nanomaterials at similar conditions. This indicated that the adsorption site for F^- ions adsorption increased through doping of HA nanomaterial using Fe^{3+} and Bi^{3+} ions.

Table 9. Calculated values of error functions for pristine and doped HA nanomaterials

Models	Parameter	HA	1% Bi-HA	1% Fe-HA	5% Fe-4% Bi-HA
Langmuir	$\chi 2$	0.524	0.289	0.433	0.221
	MSE	1.220	0.669	1.317	0.356
	$RMSE$	1.104	0.818	1.148	0.596
Freundlich	$\chi 2$	0.805	0.389	0.888	0.401
	MSE	2.187	0.806	2.526	0.587
	$RMSE$	1.479	0.897	1.589	0.766
Temkin	$\chi 2$	1.124	1.620	0.791	0.626
	MSE	2.679	5.396	3.393	1.355
	$RMSE$	1.637	2.323	1.842	1.164

4.5.9 Thermodynamics of Adsorption

The adsorption process's spontaneity character, and applicability of the adsorbent are all determined using the thermodynamic parameters of enthalpy ($\Delta H°$), entropy ($\Delta S°$), and Gibbs

free energy ($\Delta G°$) (Edet Ifelebuegu, 2020). The thermodynamic parameters for the sorption of F^- ions on pristine as well as doped HA nanomaterials was studied by taking 10 mg/L of F^- ions, 2 g/L each of the nanomaterial, and temperatures of 25, 30, 40, 50, and 60 ^oC. It was observed that the removal efficiencies of the F^- ions of the nanomaterials increased with the temperature rise. As the temperature of the system increases, the free volume of the adsorbent increases due to the increasing movement of the molecules (Nayak *et al.*, 2017). Thermodynamic factors were calculated using Equations 39 – 42 (Lima *et al.*, 2019), to analyze the feasibility and spontaneity of the sorption process.

$$\Delta G° = \Delta H° - T\Delta S° \quad (39)$$

$$\Delta G° = -RTln(K_e) \quad (40)$$

$$ln(K_e) = -\frac{\Delta H°}{RT} + \frac{\Delta S°}{R} \quad (41)$$

$$K_e = \frac{1000.b.MW[F^0]}{\Upsilon} \quad (42)$$

Where, R is universal gas constant (8.314 $JK^{-1}mol^{-1}$), T is absolute temperature (K), K_e is the thermodynamics equilibrium constant, b is the Langmuir constant, MW is the molecular weight of F^- ions, $[F^0]$ is the standard concentration of F^- ions ($19x10^3$ mg/L) and Υ is the activity coefficient of F^- ions.

The values of $\Delta S°$ and $\Delta H°$ were obtained from the intercept and slope of $ln(K_e)$ vs 1/T graph (Figure 45). The thermodynamic constants for all the nanomaterials are summarized in Table 10. The negative values of Gibbs free energy change (ΔG°) for all the nanomaterials at the studied temperatures inferred that the sorption process was spontaneous. The positive value of enthalpy change (ΔH°) indicated that the process was endothermic. Which means energy was absorbed to break the linkage between the F^- ions and H_2O molecules in the solution.

Table 10. Thermodynamic parameters for pristine and doped HA nanomaterials

Adsorbents	ΔG^0 (kJ/mol.)					ΔH^0 (kJ/mol.)	ΔS^0 (kJ/mol.)	R^2
	298	303	313	323	333			
HA	-10.58	-12.47	-16.85	-18.88	-20.33	74.53	0.287	0.966
1%Bi-HA	-11.15	-13.20	-17.17	-18.81	-21.09	72.39	0.282	0.976
1%Fe-HA	-13.40	-14.71	-18-50	-19.88	-21.52	57.17	0.238	0.966
5%Fe-4%Bi-HA	-16.88	-18.41	-22.41	-24.55	-26.82	69.08	0.289	0.985

The positive value of entropy change (ΔS°) also confirmed the sorption process's spontaneity nature and the randomness (Affonso *et al.*, 2020; Tang *et al.*, 2018). Furthermore, the decreasing tendency of the values of ΔH° and ΔS° for the doped HA nanomaterials compared to the pristine HA nanomaterial indicates that F^- ions were more readily adsorbed on the surface of the modified HA nanomaterials than that of the pristine HA nanomaterial.

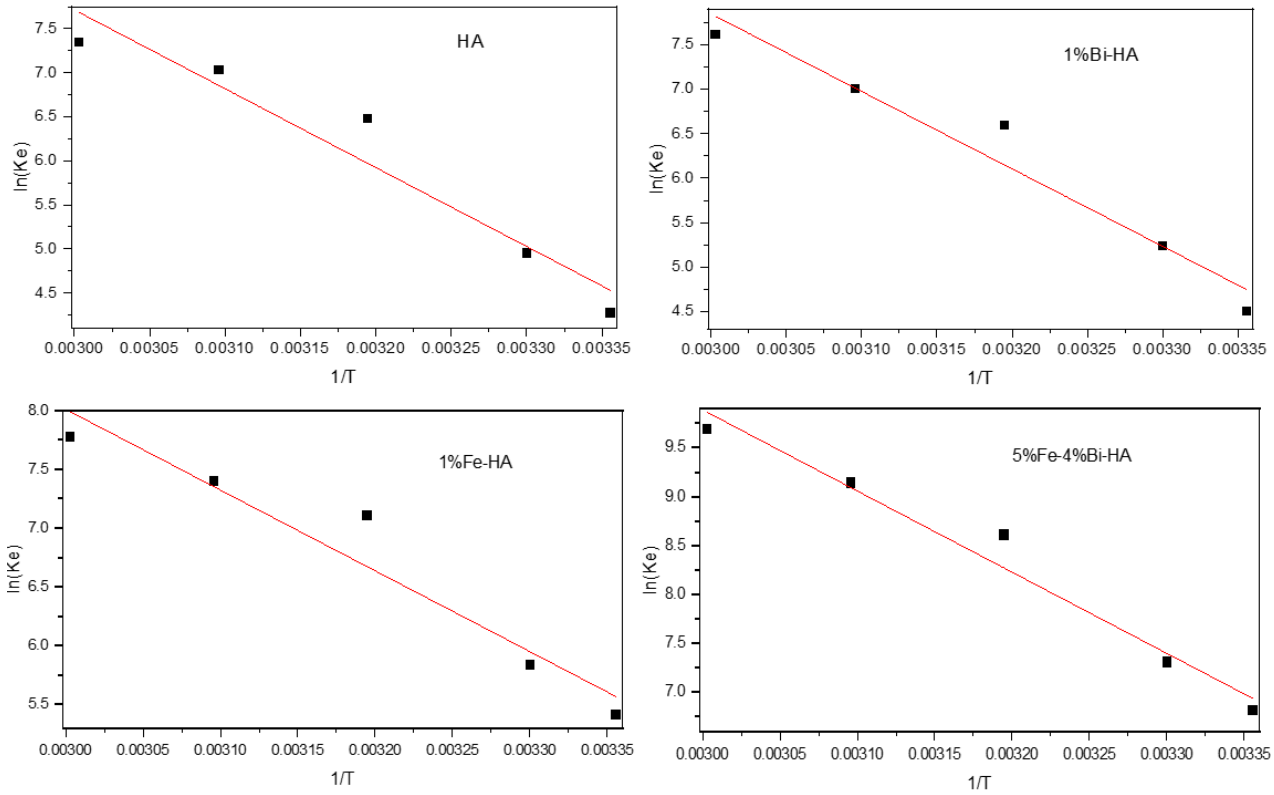

Figure 45. Van't Hoff plots for F^- ions adsorption by pristine and doped HA nanomaterials

4.5.10 Regeneration and Reusability of the Nanomaterials on Fluoride Ion Adsorption

Reusability is a crucial component of adsorption research since it shows how well the adsorbent is recovered, stability of the adsorbent, overcomes the disposal issue, and the cost effectiveness of the procedure (Mondal *et al.*, 2016; Nayak *et al.*, 2017; Sekar *et al.*, 2022). The F^- ions removal efficiencies of the synthesized HA-based nanomaterials were minimal in alkaline media, as observed during the study on the effect of pH (Section 4.5.2). For the regeneration and reusability investigation of the developed adsorbents, $40x10^3$ mg/L of NaOH solution was prepared and used, since previously a research group (Sekar *et al.*, 2022) reported high recovery

of the HA-based adsorbent using NaOH solution of the similar concentration. A mixture of 10 mg/L F^- ions and 2 g/L of each of the nanomaterial was shaken at room temperature for 3 hours at 150 rpm. Five successive adsorption-desorption cycles were done to examine the regeneration and recyclability of the nanomaterials.

The reusability results (Figure 46) showed that the F^- ions adsorption efficiencies of pristine and doped HA nanomaterials in the consecutive cycle were altered considerably. The decrease in adsorption percentage through the successive cycles may be due to the decreasing tendency of the adsorbent dose, since the mass of the adsorbent recovered after centrifugation decreased as the number of cycles increased, similar phenomenon was observed previously (He *et al.*, 2017). Other factors that make low adsorption efficiency of the adsorbent during reusability may be the type and concentration of the solvent used for regeneration. For instance, (Li X. *et al.*, 2021), obtained better reusability of the HA-based adsorbent by washing the F^- ions loaded sorbent with $8.3x10^3$ mg/L of $NaCO_3$ followed by $6.3x10^3$ mg/L HNO_3 solutions. On the other hand, a research report by (Jeyaseelan Viswanathan, 2022), showed high reusability of the HA-based adsorbent using $4x10^3$ mg/L of NaOH solution. Thus, stirring the adsorbent at high concentration of NaOH solution for a long period of time may deteriorate its identity.

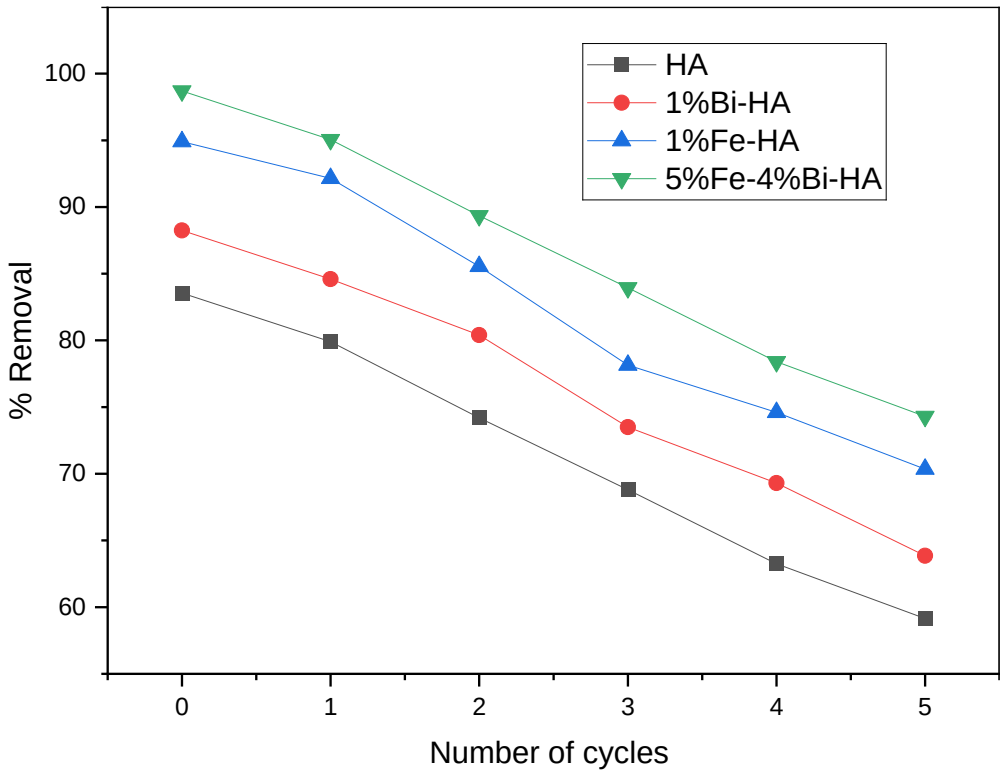

Figure 46. Reusability tests of pristine and doped HA nanomaterials for F^- ions adsorption

Compared to previous reports (Mondal *et al.*, 2016; Nagaraj *et al.*, 2018; Nayak *et al.*, 2017) on the recyclability of HA-based adsorbents for F^- ions adsorption, even in the fifth cycle, the F^- ions adsorption efficiencies of the doped HA nanomaterials used in this work have still higher values. Thus, Fe^{3+} and Bi^{3+} ions doped (especially the co-doped) HA nanomaterials show reusability nature, and the reusability can be further increased using suitable solvents of appropriate concentrations by careful regeneration of the adsorbent mass during centrifugations.

4.5.11 Mechanisms of Fluoride Ions Adsorption

Establishing the sorption mechanism is essential to understand the surface properties of an adsorbent (He *et al.*, 2017). To elucidate the mechanisms of F^- ions removal by pristine and doped HA nanomaterials, the FTIR spectra before and after sorption were compared as given in Figure 47. The spectrum of pristine HA nanomaterial showed a decrease in the intensity of the O-H stretching at 3693 cm^{-1} after F^- ions adsorption. This may be due to the partial replacement of OH^- ions by F^- ions (Chen *et al.*, 2018; He *et al.*, 2017; Nagaraj *et al.*, 2018). Similarly, the slight shift of the O-H stretching from 3427 cm^{-1} to 3416 cm^{-1} with increasing broadening may indicate the formation of the H…..F bond (Nayak *et al.*, 2017). A new band at 695 cm^{-1} (less intense) may be associated with forming the H….F bond or it may be the electrostatic interaction between Ca^{2+} ions and F^- ions (Khoudro *et al.*, 2023).

In the case of Fe^{3+} ions doped HA nanomaterial, the O-H peak shifted from 3433 to 3331 cm^{-1} with decreasing intensity and increasing broadness may be due to the formation of F-HA linkage as well as ion exchange between the F^- and OH^- ions (Nayak *et al.*, 2017). In addition, a new intense and sharp peak at 557 cm^{-1} may be associated with the linkage of negative F^- ions with the positive metal ions through complex formation (Arif *et al.*, 2018). The FTIR spectrum of Bi^{3+} ions doped HA nanomaterial also indicates the decrease in intensity of the O-H stretching at 3693 cm^{-1} after F^- ions adsorption, which may be due to partial replacement of OH^- by F^- ions. Similarly, the shift of the O-H stretching from 3389 cm^{-1} to 3431 cm^{-1} may indicate the formation of the H…..F bond. Moreover, almost all peaks for Bi^{3+} ions doped HA nanomaterials showed decrease in intensity after F^- ions adsorption, which indicates adsorption of F^- ions on the nanomaterial (Jeyaseelan Viswanathan, 2022).

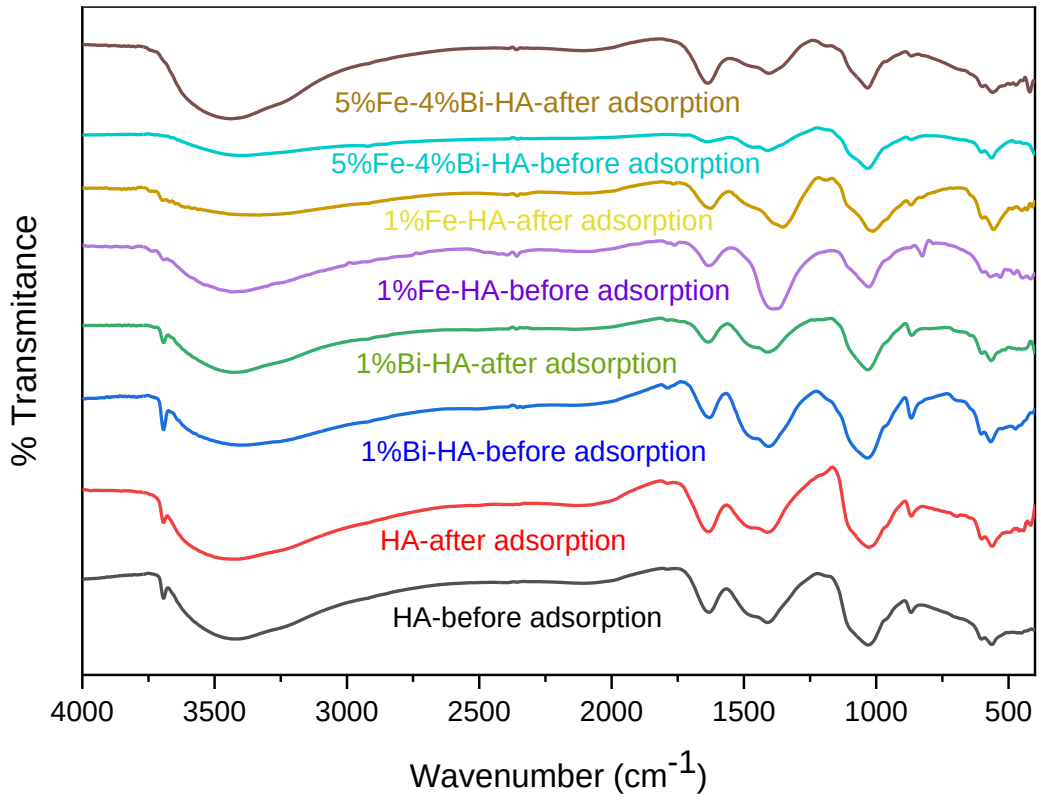

Figure 47. FTIR spectra of pristine and doped HA nanomaterials before and after F^- ions adsorption.

For the Bi^{3+} and Fe^{3+} ions co-doped HA nanomaterial, the FTIR spectra show a shift in the OH^- group (shifted from 3396 cm^{-1} to 3440 cm^{-1}), showing the presence of electrostatic/hydrogen bonding between the adsorbed water in the modified HA nanomaterial and F^- ions during the adsorption process (Nayak *et al.*, 2017). Moreover, the F^- ions loaded co-doped HA shows additional peaks at 420 cm^{-1} and 559 cm^{-1}, which might be associated with the formation of metal ions (Ca^{2+}, Fe^{3+} and Bi^{3+}) to F^- linkage through electrostatic interaction/complex formation (Arif *et al.*, 2018; Jayarathna *et al.*, 2015), or it may be the formation of H-F bonds (Andrews Johnson, 1984).

In general, the results of the FTIR spectra before and after adsorption, sorption affinity of F^- ions at different pH, the kinetics, adsorption isotherms, and thermodynamics data indicated that the probable governing mechanisms of sorption are electrostatic interaction/complexation on the surface of the nanomaterials, and ion exchange between the OH^- groups of the HA nanomaterials and F^- ions from the solution as given in Figure 48. However, from these

mechanisms of F^- ions removal by HA-based nanomaterials, the more dominant one is electrostatic interaction.

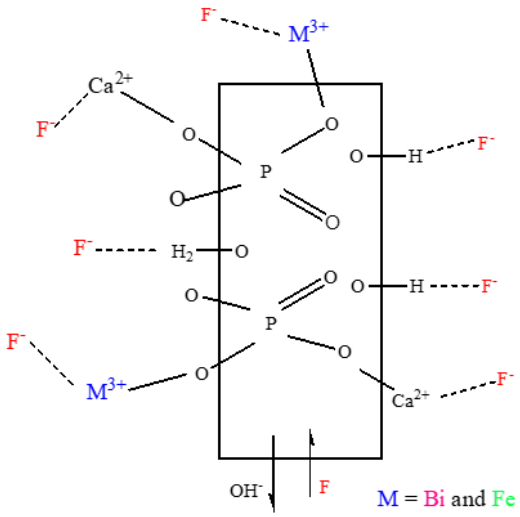

Figure 48. Possible F^- ions removal mechanisms by pristine and doped HA nanomaterials

4.6 Methyl Orange Dye Photocatalytic Degradation Performance of the Nanomaterials

4.6.1 Selection of the Photocatalyst

Before the analysis of the effect of different parameters, the HA-based nanomaterial that showed better MO photocatalytic degradation performance was identified by mixing 0.4 g/L of each of the nanomaterial with 5 mg/L MO dye at pH of 7, and irradiating the mixture for 45 minutes with continuous stirring at 600 rpm. After that, the nanomaterial was separated from the supernatant solution using centrifugation, and the absorbance of the solution was measured. The percentage degradation of MO dye using pristine and doped HA nanomaterials are given in Table 11. The result indicate that only 13.79 % of MO was degraded by the pristine HA nanomaterial after 45 minutes irradiation time. However, modification of HA nanomaterial using Bi^{3+} and Fe^{3+} ions enhanced MO dye removal efficiency. The poor MO dye removal performance of pristine HA nanomaterial may be related to its high bandgap energy besides to its high particle size, and less surface area. As already discussed in Section 4.1.3 pristine HA has light absorption in the UV region, mainly in the range of 200 – 270 nm wavelength. However, the light source used for this experiment was Halogen lamp, which generates light mostly in the visible range. Because of this HA gives poor degradation efficiency compared to the doped HA nanomaterials.

Table 11. MO dye photocatalytic degradation performance of the synthesized HA-based nanomaterials

Nanomaterials	1% Fe-HA	3% Fe-HA	5% Fe-HA	7% Fe-HA
% Degradation	18.75	20.91	23.06	35.99
Nanomaterials	1% Bi-HA	3% Bi-HA	5% Bi-HA	7% Bi-HA
% Degradation	27.58	30.17	32.76	36.85
Nanomaterials	3%Fe-6%Bi-HA	4%Fe-5%Bi-HA	5%Fe-4%Bi-HA	6%Fe-3%Bi-HA
% Degradation	39.22	42.24	48.92	66.81

The results also indicate that MO dye removal efficiency of Fe^{3+} ions doped, and Bi^{3+} ions doped HA nanomaterials increases with the increase of the respective metal ions incorporated into the HA structure, which agree with the literature (Hossain *et al.*, 2022). The increasing tendency of MO dye removal as the number of metal ions increased may be associated with decreasing bandgap energy, the high light harvesting capacity, and the increasing of positive charge of the nanomaterial for surface adsorption of MO dye, which implies that the particle size and pore volume have less effect on the photocatalytic degradation performance of HA-based nanomaterials synthesized in this work.

Fe can act as electron and hole traps and then promote the production of highly oxidizing species, including super-oxides and hydroxyl radicals (Mancuso *et al.*, 2020). Fe^{3+}, in particular, is thought to promote the Fenton reaction, which enhances photocatalytic activity by generating extremely potent hydroxyl radicals that act as oxidizers (Channei *et al.*, 2014). It has also been suggested that Fe^{3+} ions act as a means of scavenging photoelectrons (Laurier *et al.*, 2013). Similarly, the use of Bi^{3+} compounds as a photocatalyst has an advantages of: simple photo-generated electron-hole pair's separation due to the d^{10} electronic structure, the $6s^2$ orbital lone pair may cause structural disruptions by acting as a repulsive force on the bonding of its neighbors, and it enables photo-induced holes to migrate in the semiconductor's VB by reducing the bandgap through the orbital hybridization between O 2p and Bi 6s (Baaloudj *et al.*, 2022).

Furthermore, the results indicate that the co-doped HA samples have better MO dye removal efficiency than the pristine and single-doped HA nanomaterials. This may correspond to the high photocatalytic activity of Bi and Fe-containing compounds. The MO dye removal efficiency increased with the increase of Fe^{3+} amount in the co-doped HA nanomaterials. This may be related to the smaller size of the nanomaterials as Fe^{3+} amount increases, the high visible light absorption properties of Fe^{3+}, the decreasing tendency of the energy bandgap as Fe^{3+} increases, and may be the presence of Fenton reaction during the process.

The percentage of MO dye removed by adsorption on the HA nanomaterials surface was analyzed by stirring the mixture for 30 minutes in the dark, as already reported in earlier work (Shariffuddin *et al.*, 2013). Then absorbance was measured using a UV-Vis spectrophotometer. The results indicate that only 3.66, 4.25 and 9.48% MO was adsorbed by 7% Bi-HA, 7% Fe-HA and 6% Fe – 3% Bi-HA nanomaterials, respectively. The 6% Fe – 3% Bi-HA has been used for other parameter optimizations since it has the highest MO dye removal efficiency. Generally, the photocatalytic performance of a material depends on the electronic bandgap, surface area, light absorption capacity and morphology (Al-Ahmed *et al.*, 2020; Manoj *et al.*, 2019; Mohseni-Salehi *et al.*, 2018). Nanomaterials with rod-like structures show high photocatalytic degradation performance due to their high surface-to-volume ratio, which gives many active sites to interact with the pollutant molecules (Manoj *et al.*, 2019).

4.6.2 Parameter Effect Analysis for Photocatalytic Degradation

4.6.2.1 The Effect of pH

One factor that affects the photocatalytic degradation of dye molecules is the pH of the solution. The influence of pH on removing MO dye by co-doped HA nanomaterial was evaluated by taking 0.4 g/L of 6% Fe – 3% Bi-HA nanomaterial and 100 mL of 5 mg/L MO dye with pH of 3 , 5 , 7 , and 9. The MO solution's pH was adjusted by using NaOH and HCl solutions. In the acidic media (pH 3), the color of the MO dye was changed to deep red, which may be due to the protonation of MO dye. The nanomaterials and MO dye mixture were irradiated for 45 minutes with continuous stirring at 600 rpm. The photocatalyst was separated from the solution by repeated centrifugation, and the absorbance of the solution was measured using UV-Vis instrument. The results (Figure 49) show that pH has little effect on removing MO dye. The

percentage removal of MO dye at pH of 3, 5, 7, and 9 are 72.76, 72.65, 73.87, and 71.54%, respectively. This indicates that the removal of MO is relatively higher in the neutral medium (pH 7) than in acidic and alkaline conditions. The results agree with the literature on Congo red dye (one of the anionic azo dye) using Cu^{2+} ions doped-HA nanomaterial (Hossain *et al.*, 2022), and using non-HA nanoparticles such as ZnO and SnO_2 photocatalysts (Abbasi Hasanpour, 2017). The high degradation potential of the co-doped HA nanomaterial at the neutral condition may be due to the formation of different products of MO in acidic and basic media, as confirmed by the light absorption properties of the residual solutions especially at around 271 nm (characteristics of the benzene ring of the MO dye) (Liu *et al.*, 2016). In the acidic media MO may be protonated and became positively charged so that its adsorption on Bi^{3+} and Fe^{3+} ions co-doped HA (having positive surface charge at acidic medium) becomes poor, and degradation was lower. However, at the neutral condition the MO surface is negative and the photocatalyst surface is still positive (PZC > 8) hence adsorption will be enhanced, and degradation becomes high. In the alkaline condition, there may be a competition between the negatively charged OM dye and OH^- ions to be adsorbed on the photocatalyst surface, which decrease the degradation of the dye molecules.

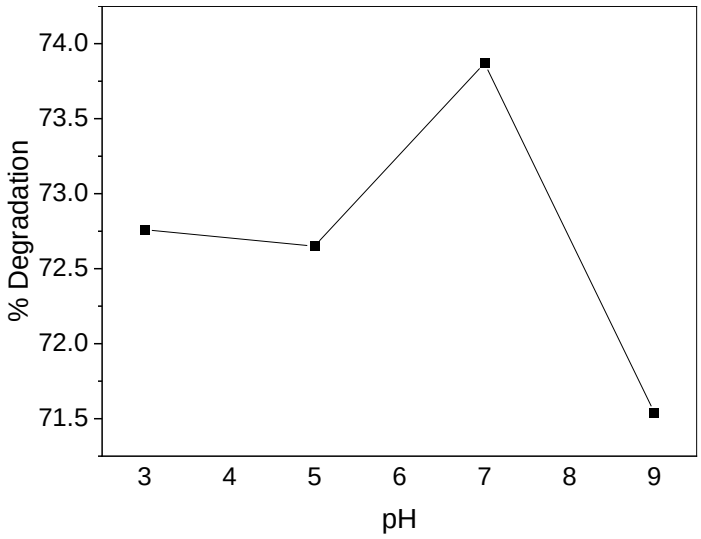

Figure 49. Effect of pH on photocatalytic degradation of MO dye using 6% Fe - 3% Bi-HA co-doped nanomaterial at 464 nm wavelength

4.6.2.2 The Effect of Methyl Orange Concentration

The photocatalytic degradation efficiency of a material is fundamentally influenced by a dye's initial concentration (Sheng *et al.*, 2011). Thus, the initial concentration effect on

photocatalytic degradation of MO was analyzed by taking MO concentrations of 5, 10, 15, and 20 mg/L, and dose of 6% Fe – 3% Bi-HA 0.4 g/L, at pH of 7. The mixture was irradiated for 45 minutes with continuous stirring at 600 rpm. The results (Figure 50) infer that the nanomaterial's photocatalytic degradation efficiency decreases as the MO concentration increases. The percentage removal of the MO decreased in the order of 73.0, 27.8, 11.4 and 4.6% as the concentration of MO became 5, 10, 15 and 20 mg/L, respectively. As the dye concentration rises, the effectiveness of photocatalytic degradation decreases. The high concentration of the dye molecule on the photocatalyst material's surface hinders the photocatalyst's light absorption capacity, while the formation of hydroxyl and superoxide radicals is almost constant due to fixed amount of photocatalyst, and the degradation rate becomes low (Azad Gajanan, 2017; Sheng *et al.*, 2011).

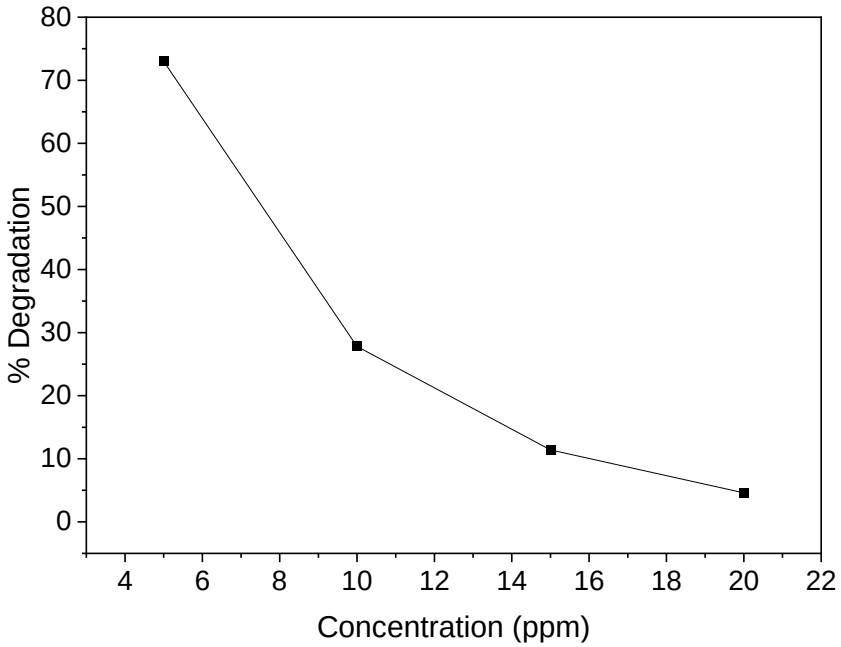

Figure 50. Effect of MO concentration on photocataytic degradation efficiency of 6% Fe - 3% Bi-HA co-doped HA nanomaterial at 464 nm wavelength

4.6.2.3 The Effect of Nanomaterial Amount

For the study of nanomaterials' amount influence on the photocatalytic degradation of MO dye by Bi^{3+} and Fe^{3+} ions co-doped HA nanomaterial, 0.3, 0.4, 0.5, and 0.6 g/L of 6% Fe – 3% Bi-HA were used. A mixture of the required amount of nanomaterial and 100 mL of 5 mg/L MO dye was irradiated for 45 minutes with continuous stirring at 600 rpm with pH of 7. The results (Figure 51) show that the removal percentage of MO dye increases as the amount of Bi^{3+} and

Fe^{3+} ions co-doped HA increases, similar trends were reported previously (Azad Gajanan, 2017; Modrogan *et al.*, 2021). The calculated degradation percentages of MO dye were 39.22, 71.48, 78.88 and 86.48% as the amount of the photocatalyst became 0.3, 0.4, 0.5 and 0.6 g/L, respectively. The increasing capacity of the MO dye removal by the co-doped HA nanomaterial as its amount increased indicates the increasing number of intermediate species (hydroxyl and/ superoxide radicals) formed during the process. Also the number of dye molecules that interact with the co-doped HA surface increases due to the increasing active sites of the catalyst as its amount increases.

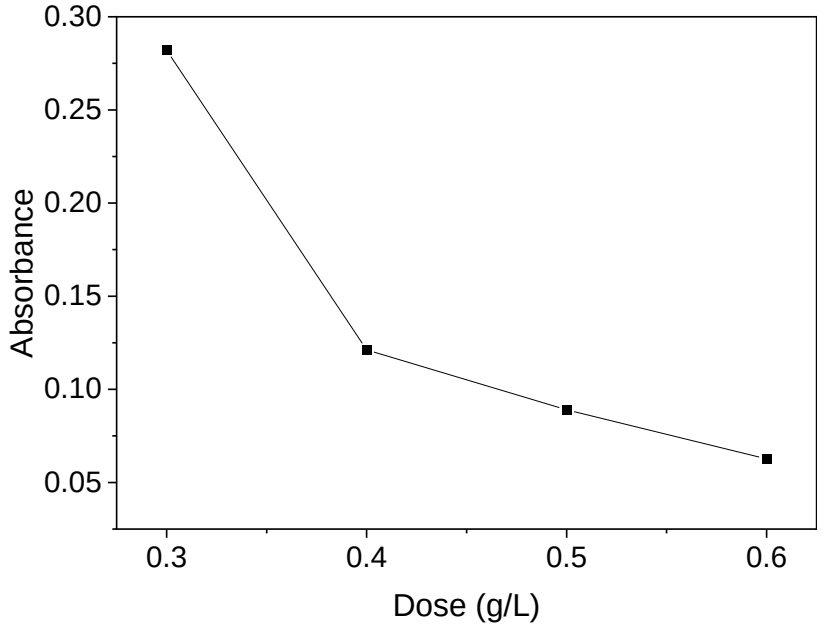

Figure 51. Effect of 6% Fe - 3% Bi-HA dose on the photocatalytic degradation of MO dye at 464 nm wavelength

4.6.2.4 The Effect of Irradiation Time and Kinetics Analysis

For the evaluation of the influence of irradiation time on MO dye photodegradation using the co-doped HA nanomaterial, 0.6 g/L of Bi^{3+} and Fe^{3+} ions co-doped HA was mixed with 100 mL of 5 mg/L MO, the mixture was first stirred for 30 min in the dark, and then irradiated up to 180 minutes with continuous stirring at 600 rpm. Samples were taken for every 20 minutes for absorbance determination. The results of time-dependent UV-Vis spectra of the photocatalytic degradation (Figure 52a), show that the maximum absorption peaks of MO dye at around 271 and 464 nm wavelength strongly decreased within a short irradiation time (40 minutes). This indicates that the rate of MO dye degradation using Bi^{3+} and Fe^{3+} ions co-doped HA as a photocatalyst material is very fast. As the irradiation period increased, it was found

that the dye's percentage of degradation increased. The photocatalytic degradation percentage became 98.57% at 180 minutes irradiation time. The result also indicated that Bi^{3+} and Fe^{3+} ions co-doped HA has better MO dye degradation potential than previous reports of modified HA photocatalysts (Liu *et al.*, 2018; Sheng *et al.*, 2011), using a visible light source (Halogen lamp), a relatively small amount of catalyst, and moderate irradiation time.

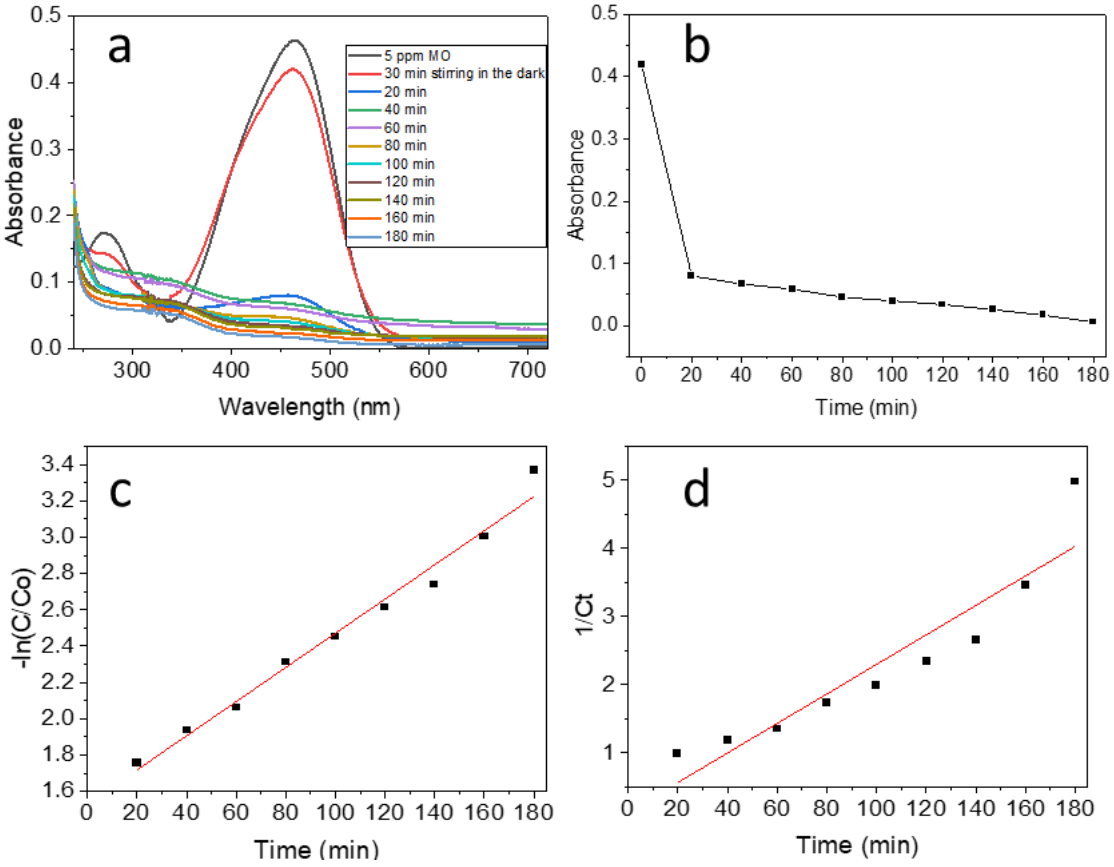

Figure 52. a) Time-dependent UV-Vis spectra, b) change in absorbance with time at 464 nm, and the degradation rates of first order c), and second order d), respectively for MO dye photocatalytic degradation by 6% Fe - 3% Bi-HA nanomaterial.

The rate of methyl orange photocatalytic degradation on Bi^{3+} and Fe^{3+} ions co-doped HA nanomaterial was analyzed using first and second order kinetic (Fatimah *et al.*, 2023; Mohseni-Salehi *et al.*, 2018), based on Equation 43 and 44, respectively.

$$-\ln\left(\frac{C_t}{C_o}\right) = k_1 t \tag{43}$$

$$\frac{1}{C_t} = k_2 t + \frac{1}{C_o} \tag{44}$$

Where C_o and C_t are the concentrations of MO dye at initial and at time t, respectively, k_1 and k_2 are the rate constants for first-order and second-order rate lows, respectively. The values of k_1 and k_2 were obtained from the slopes of $-\ln\left(\frac{C_t}{C_o}\right)$ vs t, and $\frac{1}{C_t}$ vs t plots given in Figure 52c, and d, respectively. The rate constant and regression coefficient (R^2) values for MO photocatalytic degradation using Bi^{3+} and Fe^{3+} ions co-doped HA nanomaterial as a photocatalyst are given in Table 12. The high regression coefficient value of first-order kinetics compared to second-order kinetics indicated that the photocatalytic degradation follows pseudo-first order rate law.

Table 12. Kinetics parameters of MO dye degradation

Kinetics	Rate constant	R^2
First-order	0.00942	0.991
Second-order	0.02166	0.870

4.6.2.5 Mechanism of Methyl Orange Degradation

To break down dye molecules, holes, electrons, and free radicals can all function as photocatalytic agents. When the catalyst interacts with the light source, electrons are excited from the valence band to the conduction band, creating holes; these holes have the potential to oxidize the adsorbed molecules. As the photocatalyst is still absorbing the photons, the delay in the recombination of e^- and h^+ produces more reactive species. The energy of the conduction band and valence band determines whether e^- and h^+ recombine (Hossain *et al.*, 2022). When the holes interact with the H_2O molecules adsorbed on the surface, hydroxyl radicals can be produced.

Additionally, the photogenerated electrons' reaction with oxygen reduces oxygen to superoxide radical anions. Afterward, the generated superoxide radical anions react with hydrogen ions to form hydroperoxyl radicals on the surface of the nanomaterial. MO dye then interacts with the potent oxidizing agents to create intermediates, CO_2, H_2O, and others (Mohseni-Salehi *et al.*, 2018). The possible photocatalytic degradation mechanism of Bi^{3+} and Fe^{3+} ions co-doped HA can be summarized according to the reactions in Equations 45 – 50 and Figure 53.

$$Ca_{10-(x+y)}Bi_xFe_y(PO_4)_6(OH)_2 \xrightarrow{h\nu} Ca_{10-(x+y)}Bi_xFe_y(PO_4)_6(OH)_2 + e^- + h^+ \quad (45)$$

$$e^- + h^+ + H_2O + O_2 \rightarrow \cdot O_2 + \cdot OH^- + \cdot O_2^- + H^+ + OH^- \quad (46)$$

$$\cdot OH^- + \cdot OH^- \rightarrow H_2O_2 \quad (47)$$

$$H_2O_2 + e^- + h^+ \rightarrow \cdot OH^- + \cdot OH \quad (48)$$

$$\cdot O_2^- + H^+ \rightarrow \cdot OOH \quad (49)$$

$$\cdot OH + \cdot O_2 + \cdot OH^- + \cdot O_2^- + \cdot OOH + e^- + h^+ + MO \rightarrow Intermediate + CO_2 + H_2O \quad (50)$$

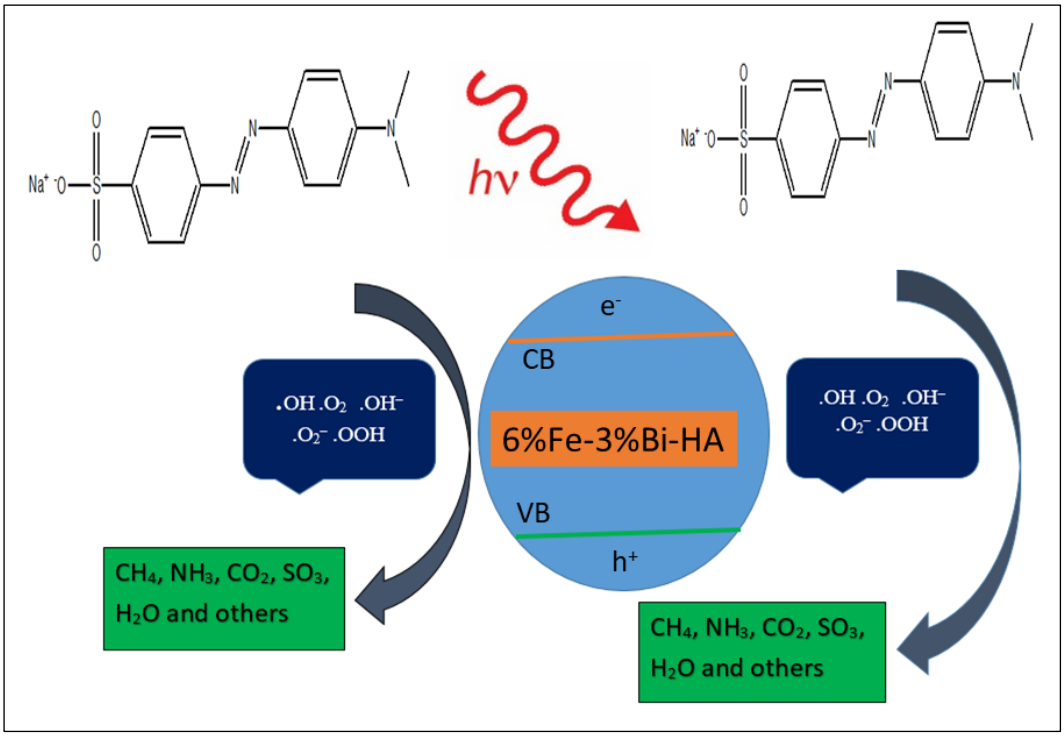

Figure 53. Photocatalytic degradation mechanisms of 6% Fe - 3% Bi- HA co-doped nanomaterial

4.7 Antibacterial Activity Analysis

4.7.1 The Qualitative Bactericidal Activity

Antibacterial activities of pristine as well as Fe^{3+} and Bi^{3+} ions doped (single and co-doped) HA nanomaterials were evaluated using a practical and low-cost approach, i.e., the disc diffusion method (Armijo *et al.*, 2020; Nie *et al.*, 2021). The analysis was done by taking 5, 10 and 20 mg/L of the nanomaterials' suspension in DMSO using serial dilution. The DMSO and Co-trimoxazole (Co-tri) were used as negative and positive controls, respectively, For the

pristine HA nanomaterial (Figure 54, and Table 13) no zone of inhibition was detected against both *E. coli* and *S. aureus* bacterial strains for all the concentrations used in the analysis, the results agree with the literature (Qiao *et al.*, 2019). This indicated that pristine HA synthesized in this work has no antibacterial activity. The absence of a zone of inhibition for DMSO (used as a solvent and negative control) indicated that it did not interfere with the antibacterial activity of the nanomaterials.

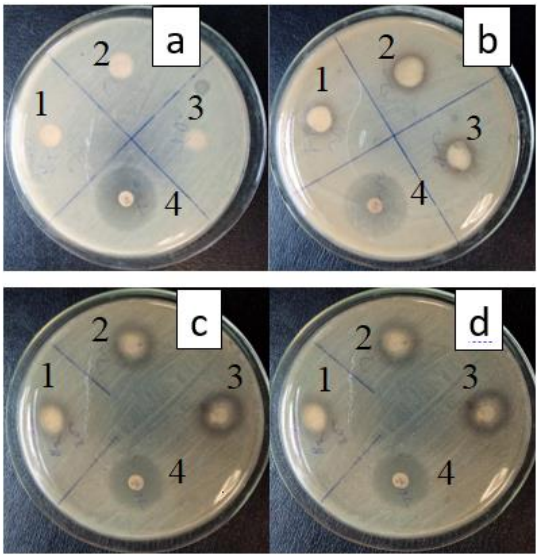

Figure 54. Images of zones of inhibition a) pristine, b) Bi^{3+} ions doped, c) Fe^{3+} ions doped, and d) Bi^{3+} and Fe^{3+} ions co-doped HA nanomaterials against S. aureus bacteria: 1, 2, 3,, and 4 represent 5 mg/L, 10 mg/L, 20 mg/L of the nanomaterials, and co-tri, respectively.

Table 13. Antibacterial activity of pristine HA against *E. coli* and *S. aureus* bacteria

Sample code	Bacterial strain	Zone of inhibition in mm (mean $\pm$ standard deviation) for different concentration (mg/L) of nanomaterial				
HA		5	10	20	Co-tri (+ve)	DMSO (-ve)
	E. coli	-	-	-	22.5 ± 0.2	-
	S. aureus	-	-	-	24.7 ± 0.3	-

The observed zone of inhibition for Fe^{3+} ions doped HA nanomaterials (Table 14) was 6.3 – 13.1 mm range. The smallest zone of inhibition (6.3 mm) was observed for *E. coli* bacteria using sample 1% Fe-HA at the nanomaterial concentration of 20 mg/L, and the largest zone of

inhibition (13.1 mm) was observed for *S.aureus* bacteria using sample 7% Fe-HA at the concentration of 20 mg/L.

Table 14. Antibacterial activity of Fe^{3+} ions doped HA nanomaterials against *E. coli* and *S. aureus* bacteria

Sample code	Bacterial strain	Zone of inhibition in mm (mean ± standard deviation) for different concentration (mg/L) of the nanomaterials			
		5	10	20	Co-tri
1% Fe-HA	*E. coli*	-	-	6.3 ± 0.1	22.6 ± 0.2
	S. aureus	-	6.4 ± 0.1	6.6 ± 0.2	24.5 ± 0.2
3% Fe-HA	*E. coli*	6.6 ± 0.1	7.1 ± 0.2	7.7 ± 0.2	22.7 ± 0.1
	S. aureus	6.9 ± 0.1	7.5 ± 0.3	8.2 ± 0.1	24.8 ± 0.3
5% Fe-HA	*E. coli*	8.6 ± 0.2	9.3 ± 0.1	10.1 ± 0.2	22.4 ± 0.2
	S. aureus	9.2 ± 0.2	9.9 ± 0.2	10.5 ± 0.2	24.6 ± 0.2
7% Fe-HA	*E. coli*	10.8 ± 0.3	11.4 ± 0.3	11.8 ± 0.1	22.7 ± 0.1
	S. aureus	11.6 ± 0.2	12.2 ± 0.3	13.1 ± 0.3	24.7 ± 0.2

The result also show an increase in the zone of inhibition with increasing amounts of Fe^{3+} ions added as dopants and the concentration of the nanomaterials against the two bacterial strains. This showed that both the concentration of the nanomaterials and the amount of Fe^{3+} ions incorporated into the HA structure influenced the antibacterial activity. In addition, Fe^{3+} ions doped HA nanomaterials have better antibacterial activity againest *S. aureus* than *E.coli*. The results are consistent with the literature on HA doped with Fe^{3+} ions (Sheikh *et al.*, 2018) and other metal ions such as Ag^{+}, Cu^{2+}, Mg^{2+}, Sr^{2+}, and Zn^{2+} (Huang S.-M. *et al.*, 2022; Qiao *et al.*, 2019). This is because the *E. coli* cell wall structure is more complicated than the *S. aureus* one. Gram-positive bacteria are comprise a much thicker peptidoglycan layer, and gram-negative bacteria are bounded by a cytoplasmic membrane (thick lipopolysaccharide layer) and an outer cell membrane, and have a thin layer of peptidoglycan between the two membranes

(Vitta *et al.*, 2020). The presence of an outer membrane in *E. coli* may prevent the easy interaction of the Fe^{3+} ions doped HA nanomaterials with the bacterial cell (Sheikh *et al.*, 2018).

According to the the report given by (Ouchari *et al.*, 2019) antibacterial activity of the material can be classified in to four regions based on the diameter of inhibtion zone: < 5 mm no activity, 5-10 mm medium, 10-20 mm strong, and > 20 mm very strong. Based on this clasification, 1% Fe-HA HA had no response on both bacterial strains at 5 mg/L, but the response became medium for *S. aureus* bacteria at 10 and 20 mg/L concentrations and for *E. coli* at 20 mg/L concentration. That of 3% Fe-HA nanomaterial was under the category of medium for both bacterial strains in all the concentrations used in the study. Similarly, the 5% Fe-HA was in the classification of medium for the concentrations of 5 and 10 mg/L, but it became strong at the high concentration (20 mg/L) for both bacterial strains. That of 7% Fe-HA was in the range of strong in all concentrations for bacterial strains, and it can be used as an antibacterial agent.

Similar to Fe^{3+} ions doped HA nanomaterials, Bi^{3+} ions doped HA nanomaterials (Table 15), also indicate that the zone of inhibitions increases with both the concentration of the nanomaterials and the amount of Bi^{3+} ions incorporated in the HA structure. The sample that contains the lowest amount of Bi^{3+} ions (1% Bi-HA) shows no zone of inhibition against both gram-negative *E. coli* and gram-positive *S. aureus* bacterial strains for all the nanomaterial concentrations used in the study. However, samples from 3% Bi-HA to 7% Bi-HA show a zone of inhibitions in the 6.1 – 11.2 mm range. The smallest zone of inhibition (6.1 mm) was observed against *S. aureus* bacteria using 3% Bi-HA at 5 mg/L concentration, and the largest zone of inhibition 11.2 mm was observed against *E. coli* bacteria using 7% Bi-HA at 20 mg/L nanomaterial concentration.

This indicated that the antibacterial activity of Bi^{3+} ions doped HA nanomaterials are effective against *E.coli* bacteria than *S. aureus* bacteria, which contradicts with the results observed on Fe^{3+} ions doped HA nanomaterials. This difference may come from the binding abilities of the metal ions with specific proteins and enzymes of the bacterial strains (Claudel *et al.*, 2020). According to previous report (Duffin *et al.*, 2020), Bi can operate to lower intracellular ATP levels and collapse the membrane potential of *E. coli*. Based on the response classification, 1% Bi-HA had no response in all the concentrations for both bacteria. That of 3% Bi-HA and 5% Bi-HA showed medium response for both bacteria in all concentrations, but 7% Bi-HA had

strong response for *E. coli* in all concentrations, and for *S. aureus* bacteria it showed medium response at 5 and 10 mg/L, and strong response at 20 mg/L. This showed that both the concentration of the nanomaterials as well as the amount of Bi^{3+} ions incorporated into the HA structure influenced the antibacterial activity.

Table 15. Antibacterial activity of Bi^{3+} ions doped HA nanomaterials against *E. coli* and *S. aureus* bacteria

Sample code	Bacterial strain	Zone of inhibition in mm (mean ± standard deviation) for different concentration (mg/L) of the nanomaterials			
		5	10	20	Co-tri
1% Bi-HA	*E. coli*	-	-	-	22.6 ± 0.4
	S. aureus	-	-	-	24.8 ± 0.3
3% Bi-HA	*E. coli*	6.2 ± 0.1	6.7 ± 0.1	7.3 ± 0.1	22.9 ± 0.2
	S. aureus	6.1 ± 0.1	6.3 ± 0.2	6.6 ± 0.2	24.5 ± 0.2
5% Bi-HA	*E. coli*	8.1 ± 0.2	8.9 ± 0.1	9.7 ± 0.2	22.8 ± 0.3
	S. aureus	7.2 ± 0.3	8.3 ± 0.2	9.1 ± 0.3	24.7 ± 0.1
7% Bi-HA	*E. coli*	9.9 ± 0.2	10.7 ± 0.1	11.2 ± 0.1	22.5 ± 0.2
	S. aureus	9.3 ± 0.1	9.8 ± 0.2	10.7 ± 0.1	24.6 ± 0.2

In general, the antibacterial activity of HA was enhanced due to the presence of Bi^{3+} ions in the apatite lattice. This may be due to the better solubility of Bi^{3+} ions doped HA as compared to the pristine HA reported earlier (Ciobanu Harja, 2019), and observed during the experiment. A sufficient amount of Bi^{3+} ions inhibits bacterial growth and may damage the bacterial cells. Numerous mechanisms of action that are likely to work have been reported for Bi^{3+} ions doped HA. It involves blocking the function of the cell membrane by attaching complexes of Bi^{3+} ions doped HA to the cell membrane, resulting in plasmolysis (the separation of the bacterial cytoplasm from the bacterial cell wall), and the strong interaction with sulfur and phosphorus-containing compounds found in the bacterial DNA, proteins, and outer membrane proteins, affecting the respiratory chain reaction. The mechanisms prevent the formation of cell walls, adenosine triphosphate (ATP) synthesis, and several *Helicobacter*-produced enzymes, including urease, catalase, and lipase, and finally cell death .

Compared to Fe^{3+} ions doped HA nanomaterials, Bi^{3+} ions doped HA nanomaterials show low antibacterial activity against both bacterial strains. This may be due to the lower ionic size of Fe^{3+} ions, which enables free entry and exit in the bacterial cells, reducing the resistance of the bacteria and finally eliminating the formation of cell walls (Huang S.-M. *et al.*, 2022). Alternatively, the potential causes high bactericidal activity of Fe^{3+} ions doped HA nanomaterials could be the presence of Fenton reaction. The Fe^{3+} ions may react with O_2 and produce H_2O_2, then H_2O_2 reacts with Fe^{3+} ions to generate OH radicals. The OH radicals damage biological macromolecules. The other factor that may work in conjunction with this is the greater penetrating power of nanoparticles of smaller sizes, which ultimately results in a more effective breakdown of the cell membrane (Sheikh *et al.*, 2018). As observed in XRD and FE-SEM results, Fe^{3+} ions doped HA nanomaterials are smaller in size than Bi^{3+} ions doped HA nanomaterials.

In the case of Bi^{3+} and Fe^{3+} ions co-doped HA nanomaterials, like that of the single-doped HA nanomaterials, the zone of inhibition (Table 16) show an increment with the increasing amount of the nanomaterials. This may be due to the increasing metal ions released from the nanomaterials.

Table 16. Antibacterial activity of Bi^{3+} and Fe^{3+} ions co-doped HA nanomaterials against *E. coli* and *S. aureus* bacteria

Sample code	Bacterial strain	Zone of inhibition in mm (mean ± standard deviation) for different concentration (mg/L) of the nanomaterials			
		5	10	20	Co-tri
3% Fe – 6% Bi-HA	*E. coli*	11.8 ± 0.2	12.5 ± 0.3	13.1 ± 0.2	22.7 ± 0.2
	S. aureus	12.2 ± 0.1	12.9 ± 0.1	13.6 ± 0.3	24.6 ± 0.3
4% Fe – 5% Bi-HA	*E. coli*	13.8 ± 0.1	14.3 ± 0.2	14.9 ± 0.1	22.5 ± 0.2
	S. aureus	14.1 ± 0.2	14.5 ± 0.3	14.9 ± 0.2	24.7 ± 0.1
5% Fe – 4% Bi-HA	*E. coli*	15.2 ± 0.3	15.8 ± 0.3	16.7 ± 0.1	22.6 ± 0.1
	S. aureus	15.8 ± 0.1	16.5 ± 0.2	17.1 ± 0.2	24.9 ± 0.2
6% Fe – 3% Bi-HA	*E. coli*	17.0 ± 0.1	17.5 ± 0.1	18.3 ± 0.3	22.7 ± 0.2
	S. aureus	17.4 ± 0.1	17.9 ± 0.2	18.6 ± 0.2	24.8 ± 0.3

Compared to Fe^{3+} ions and Bi^{3+} ions single-doped HA nanomaterials, the co-doped HA nanomaterials show larger zones of inhibition against both *S. aureus* and *E.coli* bacterial strains. All the co-doped HA nanomaterials are under the classification of strong response for both bacteria at all concentrations, because of this they can be recommended as an antibacterial agent. The high antibacterial activity of the co-doped nanomaterials may correspond to the synergetic effect (the releasing of both Bi^{3+} and Fe^{3+} ions at a time from the sample) of the two metal ions (Shokri *et al.*, 2022).

The smallest zone of inhibition (11.8 mm) was observed against *E.coli* bacteria using 3% Fe – 6% Bi-HA at the lowest concentration of the nanomaterial (5 mg/L). Whereas, the largest zone of inhibition (18.6 mm) was observed for *S. aureus* bacteria using 6% Fe – 3% Bi-HA at 20 mg/L concentration. As the amount of Fe^{3+} ions in the dopant percentage increased in the co-doped HA structure, the zone of inhibition increased against both *E.coli* and *S. aureus* bacterial strains. This may be due to the decreasing size of the nanomaterials with the increasing Fe^{3+} ions amount as determined by XRD and observed in FE-SEM analysis. Or, it may also be associated with the smaller size of Fe^{3+} ions that help easy entry and exit in the bacterial cells (Huang S.-M. *et al.*, 2022).

There are two thoughts regarding the mechanism of antibacterial activity of metal-containing nanomaterials: on one side, the antibacterial activity happens through direct interaction between nanoparticles and the bacteria; on the other hand, studies point out that the release of metal ions from nanomaterials after their dissolution is responsible (Yuan *et al.*, 2018). The interactions of the nanoparticle or the released metal ions with the active sites of the bacteria (S and P containing proteins, DNA, RNA, and enzymes) comprise the generation of reactive oxygen species such as hydrogen peroxide, superoxide anions and hydroxyl radicals. These chemically reactive species create oxidative stress in the cellular membrane and cause cell walls to fall out and leak intracellular substances (Das *et al.*, 2020; Vitta *et al.*, 2020).

In general, the zone of inhibition results obtained for Fe^{3+} and Bi^{3+} ions single-doped HA nanomaterials are lower than the inhibition zone of the positive control (co-tri) used in this study for both bacterial strains. However, in the case of co-doped HA nanomaterials, zone of inhibitions are relatively close to the positive control compared to the single-doped HA nanomaterials. The inhibition zone results obtained for Fe^{3+} and Bi^{3+} ions single-doped HA

nanomaterials are comparable to previous works on Mg^{2+}, Zn^{2+} and Sm^{3+} single-doped HA nanomaterials (Alioui *et al.*, 2019; Iconaru *et al.*, 2020). But, inhibition zones of Bi^{3+} and Fe^{3+} co-doped HA nanomaterials are better than the reports on Ma^{2+} and Zn^{2+} co-doped HA nanopowders (Alioui *et al.*, 2019).

4.7.2 The MIC and MBC Analysis

The MIC test typically measures the lowest amount of an antibiotic that can prevent bacteria from growing. Meanwhile, the lowest material concentration required to kill the bacteria is considered as MBC (Owuama, 2017). In this study, the MIC and MBC were determined only for samples showing the highest inhibition zone from each class of HA-based nanomaterials, and the results are summarized in Table 17. The results indicated that the co-doped sample has the lowest MIC and MBC values compared to the single-doped HA nanomaterials. Which correspond to the synergistic role of Bi^{3+} and Fe^{3+} ions in the co-doped HA nanomaterials. It also showed that *S. aureus* bacteria was more susceptible to Fe^{3+} ions doped HA than Bi^{3+} ions doped HA nanomaterial. However, the reverse was observed for *E. coli* bacteria.

Table 17. MIC and MBC values for Fe^{3+} and Bi^{3+} ions doped (single and co-doped) HA nanomaterials

	E.coli		*S. aureus*	
	MIC (μg/L)	MBC (μg/L)	MIC (μg/L)	MBC (μg/L)
7% Bi-HA	148.5	165.0	175.25	215.0
7% Fe-HA	124.25	135.5	115.25	165.25
6% Fe – 3% Bi-HA	85.25	105.5	75.5	95.6

This may correspond to the structural difference between gram-negative and gram-positive bacterial strains. Gram-positive bacteria comprise a much thicker peptidoglycan layer, and gram-negative bacteria are bounded by a cytoplasmic membrane (thick lipopolysaccharide layer) and an outer cell membrane and have a thin layer of peptidoglycan between the two membranes (Vitta *et al.*, 2020). This indicates that Fe^{3+} ions strongly interact with the peptidoglycan layer while Bi^{3+} ions interacts with the outer cell membrane of the bacteria. The MIC values of Fe^{3+} and Bi^{3+} ions doped HA nanomaterials are comparable to the values

reported previously on Ag^{+} ions doped HA nanomaterials (Chen *et al.*, 2019; Wilcock *et al.*, 2017).

5 CONCLUSION AND RECOMMENDATION

5.1 Conclusions

Currently, synthesis of nanomaterials having interdisciplinary application is the concern of researchers. Pristine, Fe^{3+} ions doped Bi^{3+} ions doped, and Bi^{3+} and Fe^{3+} ions co-doped HA nanomaterials were successfully synthesized by the co-precipitation technique. The synthesized nanomaterials were characterized by XRD, FTIR, SEM, FE-SEM, HR-TEM, EDS, XPS, BET, and UV-Vis/DRS techniques. The synthesized and characterized nanomaterials were applied for F – ions removal, MO dye photocatalytic degradation, and antibacterial activity against *S. aureus* and *E. coli* bacteria. The effects of pH, temperature, interaction time, adsorbent dose, F^{-} ions concentration, desorption, and re-usability were studied during the F^{-} ions absorption study. The F^{-} ions sorption mechanism was predicted from FTIR results and the data obtained from kinetics, isotherm, pH, and thermodynamics. Similarly, the effect of irradiation time, concentration of MO, pH, and catalytic dose were evaluated during MO degradation analysis. Moreover, the inhibition zone at different concentrations of the synthesized nanomaterials, minimum inhibitory MIC, and MBC were determined using disc diffusion and the dilution method, respectively for both *S. aureus* and *E. coli* bacterial strains.

Doping of Bi^{3+} and Fe^{3+} ions in the HA nanostructure resulted structural distortion, change in mrphology, light absorption properties, Ca/P ratio, and surface properties. All these change indicates that the dopant ions having different ionic radii than Ca^{2+} ions are successfully inserted in the HA lattice. The batch F^{-} ions adsorption depends on the type of HA-based synthesized nanomaterials, and laboratory conditions. The adsorption followed pseudo-second order kinetics and Langmuir isotherm models. This indicated that the F^{-} ions adsorption process is chemisorption by forming a monolayer through a homogeneous surface. Linear and non-linear fitting analysis of F^{-} ions adsorption suggested that linearization leads biased result. Adsorption capacity of the co-doped HA nanomaterial is higher than the pristine, single-doped,

and most of the HA-based materials reported so far (Table 1). This may be associated with the presence of sufficient amounts of active sites to interact with F^- ions, and the high surface area with a minimum size of the co-doped HA nanomaterial. The FTIR spectra of F^- ions loaded adsorbents showed changes in peak position and intensity, and the formation of new peaks. This suggests that adsorption could occur by hydrogen bonding and/or complexation between F^- ions and cations on the surface, and by ion exchange between OH^- ions and F^- ions.

Similarly, the photocatalytic degradation of MO strongly influenced by the type of dopant, and the change in environmental condition during the analysis. The decolourization of MO dye using Bi^{3+} and Fe^{3+} ions co-doped HA nanomaterial indicated that the percentage removal of the dye was affected by presence of light, catalyst dose, initial concentration of MO, and irradiation time. Photodegradation of the MO dye in the presence of Bi^{3+} and Fe^{3+} ions co-doped HA follows pseudo-first order rate law having comparable degradation efficiency with TiO_2-modified HA materials reported so far, may be due to its high visible light absorption capacity, low bandgap energy, and high surface area.

Likewise, doping of HA nanomaterial using Bi^{3+} and Fe^{3+} ions have different antibacterial activities against *S. aureus* and *E. coli* bacteria. This may be associated with the difference in cell wall structure of gram-negative and gram-positive bacteria, and the different mechanisms of action of Bi^{3+} and Fe^{3+} ions against the two different bacterial strains. The zone of inhibition and bactericidal activities of the co-doped HA nanomaterials are better than singl-doped HA nanomaterials which may be due to the synergistic effects of Bi^{3+} and Fe^{3+} ions.

Generally, Fe^{3+} and Bi^{3+} ions doped HA nanomaterial can be considered as an efficient and valuable material for the removal of F^- ions, MO dye, and antibacterial agent because of its biocompatibility, renewability, reusability, low cost, better sorption capacity, high photocatalytic performance, and bactericidal activity.

5.2 Recommendations

Due to the limited time and resources, this work does not include analysis of natural wastewater for F^- ions adsorption and dye degradation. Thus, it is recommended that the effect of the matrix

in the natural wastewater system be studied to fully conclude and scale up the applications of Bi^{3+} ions and Fe^{3+} ions doped HA nanomaterials for F^{-} ions adsorption and dye photocatalytic degradation. The work focused only on the batch adsorption experiments of F^{-} ions on the surface of the nanomaterial; thus, column adsorption experiments must be checked to use the HA nanomaterials for further use. For the complete understanding of the Bi^{3+} and Fe^{3+} ions-doping and the F^{-} ions removal mechanisms, computational studies are recommended in future work. During the photocatalytic experiments, regeneration and reusability tests are not studied, this should be included to conclude the economic feasibility of Bi^{3+} and Fe^{3+} ions-doped HA nanomaterials for photocatalytic degradation application. This work also covers only the *in vitro* antibacterial activity of the nanomaterials. Hence, it is necessary to check the *in vivo* antibacterial activity and the cytotoxicity of the nanomaterials for the intended use. The ion release capacity in different conditions must be studied further to use Bi^{3+} and Fe^{3+} ions doped HA nanomaterials for different applications.

6 REFERENCES

Abbasi, S.and Hasanpour, M. (2017). The effect of pH on the photocatalytic degradation of methyl orange using decorated ZnO nanoparticles with SnO_2 nanoparticles. *Journal of materials science: Materials in electronics, 28*, 1307-1314.

Adamiano, A., *et al.* (2017). Biomineralization of a titanium-modified hydroxyapatite semiconductor on conductive wool fibers. *Journal of Materials Chemistry B, 5*(36), 7608-7621.

Adeogun, A. I., *et al.* (2018). Biowaste-derived hydroxyapatite for effective removal of reactive yellow 4 dye: equilibrium, kinetic, and thermodynamic studies. *American Chemical Society omega, 3*(2), 1991-2000.

Affonso, L. N., *et al.* (2020). Removal of fluoride from fertilizer industry effluent using carbon nanotubes stabilized in chitosan sponge. *Journal of Hazardous Materials, 388*, 122042.

Agbeboh, N., *et al.* (2020). Environmentally sustainable processes for the synthesis of hydroxyapatite. *Heliyon, 6*(4).

Ahmed, S., *et al.* (2017). Dopant ion concentration and calcination temperature dependent crystallographic behaviour of fluoride and iron doped hydroxyapatite. *Transactions of the Indian Ceramic Society, 76*(4), 215-221.

Ajiboye, T. O., *et al.* (2021). The performance of bismuth-based compounds in photocatalytic applications. *Surfaces and Interfaces, 23*, 100927.

Akhtar, K., *et al.* (2018). Scanning electron microscopy: Principle and applications in nanomaterials characterization. *Handbook of materials characterization*, 113-145.

Al-Ahmed, Z. A., *et al.* (2020). Dye removal, antibacterial properties, and morphological behavior of hydroxyapatite doped with Pd ions. *Arabian Journal of Chemistry, 13*(12), 8626-8637.

Al-Hazmi, F. E. (2016). Synthesis and electrical properties of Bi doped hydroxyapatite ceramics. *Journal of Alloys and Compounds, 665*, 119-123.

Alhassan, S. I., *et al.* (2021). Fluoride removal from water using alumina and aluminum-based composites: A comprehensive review of progress. *Critical reviews in environmental science and technology*, *51*(18), 2051-2085.

Alioui, H., *et al.* (2019). Toward an efficient antibacterial agent: Zn-and Mg-doped hydroxyapatite nanopowders. *Journal of Environmental Science and Health, Part A, 54*(4), 315-327.

Alkurdi, S. S., *et al.* (2019). Bone char as a green sorbent for removing health threatening fluoride from drinking water. *Environment international, 127*, 704-719.

Alwine, S., *et al.* (2023). Crosslinkable fluorophenoxy-substituted poly [bis (octafluoropentoxy) phosphazene] biomaterials with improved antimicrobial effect and hemocompatibility. *Journal of Biomedical Materials Research Part B: Applied Biomaterials, 111*(8), 1533-1545.

Andrews, L.and Johnson, G. L. (1984). Fourier-transform infrared spectra of hydrogen fluoride ((HF)n) species in solid argon. *The Journal of Physical Chemistry, 88*(3), 425-432.

Anwar, A., *et al.* (2017). Synthesis and characterization of pure and nanosized hydroxyapatite bioceramics. *Nanotechnology Reviews, 6*(2), 149-157.

Arif, M., *et al.* (2018). Synthesis and optical properties of metal fluoride complexes. *Journal of Ovonic Research Vol, 14*(3), 235-241.

Armijo, L. M., *et al.* (2020). Antibacterial activity of iron oxide, iron nitride, and tobramycin conjugated nanoparticles against Pseudomonas aeruginosa biofilms. *Journal of Nanobiotechnology, 18*(1), 1-27.

Arole, V.and Munde, S. (2014). Fabrication of nanomaterials by top-down and bottom-up approaches-an overview. *Journal of Materials Science, 1*, 89-93.

Avakyan, L., *et al.* (2021). Iron in hydroxyapatite: interstitial or substitution sites? *Nanomaterials, 11*(11), 2978.

Aw, S., *et al.* (2022). Removal of fluoride in groundwater by adsorption using hydroxyapatite modified Corbula trigona shell powder. *Chemical Engineering Journal Advances, 12*, 100386.

Awoke, A., *et al.* (2016). River water pollution status and water policy scenario in Ethiopia: raising awareness for better implementation in developing countries. *Environmental management, 58*(4), 694-706.

Azad, K.and Gajanan, P. (2017). Photodegradation of methyl orange in aqueous solution by the visible light active Co: La: TiO_2 nanocomposite. *Chem. Sci. J, 8*(3), 1000164-1000174.

Azzaza, S., *et al.* (2016). Nanomaterials for heavy metal removal. *Advanced Environmental Analysis* (pp. 139-166).

Baaloudj, O., *et al.* (2022). Bismuth sillenite crystals as recent photocatalysts for water treatment and energy generation: A critical review. *Catalysts, 12*(5), 500.

Balamurugan, A., *et al.* (2006). Synthesis and structural analysis of sol gel derived stoichiometric monophasic hydroxyapatite. *Ceramics- Silikaty, 50*(1), 27-31.

Balasooriya, I. L., *et al.* (2022). Applications of nano hydroxyapatite as adsorbents: A review. *Nanomaterials, 12*(14), 2324.

Balhuc, S., *et al.* (2021). Dental applications of systems based on hydroxyapatite nanoparticles—An evidence-based update. *Crystals, 11*(6), 674.

Basu, S.and Basu, B. (2019). Doped biphasic calcium phosphate: synthesis and structure. *Journal of Asian Ceramic Societies, 7*(3), 265-283.

Bazin, T., *et al.* (2022). Exotic Fe(II)/Fe(III) local environments in the hexagonal channels of hydroxyapatite. *Inorganic chemistry, 61*(36), 14377-14388.

Bello, O. S., *et al.* (2017). Sustainable conversion of agro-wastes into useful adsorbents. *Applied Water Science, 7*(7), 3561-3571.

Benmessaoud, A., *et al.* (2020). A comparative study of the linear and non-linear methods for determination of the optimum equilibrium isotherm for adsorption of Pb^{2+} ions onto Algerian treated clay. *Iranian Journal of Chemistry and Chemical Engineering*, *39*(4), 153-171.

Bhattacharjee, A., *et al.* (2020). Effect of Zn and Co doping on antibacterial efficacy and cytocompatibility of spark plasma sintered hydroxyapatite. *Journal of the American Ceramic Society, 103*(8), 4090-4100.

Bordea, I. R., *et al.* (2020). Nano-hydroxyapatite use in dentistry: A systematic review. *Drug metabolism reviews, 52*(2), 319-332.

Bouyarmane, H., *et al.* (2021). Photocatalytic degradation of emerging antibiotic pollutants in waters by TiO_2/Hydroxyapatite nanocomposite materials. *Surfaces and Interfaces, 24*, 101155.

Brinker, C. J.and Scherer, G. W. (2013). *Sol-gel science: the physics and chemistry of sol-gel processing*: Academic press.

Bystrov, V., *et al.* (2016). Oxygen vacancies, the optical band gap (Eg) and photocatalysis of hydroxyapatite: Comparing modelling with measured data. *Applied Catalysis B: Environmental, 196*, 100-107.

Cacciotti, I. (2016). Cationic and anionic substitutions in hydroxyapatite *Handbook of bioceramics and biocomposites*: Springer International Publishing Cham, Switzerland, pp. 145-211):

Cacciotti, I. (2019). Multisubstituted hydroxyapatite powders and coatings: The influence of the codoping on the hydroxyapatite performances. *International Journal of Applied Ceramic Technology, 16*(5), 1864-1884.

Cai, Z., *et al.* (2019). Large-scale and fast synthesis of nano-hydroxyapatite powder by a microwave-hydrothermal method. *Royal Society of Chemistry Advances, 9*(24), 13623-13630.

Cengiz, B., *et al.* (2008). Synthesis and characterization of hydroxyapatite nanoparticles. *Colloids and Surfaces A: Physicochemical and Engineering Aspects, 322*(1-3), 29-33.

Chahal, S., *et al.* (2020). Zn doped α-Fe_2O_3: an efficient material for UV driven photocatalysis and electrical conductivity. *Crystals, 10*(4), 273.

Channei, D., *et al.* (2014). Photocatalytic degradation of methyl orange by CeO_2 and Fe–doped CeO_2 films under visible light irradiation. *Scientific reports, 4*(1), 5757.

Chawla, P., *et al.* (2010). Optical characterization of Bi doped SrS nanophosphors. *Materials Research Bulletin, 45*(7), 783-786.

Chen, K., *et al.* (2019). Biological response of and blood plasma protein adsorption on silver-doped hydroxyapatite. *American Chemical Socity Biomaterials Science & Engineering, 5*(2), 561-571.

Chen, L., *et al.* (2021). Hydroxyapatite in oral care products—a review. *Materials, 14*(17), 4865.

Chen, L., *et al.* (2022). Effect of doping cation on the adsorption properties of hydroxyapatite to uranium. *Journal of Solid State Chemistry*, 123687.

Chen, L., *et al.* (2016). Enhanced fluoride removal from water by sulfate-doped hydroxyapatite hierarchical hollow microspheres. *Chemical Engineering Journal, 285*, 616-624.

Chen, M.-H., *et al.* (2014). Photoluminescence and doping mechanism of theranostic Eu^{3+}/Fe^{3+} dual-doped hydroxyapatite nanoparticles. *Science and Technology of Advanced Materials, 23, 56-78.*

Chen, X. (2015). Modeling of experimental adsorption isotherm data. *Information, 6*(1), 14-22.

Chen, Z., *et al.* (2018). Effect of cation doping on the structure of hydroxyapatite and the mechanism of defluoridation. *Ceramics International, 44*(6), 6002-6009.

Chenoweth, J. (2008). A re-assessment of indicators of national water scarcity. *Water International, 33*(1), 5-18.

Chuaicham, C., *et al.* (2023). Simultaneous photocatalytic sugar conversion and hydrogen production using Pd nanoparticles decorated on iron-doped hydroxyapatite. *Catalysts, 13*(4), 675.

Chusuei, C. C., *et al.* (1999). Calcium phosphate phase identification using XPS and time-of-flight cluster SIMS. *Analytical chemistry, 71*(1), 149-153.

Ciobanu, C., *et al.* (2015). Evaluation of samarium doped hydroxyapatite, ceramics for medical application: Antimicrobial activity. *Journal of Nanomaterials, 2015*, 14-14.

Ciobanu, G., *et al.* (2015). New bismuth-substituted hydroxyapatite nanoparticles for bone tissue engineering. *Journal of the Minerals, Metals, and Material Society, 67*(11), 2534-2542.

Ciobanu, G.and Harja, M. (2019). Bismuth-doped nanohydroxyapatite coatings on Titanium implants for improved radiopacity and antimicrobial activity. *Nanomaterials, 9*(12), 1696.

Claudel, M., *et al.* (2020). New antimicrobial strategies based on metal complexes. *Chemistry, 2*(4), 849-899.

Corral-Capulin, N., *et al.* (2019). Comparison of the removal behavior of fluoride by Fe^{3+} modified geomaterials from water. *Applied Clay Science, 173*, 19-28.

Cox, S. C., *et al.* (2015). Comparison of techniques for the synthesis of hydroxyapatite. *Bioinspired, Biomimetic and Nanobiomaterials, 4*(1), 37-47.

Das, S., *et al.* (2020). Synthesis, morphological analysis, antibacterial activity of iron oxide nanoparticles and the cytotoxic effect on lung cancer cell line. *Heliyon, 6*(9), e04953.

Demelash, H., *et al.* (2019). Fluoride concentration in ground water and prevalence of dental fluorosis in Ethiopian Rift Valley: systematic review and meta-analysis. *Biomedical Chemistry and Public Health, 19*(1), 1-9.

Demirel, B., *et al.* (2021). Synthesis of Gd^{+3} doped hydroxyapatite ceramics: Optical, thermal and electrical properties. *Journal of Asian Ceramic Societies, 9*(3), 865-873.

Dorenbos, P. (2021). Electronic structure of Bi-activated luminescent compounds and pure bismuth photocatalytic compounds. *Europian Chemical Socity Journal of Solid State Science and Technology, 10*(8), 086002.

Dorozhkin, S. V. (2016). Calcium orthophosphates ($CaPO_4$): occurrence and properties. *Progress in Biomaterials, 5*(1), 9-70.

Dou, L., *et al.* (2018). Advances in synthesis and functional modification of nanohydroxyapatite. *Journal of Nanomaterials, 2018*.

Duffin, R. N., *et al.* (2020). Antimony and bismuth as antimicrobial agents. *Advances in Inorganic Chemistry*: Elsevier, Vol. 75, pp. 207-255).

Dutta, S. K., *et al.* (2022). Removal of toxic methyl orange by a cost-free and eco-friendly adsorbent: Mechanism, phytotoxicity, thermodynamics, and kinetics. *South African Journal of Chemical Engineering, 40*, 195-208.

Edet, U. A.and Ifelebuegu, A. O. (2020). Kinetics, isotherms, and thermodynamic modeling of the adsorption of phosphates from model wastewater using recycled brick waste. *Processes, 8*(6), 665.

Edis, Z., *et al.* (2022). Antimicrobial biomaterial on sutures, bandages and face masks with potential for infection control. *Polymers, 14*(10), 1932.

El-Kafrawy, A. F., *et al.* (2017). Adsorbents based on natural polymers for removal of some heavy metals from aqueous solution. *Egyptian Journal of Petroleum, 26*(1), 23-32.

El-Naas, M. H.andAlhaija, M. A. (2013). Modeling of adsorption processes. *Mathimatical Model*, 579-600.

Emmanuel, S. S., *et al.* (2023). A pragmatic review on photocatalytic degradation of methyl orange dye pollutant using greenly bio-functionalized nano-metallic materials: A focus on aquatic body. *Applied Organometallic Chemistry*, e7108.

Faeghinia, A.andEbadzadeh, T. (2020). Effect of microwave conditions on sintering of hydroxyapatite ceramics. *Science of Sintering, 52*(4), 469-479.

Fatimah, I., *et al.* (2023). Hydrothermally synthesized titanium/hydroxyapatite as photoactive and antibacterial biomaterial. *Heliyon, 9*(3).

Fernando, M. S., *et al.* (2015). Synthesis, characterization, and application of nano hydroxyapatite and nanocomposite of hydroxyapatite with granular activated carbon for the removal of Pb^{2+} from aqueous solutions. *Applied Surface Science, 351*, 95-103.

Fernando, M. S., *et al.* (2021). Biopolymer-based nanohydroxyapatite composites for the removal of fluoride, lead, cadmium, and arsenic from water. *American Chemical Socity omega, 6*(12), 8517-8530.

Fernando, M. S., *et al.* (2019). Improved nanocomposite of montmorillonite and hydroxyapatite for defluoridation of water. *Royal Socity of Chemistry Advances, 9*(61), 35588-35598.

Ferreira, A. S., *et al.* (2019). Equilibrium and kinetic modelling of adsorption: Evaluating the performance of an adsorbent in softening water for irrigation and animal consumption. *Rev. Virtual Quim, 11*, 1752-1766.

Ferri, E. A. V., *et al.* (2008). Chemical characterization of $BiFeO_3$ obtained by Pechini method. *Journal of the Brazilian Chemical Society, 19*, 1153-1157.

Fihri, A., *et al.* (2017). Hydroxyapatite: A review of syntheses, structure and applications in heterogeneous catalysis. *Coordination Chemistry Reviews, 347*, 48-76.

Folawewo, A. D.and Bala, M. D. (2022). Nanocomposite zinc oxide-based photocatalysts: Recent developments in their use for the treatment of dye-polluted wastewater. *Water, 14*(23), 3899.

Frickmann, H., *et al.* (2019). On the etiological relevance of Escherichia coli and Staphylococcus aureus in superficial and deep infections–a hypothesis-forming, retrospective assessment. *European Journal of Microbiology and Immunology, 9*(4), 124-130.

Gai, W.-Z.and Deng, Z.-Y. (2021). A comprehensive review of adsorbents for fluoride removal from water: Performance, water quality assessment and mechanism. *Environmental Science: Water Research & Technology, 7*(8), 1362-1386.

Gambhir, R. S., *et al.* (2012). Water pollution: Impact of pollutants and new promising techniques in purification process. *Journal of Human Ecology, 37*(2), 103-109.

Gao, M., *et al.* (2019). Hydrothermal synthesis of hierarchical hollow hydroxyapatite microspheres with excellent fluoride adsorption property. *Microporous and mesoporous materials, 289*, 109620.

Garbo, C., *et al.* (2020). Advanced Mg, Zn, Sr, Si multi-substituted hydroxyapatites for bone regeneration. *International journal of nanomedicine*, 1037-1058.

Girish, C. (2017). Various isotherm models for multicomponent adsorption: a review. *International Journal of Civil Engineering Technology, 8*(10), 80-86.

Goldberg, M., *et al.* (2020). The enhancement of hydroxyapatite thermal stability by Al doping. *Journal of Materials Research and Technology, 9*(1), 76-88.

González-López, M. E., *et al.* (2022). A critical overview of adsorption models linearization: methodological and statistical inconsistencies. *Separation and Purification Reviews, 51*(3), 358-372.

Goodarzi, N., *et al.* (2023). Recent progress on semiconductor heterogeneous photocatalysts in clean energy production and environmental remediation. *Catalysts, 13*(7), 1102.

Gopi, D., *et al.* (2015). Synthesis of pure and substituted hydroxyapatite nanoparticles by cost effective facile methods. *Handbook of Nanoparticles*, 167-190.

Guo, H., *et al.* (2019). Synthesis of magnetic Fe-doped hydroxyapatite nanocages with highly efficient and selective adsorption for Cd^{2+}. *Materials Letters, 253*, 144-147.

Haber, J., *et al.* (1976). X-ray photoelectron spectra of oxygen in oxides of Co, Ni, Fe and Zn. *Journal of Electron Spectroscopy and Related Phenomena, 9*(5), 459-467.

Hadagalli, K., *et al.* (2021). Effect of Fe^{3+} substitution on the structural modification and band structure modulated UV absorption of hydroxyapatite. *International Journal of Applied Ceramic Technology, 18*(2), 332-344.

Han, Q. (2021). Advances in preparation methods of bismuth-based photocatalysts. *Chemical Engineering Journal, 414*, 127877.

He, F., *et al.* (2014). IR and Raman spectra properties of Bi_2O_3-ZnO-B_2O_3-BaO quaternary glass system. *American Journal of Analytical Chemistry, 5*(16), 1142.

He, J., *et al.* (2017). A biocompatible and novelly-defined Al-HAP adsorption membrane for highly effective removal of fluoride from drinking water. *Journal of Colloid and Interface Science, 490*, 97-107.

He, J., *et al.* (2020). Review of fluoride removal from water environment by adsorption. *Journal of Environmental Chemical Engineering, 8*(6), 104516.

He, J., *et al.* (2016). Performance of novel hydroxyapatite nanowires in treatment of fluoride contaminated water. *Journal of hazardous materials, 303*, 119-130.

Hegde, R. M., *et al.* (2020). Bio-inspired materials for defluoridation of water: a review. *Chemosphere, 253*, 126657.

Helen, S.and Kumar, A. R. (2019). Study of structural, mechanical and dielectrical properties of ions doped apatite for antibacterial activity. *Materials Chemistry and Physics, 237*, 121867.

Hochvaldová, L., *et al.* (2022). Antibacterial nanomaterials: upcoming hope to overcome antibiotic resistance crisis. *Nanotechnology Reviews, 11*(1), 1115-1142.

Hossain, M. S., *et al.* (2022). Enhancement of photocatalytic efficacy by exploiting copper doping in nano-hydroxyapatite for degradation of Congo red dye. *Royal Socity of Chemistry Advances, 12*(52), 34080-34094.

Hossain, M. Z. (2015). Water: the most precious resource of our life. *Global Journal of Advanced Research, 2*(9), 1-11.

Hrubiak, A. B., *et al.* (2018). The electrical conductivity and photocatalytic activity of ultrafine iron hydroxide/oxide systems. *Molecular Crystals and Liquid Crystals, 670*(1), 97-111.

Huang, L., *et al.* (2022). Applications of biomass-based materials to remove fluoride from wastewater: A review. *Chemosphere*, 134679.

Huang, S.-M., *et al.* (2022). Morphological changes, antibacterial activity, and cytotoxicity characterization of hydrothermally synthesized metal ions-incorporated nanoapatites for biomedical application. *Pharmaceuticals*, *15*(7), 885.

Huang, S., *et al.* (2020). Fluoride sorption from aqueous solution using $Al(OH)_3$-modified hydroxyapatite nanosheet. *Fuel*, *279*, 118486.

Huang, W., *et al.* (2018). Synthesis and characterisation of fluorescent and biocompatible hydroxyapatite nanoparticles with cerium doping. *Micro and Nano Letters*, *13*(5), 699-703.

Huang, Y., *et al.* (2015). Osteoblastic cell responses and antibacterial efficacy of Cu/Zn co-substituted hydroxyapatite coatings on pure titanium using electrodeposition method. *Royal Socity of Chemistry Advances*, *5*(22), 17076-17086.

Iannotti, V., *et al.* (2017). Fe-doping-induced magnetism in nano-hydroxyapatites. *Inorganic chemistry*, *56*(8), 4446-4458.

Ibrahim, M., *et al.* (2020). Hydroxyapatite, a multifunctional material for air, water and soil pollution control: A review. *Journal of Hazardous Materials*, *383*, 121139.

Iconaru, S. L., *et al.* (2020). Antimicrobial properties of samarium doped hydroxyapatite suspensions and coatings. *Coatings*, *10*(11), 1124.

Ignjatović, N. L., *et al.* (2019). Rare-earth (Gd^{3+}, Yb^{3+}/Tm^{3+}, Eu^{3+}) co-doped hydroxyapatite as magnetic, up-conversion and down-conversion materials for multimodal imaging. *Scientific reports*, *9*(1), 16305.

Indah, S., *et al.* (2018). Studies on desorption and regeneration of natural pumice for iron removal from aqueous solution. *Water Science and Technology*, *2017*(2), 509-515.

Irfan, S., *et al.* (2017). Enhanced photocatalytic activity of La^{3+} and Se^{4+} co-doped bismuth ferrite nanostructures. *Journal of Materials Chemistry A*, *5*(22), 11143-11151.

Irshad, R., *et al.* (2017). Antibacterial activity of biochemically capped iron oxide nanoparticles: A view towards green chemistry. *Journal of Photochemistry and Photobiology B: Biology*, *170*, 241-246.

Iyyapushpam, S., *et al.* (2015). Synthesis of β-Bi_2O_3 towards the application of photocatalytic degradation of methyl orange and its instability. *Journal of Physics and Chemistry of Solids*, *81*, 74-78.

Jadalannagari, S., *et al.* (2014). Antimicrobial activity of hemocompatible silver doped hydroxyapatite nanoparticles synthesized by modified sol–gel technique. *Applied Nanoscience, 4*, 133-141.

Jafari, A., *et al.* (2011). Synthesis and antibacterial properties of zinc oxide combined with copper oxide nanocrystals. *Oriental Journal of Chemistry, 27*(3), 811.

Janaćkovića, D., *et al.* (2007). Influence of synthesis parameters on the particle sizes of nanostructured calcium-hydroxyapatite. *Calcium phosphate Ceramics-Bioresorbable Polymer Composite Biomaterials: from synthesis to applications:(1999-2007), 192*(195), 103.

Jayarathna, L., *et al.* (2015). Fluoride adsorption on γ−Fe_2O_3 nanoparticles. *Journal of Environmental Health Science and Engineering, 13*(1), 1-10.

Jeong, J., *et al.* (2019). Bioactive calcium phosphate materials and applications in bone regeneration. *Biomaterials research, 23*(1), 1-11.

Jeyaseelan, A.andViswanathan, N. (2022). Investigation of hydroxyapatite-entrenched cerium organic frameworks incorporating biopolymeric beads for efficient fluoride removal. *Industrial & Engineering Chemistry Research, 61*(23), 7911-7925.

Jiménez-Flores, Y., *et al.* (2017). Characterization of Tb-doped hydroxyapatite for biomedical applications: optical properties and energy band gap determination. *Journal of Materials Science, 52*(17), 9990-10000.

Jiménez-Flores, Y., *et al.* (2017). Sol–gel synthesis of Tb-doped hydroxyapatite with high performance as photocatalyst for 2, 4 dichlorophenoxyacetic acid mineralization. *Journal of Chemical Technology & Biotechnology, 92*(7), 1521-1530.

Kalita, J., *et al.* (2022). Synergistic effect of iron and copper in hydroxyapatite nanorods for Fenton-like oxidation of organic dye. *Colloids and Surfaces A: Physicochemical and Engineering Aspects, 643*, 128750.

Karimi, S., *et al.* (2019). A comprehensive review of the adsorption mechanisms and factors influencing the adsorption process from the perspective of bioethanol dehydration. *Renewable and Sustainable Energy Reviews, 107*, 535-553.

Karunakaran, G., *et al.* (2019). Ascorbic acid-assisted microwave synthesis of mesoporous Ag-doped hydroxyapatite nanorods from biowaste seashells for implant applications. *American Chemical Socity Applied Bio Materials, 2*(5), 2280-2293.

Kaygili, O., *et al.* (2021). Ce/Sm co-doped hydroxyapatites: synthesis, characterization, and band structure calculation. *Journal of the Australian Ceramic Society, 57*(1), 305-317.

Kgatle, M., *et al.* (2021). Degradation kinetics of methyl orange dye in water using trimetallic Fe/Cu/Ag nanoparticles. *Catalysts, 11*(4), 428.

Khan, A., *et al.* (2022). Synthesis of titanium doped hydroxyapatite using waste marble powder for the degradation of Congo Red dye in wastewater. *Materials Today: Proceedings, 57*, 1645-1653.

Khan, A. U., *et al.* (2022). Biological mineralization of methyl orange by pseudomonas aeruginosa. *Water, 14*(10), 1551.

Khan, H.and Swati, I. K. (2016). Fe^{3+}-doped anatase TiO_2 with d–d transition, oxygen vacancies and Ti^{3+} centers: synthesis, characterization, UV–vis photocatalytic and mechanistic studies. *Industrial & Engineering Chemistry Research, 55*(23), 6619-6633.

Khoudro, A., *et al.* (2023). Studying the infrared spectroscopy of compounds fluoride that blotched by in. *Journal of Applied Material Science and Enggineering Research, 7*(1), 43-49.

Kishor, R., *et al.* (2021). Degradation mechanism and toxicity reduction of methyl orange dye by a newly isolated bacterium Pseudomonas aeruginosa MZ520730. *Journal of Water Process Engineering, 43*, 102300.

Koohestani, H.and Sadrnezhaad, S. K. (2016). Photocatalytic degradation of methyl orange and cyanide by using TiO_2/CuO composite. *Desalination and Water Treatment, 57*(46), 22029-22038.

Kowalczyk, M., *et al.* (2020). Optical investigation of Eu^{3+} doped $Bi_{12}GeO_{20}$ (BGO) crystals. *Crystals, 10*(4), 285.

Krishnamoorthy, R., *et al.* (2021). Long-term exposure to azo dyes from textile wastewater causes the abundance of Saccharibacteria population. *Applied Sciences, 11*(1), 379.

Krukowski, S., *et al.* (2018). The influence of substituted hydroxyapatites heat treatment on citrate sorption behavior–infrared spectroscopy experiments and adsorption studies. *Colloids and Surfaces A: Physicochemical and Engineering Aspects, 558*, 23-32.

Kuang, Y., *et al.* (2020). Adsorption of methylene blue in water onto activated carbon by surfactant modification. *Water, 12*(2), 587.

Kurinjinathan, P.and Arul, K. T. (2018). Optical and magnetic properties of cobalt ions doped calcium phosphate by ultrasonication. *Recent Patents on Materials Science, 11*(2), 91-96.

Kurinjinathan, P., *et al.* (2020). Effect of nickel doping on the properties of hydroxyapatite nanoparticles. *Journal of nanoscience and nanotechnology, 20*(4), 2482-2487.

Labib, S. (2017). Preparation, characterization and photocatalytic properties of doped and undoped Bi2O3. *Journal of Saudi Chemical Society, 21*(6), 664-672.

Labrag, J., *et al.* (2020). *A comparative study of the photocatalytic efficiency of metal oxide/hydroxyapatite nanocomposites in the degradation kinetic of ciprofloxacin in water.* Paper presented at the E3S Web of Conferences.

Labrag, J., *et al.* (2021). Porous and bifunctional ZnO-hydroxyapatite nanostructure for photocatalytic degradation of paracetamol and methylene blue in water. *Iranian Journal of Catalysis, 11*(4), 389-395.

Landi Jr, S., *et al.* (2022). Use and misuse of the Kubelka-Munk function to obtain the band gap energy from diffuse reflectance measurements. *Solid state communications, 341*, 114573.

Largitte, L.and Pasquier, R. (2016). A review of the kinetics adsorption models and their application to the adsorption of lead by an activated carbon. *chemical engineering research and design, 109*, 495-504.

Laurier, K. G., *et al.* (2013). Iron (III)-based metal–organic frameworks as visible light photocatalysts. *Journal of the American Chemical Society, 135*(39), 14488-14491.

Lee, S. Y., *et al.* (2020). Photocatalytic degradation of rhodamine B dye by TiO_2 and gold nanoparticles supported on a floating porous polydimethylsiloxane sponge under ultraviolet and visible light irradiation. *American Chemical Socity omega, 5*(8), 4233-4241.

Lei, E., *et al.* (2019). Composition, morphology, structure and photocatalytic performances of photocatalysts prepared from titanium potassium oxalate. *Solid State Sciences, 88*, 36-40.

Lei, X., *et al.* (2020). Hollow hydroxyapatite microspheres modified by CdS nanoparticles for efficiently photocatalytic degradation of tetracycline. *Journal of the Taiwan Institute of Chemical Engineers, 106*, 148-158.

Li, D., *et al.* (2021). The interaction of Ag_2O nanoparticles with Escherichia coli: Inhibition–sterilization process. *Scientific reports, 11*(1), 1703.

Li, Q., *et al.* (2022). Antibacterial properties and biocompatibility of hydroxyapatite coating poped with various Cu contents on titanium. *Materials Ttransactions, 63*(7), 1072-1079.

Li, X., *et al.* (2021). Preparation, characterization serpentine-loaded hydroxyapatite and its simultaneous removal performance for fluoride, iron and manganese. *Royal Socity of Chemistry Advances, 11*(27), 16201-16215.

Lim, Q. R. T., *et al.* (2023). An insight to the various applications of hydroxyapatite. *Advanced Materials Science and Technology, 5*(2).

Lima, E. C., *et al.* (2019). A critical review of the estimation of the thermodynamic parameters on adsorption equilibria. Wrong use of equilibrium constant in the Van't Hoof equation for calculation of thermodynamic parameters of adsorption. *Journal of Molecular Liquids, 273*, 425-434.

Liu, W., *et al.* (2018). The growth mechanism of titania/hydroxyapatite and its application in the photodegradation of methyl orange dye under UV irradiation. *Results in Physics, 11*, 112-117.

Liu, W., *et al.* (2016). Facile synthesis of spherical nano hydroxyapatite and its application in photocatalytic degradation of methyl orange dye under UV irradiation. *Materials Letters, 178*, 15-17.

Liu, Y., *et al.* (2022). Degradation of azo dyes with different functional groups in simulated wastewater by electrocoagulation. *Water, 14*(1), 123.

Loo, S., *et al.* (2010). Biomedical applications of hydroxyapatite nanoparticles. *Current pharmaceutical biotechnology, 11*(4), 333-342.

Loo, S. C. J., *et al.* (2008). Synthesis and hydrothermal treatment of nanostructured hydroxyapatite of controllable sizes. *Journal of Materials Science: Materials in Medicine, 19*(3), 1389-1397.

Lu, H. B., *et al.* (2000). Surface characterization of hydroxyapatite and related calcium phosphates by XPS and TOF-SIMS. *Analytical chemistry, 72*(13), 2886-2894.

Lv, C., *et al.* (2024). Earth-abundant insulator hydroxyapatite-based composite for full-spectrum photocatalytic degradation of 2, 4-dichlorophenol. *Applied Catalysis B: Environmental, 340*, 123248.

Lv, X., *et al.* (2020). Recent advances in pH-responsive nanomaterials for anti-infective therapy. *Journal of Materials Chemistry B, 8*(47), 10700-10711.

Machado, T. R., *et al.* (2019). Designing biocompatible and multicolor fluorescent hydroxyapatite nanoparticles for cell-imaging applications. *Materials Today Chemistry, 14*, 100211.

Mahanty, A.and Shikha, D. (2023). Microstructural, biocompatibility and mechanical investigation of MgHAp and AgHAp: Comparative report. *Journal of Materials Science: Materials in Medicine, 34*(5), 22.

Mahmood, B. K., *et al.* (2020). Effects of strontium-erbium co-doping on the structural properties of hydroxyapatite: An experimental and theoretical study. *Ceramics International, 46*(10), 16354-16363.

Mahmood, T., *et al.* (2011). Comparison of different methods for the point of zero charge determination of NiO. *Industrial & Engineering Chemistry Research, 50*(17), 10017-10023.

Manatunga, D. C., *et al.* (2018). Metal and polymer-mediated synthesis of porous crystalline hydroxyapatite nanocomposites for environmental remediation. *Royal Society open science, 5*(1), 171557.

Mancuso, A., *et al.* (2020). Enhanced visible-light-driven photodegradation of Acid Orange 7 azo dye in aqueous solution using Fe-N co-doped TiO_2. *Arabian Journal of Chemistry, 13*(11), 8347-8360.

Manoj, M., *et al.* (2019). Facile development and structural investigations of HAp and HAp/Ta nanostructures: Photocatalytic activity against Turq blue GL dye. *Materials Research Express, 7*(1), 015012.

Mariappan, A., *et al.* (2017). Structural, optical and antimicrobial activity of copper and zinc doped hydroxyapatite nanopowders using sol-gel method. *Mechanics, Materials Science and Engineering Journal, 9*(1).

Martínez-Hernández, H., *et al.* (2020). Development of novel nano-hydroxyapatite doped with silver as effective catalysts for carbon monoxide oxidation. *Chemical Engineering Journal, 401*, 125992.

Mateus, A. P., *et al.* (2013). Nanoparticles of hydroxyapatite: preparation, characterization and cellular approach-An Overview. *Revista Mutis, 3*(2), 43-56.

Mathew, M.and Takagi, S. (2001). Structures of biological minerals in dental research. *Journal of Research of the National Institute of Standards and Technology, 106*(6), 1035.

Meng, S., *et al.* (2022). Modification of hydroxyapatite by doping lithium through acid-base reaction. *Journal of the Ceramic Society of Japan, 130*(9), 802-806.

Mercado, D. F., *et al.* (2014). Paramagnetic iron-doped hydroxyapatite nanoparticles with improved metal sorption properties. A bioorganic substrates-mediated synthesis. *American Chemical Socity Applied Materials and Interfaces, 6*(6), 3937-3946.

Modrogan, C., *et al.* (2021). Modified composite based on magnetite and polyvinyl alcohol: Synthesis, characterization, and degradation studies of the methyl orange dye from synthetic wastewater. *Polymers, 13*(22), 3911.

Mohseni-Salehi, M. S., *et al.* (2018). Effect of dopant (Co, Ni) concentration and hydroxyapatite compositing on photocatalytic activity of titania towards dye degradation. *Journal of Photochemistry and Photobiology A: Chemistry, 356*, 57-70.

Moirana, R. L., *et al.* (2023). Hydroxyapatite-activated seaweed biochar for enhanced remediation of fluoride contaminated soil at various pH ranges. *Environmental Advances, 11*, 100329.

Mondal, P., *et al.* (2016). Defluoridation studies with synthesized magnesium-incorporated hydroxyapatite and parameter optimization using response surface methodology. *Desalination and Water Treatment, 57*(56), 27294-27313.

Moradi, K.and Alvani, A. S. (2019). First-principles study on Sr-doped hydroxyapatite as a biocompatible filler for photo-cured dental composites. *Journal of the Australian Ceramic Society*, 1-8.

Morsi, M. A.andAbd Elhamid, M. H. (2019). Effect of iron doped hydroxyapatite nanoparticles on the structural, morphological, mechanical and magnetic properties of polylactic acid polymer. *Journal of Materials Research and Technology, 8*(2), 2098-2106.

Munir, M. U., *et al.* (2022). Synthesis, characterization, functionalization and bio-applications of hydroxyapatite nanomaterials: an overview. *International journal of nanomedicine*, 1903-1925.

Murzin, A. O., *et al.* (2023). Diffuse reflectance spectroscopy with dilution: A Powerful method for halide perovskites study. *Molecules*, *28*(1), 350.

Nabizadeh, R., *et al.* (2015). Modelling the effects of competing anions on fluoride removal by functionalized polyacrylonitrile coated with iron oxide nanoparticles. *South African Journal of Chemistry, 68*, 201-207.

Nagaraj, A., *et al.* (2018). Hydrothermal synthesis of a mineral-substituted hydroxyapatite nanocomposite material for fluoride removal from drinking water. *New Journal of Chemistry, 42*(15), 12711-12721.

Nagyne-Kovacs, T., *et al.* (2018). Synthesis and characterization of Sr and Mg-doped hydroxyapatite by a simple precipitation method. *Ceramics International, 44*(18), 22976-22982.

Nam, P. T., *et al.* (2018). Synthesis, characterization and antimicrobial activity of copper doped hydroxyapatite. *Vietnam Journal of Chemistry, 56*(6), 672-678.

Nardi, M. V., *et al.* (2021). Synthesis and characterization of Nd^{3+}-Yb^{3+} doped hydroxyapatite nanoparticles. *Optical Materials: X, 12*, 100118.

Natarajan, S., *et al.* (2018). Recent advances based on the synergetic effect of adsorption for removal of dyes from waste water using photocatalytic process. *Journal of Environmental Sciences, 65*, 201-222.

Nayak, A. K. (2010). Hydroxyapatite synthesis methodologies: an overview. *International Journal of ChemTech Research, 2*(2), 903-907.

Nayak, B., *et al.* (2017). Comprehensive understanding of the kinetics and mechanism of fluoride removal over a potent nanocrystalline hydroxyapatite surface. *American Chemical Socity omega, 2*(11), 8118-8128.

Neacsu, I. A., *et al.* (2019). Luminescent hydroxyapatite doped with rare earth elements for biomedical applications. *Nanomaterials, 9*(2), 239.

Neethu, N.and Choudhury, T. (2018). Treatment of methylene blue and methyl orange dyes in wastewater by grafted titania pillared clay membranes. *Recent patents on nanotechnology, 12*(3), 200-207.

Nie, L., *et al.* (2021). Silver-doped biphasic calcium phosphate/alginate microclusters with antibacterial property and controlled doxorubicin delivery. *Journal of Applied Polymer Science, 138*(19), 50433.

Nie, Y., *et al.* (2012). Enhanced fluoride adsorption using Al(III) modified calcium hydroxyapatite. *Journal of Hazardous Materials, 233*, 194-199.

Ogata, F., *et al.* (2020). Removal of fluoride using magnesium and iron complex hydroxides. *Water Supply, 20*(7), 2815-2825.

Olejarczyk, M., *et al.* (2022). Management of solid waste containing fluoride - A Review. *Materials, 15*(10), 3461.

Omo-Okoro, P. N., *et al.* (2018). A review of the application of agricultural wastes as precursor materials for the adsorption of per-and polyfluoroalkyl substances: a focus on current approaches and methodologies. *Environmental Technology & Innovation, 9*, 100-114.

Ossman, M. E. (2017). Similarity removal of heavy metals from aqueous solutions using advanced materials, with emphasis of synthetic and nanomaterials. *Water Desalination Research. Journal, 1*(1), 1-44.

Othman, R., *et al.* (2016). Effect of calcium precursors and pH on the precipitation of carbonated hydroxyapatite. *procedia chemistry, 19*, 539-545.

Ouchari, L., *et al.* (2019). Antimicrobial potential of actinomycetes isolated from the unexplored hot Merzouga desert and their taxonomic diversity. *Biology open, 8*(2), bio035410.

Owuama, C. I. (2017). Determination of minimum inhibitory concentration (MIC) and minimum bactericidal concentration (MBC) using a novel dilution tube method. *African journal of microbiology research, 11*(23), 977-980.

Özsin, G., *et al.* (2019). Chemically activated carbon production from agricultural waste of chickpea and its application for heavy metal adsorption: equilibrium, kinetic, and thermodynamic studies. *Applied Water Science, 9*(3), 56.

Padmanabhan, V. P., *et al.* (2019). Advanced lithium substituted hydroxyapatite nanoparticles for antimicrobial and hemolytic studies. *New Journal of Chemistry, 43*(47), 18484-18494.

Panchu, S. E., *et al.* (2022). Enriching trace level adsorption affinity of As^{3+} ion using hydrothermally synthesized iron-doped hydroxyapatite nanorods. *Journal of Inorganic and Organometallic Polymers and Materials*, 1-16.

Panda, S., *et al.* (2021). A comprehensive review on the preparation and application of calcium hydroxyapatite: A special focus on atomic doping methods for bone tissue engineering. *Ceramics International, 47*(20), 28122-28144.

Pang, Y.and Bao, X. (2003). Influence of temperature, ripening time and calcination on the morphology and crystallinity of hydroxyapatite nanoparticles. *Journal of the European Ceramic Society, 23*(10), 1697-1704.

Paranjape, P.and Sadgir, P. (2023). Linear and nonlinear regression methods for isotherm and kinetic modelling of iron ions bioadsorption using Ocimum sanctum Linn. leaves from aqueous solution. *Water Practice and Technology, 18*(8), 1807-1827.

Pazourková, L., *et al.* (2015). Preparation and mechanical properties of polymeric nanocomposites with hydroxyapatite. *Clay Mineral Fillers-Review, Journal of Nanotechnology, Nanomedcien and Nanobiotechnoogyl, 2*(7).

Pereira Rocha, R. L., *et al.* (2021). Gallium-containing hydroxyapatite as a promising material for photocatalytic performance. *Minerals, 11*(12), 1347.

Phatai, P., *et al.* (2018). Structural characterization of cerium-doped hydroxyapatite nanoparticles synthesized by an ultrasonic-assisted sol-gel technique. *Results in Physics, 10*, 956-963.

Piburn, G.and Barron, A. (2013). An introduction to energy dispersive X-ray spectroscopy. *Physical Methods in Chemistry and Nano Science*, 90-98.

Pileni, M.-P. (2003). The role of soft colloidal templates in controlling the size and shape of inorganic nanocrystals. *Nature materials, 2*(3), 145-150.

Poolman, J. T.and Anderson, A. S. (2018). Escherichia coli and Staphylococcus aureus: leading bacterial pathogens of healthcare associated infections and bacteremia in older-age populations. *Expert Review of Vaccines, 17*(7), 607-618.

Pradhan, S., *et al.* (2020). Anticancer activity of novel surface functionalized metal doped hydroxyapatite. *Archiology Pharmacy and Pharmacitical Science, 4*, 021-026.

Priyadarshini, B., *et al.* (2017). Preparation and characterization of sol-gel derived Ce^{4+} doped hydroxyapatite and its in vitro biological evaluations for orthopedic applications. *Materials and Design, 119*, 446-455.

Prodan, A. M., *et al.* (2019). Silver-doped hydroxyapatite thin layers obtained by sol-gel spin coating procedure. *Coatings, 10*(1), 14.

Qiao, H., *et al.* (2019). Si, Sr, Ag co-doped hydroxyapatite/TiO_2 coating: enhancement of its antibacterial activity and osteoinductivity. *Royal Socity of Chemistry Advances, 9*(24), 13348-13364.

Radulescu, D.-E., *et al.* (2023). Latest research of doped hydroxyapatite for bone tissue engineering. *International Journal of Molecular Sciences, 24*(17), 13157.

Raliya, R., *et al.* (2017). Photocatalytic degradation of methyl orange dye by pristine titanium dioxide, zinc oxide, and graphene oxide nanostructures and their composites under visible light irradiation. *Applied Nanoscience, 7*, 253-259.

Ramakrishnan, P., *et al.* (2016). Cation doped hydroxyapatite nanoparticles enhance strontium adsorption from aqueous system: A comparative study with and without calcination. *Applied Clay Science, 134*, 136-144.

Ramya, J. R., *et al.* (2014). Physicochemical and biological properties of iron and zinc ions co-doped nanocrystalline hydroxyapatite, synthesized by ultrasonication. *Ceramics International, 40*(10), 16707-16717.

Rathnayake, A., *et al.* (2022). Essence of hydroxyapatite in defluoridation of drinking water: A review. *Environmental Pollution*, 119882.

Reger, N. C., *et al.* (2019). Structural and phase analysis of multi-ion doped hydroxyapatite for biomedical applications. *Ceramics International, 45*(1), 252-263.

Renaudin, G., *et al.* (2017). First-row transition metal doping in calcium phosphate bioceramics: A detailed crystallographic study. *Materials, 10*(1), 92.

Robles-Águila, M., *et al.* (2017). Structural analysis of metal-doped (Mn, Fe, Co, Ni, Cu, Zn) calcium hydroxyapatite synthetized by a sol-gel microwave-assisted method. *Ceramics International, 43*(15), 12705-12709.

Rocha, R. L. P., *et al.* (2022). Light-activated hydroxyapatite photocatalysts: New environmentally-friendly materials to mitigate pollutants. *Minerals*, *12*(5), 525.

Rojas-Trigos, J., *et al.* (2019). Sol–gel synthesis and characterization of calcium-deficient hydroxyapatite photocatalysts suitable for hydrogen production: influence of the drip rate in the photocatalytic activity. *Applied Sciences*, *1*(11), 1410.

Rosman, C. W., *et al.* (2022). Interactions between the foreign body reaction and Staphylococcus aureus biomaterial-associated infection. Winning strategies in the derby on biomaterial implant surfaces. *Critical Reviews in Microbiology*, *48*(5), 624-640.

Roy, S.and Das, P. (2016). Thermodynamic and kinetics study of de-fluoridation in wastewater using hydroxyapatite (Hap) as adsorbent: optimization using response surface methodology, Frontiers in *Nanoscience and Nanotechnology*, *2*(3), 121-128.

Sadegh, H., *et al.* (2017). The role of nanomaterials as effective adsorbents and their applications in wastewater treatment. *Journal of Nanostructure in Chemistry*, *7*(1), 1-14.

Safarzadeh, M., *et al.* (2020). Sintering behaviour of carbonated hydroxyapatite prepared at different carbonate and phosphate ratios. *Boletín de la Sociedad Española de Cerámica y Vidrio*, *59*(2), 73-80.

Salhi, A., *et al.* (2015). Study of the photocatalytic degradation of methylene blue dye using titanium-doped hydroxyapatite. *Mediterranian Journal of Chemistry*, *4*, 59-67.

Samant, A., *et al.* (2017). Kinetics and mechanistic interpretation of fluoride removal by nanocrystalline hydroxyapatite derived from Limacine artica shells. *Journal of Environmental Chemical Engineering*, *5*(6), 5429-5438.

Sathiyavimal, S., *et al.* (2020). Facile synthesis and characterization of hydroxyapatite from fish bones: Photocatalytic degradation of industrial dyes (crystal violet and Congo red). *Progress in Organic Coatings*, *148*, 105890.

Scheverin, V., *et al.* (2022). Novel hydroxyapatite-biomass nanocomposites for fluoride adsorption. *Results in Engineering*, *16*, 100648.

Sekar, S., *et al.* (2022). Enhanced stability of hydroxyapatite/sodium alginate nanocomposite for effective fluoride adsorption. *Materials Today: Proceedings*, *58*, 909-917.

Serantes, D.and Baldomir, D. (2021). Nanoparticle size threshold for magnetic agglomeration and associated hyperthermia performance. *Nanomaterials*, *11*(11), 2786.

Shaji, E., *et al.* (2024). Fluoride contamination in groundwater: A global review of the status, processes, challenges, and remedial measures. *Geoscience Frontiers*, *15*(2), 101734.

Shariffuddin, J. H., *et al.* (2013). Greener photocatalysts: Hydroxyapatite derived from waste mussel shells for the photocatalytic degradation of a model azo dye wastewater. *chemical engineering research and design, 91*(9), 1693-1704.

Sharma, S., *et al.* (2022). Synthesis of hydroxyapatite nanoparticles by modified co-precipitation technique and investigation of the ceramic characteristics upon thermal treatment for their potential applications for water treatment *Contaminants of Emerging Concerns and Reigning Removal Technologies*: CRC Press, pp. 151-169.

Sharmin, S., *et al.* (2021). Nanoparticles as antimicrobial and antiviral agents: A literature-based perspective study. *Heliyon, 7*(3).

Sheikh, L., *et al.* (2018). Traversing the profile of biomimetically nanoengineered iron substituted hydroxyapatite: synthesis, characterization, property evaluation, and drug release modeling. *Rsc Advances, 8*(35), 19389-19401.

Sheng, G., *et al.* (2011). Preparation of TiO_2/hydroxyapatite composite and its photocatalytic degradation of methyl orange. *Journal of Environmental Engineering, 137*(7), 611-616.

Shokri, M., *et al.* (2022). Synergic role of zinc and gallium doping in hydroxyapatite nanoparticles to improve osteogenesis and antibacterial activity. *Biomaterials advances, 134*, 112684.

Shu, K., *et al.* (2023). In-situ hydrothermal synthesis of Fe-doped hydroxyapatite photocatalyst derived from converter slag toward xanthate photodegradation and Cr(VI) reduction under visible-light irradiation. *Chemical Engineering Journal, 459*, 141474.

Shuaishuai, W., *et al.* (2023). Implantable biomedical materials for treatment of bone infection. *Frontiers in Bioengineering and Biotechnology, 11*, 1081446.

Singh, S., *et al.* (2020). Enhanced fluoride removal from drinking water using non-calcined synthetic hydroxyapatite. *Journal of Environmental Chemical Engineering, 8*(2), 103704.

Sprio, S., *et al.* (2020). Enhancement of the biological and mechanical performances of sintered hydroxyapatite by multiple ions doping. *Frontiers in Materials, 7*, 224.

Srilakshmi, C.and Saraf, R. (2016). Ag-doped hydroxyapatite as efficient adsorbent for removal of Congo red dye from aqueous solution: Synthesis, kinetic and equilibrium adsorption isotherm analysis. *Microporous and mesoporous materials, 219*, 134-144.

Stephens, L. J., *et al.* (2020). Is bismuth really the “green” metal? Exploring the antimicrobial activity and cytotoxicity of organobismuth thiolate complexes. *Inorganic chemistry, 59*(6), 3494-3508.

Sternitzke, V., *et al.* (2012). Uptake of fluoride from aqueous solution on nano-sized hydroxyapatite: examination of a fluoridated surface layer. *Environmental science and technology, 46*(2), 802-809.

Stevie, F. A.and Donley, C. L. (2020). Introduction to x-ray photoelectron spectroscopy. *Journal of Vacuum Science and Technology A, 38*(6).

Subramanian, R., *et al.* (2019). Effect of piperine on size, shape and morphology of hydroxyapatite nanoparticles synthesized by the chemical precipitation method. *Journal of King Saud University-Science, 31*(4), 667-673.

Sujana, M. G.and Anand, S. (2010). Iron and aluminium based mixed hydroxides: a novel sorbent for fluoride removal from aqueous solutions. *Applied Surface Science, 256*(23), 6956-6962.

Sulyman, M., *et al.* (2017). Low-cost adsorbents derived from agricultural by-products/wastes for enhancing contaminant uptakes from wastewater: A Review. *Polish Journal of Environmental Studies, 26*(3).

Suresh Kumar, C., *et al.* (2020). Hydroxyapatite for bone related applications derived from sea shell waste by simpleprecipitation method. *Journal of Asian Ceramic Societies, 8*(2), 416-429.

Suriyaraj, S.and Selvakumar, R. (2016). Advances in nanomaterial based approaches for enhanced fluoride and nitrate removal from contaminated water. *Royal Socity of Chemistry Advances, 6*(13), 10565-10583.

Tadesse, M., *et al.* (2018). Assessment of the level of some physico-chemical parameters and heavy metals of Rebu river in oromia region, Ethiopia. *Molecular Journal of Biology and Medicine, 3*(4), 99-118.

Tang, Q., *et al.* (2018). Enhanced defluoridation capacity from aqueous media via hydroxyapatite decorated with carbon nanotube. *Frontiers in chemistry, 6*, 104.

Targonska, S., *et al.* (2020). Theranostic applications of nanostructured silicate-substituted hydroxyapatite codoped with Eu^{3+} and Bi^{3+} ions - a novel strategy for bone regeneration. *American Chemical Socity Biomaterials Science and Engineering, 6*(11), 6148-6160.

Tite, T., *et al.* (2018). Cationic substitutions in hydroxyapatite: Current status of the derived biofunctional effects and their in vitro interrogation methods. *Materials, 11*(11), 2081.

Tolkou, A. K., *et al.* (2021). Recently developed adsorbing materials for fluoride removal from water and fluoride analytical determination techniques: A review. *Sustainability, 13*(13), 7061.

Tomar, G., *et al.* (2015). Enhanced fluoride removal by hydroxyapatite-modified activated alumina. *International Journal of Environmental Science and Technology, 12*(9), 2809-2818.

Trinkunaite-Felsen, J., *et al.* (2015). Synthesis and characterization of iron-doped/substituted calcium hydroxyapatite from seashells Macoma balthica (L.). *Advanced Powder Technology, 26*(5), 1287-1293.

Ungureanu, E., *et al.* (2023). In vitro evaluation of Ag-and Sr-doped hydroxyapatite coatings for medical applications. *Materials, 16*(15), 5428.

Valizadeh, S., *et al.* (2014). Modified Fe_3O_4-hydroxyapatite nanocomposites as heterogeneous catalysts in three UV, Vis and Fenton like degradation systems. *Applied Surface Science, 319*, 358-366.

Vazquez-Munoz, R., *et al.* (2020). Bismuth nanoparticles obtained by a facile synthesis method exhibit antimicrobial activity against Staphylococcus aureus and Candida albicans. *Biomedical Chemistry and Biomedical Engineering, 2*(1), 1-12.

Vitta, Y., *et al.* (2020). Synthesis of iron nanoparticles from aqueous extract of Eucalyptus robusta Sm and evaluation of antioxidant and antimicrobial activity. *Materials science for energy technologies, 3*, 97-103.

Wan, K., *et al.* (2021). Removal of fluoride from industrial wastewater by using different adsorbents: A review. *Science of the Total Environment, 773*, 145535.

Wang, H., *et al.* (2022). A review on heterogeneous photocatalysis for environmental remediation: From semiconductors to modification strategies. *Chinese Journal of Catalysis, 43*(2), 178-214.

Wang, J.andGuo, X. (2020). Adsorption kinetic models: Physical meanings, applications, and solving methods. *Journal of Hazardous Materials, 390*, 122156.

Wang, L., *et al.* (2017). Insight into mechanisms of fluoride removal from contaminated groundwater using lanthanum-modified bone waste. *Royal Socity of Chemistry Advances, 7*(85), 54291-54305.

Wei, L., *et al.* (2019). Synthesis and structure properties of Se and Sr co-doped hydroxyapatite and their biocompatibility. *Journal of Materials Science, 54*(3), 2514-2525.

Wei, W., *et al.* (2015). Fast removal of methylene blue from aqueous solution by adsorption onto poorly crystalline hydroxyapatite nanoparticles. *Journal of Nanomaterials and Biostructures, 19*, 1343-1363.

Wei, Y., *et al.* (2022). Synergistic fluoride adsorption by composite adsorbents synthesized from different types of materials - A Review. *Frontiers in chemistry, 10*.

Weng, W., *et al.* (2003). Sol–gel preparation of bioactive apatite films. *Surface and Coatings Technology, 167*(2-3), 292-296.

Wilcock, C., *et al.* (2017). Preparation and antibacterial properties of silver-doped nanoscale hydroxyapatite pastes for bone repair and augmentation. *Journal of biomedical nanotechnology, 13*(9), 1168-1176.

Wimalasiri, A. V. K., *et al.* (2021). Structure–activity relationship of lanthanide-incorporated nano-hydroxyapatite for the adsorption of fluoride and lead. *American Chemical Socity omega, 6*(21), 13527-13543.

Wimalasiri, A. V. K., *et al.* (2021). Microwave assisted accelerated fluoride adsorption by porous nanohydroxyapatite. *Materials Chemistry and Physics, 257*, 123712.

Wu, L., *et al.* (2021). Study on the adsorption properties of methyl orange by natural one-dimensional nano-mineral materials with different structures. *Scientific reports, 11*(1), 10640.

Xu, W.-l., *et al.* (2022). A facile strategy for one-step hydrothermal preparation of porous hydroxyapatite microspheres with core–shell structure. *Journal of Materials Research and Technology, 17*, 320-328.

Xu, Z., *et al.* (2020). Using polyacrylamide to control particle size and synthesize porous nano hydroxyapatite. *Results in Physics, 16*, 102991.

Xuan, T.-C., *et al.* (2015). Comparative characterization of microstructure and luminescence of europium doped hydroxyapatite nanoparticles via coprecipitation and hydrothermal method. *Optik, 126*(24), 5019-5021.

Yahia, I., *et al.* (2017). Facile microwave-assisted synthesis of Te-doped hydroxyapatite nanorods and nanosheets and their characterizations for bone cement applications. *Materials Science and Engineering: C, 72*, 472-480.

Yan, Y., *et al.* (2022). Robust and multifunctional 3D graphene-based aerogels reinforced by hydroxyapatite nanowires for highly efficient organic solvent adsorption and fluoride removal. *American Chemical Socity Applied Materials and interfaces, 14*(22), 25385-25396.

Yang, D., *et al.* (2023). Nanotherapeutics with immunoregulatory functions for the treatment of bacterial infection. *Biomaterials research, 27*(1), 73.

Ye, H., *et al.* (2009). Characterization of sintered titanium/hydroxyapatite biocomposite using FTIR spectroscopy. *Journal of Materials Science: Materials in Medicine, 20*, 843-850.

Yedekçi, B., *et al.* (2021). Synthesis and sintering of B, Sr, Mg multi-doped hydroxyapatites: Structural, mechanical and biological characterization. *Journal of the Mechanical Behavior of Biomedical Materials, 115*, 104230.

Yilmaz, B., *et al.* (2019). Co-doped hydroxyapatites as potential materials for biomedical applications. *Microchemical Journal, 144*, 443-453.

Yu, X., *et al.* (2013). Removal of fluoride from drinking water by cellulose@ hydroxyapatite nanocomposites. *Carbohydr Polym, 92*(1), 269-275.

Yu, Y., *et al.* (2018). Yttrium-doped iron oxide magnetic adsorbent for enhancement in arsenic removal and ease in separation after applications. *Journal of colloid and interface science, 521*, 252-260.

Yuan, Q., *et al.* (2018). Bioactive silver doped hydroxyapatite composite coatings on metal substrates: synthesis and characterization. *Materials Chemistry and Physics, 218*, 130-139.

Zeng, R., *et al.* (2019). Preparation of anionic-cationic co-substituted hydroxyapatite for heavy metal removal: Performance and mechanisms. *Journal of Solid State Chemistry, 280*, 120960.

Zhao, Z., *et al.* (2016). Ion-doping as a strategy to modulate hydroxyapatite nanoparticle internalization. *Nanoscale, 8*(3), 1595-1607.

Zinabu, E., *et al.* (2018). Impacts and policy implications of metals effluent discharge into rivers within industrial zones: A Sub-Saharan perspective from Ethiopia. *Environmental management, 61*(4), 700-715.

Zou, R., *et al.* (2020a). Novel and efficient red phosphorus/hollow hydroxyapatite microsphere photocatalyst for fast removal of antibiotic pollutants. *Journal of Physics and Chemistry of Solids, 139*, 109353.

Zou, R., *et al.* (2020b). Novel design of porous hollow hydroxyapatite microspheres decorated by reduced graphene oxides with superior photocatalytic performance for tetracycline removal. *Solid State Sciences, 99*, 106067.

7. APPENDIX

Appendix 1 Single Factor ANOV Statistical Test result of Fe^{3+} ions doped HA nanomaterials for F^- ions adsorption

Source of variation	Sum of squares	Difference	Mean square	F	P	F crit.
Between Groups	5.64225	3	1.88075	8.590842	0.032289	6.591382
Within Groups	0.8757	4	0.218925			
Total	6.51795	7				

Appendix 2 Single Factor ANOV Statistical Test result of Bi^{3+} ions doped HA nanomaterials for F^- ions adsorption

Source of variation	Sum of squares	Difference	Mean square	F	P	F crit.
Between Groups	1.24605	3	0.41535	0.857674	0.531519	6.591382
Within Groups	1.9371	4	0.484275			
Total	3.18315	7				

Appendix 3 Single Factor ANOV Statistical Test result of Bi^{3+} and Fe^{3+} ions co-doped HA nanomaterials for F^{-} ions adsorption

Source of variation	Sum of squares	Difference	Mean square	F	P	F crit.
Between Groups	34.19074	3	11.39691	182.6062	0.066234	6.591382
Within Groups	0.24965	4	0.062413			
Total	34.44039	7				

Appendix 4 Single Factor ANOV Statistical Test results for the comparison of Fe^{3+} ions doped HA with Bi^{3+} ions doped HA nanomaterials for F^{-} ions adsorption

Source of variation	Sum of squares	Difference	Mean square	F	P	F crit.
Between Groups	50.50125	1	50.50125	96.88489	0.042718	5.987378
Within Groups	3.1275	6	0.521253			
Total	53.62875	7				

Appendix 5 Single Factor ANOV Statistical Test results for the comparison of Fe^{3+} ions doped HA with Bi^{3+} ions and Fe^{3+} ions co-doped HA nanomaterials for F^{-} ions adsorption

Source of variation	Sum of squares	Difference	Mean square	F	P	F crit.
Between Groups	49.005	1	49.005	14.88383	0.008382	5.987378
Within Groups	19.755	6	3.2925			
Total	68.76	7				

Appendix 6 Single Factor ANOV Statistical Test results for the comparison of Bi^{3+} ions doped HA with Fe^{3+} ions and Bi^{3+} ions co-doped HA nanomaterials for F^{-} ions adsorption

Source of variation	Sum of squares	Difference	Mean square	F	P	F crit.
Between Groups	199.0013	1	199.0013	67.2775	0.000177	5.987378
Within Groups	17.7475	6	3.2925			
Total	216.7488	7				

8. PUBLICATIONS

1. Dagne Bayih Adamu, Enyew Amare Zereffa, Teshome Abdo Segne, Mohd Hasmizam Razali, Bundi Roba Lemu. Synthesis and characterization of bismuth-doped hydroxyapatite nanorods for fluoride removal. *Environmental Advances* 2023, 12:100360. **Elsiver**, scopus and DOAJ indexed.
   https://doi.org/10.1016/j.envadv.2023.100360

2. Dagne Bayih Adamu, Enyew Zereffa, Teshome Abdo Segne, Mohd Hasmizam Razali, Bundi Roba Lemu. Synthesis of iron-substituted hydroxyapatite nanomaterials by co-precipitation method for defluoridation. *Materials Research Express* 2023, 10(4):045006. **IOP publishers**, Scopus indexed.
   DOI 10.1088/2053-1591/acca65

3. Dagne Bayih Adamu, Lemma Teshome Tufa, Jaebeom Lee, Enyew Zereffa, Teshome Abdo Segne, Mohd Hasmizam Razali. Facile synthesis of bismuth and iron co-doped hydroxyapatite nanomaterials for high-performance fluoride ions adsorption. Journal of Environmental Chemical Engineering. 2023, 11(6):111196. **Elsiver**, Science Citation Index Expanded and INSPEC indexed.
   https://doi.org/10.1016/j.jece.2023.111196